

Microfluidic devices for automated analysis of ingested bacteria in the *Caenorhabditis elegans* intestine

Présentée le 22 novembre 2023

Faculté des sciences et techniques de l'ingénieur
Laboratoire de microsystemes 2
Programme doctoral en microsystemes et microélectronique

pour l'obtention du grade de Docteur ès Sciences

par

Farzad REZAEIANARAN

Acceptée sur proposition du jury

Prof. H. Shea, président du jury
Prof. M. Gijs, directeur de thèse
Prof. P. Rezai, rapporteur
Prof. W. Keil, rapporteur
Prof. G. Villanueva, rapporteur

And what is the human experience in its rawest form? The eternal tension between ever-evolving dreams and fears.

Inspired by "The Void", 2008 by Ice-Pick Lodge

Acknowledgments

I would like to begin by thanking my supervisor **Prof. Martin Gijs** for giving me the opportunity to pursue my doctoral studies in **LMIS2**. Thanks to his knowledge, kindness and broad vision, the last 5 years have been fruitful not only for my scientific growth but also for my personal development. Under his guidance, I was given the freedom to satisfy my scientific curiosities without being pressured or stressed to meet tight deadlines. While my efforts did not always lead to success, Martin always supported me by highlighting the positive aspects of my work, giving me confidence, and reminding me of my potential. In particular, the last 18 months of my PhD were fraught with anxiety, self-doubt and lack of motivation. It was thanks to Martin's support that I managed to grow as a person, overcome the difficulties, and complete my PhD studies. I am indebted to him for his compassion, understanding and kindness.

I am also sincerely thankful to **Melis** and **Lucie** for going not just one but a thousand extra miles for me. Their support during the last 18 months of my PhD was indispensable to my success. I want to thank them for taking time out of their busy schedules to meet with me, listen to my worries and feelings, and comfort me.

I would like to thank **Prof. Pierre Gönczy** and **Ella Muller** at "Gönczy Lab" for the fruitful collaboration. Additionally, I want to express my gratitude to **Prof. Harm-Anton Klok** and **Dr. Corey Stevens** at "Laboratoire des Polymères" for their help and scientific inputs. I would like to also thank the **CMi** and **BIOP** staff members for their help with the microfabrication processes and optical microscopy, respectively. I would like to thank **Prof. Herbert Shea**, **Prof. Pouya Rezai**, **Prof. Wolfgang Keil** and **Prof. Guillermo Villanueva** for accepting to be the jury members of this thesis and for their valuable scientific inputs.

I would like to express my thanks to **Baris**, **Roger**, **Yang**, **Daniel**, **Alix** and **Xiaopeng**, the previous members of **LMIS2**. In addition, I would like to thank **Vittorio** and **Lin** for the delicious foods they made whenever I visited them. I greatly enjoyed the moments that we shared together. I would like to thank **Muaz** for sharing moments in "Holy Cow!", and also for our numerous never-ending discussions! I am also thankful to **Jalil** for the wonderful discussions we had on the subtleties of microfabrication processes. I admire your vision and perspective on teaching. Serving as the teaching assistant for your practical course on microfabrication was a great pleasure for me.

I would like to express my gratitude to **Elizabeth**, **Patrick** and **Nathalie** from the "Crissier house" where I stayed during my PhD studies. You received me with open arms since the first day. I am thankful for your openness, kindness and patience throughout these last 5 years. I enjoyed the time that we spent together, in particular, being able to have dinner every night with you was a great gift to me. Thank you for making the "Crissier house" a second home for me. Thank you for being my second family in Switzerland. Also sorry for not learning to speak French; I promise to learn it if I end up staying in the French-speaking part of Switzerland. I would like to also express my gratitude to **Reza**, whom I met at the "Crissier house". It was that fateful meeting on a Thursday afternoon, the heart-to-heart

connection made on that day, that gave me the resolve and the courage to fight for my dreams. Thank you, my friend!

Last but not the least, I would like to thank my family during these last 8 years that I have been studying in Switzerland. Thank you, my dear sister **Farzaneh**, for sending me messages and calling me, asking how I am doing. Thank you for the good times that I spent with you and **Farzad** during Christmas and Easter holidays. More than anyone, I want to thank my **father** and **mother** for their never-ending compassion and kindness. I wouldn't be here without your support. No matter what words I use, I can never thank you enough. If I am who I am today, it is because of your constant care and attention. I am forever indebted to you. Thank you from the bottom of my heart!

Farzad

Crissier, 16.08.2023

Abstract

Host-microbiota interactions play an important role in health, diseases, and ageing in humans. Obesity, diabetes, and neurodegenerative disorders are examples of diseases that are influenced by the gut microbiota. Additionally, gut microbiota mediates drug action and can help with fighting against pathogens and toxins. However, due to the variation in the genome of humans and complexity of the intestinal microbiota, the mechanism by which microbiota can have such wide-ranging impact are not well understood. The nematode *Caenorhabditis elegans* (*C. elegans*) is a genetically tractable organism with similarity to human genome and is a powerful model organism for studying host-microbiota interactions. In particular, studies on microbial pathogenesis and innate immunity that employed this nematode, were successful in discovering virulent mechanism of pathogenic bacteria as well as the evolutionary conserved innate immunity pathways.

In this thesis, we explored on-chip high-resolution imaging of the fate of intestinal bacteria. In the first part of our work, we developed a framework that enabled us to perform, for the first time, high-resolution imaging and analysis of the intestinal bacterial load of *C. elegans* during early adulthood. In the second part, we used our framework to investigate bacterial food digestion and accumulation in wild-type adult worms that fed on either commensal or pathogenic bacteria. As the developed framework relied on immobilizing the worms via fixation, in the third part, we attempted to carry out on-chip reversible immobilization and high-resolution *in vivo* imaging of the gut microbiota as well as worm embryos.

In the first part, we carried out high-resolution z-stack fluorescence imaging of Red Fluorescent Protein (RFP)-labelled *Escherichia coli* (*E. coli*) OP50 in the intestine of *C. elegans* using a spinning disk confocal microscope (SDCM) equipped with a 60x oil immersion objective. To enable z-stack fluorescence imaging at such a resolution, the worms were loaded and fixed on microfluidic chips based on a thin cover glass substrate. The obtained z-stack fluorescent images were afterwards analysed using IMARIS software, whereby a 3D representation of the bacteria in the intestine of each worm was constructed. Subsequently, bacterial spots were detected by IMARIS software and were later analysed in an automated fashion through bivariate histograms that displayed the intensities and the volumes of these spots. Our results showed the importance of single-worm resolution analysis, which is missing from all the previously conducted studies on bacterial presence in the *C. elegans* gut, carried out either using conventional methods or via microfluidics.

In the second part, using our framework for high-resolution imaging and analysis, we investigated the bacterial food digestion and accumulation in adult *C. elegans* worms that have fed on either non-pathogenic RFP-labelled *E. coli* OP50 or pathogenic RFP-labelled *Pseudomonas aeruginosa* (*P. aeruginosa*) PAO1 during the first 4 days of adulthood. We discovered that the pattern of the bacteria-derived fluorescence signal in the intestine of the worms depended on the bacteria they were fed. In the case of RFP-labelled *E. coli* OP50-fed worms, individual fluorescent spots, originating from intact bacteria, could be observed in the intestine. In contrast, in the case of RFP-labelled *P. aeruginosa* PAO1-fed worms, we could observe individual fluorescent spots (originating from intact bacteria)

dispersed in large regions of diffuse fluorescence (RDF) which originate from disrupted bacteria. For both cases, the quantitative analysis showed the intestinal bacterial load generally increases with age of the worm, albeit at a faster rate for RFP-labelled *P. aeruginosa* PAO1-fed worms. The qualitative observations and the quantitative results, when understood in the context of previous studies, suggest a reduced metabolism in RFP-labelled *P. aeruginosa* PAO1-fed worms compared to those fed on RFP-labelled *E. coli* OP50.

As our framework for high-resolution imaging and analysis of ingested bacteria relied on worm fixation, in the third part, we made efforts to replicate the same level of high-resolution imaging and analysis but achieved *in vivo* on a microfluidic chip capable of immobilizing the worm reversibly. We thus designed a number of microfluidics devices all of which featured valves for the reversible immobilization of the worms present in rectangular culture chambers. While we could sufficiently immobilize the worms for high-resolution imaging of intestinal bacteria, we could not reliably control the positions where the worms were immobilized, which is essential for the automation of the imaging procedure. More importantly, due to intestinal peristalsis, the bacteria are regularly displaced within the intestinal lumen and therefore it was not possible to acquire z-stack fluorescent images, which are necessary for constructing 3D representations of intestinal bacteria. Overall, performing *in vivo* automated high-resolution z-stack fluorescence imaging was out of reach.

Lastly, in a collaborative work with the lab of Prof. Gönczy, we designed several polydimethylsiloxane (PDMS) microwell arrays for investigating symmetry breaking and polarity establishment in one-cell stage *C. elegans* embryos. The conventional approach for studying symmetry breaking and polarity establishment relies on time-lapse z-stack fluorescence imaging of one-cell stage embryos that are mounted horizontally on agarose pads. However, since the symmetry breaking event occurs near the future posterior pole, it is preferable to image the embryos vertically from the future posterior pole. Consequently, we designed and fabricated arrays of PDMS microwells with different shapes and sizes to facilitate the placement of the ellipsoid embryos in the vertical orientation and thereby enable vertical imaging of symmetry breaking and polarity establishment from the poles. We evaluated the fabricated microwells in terms of the ease of embryo insertion, the verticality of the placed embryos and the consistency of the approach. We also checked the embryos for potential deformations or viability issues.

Keywords

C. elegans, high-resolution imaging and analysis, bacterial load, microfluidics, symmetry breaking

Résumé

Les interactions entre l'hôte et le microbiote jouent un rôle important dans la santé, les maladies et le vieillissement chez l'homme. L'obésité, le diabète et les troubles neurodégénératifs sont des exemples de maladies influencées par le microbiote intestinal. En outre, le microbiote intestinal joue un rôle de médiateur dans l'action des médicaments et peut aider à lutter contre les agents pathogènes et les toxines. Cependant, en raison de la variation du génome humain et de la complexité du microbiote intestinal, le mécanisme par lequel le microbiote peut avoir un impact aussi large n'est pas bien compris. Le nématode *Caenorhabditis elegans* (*C. elegans*) est un organisme génétiquement traitable qui présente des similitudes avec le génome humain et constitue un puissant organisme modèle pour l'étude des interactions entre l'hôte et le microbiote. En particulier, les études sur la pathogenèse microbienne et l'immunité innée qui ont utilisé ce nématode ont permis de découvrir le mécanisme virulent des bactéries pathogènes ainsi que les voies de l'immunité innée conservées au cours de l'évolution.

Dans cette thèse, nous avons exploré l'imagerie haute résolution sur puce du devenir des bactéries intestinales. Dans la première partie de notre travail, nous avons développé un cadre qui nous a permis d'effectuer, pour la première fois, l'imagerie et l'analyse à haute résolution de la charge bactérienne intestinale de *C. elegans* au début de l'âge adulte. Dans la deuxième partie, nous avons utilisé notre cadre pour étudier la digestion et l'accumulation de nourriture bactérienne chez les vers adultes de type sauvage qui se sont nourris de bactéries commensales ou pathogènes. Comme le cadre développé repose sur l'immobilisation des vers par fixation, dans la troisième partie, nous avons tenté de réaliser une immobilisation réversible sur puce et une imagerie *in vivo* à haute résolution du microbiote intestinal ainsi que des embryons de vers.

Dans la première partie, nous avons réalisé une imagerie de fluorescence z-stack à haute résolution d'*Escherichia coli* (*E. coli*) OP50 marqué à la Protéine Fluorescente Rouge (PFR) dans l'intestin de *C. elegans* à l'aide d'un Microscope Confocal à Disque Rotatif (MCDR) équipé d'un objectif à immersion d'huile 60x. Pour permettre l'imagerie de fluorescence en z-stack à une telle résolution, les vers ont été chargés et fixés sur des puces microfluidiques basées sur un substrat mince en lamelle couvre-objet. Les images fluorescentes z-stack obtenues ont ensuite été analysées à l'aide du logiciel IMARIS, ce qui a permis de construire une représentation 3D des bactéries présentes dans l'intestin de chaque ver. Les taches bactériennes ont ensuite été détectées par le logiciel IMARIS et analysées de manière automatisée à l'aide d'histogrammes bivariés affichant les intensités et les volumes de ces taches. Nos résultats ont montré l'importance de l'analyse de la résolution d'un seul ver, qui est absente de toutes les études précédentes sur la présence bactérienne dans l'intestin de *C. elegans*, réalisées soit à l'aide de méthodes conventionnelles, soit par microfluidique.

Dans la deuxième partie, en utilisant notre cadre pour l'imagerie et l'analyse à haute résolution, nous avons étudié la digestion et l'accumulation des aliments bactériens chez les vers *C. elegans* adultes qui se sont nourris soit d'*E. coli* OP50 non pathogène marqué par PFR, soit de *Pseudomonas aeruginosa* (*P. aeruginosa*) PAO1 pathogène marqué par PFR au cours des 4 premiers jours de l'âge adulte. Nous

avons découvert que le profil du signal de fluorescence généré par les bactéries dans l'intestin des vers dépendait de la bactérie dont ils étaient nourris. Dans le cas des vers nourris avec *E. coli* OP50 marqué par PFR, des taches fluorescentes individuelles, provenant de bactéries intactes, ont pu être observées dans l'intestin. En revanche, dans le cas des vers nourris avec *P. aeruginosa* PAO1 marqué par PFR, nous avons pu observer des taches fluorescentes individuelles (provenant de bactéries intactes) dispersées dans de vastes Régions de Fluorescence Diffuse (RFD) provenant de bactéries perturbées. Dans les deux cas, l'analyse quantitative a montré que la charge bactérienne intestinale augmente généralement avec l'âge du ver, bien qu'à un rythme plus rapide pour les vers nourris de *P. aeruginosa* PAO1 marqué par PFR. Les observations qualitatives et les résultats quantitatifs, lorsqu'ils sont compris dans le contexte d'études antérieures, suggèrent un métabolisme réduit chez les vers nourris avec *P. aeruginosa* PAO1 marqué par PFR par rapport à ceux nourris avec *E. coli* OP50 marqué par PFR.

Comme notre cadre pour l'imagerie et l'analyse à haute résolution des bactéries ingérées reposait sur la fixation du ver, nous nous sommes efforcés, dans la troisième partie, de reproduire le même niveau d'imagerie et d'analyse à haute résolution, mais réalisé *in vivo* sur une puce microfluidique capable d'immobiliser le ver de manière réversible. Nous avons donc conçu un certain nombre de dispositifs microfluidiques, tous dotés de valves pour l'immobilisation réversible des vers présents dans des chambres d'élevage rectangulaires. Bien que nous ayons pu immobiliser suffisamment les vers pour l'imagerie à haute résolution des bactéries intestinales, nous n'avons pas pu contrôler de manière fiable les positions où les vers étaient immobilisés, ce qui est essentiel pour l'automatisation de la procédure d'imagerie. Plus important encore, en raison du péristaltisme intestinal, les bactéries sont régulièrement déplacées dans la lumière intestinale et il n'a donc pas été possible d'acquérir des images fluorescentes en z-stack, qui sont nécessaires pour construire des représentations 3D des bactéries intestinales. Dans l'ensemble, la réalisation d'une imagerie de fluorescence z-stack automatisée à haute résolution *in vivo* était hors de portée.

Enfin, dans le cadre d'une collaboration avec le laboratoire du professeur Gönczy, nous avons conçu plusieurs réseaux de micropuits en polydiméthylsiloxane (PDMS) pour étudier la rupture de symétrie et l'établissement de la polarité dans les embryons de *C. elegans* au stade d'une cellule. L'approche conventionnelle pour étudier la rupture de symétrie et l'établissement de la polarité s'appuie sur l'imagerie de fluorescence z-stack time-lapse d'embryons au stade d'une cellule qui sont montés horizontalement sur des coussinets d'agarose. Cependant, comme la rupture de symétrie se produit près du futur pôle postérieur, il est préférable d'imager les embryons verticalement à partir du futur pôle postérieur. Par conséquent, nous avons conçu et fabriqué des réseaux de micropuits en PDMS de différentes formes et tailles pour faciliter le placement des embryons ellipsoïdes dans l'orientation verticale et permettre ainsi l'imagerie verticale de la rupture de symétrie et de l'établissement de la polarité à partir des pôles. Nous avons évalué les micropuits fabriqués en termes de facilité d'insertion des embryons, de verticalité des embryons placés et de cohérence de l'approche. Nous avons également vérifié que les embryons ne présentaient pas de déformations potentielles ou de problèmes de viabilité.

Mots-clés

C. elegans, imagerie et analyse à haute résolution, charge bactérienne, microfluidique, rupture de symétrie

Contents

Acknowledgments	III
Abstract	V
Résumé.....	VII
Contents	X
List of figures	XIII
1 Introduction.....	1
1.1 Thesis outline	1
1.2 <i>C. elegans</i> and host-microbiota interactions	2
1.3 A general overview of <i>C. elegans</i> and commensal bacteria	3
1.4 <i>C. elegans</i> and pathogenic bacteria	5
2 State of the art.....	14
2.1 The need for devices enabling high-throughput and high-resolution studies	14
2.2 A brief overview of microfluidic devices for <i>C. elegans</i> studies	15
2.3 Long-term high-resolution imaging in microfluidic devices.....	16
2.4 Microfluidic devices for host-microbiota studies	28
2.5 Imaging modalities for <i>C. elegans</i> studies	34
2.6 Immobilization strategies for high-resolution <i>in vivo</i> imaging of intestinal bacteria	36
3 High-resolution imaging and analysis of the intestinal bacterial load of <i>Caenorhabditis elegans</i> during early adulthood.....	39
3.1 Introduction	40
3.2 Materials and methods.....	42
3.2.1 Chip materials and chemicals	42
3.2.2 Worm and bacteria culture and preparation.....	42
3.2.3 Fabrication of the microfluidic chip	43
3.2.4 Image processing and statistical analysis.....	43
3.2.5 Microscopy platform and the imaging parameters	44
3.3 Experimental.....	44
3.3.1 Operation of the microfluidic device	44

3.3.2	Experimental planning	45
3.3.3	Imaging procedure and analysis	47
3.4	Results.....	52
3.5	Discussion.....	58
3.6	Conclusions	60
4	Difference in intestine content of <i>Caenorhabditis elegans</i> when fed on non-pathogenic or pathogenic bacteria	61
4.1	Introduction	62
4.2	Materials and methods.....	64
4.2.1	Materials and chemicals	64
4.2.2	Worm and bacteria culture and preparation.....	65
4.2.3	Fabrication of the microfluidic chip	65
4.2.4	Image processing and statistical analysis.....	66
4.2.5	Microscopy platform and the imaging parameters	66
4.3	Experimental.....	67
4.3.1	The design and operation of the microfluidic chip platform	67
4.3.2	Experiment planning	68
4.3.3	Imaging procedure and analysis	70
4.4	Results.....	76
4.5	Discussion.....	80
4.6	Conclusion.....	81
5	High-resolution in vivo imaging of bacteria in the <i>C. elegans</i> gut.....	82
5.1	Introduction	83
5.2	Design and fabrication of microfluidic devices	84
5.3	High-resolution <i>in vivo</i> imaging of intestinal bacteria	88
5.4	Conclusions	91
6	Studying symmetry breaking in one-cell stage <i>C. elegans</i> embryos using PDMS microwell arrays	92
6.1	Introduction	93
6.2	Materials and methods.....	95
6.2.1	Materials and chemicals	95

6.2.2	Worm strains.....	95
6.2.3	Design and fabrication of the PDMS microwells.....	96
6.2.4	Evaluating the different PDMS microwell designs and the live imaging of symmetry breaking.....	97
6.3	Results and discussions.....	97
6.4	Conclusions	100
7	Conclusion and future perspectives.....	102
7.1	Achieved results.....	102
7.2	Future perspectives	103
	Bibliography.....	105
	Curriculum Vitae	115

List of figures

- Figure 1-1- (a) An example of a competition assay in which worms fed on lawns with different ratios of streptomycin-resistant *E. coli* OP50 to *S. Typhimurium* SL1344 (10:1,000, 10:10, 10:0.1) for 6 h. The intestinal bacterial load was measured after 24 hours of feeding on a streptomycin-susceptible *E. coli* OP50. (b), (c) and (d) Fluorescence imaging of worms after feeding for 12 hours on a mixed lawn of *E. coli* OP50-pGB5 and *S. Typhimurium* SL1344-pRZT3 at a ratio of 10:0.1 (100-fold *E. coli* excess). Reproduced from [51]...... 7
- Figure 1-2- (a) Variation in shifting assays showing the persistence of *E. coli* OP50 colonies in the intestine of the worms after they were transferred from an *E. coli* OP50 lawn to a *S. typhimurium* SL1344 lawn. The bacterial levels in the intestine are shown after 24, 48 and 96 hours of feeding on *S. typhimurium* SL1344 lawn. Reproduced from [51]. (b) Young adult worms fed for 5 hours either on a mixed lawn of *S. typhimurium* SL1344–GFP and *E. coli* DH5 α at ratio of 1:1000 or on plates containing only *E. coli* DH5 α –GFP. Afterwards, they were transferred to a *E. coli* OP50 lawns and the bacterial levels in the intestine were measured every 24 hours. Reproduced from [54]. 7
- Figure 1-3- TEM micrographs of midbody cross-sections of worms fed on heat-killed *E. coli* OP50 (a, c, e) and *S. aureus* NCTC8325 (b, d, f) for 12 (a, b), 24 (c, d) and 36 h (e, f). Scale bar = 1 μ m. iec, intestinal epithelial cell; mv, microvilli; b, bacterial cell; bwm, body wall muscle; aj, apical junctions, asterisk in b indicates membrane blebbing. Reproduced from [56]...... 9
- Figure 1-4- TEM micrographs of midbody cross-sections of worms fed on *E. coli* OP50 (a, c) and *P. aeruginosa* PA14 (b, d, e, f) for 8 (a, b), 24 (c, d) and 48 h (e, f). Black asterisk and arrowheads highlight the disruption of the microvilli and OMV shedding from the bacterial cells, respectively, in f. Scale bar in a-d, 2 μ m; in e, 1 μ m; in f, 0.5 μ m. iec, intestinal epithelial cell; mv, microvilli; b, bacterial cell; bwm, body wall muscle; aj, apical junctions; em, extracellular material. Reproduced from [56]. 12
- Figure 2-1- (a) An array of chambers and tapered channels (clamps) for on-chip lifespan studies and imaging of *C. elegans* worms. (b) Culturing of *C. elegans* worms in the chambers. (c) Brightfield images of worms immobilized in tapered channels. Reproduced from [81]...... 17
- Figure 2-2- (a) Wormspa microfluidic device for automated long-term monitoring of *C. elegans* worms while maintaining the identity of individual worms. The worms are confined within traps and thus their movement is restricted. (b) a step module allows enables a fast exchange of the media (c) a concentration gradient allows the delivery of different doses to 32 channels. (d) Tracking of eggs released by worms cultured on chip through automated imaging and image analysis shows that worms maintained on chip and NGM plates have similar egg release rate. (e) Food restriction-induced nuclear localization of DAF-16::GFP captured through fluorescence imaging. (f) Diffusive pattern of DAF-16::GFP in a well-fed worm (left) in contrast to the localized expression of DAF-16::GFP in the nuclei of cells in the head of starved worms (right). Reproduced from [82]. 18
- Figure 2-3- Microfluidic device for automated high-content phenotyping of *C. elegans* worms. (a) Design of the microfluidic device. Automated long-term monitoring of (b) the volume and (c) the

motility of *hsp-6::gfp* worms in different feeding conditions. (d) Automated fluorescence imaging and analysis yielding the number of fluorescent protein aggregates in *p_{unc-54}::Q40::YFP* worms fed under *ad libitum* (AL) and diet restriction (DR) conditions. Reproduced from [83]. 19

Figure 2-4- Microfluidic device for laser axotomy and longitudinal studies of nerve regeneration in *C. elegans* worms. (a) The design of the microfluidic device. (b) The profile of the 3D-tapered channel; the width and the height of the channel both change across the length of the channel. High-resolution fluorescent image of (c) a non-regrowing PLM neuron in an *egl-20* mutant and (d) regrowing PLM neuron in a *zdis5* mutant. Scale bar = 10 μ m. Reproduced from [84]...... 19

Figure 2-5- a 2-layer microfluidic chip for laser axotomy and nerve regeneration studies. (a) Overview of the microfluidic device in which the trap area (for immobilization and surgery) is shown with a yellow rectangle while the three recovery chambers are delineated by a blue rectangle (b) Magnified view of the trap area; 4 valves (indicated by the yellow rectangles) are used to enable regulation of the inlet flow (1), fine positioning of the worm (2, 3) and transfer to the recovery chambers (4). (c) 3D view of the red rectangle in (b) showing how the pressure-mediated deformation of the membrane immobilizes the worm (in green) for imaging and surgery. (d) Two-photon imaging characterizing the deformation profile of the membrane at different air pressures ranging from 0 to 35, 70, 105, 140 and 175 kPa. (e) Two-photon imaging displaying a immobilized worm at 105 and 140 kPa. (f) Time-lapse imaging of nerve regeneration. Reproduced from [87]...... 20

Figure 2-6- The design of the microfluidic device for fully automated on-chip laser axotomy. Reproduced from [86]...... 21

Figure 2-7- (a) In the trapping area, the worm is pushed against the sieve structure and afterwards is immobilized via the pressure-mediated deformation of the membrane (b) Two types of valves. A partially sealing valve on the left and the completely sealing valve on the right. The presence of a 3D interconnect (middle) in the microfluidic device allows the implementation of a completely sealing valve in 2-layer device which is required for fine positioning of the worm during immobilization. In this implementation, only a thin cover slip lies in between the worm and the microscope objective and thus optical distortions are reduced to a minimum. Reproduced from [86]. 22

Figure 2-8-(a) The design of the 2-layer microfluidic device where the flow layer and the compression layer are shown with red and blue colors, respectively. (b) The magnified view of the circular chamber and its cross-section. As the height of the flow layer is only 20 μ m, the compression layer is kept in vacuum to increase the height of the chamber to accommodate worms from L1 stage till the onset of egg laying. Scale bar =250 μ m. (c) The immobilization principle: a flow in the flow layer first pushes the worm toward the filters and, afterwards, the pressurization of the compression layer deforms the membrane and gently immobilizes the worm against the filters. (d) The device can support the development of the worm from the L1 stage till the onset of egg laying. The pressure-mediated deformation of the membrane can immobilize the worms regardless of their age. Scale bar = 100 μ m. Reproduced from [85]...... 23

Figure 2-9- A single-layer microfluidic device featuring traps and valves for the long-term immobilization and high-resolution imaging of *C. elegans*. a) The design of the microfluidic devices.

Scale bar = 1000 μm . b-e) The worm loading sequence. Scale bar = 100 μm . b) empty chamber. c) The first valve (on the left) is opened to allow the entry of the worm to the trap while the second valve (on the right) remains closed. d) The worm is immobilized by keeping both valves closed. The immobilized worm can still feed and release eggs. (e) Unsuitable worms can be released by opening the second valve. f) An adult worm maintained on the device for 48 hours. g) High-resolution fluorescence and DIC imaging of the germ cells using a 60x/NA 1.2 objective. The germ cell nuclei and cell membranes can be identified via fluorescently-labelled histone (*mCherry::H2B*) and t-SNARE transgenes (*syn-4p::GFP*), respectively. Scale bar = 25 μm . Reproduced from [93]. 24

Figure 2-10- The design of the 2-layer microfluidic device for developmental studies on *C. elegans*. (a) The design of the flow layer, where the loading inlet (for worms and bacterial solution), PF127 inlet, chambers and the waste outlet are highlighted. (b) The design of the heating layer showing the heating channels which deliver the hot liquid required for the thermogelling of PF127 solution. Additionally, the valves controlling the flow layer inlets and valves for keeping the worms in the chambers are shown. Reproduced from [89]. 25

Figure 2-11- Imaging procedure. (a) During the culturing period, the chamber is filled with M9 buffer containing *E. coli* OP50. (b) To acquire images, the M9 buffer is first replaced with the PF127 solution. (c) The chambers are then heated to trigger the sol-to-gel transition in PF127 solution which immobilizes the worms for imaging. (d) Once the images are acquired, the heating is stopped and the PF127 becomes a liquid again which can be then removed from the chamber. Scale bar = 60 μm . Reproduced from [89]. 26

Figure 2-12- Different modules of a hydrogel-droplet microfluidic device for manipulation, high-resolution imaging and sorting of *C. elegans* worms. (a) Droplet production. (b) Storage and immobilization in a serpentine channel for imaging. (c) Sorting. Reproduced from [90]. 26

Figure 2-13- High-resolution images of L1 worms immobilized in PF127 droplets obtained utilizing a 63x objective. (a) Brightfield image. Scale bar = 25 μm . Fluorescent images of (b) a URX neuron in the head and (c) a coelomocyte. Scale bars = 12 μm in (b) and (c). Reproduced from [90]. 27

Figure 2-14- (a) The main elements of the microfluidic platform. (b) Photograph of the device and the schematic picture of the temperature control system. (c) Cross-section view of the assembled device. The inset shows the part of the microfluidic chip that can be observed from the imaging area. Scale bar = 2 mm (d) Different designs of microfluidic chips with (i) 1, (ii) 4 and (iii) 32 culture chambers. Scale bars = 200 μm . Reproduced from [88]. 28

Figure 2-15- Time-lapse fluorescence imaging of four ALS model worms immobilized using PF127. These are transgenic worms (strain AM725) which express mutated human SOD1-YFP fusion proteins in the body wall muscle cells. Scale bar = 100 μm . (b) Growth rate of SOD1-YFP aggregates in each worm. (c) Average protein aggregate area per worm area over time. (d) High-resolution brightfield and fluorescent images of worm 1 acquired 91 hours after the worm was loaded on the device using a 63x/1.4 NA oil immersion objective. The morphology of the aggregates can be mapped. (e) Superimposed high-resolution brightfield and fluorescent images of worm 4 acquired 43 and 60 hours

after the worm was loaded on the chip. The arrow heads point at the specific SOD1-YFP aggregates which can be tracked over time. Scale bars = 20 μ m. Reproduced from [88]..... 28

Figure 2-16- The First microfluidic device reported for, exposing worms to pathogenic bacteria and their subsequent treatment with antimicrobial compounds. (a) 4 CGGs supplying 8 unique chambers with different concentration of antimicrobials compounds. Worms and subsequently pathogenic bacteria are loaded in the chambers from the central inlet. (b) Survival of worms exposed to *S. aureus* or *E. coli* in different media (c) The survival of worms that were initially exposed to *S. aureus* for 6 hours and were subsequently treated with amoxicillin. (d) The effect of the antimicrobial compound and its dose on the survival of infected worms (exposed to *S. aureus* for 6 hours). Reproduced from [95]. 29

Figure 2-17- HandKAchip, a microfluidic device enabling automated killing assays using *C. elegans*. (a) The design of the microfluidic device. (b) The low contrast of dead worms with respect to the background allows the automated monitoring of worm survival over time. (c) The infection gene response (*irg-1::GFP*) monitored through fluorescence imaging. D) The displacement of the worms between two acquired frames yields the motility of the worms. Single-worm resolution analysis represented through the cumulative distribution function (CDF) of (e) infection gene response (*irg-1::GFP*) and (f) motility. Reproduced from [96]. 30

Figure 2-18- Microfluidic device for automated studies on bacterial transit in *C. elegans* worms. (a) The design of microfluidic device. (b) Two example images from time-lapse fluorescence imaging of freely-moving worms feeding on GFP-tagged *E. coli* HT115. (c) Analyzing the time-lapse fluorescent images (in b) yields the spatiotemporal evolution of bacterial load in the body of worms. Spatial averaging over the first third and the last third of the worm body yields the bacterial load in the pharynx and hindgut, respectively. d) Time-evolution of bacterial load in pharynx and hindgut of worms fed on GFP-tagged *E. coli* HT115. e) One example image from time-lapse fluorescence imaging of immobilized worms. (f) Time-evolution of bacterial load in the pharynx of immobilized worms. Reproduced from [97] 32

Figure 2-19- Microfluidic device for automated studies on bacterial load dynamics and digestion. (a) The design of the microfluidic devices. (b) The worms are immobilized within a trapping channel. (c) Example of an immobilized adult worm. (d) High-resolution brightfield/fluorescent images of intestinal bacteria. (e-g) Using a brightness level thresholding protocol, the total fluorescence intensity (e) and the fluorescence intensity of intact (f) and disrupted bacteria (g) can be extracted from d. (h) Time-lapse high-resolution images of bacteria in the hindgut of an immobilized worm fed RFP-labelled *E. coli* OP50. (i) The time evolution of the intensity of disrupted bacteria (extracted from h according to the protocol described in e-g) was used to estimate a bacterial digestion time constant of 14 ± 4 s. Reproduced from [98]. 33

Figure 2-20- Simplified schematics demonstrating the principle of operation in (a) widefield fluorescence microscopy and (b) Laser Scanning Confocal Microscopy (LSCM). (a) In widefield epifluorescence microscopy, the out-of-focus light is collected by the camera resulting in a blurry image with reduced contrast. Reproduced from [99]. (b) In LSCM, most of the out-of-focus light (blue

and green dashed line) is blocked by the pinhole while the in-focus light (red solid line) passes through the pinhole and is collected by the PMT. For the sake of simplicity, the galvanometer mirror for the scanning of the excitation laser beam is not shown. Reproduced from [103]...... 34

Figure 2-21- (a) Schematic drawing of the Yokogawa implementation of SDCM featuring an array of micro lenses to increase the illumination throughput. Reproduced from [107]. (b) A simplified schematic demonstrating the principle of operation in light sheet microscopy. Optical sectioning capability is acquired by illuminating only a thin layer of the sample. Reproduced from [99]...... 36

Figure 3-1-Microfluidic device for high-resolution imaging of *E. coli* OP50 in the *C. elegans* gut. (a) Schematic representation of one of the five lanes in each device. The lanes are 1300 μm wide and 75 μm high. The filters serve to contain the worms in the channel. Scale bar = 2 mm. (b) Image of a fabricated microfluidic chip where the channels are filled with a blue dye. Scale bar = 2 cm. (c) Brightfield image of the filter structures. Scale bar = 300 μm . (d) Brightfield image of the worms in the channel. Scale bar = 0.8 mm 45

Figure 3-2- The experimental steps involved in high-resolution imaging of fluorescent *E. coli* in the *C. elegans* gut. a) Suspending adult worms in S-medium overnight yields numerous synchronized L1s in developmental arrest the next day. b) ~ 100 synchronized L1s are transferred to an NGM plate seeded with *E. coli* OP50 and kept there until they become adults (46 hours at 22 C°). c) The adult worms are taken from the NGM plate and are washed in S-medium in a 1.5 ml Eppendorf tube; since adults naturally sediment at the bottom of the tube, the supernatant is removed (1:10 dilution) and the process is repeated until the number of *E. coli* OP50 present is reduced to a minimum (a total of $1:10^{10}$ dilution). d) The adults are now transferred to an NGM plate seeded with *E. coli* OP50 expressing RFP and kept there for 24 h. e) To remove the progenies of the adult worms, every 24 h, the adults are taken from the plate and are suspended in S-medium and a total of $1:10^{10}$ dilution is performed (similar to “step c”). Afterwards, the adult worms are transferred to new NGM plates seeded with *E. coli* OP50 expressing RFP. Given the number of the days, adult worms are planned to be fed on *E. coli* OP50 expressing RFP (1 day, 2 days, 3 days and 4 days), steps d and e are repeated as many times as required (0x, 1x, 2x and 3x for 1 day, 2 days, 3 days and 4 days feeding, respectively). Once the last repetition of “step e” is done, the worms are instead kept in the Eppendorf tube containing S-medium for one hour to ascertain that recently ingested bacteria are fully processed. f) The worms are loaded on the microfluidic chip and are fixed with a 4%PFA solution. Afterwards, the tubings are cut and clipped and the microfluidic chip is transferred to an SDCM for high-resolution imaging of the gut bacteria. 46

Figure 3-3- Imaging of typical fixed worms that have fed on RFP *E. coli* OP50 (for 1 day in a and 4 days in b, c and d). a) Brightfield image of fixed worms, in which, the hindgut, as area of interest, is delineated. High-resolution b) Brightfield image, c) RFP channel image where the bacteria in the hindgut can be seen and d) GFP channel image where the worm autofluorescence can be observed. (a: 10x objective, scale bar = 250 μm ; b, c and d: High-resolution imaging using an oil-immersive 60x objective, scale bar = 40 μm) 48

Figure 3-4- Z-stack fluorescence imaging of typical fixed worms that have fed on RFP *E. coli* OP50 for 4 days. The z-stacks are taken using a 60X oil-immersion objective in both RFP and GFP channels. They include 250 slices with a step size of 200 nm and total focal range of 50 μm . a) The three example slices with their associated planes of focus, positioned relative to a schematic worm cross-section. Typical images acquired at these slices are shown both in the RFP channel (b, c and d) and the GFP channel (e, f and g), where the z numbers of images e, f and g are the same as those of images b, c and d, respectively.) Focusing reveals RFP *E. coli* OP50 in the different regions of the hindgut, as highlighted by the white dashed lines in b-d). The signal in the GFP channel originates from autofluorescence in the adult worms. In the presence of strong autofluorescence, the latter signal can also be observed in the RFP channel, as delineated by the yellow dashed lines in (b and e) and (d and g). In these cases, the RFP signal present in the yellow dashed line-limited area in (b and d) should not be attributed to the existence of bacteria and therefore should be omitted from any visualization/analysis pertaining to bacterial load. (Scale bar = 40 μm) 49

Figure 3-5- Visualization and processing of z-stack fluorescent images in IMARIS. a) 3D presentation of a z-stack image by assembling all the slices from each channel together (RFP and GFP) and displaying both channels at the same time. In this case, a worm that has fed on RFP *E. coli* OP50 for 3 days is being shown. Scale bar = 15 μm b) *E. coli* OP50 are seen as orange spots, while the yellow spots originate from the worm's autofluorescence. Since the worm's autofluorescence is strong in these spots, the signal is present both in the GFP channel and the RFP channel and thus the spots appear yellow (as shown by the arrows) due to the overlap of the green color and the red color. A proper bacterial spot detection procedure should identify the orange spots and ignore the yellow ones. Scale bar = 10 μm . c) The spot detection relies on an estimated of the smallest spot size and an IMARIS parameter called "Quality". In our case, we used 1 μm in x and y directions and 2 μm in z direction. The parameter "Quality" is related to the intensity at the center of a spot while including corrections for the background intensity around that spot. This parameter acts as threshold and thus only spots with higher intensities than this threshold value will be accepted. The optimized "Quality" parameter value was 150 and it was such that the detected spots matched the actual spots we could observe, and no false positives were present. In addition, a threshold limit (3500-4000) was also set on the intensity of the GFP channel to reject the spots that originate from the worm autofluorescence. The white ellipsoids shown are the spots detected using the above-mentioned parameters. It should be noted that at this stage, all the spots are assumed to have the same size that is set by the smallest spots size we used for the spot detection algorithm. It's only due to the perspective projection that the farther spots are seen smaller. Scale bar = 10 μm . d) The centers of the detected spots are used as seeds and by using a "local contrast" method the spot size is determined. In this approach, the intensity distribution around the center of the detected spot is first adjusted by subtracting from it the intensity of the background in the vicinity of that spot. After this correction, only the region that has intensity higher than a threshold value is considered to be a part of the spot. The optimized threshold value was 80.4 and at this value the finalized spots matched visually to the actual spots. The white ellipsoids seen are the finalized detected spots. Since an actual bacterial region may not be always ellipsoid, the size determination algorithm uses the volume of this region to construct an ellipsoid that has the same volume as this region. Therefore, there is not always a perfect overlap

between the actual bacterial spot and the finalized detected spot (as shown by the arrows in d). Scale bar = 10 μm 51

Figure 3-6- Analysis of the detected bacterial spots in a single worm that has fed on RFP labelled *E. coli* OP50 for 4 days. a) The table contains the volume (Vol) and the average intensity of the detected bacterial spots (Int), as extracted from IMARIS. C. Int is the average spot intensity corrected for the background. The product of the volume and the corrected average intensity of each spot (Vol · C. Int) is proportional to the number of bacteria within that spot. The summation of (Vol · C. Int) over all the bacteria spots in one worm is proportional to the total bacterial load in that worm. b) Histogram of the volume of the detected bacterial spots. c) Histogram of the average intensity of the detected bacterial spots. d) The bivariate histogram showing the distribution of the volume and the average intensity of the bacterial spots. 54

Figure 3-7- Bivariate histograms displaying the average distribution of the volumes and the average intensities of the bacterial spots in the hindgut of worms that have fed on RFP-labelled *E. coli* OP50 for a) one day (n = 10), b) two days (n = 16), c) three days (n = 11) and d) four days (n = 12). e) The total bacterial load of each worm after each day of feeding on fluorescent bacteria. The horizontal bar shows the average total bacterial load for each day while the error bars represent the range of bacterial load in each day. * $p \leq 0.05$ 55

Figure 3-8- Bivariate histograms of 3 selected worms that have fed on RFP-labelled *E. coli* OP50 for 4 days. The total number of bacterial spots is a) 31, b) 100 and c) 422. The total bacterial load is a) $2.2042\text{E}+05 \mu\text{m}^3 \cdot \text{au}$ b) $1.8478\text{E}+06 \mu\text{m}^3 \cdot \text{au}$ and c) $6.7720\text{E}+06 \mu\text{m}^3 \cdot \text{au}$ 57

Figure 4-1- Microfluidic chip for high-resolution imaging of bacteria in the intestine of *C. elegans*. a) The schematic shows the typical design of the lanes in the device. Every device has 5 lanes that are 1300 μm wide and 75 μm high. The worms are contained in the channel by the filters. Scale bar = 2 mm. b) Photograph of a fabricated microfluidic device. The tubing and the channels of the device are filled with a blue dye for better visibility. Scale bar = 2 cm. c) Brightfield image showing the filter structures. Scale bar = 300 μm . d) Brightfield image showing the worms that are loaded in the microfluidic chip. Scale bar = 0.8 mm 67

Figure 4-2- Protocol and experimental planning for high-resolution imaging of fluorescent *E. coli* and *P. aeruginosa* in the intestine of *C. elegans*. a) An adult population of worms are suspended overnight in S-medium to obtain a multitude of synchronized L1s in developmental arrest the following day. b) ~ 100 synchronized L1s are placed on an NGM plate seeded with *E. coli* OP50 and grown there for 46 hours at 22 °C until they reach adulthood. c) Using S-medium, the adult worms are removed from the NGM plate and are placed inside a 1.5 ml Eppendorf tube, where they naturally settle at its bottom. This allows the removal of *E. coli* OP50 through the replacement of the supernatant with fresh S-medium (dilution of 1:10). This procedure is repeated 10 times ($1:10^{10}$ total dilution) to drastically reduce the number of *E. coli* OP50 present. d) The adults are then fed for 24 hours by being placed on an NGM plate, that depending on the experiment to be performed, is either seeded with RFP-labelled *E. coli* OP50 or RFP-labelled *P. aeruginosa* PAO1. e) To prevent the progenies from overcrowding the plates and mixing with the adult population, every 24 hours the adults along with their progenies are

washed off the plate using S-medium and are placed inside a 1.5 ml Eppendorf tube. As the L1 progenies remain suspended in S-medium, similar to “step c”, a total of 1:10¹⁰ dilution is carried out to remove them and the remaining adults are then moved to a new NGM plate seeded with the same bacteria as before (e.g., if the adult worms were feeding on RFP-labelled *E. coli* OP50, the new NGM plate is also seeded with this bacteria). Steps d and e are repeated according to the number of days the adult worms are planned to be fed on either RFP-labelled *E. coli* OP50 or RFP-labelled *P. aeruginosa* PAO1 (0x, 1x, 2x and 3x of repetitions for 1 day, 2 days, 3 days and 4 days of feeding, respectively). After the last iteration of “step e”, the worms stay for an hour within the Eppendorf tube containing S-medium to ensure the complete digestion of recently eaten bacteria. f) The worms are then transferred to the microfluidic device where they are fixed using a 4% PFA solution. Shortly after, the tubings are cut and fastened with clips and the microfluidic device is moved to an SDCM, where high-resolution imaging of the intestinal bacteria is carried out..... 69

Figure 4-3- Imaging of representative fixed worms that had RFP-expressing *P. aeruginosa* PAO1 as their food source (duration of feeding is 1 day in figure a and 2 days in figures b, c and d). a) Brightfield image of the fixed worms where the hindgut, as the key area for high-resolution imaging, is marked. High-resolution b) Brightfield image, c) RFP channel image showing the diffuse fluorescence originating from the disrupted bacteria and d) GFP channel image showing the worm’s autofluorescence. Lack of overlap in the fluorescence signal in figure c and d, indicates that fluorescence in the RFP channel is not due to the worm’s autofluorescence. r (a: 10x objective, scale bar = 250 µm; b, c and d: High-resolution imaging using an oil-immersive 60x objective, scale bar = 40 µm)..... 72

Figure 4-4- High-resolution z-stack fluorescence imaging (in the RFP channel) of representative fixed worms that had RFP-labelled bacteria (*P. aeruginosa* PAO1 or *E. coli* OP50) as their food source for 4 days. a) An illustration of the worm cross-section where individual fluorescent spots originating from intact fluorescent bacteria (*P. aeruginosa* PAO1 or *E. coli* OP50) and diffuse fluorescence, originating from disrupted bacteria, that is present only in fluorescent *P. aeruginosa* PAO1-fed worms, can be observed in one of the slices (Z₁). Z-stack imaging is required to capture all fluorescence signals across the height of the intestine. Example slices from the z-stack images (in the RFP channel) of worms that have fed on fluorescent *P. aeruginosa* PAO1 (b) and *E. coli* OP50 (d). c) Magnified view of the blue rectangle in “b” which shows diffuse fluorescence and individual fluorescent spots (marked by the white circle) in fluorescent *P. aeruginosa* PAO1-fed worms. The presence of diffuse fluorescence from disrupted *P. aeruginosa* PAO1 does not exclude the presence of intact *P. aeruginosa* PAO1. e) Magnified view of the blue rectangle in “d”, in which individual fluorescent spots (delineated by the white dashed line) originating from intact fluorescent *E. coli* OP50 can be clearly observed. b and d: scale bar = 40 µm. c and d: scale bar = 20 µm. 73

Figure 4-5- Visualization and analysis of the raw z-stack fluorescent images in IMARIS. 3D images of representative worms fed on either fluorescent *E. coli* OP50 (for 3 days) or fluorescent *P. aeruginosa* PAO1 (for 2 days) are constructed by assembling all the slices of the z-stack fluorescent images in the RFP channel. a) Individual fluorescence spots (as shown by green arrows) originating from intact bacteria spread through the intestine of RFP-labelled *E. coli* OP50-fed worms. b) Individual fluorescent

spots dispersed (as shown by green arrows) in a region of diffuse fluorescence (RDF) in the intestine of fluorescent *P. aeruginosa* PAO1-fed worms. As the pattern of the fluorescence signal is different in a and b, two different methods are used to analyze the bacterial load. c) Spot detection is governed by an estimation of the smallest fluorescent spot size as well as the threshold value for the local background-corrected intensity at the center of the spots, which is referred to as the "Quality" parameter in IMARIS. We chose the value of the "Quality" parameter such that detected spots match the actual spots and false positives were not present. Once the spots are detected, their sizes still need to be determined through the IMARIS "local contrast" method in which only the region around the center of the spot that has an intensity higher than a certain threshold, is considered to be part of the spot. It should be mentioned that the perceived spot size is affected by the perspective projection that is used to display the 3D image. d) Surface detection in IMARIS is done by setting a threshold value for the fluorescence intensity that can be then used to define a surface. In our case, we set this value such that it is always 600 higher than the average background noise in each set of experiments. Afterwards, using this surface one can define the RDF as the volume within which the fluorescence intensity exceeds the threshold value. Scale bar = 20 μm 75

Figure 4-6 High-resolution fluorescent images acquired in the RFP channel of representative fixed worms that have fed on RFP-expressing *P. aeruginosa* PAO1 for different durations. The ratio of the background-corrected average signal intensity in the intestinal lumen (as indicated by the yellow ribbon) to the background-corrected average signal intensity of an area outside of the intestinal lumen (as shown by blue rectangle) is equal to (a) 14, (b) 26, (c) 52 and (d) 30..... 76

Figure 4-7-. Single-worm-resolution analysis of bacterial load in adult worms that have fed on RFP-labelled bacteria for 1, 2, 3 and 4 days. Each data point is calculated for a single worm. The horizontal bars denote the average value and the error bars (where applicable) show the range of the data. The number of worms devoid of bacteria at each day is mentioned inside the plot alongside the data points of the respective day (applicable to a, b, e and f). An AVG intensity of zero indicates worms whose intestines are devoid of bacteria (applicable to c and d). a) The total volume of fluorescent spots, c) the background-corrected average intensity of fluorescent spots and e) the multiplication of a and c which is proportional to the total number of intact bacteria. a, c and e are obtained from fluorescent *E. coli* OP50-fed worms with worm sample size of 10, 16, 11 and 12, for day 1 to day 4, respectively. b) The total volume of RDF, d) the average intensity of RDF and f) the multiplication of the b and d which is proportional to the SIDM. b, d and f are obtained from fluorescent *P. aeruginosa* PAO1-fed worms with worm sample size of 13, 12, 13 and 11 for day 1 to day 4, respectively. * $p \leq 0.05$, ** $p \leq 0.01$ 79

Figure 5-1- The initial design of the microfluidic device and the immobilization procedure. (a) The design of a single lane featuring the flow (blue) and the control (green) layers. (b) An enlarged top view (control layer not shown) of the leftmost chamber and its cross-section. Notice that since the cross-section of the leftmost chamber is displayed, the control layer is enclosed only on the left side. The chambers are 2.1 mm long and 1.4 mm wide and are used for culturing and imaging the worms. (c) The immobilization procedure. (c) A fluid flow in the flow layer pushes the worm towards the filter structure for a duration of T_w . (d) Afterwards, while maintaining the same flow rate in the flow layer,

the control layer is gradually pressurized by applying a constant flow rate in the control layer. The pressure-mediated deformation of the membrane gradually and gently immobilizes the worm. Once sufficient immobilization is achieved (at a critical pressure resulting from maintain the flow rate for a duration of T_c), the flow rate in the control layer is brought to zero and the flow rate in the flow layer is reduced, and imaging can be carried out..... 85

Figure 5-2- Patterning of Cr/glass masks. (a) Spin-coating of PR. (b) UV exposure of PR using a direct laser writer. (c) Development of PR. (d) Etching of Cr (e) PR stripping and rinsing..... 86

Figure 5-3- SU-8 molds for PDMS molding. (a) Spin-coating of SU-8 followed by a soft bake step. (b) Exposure of SU-8 followed by a post-exposure bake and a relaxation step. (c) Development of SU-8 followed by a hard-bake step. (d) TMCS surface treatment. (e) Spin-coating or casting of degassed liquid (uncured) PDMS followed by a second degassing step before curing process can take place. (f) casted PDMS can manually detached from the mold..... 87

Figure 5-4- (a) Detaching the spin-coated flow layer from the respective SU-8 mold. (b) Potential bonding issue between the flow-layer and the glass substrate due to the deformation of the flow layer after removal from the SU-8 mold..... 88

Figure 5-5- (a and b) Brightfield images of worms becoming immobilized near the chamber walls. (a) The blue- and red arrows show the chamber wall and the faint outline of the deformed membrane, respectively. Scale bar = 500 μm . (b) Scale bar = 250 μm 89

Figure 5-6- Brightfield and fluorescence microscopy images of a moderately immobilized adult wild-type worm shortly after being fed RFP-labelled *E. coli* OP50. (a) Brightfield and (b) fluorescent image of the worm in the RFP channel; bacteria can be seen both in the grinder and just after the pharyngeal-intestinal valve. Contrary to our intention, the worm is immobilized next to the chamber wall instead of the filters. Scale bar = 50 μm 89

Figure 5-7- Fluorescence microscopy of adult wild-type *C. elegans* fed with RFP-labelled *E. coli* OP50 bacteria. The dashed lines and the greens arrows, respectively, show the outline of worm and the beginning of the intestine. (a) The orange arrow shows a group of bacteria in the pharynx; single bacteria can be resolved both in the intestine and the microfluidic channel. (b) The intestine gives a uniform fluorescence signal. (c) Single bacteria in the intestine can be resolved. (d) Single bacteria cannot be resolved when having a tightly-packed group of bacteria. Scale bar = 50 μm 90

Figure 5-8-(a) Variations in the design of the chambers (filters, trap, width, length and height) to enable immobilization of the worm in the area delineated by the red dashed line. (b-f) An example of a successful sequence of worm immobilization. Scale bar = 500 μm 91

Figure 6-1- Establishment of polarization in one-cell stage *C. elegans* embryo. Anterior (A) and Posterior (P) poles are on the left and right side of the embryo, respectively. (a) Initially, active RhoA, Myosin II and anterior PAR complex are enriched on the cortex, while the posterior PAR proteins are present uniformly throughout the cytoplasm (not shown). (b) and (c) During polarity establishment, the sperm-derived centrosomes locally inhibit the activity of RhoA in the posterior pole which results in the anterior-directed actomyosin flows. These flows lead to the presence of anterior PAR complex

on the posterior pole of the embryo and at the same time, the posterior PAR proteins are loaded on the posterior pole. 94

Figure 6-2- Z-stack time-lapse imaging of symmetry breaking and polarization from the posterior pole. 95

Figure 6-3- Design of the PDMS microwells. An array of cylindrical (a) microwells, (b) microwells with two outlets and (c) microwells with four outlets. D and S represent the diameters of the circular cross-section and the distance (spacing) between the microwells, respectively. 96

Figure 6-4- Screening of the PDMS microwells for the vertical placement of the embryos. Microwells with a depth of 50 μm and radii of (a) 30, (b) 32, (c) 34 and (d) 36 μm . The marked area in (c) highlights a region near the pole of the embryo. (e) A microwell with a depth of 45 μm in which one pole of the embryo is sticking out. In a-e, the topside of the well (near the coverslip) is in focus which enables the qualitative evaluation of the verticality of embryo placement. Microwells with (f) two and (g) four outlets. In f and g, the midsection of the embryo is in focus to better visualize the deformation of the embryos near the outlets. (h) Contortion (marked by the dashed line) in an embryo placed inside a microwell with four outlets. Scalebar: a-e, 15 μm and f-h, 20 μm 98

Figure 6-5- Time-lapse z-stack brightfield and fluorescence imaging of symmetry breaking and polarity establishment in a single-cell stage embryo placed inside a PDMS microwell. NMY-2, the activity of which is necessary for the contractility in the actomyosin network, is tagged with an RFP label while the PAR-2 protein and the centrosomes are tagged with a GFP label. To represent the fluorescent images in the RFP and in the GFP channels, a single plane with the best signal for each respective channel was chosen from the z-stack images. The yellow dashed lines delineate NMY-2. The orange arrows point at the centrosomes. The black dashed line delineates PAR-2 proteins. The local cessation in the contractility of the actomyosin network, and the loading of PAR-2 proteins on the cortex and in the vicinity of the centrosomes can be observed at 8^m 52^s which indicate that the symmetry breaking process has occurred. The actomyosin network-derived signal appearing as a circular area at 0^m 00 and 2^m 48^s, and the loading of PAR-2 proteins and the presence of centrosomes on the rightmost side of the embryo at 8^m 52^s indicate that the embryo is squeezed by the coverslip and is sitting inside the microwell with a tilted orientation. Scale bar (in purple) = 15 μm 99

Figure 6-6- The placement of embryos inside the PDMS microwells. (a) An ideally placed embryo has a vertical orientation and does not experience any deformations. (b) In practice, the embryo is squeezed by the coverslip and has a tilted orientation. 100

1 Introduction

1.1 Thesis outline

In this thesis, we explore on-chip high-resolution imaging of the intestinal bacteria in adult *Caenorhabditis elegans* (*C. elegans*) worms. The first chapter starts with setting the background and explaining the general motivation of studies on host-microbiota interactions using *C. elegans*. Afterwards, a basic overview of the relationship between the worm and bacteria *Escherichia coli* (*E. coli*) OP50 is given. Lastly, the various interactions between the worm and different pathogenic bacteria and the assays involved in these studies are reviewed.

The second chapter mainly discusses the application of microfluidic devices in *C. elegans* research. The advantages of microfluidic devices for *C. elegans* studies are explained. Representative microfluidic devices for long-term high-resolution studies on *C. elegans* are highlighted. In particular, the state-of-the-art microfluidic devices applied to host-microbiota studies are reviewed in detail. The common imaging modalities for studying *C. elegans* are also briefly reviewed.

The third chapter describes in detail our framework for high-resolution imaging and analysis of gut bacteria. In particular, we describe our procedure for on-chip fixation and subsequent high-resolution z-stack fluorescence imaging of adult worms fed fluorescent bacteria. We also explain how we use IMARIS to reconstruct the acquired z-stack images into 3D images and automatically detect the bacterial spots in the intestine. We show the potential of our framework by analyzing the intestinal bacteria in adult worms that were fed fluorescent *E. coli* OP50.

The fourth chapter describes how, using our high-resolution imaging and analysis framework, we investigated the bacterial food digestion and accumulation in adult *C. elegans* worms fed non-pathogenic fluorescent *E. coli* OP50 and pathogenic *Pseudomonas aeruginosa* (*P. aeruginosa*) PAO1.

The fifth chapter details our efforts to replicate the same level of imaging resolution and analysis but carried out *in vivo* using microfluidic devices featuring valves for the immobilization of the worm. We discuss the design and the fabrication of our microfluidic devices, and their performances, in terms of the degree of immobilization and imaging resolution when applied to imaging the intestinal bacteria.

The sixth chapter describes our collaborative work with the lab of Prof. Gönczy, in which we fabricated arrays of polydimethylsiloxane (PDMS) microwells in an attempt to facilitate the vertical placement of one-cell stage embryos and thus enable the imaging of symmetry breaking from the posterior pole.

The seventh chapter provides a summary of the results achieved in this thesis and provides an outlook and direction for further research in the fields addressed in this thesis.

1.2 *C. elegans* and host-microbiota interactions

Host-microbiota interactions have a wide-ranging impact on the health/diseases in humans [1]–[5]. Studies have shown correlations between host microbiota and diseases such as diabetes, obesity, and cardiovascular disease [6], [7]. The microbiota also mediates drug action and helps in fighting against toxins and pathogens [5], [8] and influences the development and the function of nervous system through the gut-brain axis [9]–[11]. It has been reported that the composition of the microbiota in young and old populations are different and may have a role on aging processes [12], [13]. Unfortunately, these studies are mostly of correlative nature and thus the underlying mechanisms are not well understood [1], [14]. This is both due to the variation in the human genome and the complexity of the gut microbiota. The gut microbiota varies among different individuals, and most of the bacteria present in the gut are difficult to culture in laboratories and as a result the genetics of these bacteria are also unknown [14].

C. elegans as a genetically tractable organism is a powerful model organism for studying host-microbiota interactions [1], [2], [8], [15]–[19]. This organism rose to prominence through the work of Sydney Brenner [20] in 1974 that established the nematode as a genetics model organism for studying developmental biology and neurobiology. Featuring a large number of protein-coding genes (7763 of its ~21,000 genes) with human orthologues makes this organism relevant to human biology and diseases [15]. For instance, *C. elegans* has been used to model neurodegenerative diseases such as Alzheimer's disease, Parkinson's disease (PD), amyotrophic lateral sclerosis (ALS), Huntington disease [21]. This bacterivorous nematode is a self-fertilizing hermaphrodite, with a 1 mm long transparent body and can be easily maintained monoxenically (usually *E. coli* OP50) in laboratories [22]. The intestine of the worm is made up of 20 non-renewable epithelial cells that form a cylindrical shape [23]. The apical surface of intestinal cells has a brush border that consists of microvilli that are similar in terms of morphology and function to the their counterparts present in the intestine of humans [19], [24]. The intestine of the worm is involved in digestion, absorption and storage of nutrients, removal of waste via defecation and protection against pathogens and toxins [25]. The small size and the transparency allow the monitoring of the nematode and its internal organs through microscopy and in particular fluorescence imaging [22]. Furthermore, as the organism can be maintained on a single bacterial species, it allows us to isolate and the studying interactions of a single bacterial species with the host [8]. More importantly, the genome of *C. elegans* is sequenced and mutants are readily available which allow investigation of molecular mechanisms of various biological process in the host, including but not limited to those related to evolutionary conserved innate immunity pathways [17]. This together with the fact that the same type of genetic analysis can be applied to the bacteria of interest makes *C. elegans* a powerful model organism for discovering molecular mechanisms underlying the interactions of the bacteria, including pathogenic, commensal and probiotic with the host [8], [17], [19], [26]–[29].

1.3 A general overview of *C. elegans* and commensal bacteria

In nature, *C. elegans* worms, as a bacterivorous organism, are found in rotting vegetables and fruits that are hosts to a variety of bacterial species, including pathogenic ones. As a result, the native microbiome in the intestine of the *C. elegans* is composed of different bacterial species [2], [2], [18], [30]. Dirksen et al characterized the microbial communities in wild type worms found in nature. They isolated the bacteria found in wild type worms and used them to establish an experimental microbiome under laboratory conditions. Their study showed that the native microbiome improves host fitness under standard and stressful conditions and also enhances the resistance of the worm against fungal pathogens [2]. Furthermore, it has been also reported that due to the exposure to numerous bacterial species in nature, *C. elegans* have developed defense mechanisms to avoid pathogenic bacteria [31]. While studying this nematode in the presence of its native microbiome is necessary for obtaining a complete understanding of the functions of its genome [32], in practice, this organism is often studied using a single isolate, the N2 strain, that is fed a single bacterial species, namely, *E. coli* OP50.

The relationship of the worm and the *E. coli* OP50 is dynamic and changes with the age of the worm [8]. In larval stages, the worm is a predator of *E. coli* OP50 as the devoured bacteria are disrupted by the pharyngeal grinder of the worm and in principle, no live bacteria reach the intestine of the worm [33]. Around the L4 stage and the beginning of adulthood, few bacteria manage to survive the pharyngeal grinder and establish small colonies in the intestine of the worm. At this point, the relationship of the worm and the bacteria has become a special case of commensalism, namely a cannibalistic commensalism [8], [34]. The devoured *E. coli* OP50 bacteria that reach the intestine in a disrupted state are a source of food both for the worm and the *E. coli* OP50 colonies present in its intestine. As the worm ages, the excessive proliferation of the *E. coli* OP50 in the intestine becomes detrimental to the health of the worm and can cause constipation in the intestine both of which reflect yet another change in the relationship of the worm and the bacteria, as now *E. coli* OP50 exhibits mildly pathogenic effects [35], [36].

E. coli OP50 bacteria or bacterial food in general provide the worm with both macronutrients and micronutrients [16]. Macronutrients making up the majority of the diet, include carbohydrates, fats and proteins that provide the worm with energy or are absorbed into biomass. In the case of the worm, the bacterial biomass is the main source of macronutrients. Micronutrients including vitamins, cofactors and minerals, make up a much smaller portion of the diet and their influence on the worm's metabolism is indirect and yet significant. Live bacteria can provide the worm micronutrients by delivering the compounds they absorbed from the environment. For example, *E. coli* is itself incapable of synthesizing B12 vitamin, yet is able to absorb it from a culturing media such as LB broth [16]. B12 vitamin is crucial for the health of *C. elegans* worms and the worms that have B12 vitamin-deficiency (as result of having a diet lacking B12 vitamin), have significantly shorter lifespans, longer developmental cycle and are lay considerably fewer eggs [37]. Alternatively, live bacteria can also provide the worms with micronutrients through the by-products of their metabolism. For example, *E.*

coli synthesizes folate and worms that are fed a strain of *E. coli* incapable of producing this vitamin, have increased lifespan [38]. It should be however mentioned that studies show that both the excess or the deficiency in folate can reduce lifespan of the worms and thus it seems that in between these two extremes, a healthy level folate in the worm should exist [38], [39]. Interestingly, studies suggest that *C. elegans* may have a need for live bacteria, as worms cultured on axenic medium or monoxenic medium with killed bacteria have reduced developmental rate and fertility [40], [41]. Lastly, live bacteria can also mediate the impact of the drugs on the worm. It has been reported that the anti-diabetic drug metformin extends the lifespan of the worms by influencing the bacterial folate and methionine metabolism [42]. Interestingly, metformin reduces the lifespans of the worms when they are cultured in axenic mediums or are fed dead bacteria [42]. Additionally, whether metformin decreases or increases the lifespan of the worms depends also on the strain of the bacteria [42].

The degree of intestinal colonization and its impact on the health of the worm depend on the defense mechanisms of the worm and the strain of bacterial food [34]. The worm's first line of defense is its pharyngeal grinder which disrupts ingested bacteria before it enters the intestine [43]. The worm's innate immune system protects the worm from bacteria through evolutionary conserved signaling pathways [17], [44]. These pathways include but are not limited to: (i) DAF-2, an insulin or insulin-like growth factor (IGF)-1 pathway involved in expression of a set of stress responses and antimicrobial genes [34], (ii) p38-like mitogen-activated protein kinase pathway (MAPK) involved in protection against Gram-negative and Gram-positive bacteria and pathogenic fungi [45], [46], (iii) a transforming growth factor-beta (TGF- β) pathway which among other numerous functions also confers pathogenic resistance [47], [48]. Lastly, the peristalsis motion in the intestine and defecation can also help with the removal of bacteria from the intestine [49]. As the worms age, these defense mechanisms decline in their functioning and correlated with this change, the intestinal bacterial in the gut increases until reaches a bacterial strain-dependent saturation limit [34], [50].

Genetic modifications, which influence the functioning of any of the mentioned defense mechanisms, alter the life span and the level of intestinal bacterial colonization of the worms. It should be noted that the life span is generally defined as the time at which 50% of the worm population has died and is represented by the symbol TD_{50} . In the case of *phm-2* mutants, which have defective pharyngeal grinder, ingested bacteria are not disrupted and enter the intestine while being alive. Consequently, the intestines of these mutants when fed on *E. coli* OP50 contain more bacteria at all ages compared to wild type worms [34]. Furthermore, the life span of *phm-2* worms is on average 30% shorter than the life span of wild type worms which again indicates an inverse relationship between intestinal bacterial accumulation and life span [51].

Enhancing the worms' innate immune system through genetic modification can greatly increase the life span of worms [52]. For example, *daf-2* mutants (reduced *daf-2* signaling) fed on *E. coli* OP50 have a TD_{50} of 26 days while wild-type worms with same bacterial diet have a TD_{50} of 13 days (life span extension by 100%) [34]. Concomitant with this phenotype, the number of intestinal bacteria in *daf-2* mutants is 10 times less than the number of intestinal bacteria in wild-type worms [34]. Similar to the case of *phm-2* mutants, this observation suggests an inverse relationship between the intestinal bacterial load and life span.

Interestingly in the case of *daf-2;phm-2* double mutants, until the first 2 days of adulthood, the level of intestinal bacterial load is close to the level of intestinal bacterial load in *phm-2* mutants [34]. However, as the *daf-2;phm-2* worms ages, the level of intestinal bacterial load reduces and becomes close to the level of intestinal bacterial load in *daf-2* worms [34]. This shows one of the many intricacies in the relationship between the different aspects of host defenses and bacteria and reveals a need for genetic analysis and high-throughput screening of the worm. Furthermore, as the worm possesses innate immunity signaling pathways that are evolutionary conserved, these studies are also beneficial in understanding the host-microbiota in mammals including humans [17], [19], [53].

1.4 *C. elegans* and pathogenic bacteria

Having briefly discussed the role of the worm's defense mechanisms, we now examine in more detail how more pathogenic bacterial strains (compared to *E. coli* OP50) affect the health of the worm. Studies have demonstrated that a large number of mammalian pathogens are capable of causing infection and disease in *C. elegans* [17], [19], [53]. More interestingly, the virulence mechanisms that these pathogenic bacteria employ to cause diseases in mammals are relevant to diseases caused by the same pathogens in *C. elegans*. Furthermore, most bacteria, similar to *C. elegans*, can be subjected to genetic analysis and screening. That is why *C. elegans* is a powerful model organism for mechanistic understanding of evolutionarily conserved innate immunity signaling pathways and bacterial pathogenesis.

Salmonella typhimurium (*S. typhimurium*) is a gram-negative pathogen that is capable of causing intestinal colonization and infection in *C. elegans* [34], [51]. The worms feeding on pathogenic *S. typhimurium* exhibit gradual reduction in the rate of pharyngeal pumping as well as decreased motility [54]. The average life span of worms fed on this bacterium is 16% shorter than the same worms fed on *E. coli* OP50 [34]. Additionally, the intestinal bacterial load of worms fed on this bacterium is on average 2.9 times the intestinal bacterial load of the same worms fed on *E. coli* OP50 (measured at 2 days after L4 stage) [34]. However, the starkest difference between the two bacteria, is the ability of *S. typhimurium* to maintain a persistent infection in the intestine of *C. elegans* regardless of the worm age or genotype [51], [54]. Persistent infection capability of any bacteria can be studied using shift and competition assays.

In a typical shift assay, *C. elegans* embryos are grown on Nematode Growth Medium (NGM) plates containing a founder bacterium (in this case [51], *E. coli* OP50 or *S. typhimurium*. SL1344). At 48 hours (day 2) or 96 hours (day 4), the worms are washed and transferred another NGM plate seeded with a different (introduced) bacterium (either *E. coli* OP50 or *S. typhimurium*. SL1344). After 24 hours, of feeding on the second (introduced) bacterial strain, 10 of the worms are selected, washed and homogenized by grinding to obtain the average number of remaining viable founder bacterium and the number of viable introduced bacterium. It was observed that the intestine of worms that were fed *S. typhimurium*. SL1344 for 48 hours, as the founding bacteria, still contained *S. typhimurium* SL1344 bacteria after feeding on *E. coli* OP50 for 24 hours, as the introduced bacterium, regardless of the

worm genotype (wild type, *daf-2*, *daf-16* and *phm-2*) [51]. However, in the case of worms fed *E. coli* OP50 as the founder bacterium, only in worms that fed on this bacterium for 96 hours (and thus worms that are older in age) could the founder *E. coli* OP50 maintain its presence in the face of introduced *S. typhimurium*. SL1344 [51]. Nevertheless, it should be mentioned that in *daf-2* mutants, no *E. coli* OP50 bacteria could be found after the introduction of *S. typhimurium* SL1344 (even after feeding on founder *E. coli* OP50 for 96 hours) [51].

The superior (compared to *E. coli* OP50) capability of *S. typhimurium* to colonize the intestine of *C. elegans* can also be revealed through competition assays. In a typical competition assay, *C. elegans* worms are grown on NGM plates seeded with a mutant strain of *E. coli* OP50 that is susceptible to a given antibiotic (in this particular case [51], streptomycin). At a certain time (in this case at third day of adulthood), the worms are washed and then transferred to NGM plates that contain the same antibiotic (in this case streptomycin) and a mixed lawn of *E. coli* OP50 and *S. typhimurium* SL1344 at different ratios (in this case 0.1:10, 10:10 and 10:0.1). It must be mentioned that the competing bacterial strains present in the mixed lawn should be strains that are resistant to the administered antibiotic (in this case streptomycin). After feeding on this mixed lawn for a certain duration (6 hours in this case), the worms are then washed and transferred to NGM plates seeded with *E. coli* OP50 that is again susceptible the same antibiotic. After spending a certain time feeding on this plate (in this case 24 hours), 10 worms are selected for quantification of the average number of each of the competing strains (antibiotic resistant *E. coli* OP50 and *S. typhimurium* SL1344) in the intestine. Carrying out the competition assay as described above showed that *S. typhimurium* SL1344 could persist in the gut of the worms even when its concentration is 100 times less than the concentration of *E. coli* OP50 in the mixed lawn (Figure 1-1a) [51], while *E. coli* OP50 could persist in the gut only when its concentration was 100 times higher than the concentration of *S. typhimurium* SL1344 in the mixed lawn. This patent difference in the intestinal colonization capability of *S. typhimurium* SL1344 can also be observed using fluorescence imaging (Figure 1-1b, c and d) [51].

The shifting and competition assays can be further modified to assess whether the persistent bacterium is capable of proliferating in the gut. In both assays, the worms are observed at a certain time point after being shifted to a new plate. In the shifting assays, this is the plate with the introduced bacterial strain while in the competition assay, this is usually the plate seeded with antibiotic susceptible bacterial strain. By monitoring how the number of viable persistent bacteria changes with the duration that worms have fed on the new plates, we can determine whether the persistent bacterium is capable of proliferation in the intestine. Figure 1-2 shows an example of modified shifting and competition assays. It can be clearly observed that while *E. coli* OP50 is at best capable of maintaining its presence in the gut, *S. typhimurium* SL1344 easily proliferates in the gut to a great extent (from 1 colony forming unit (CFU) /worm after 5 hours exposure of the worm this pathogenic bacterium to 10^4 CFU/worm after 4 day) [51], [54]. In addition, the results of these modified assays are easier to interpret compared to the typical assay for measuring the number of CFU of intestinal bacteria. In the typical assays, after feeding the worms on a certain bacterial strain for a given duration, 10 worms are selected and grinded by homogenization and afterwards the average number of CFU is determined.

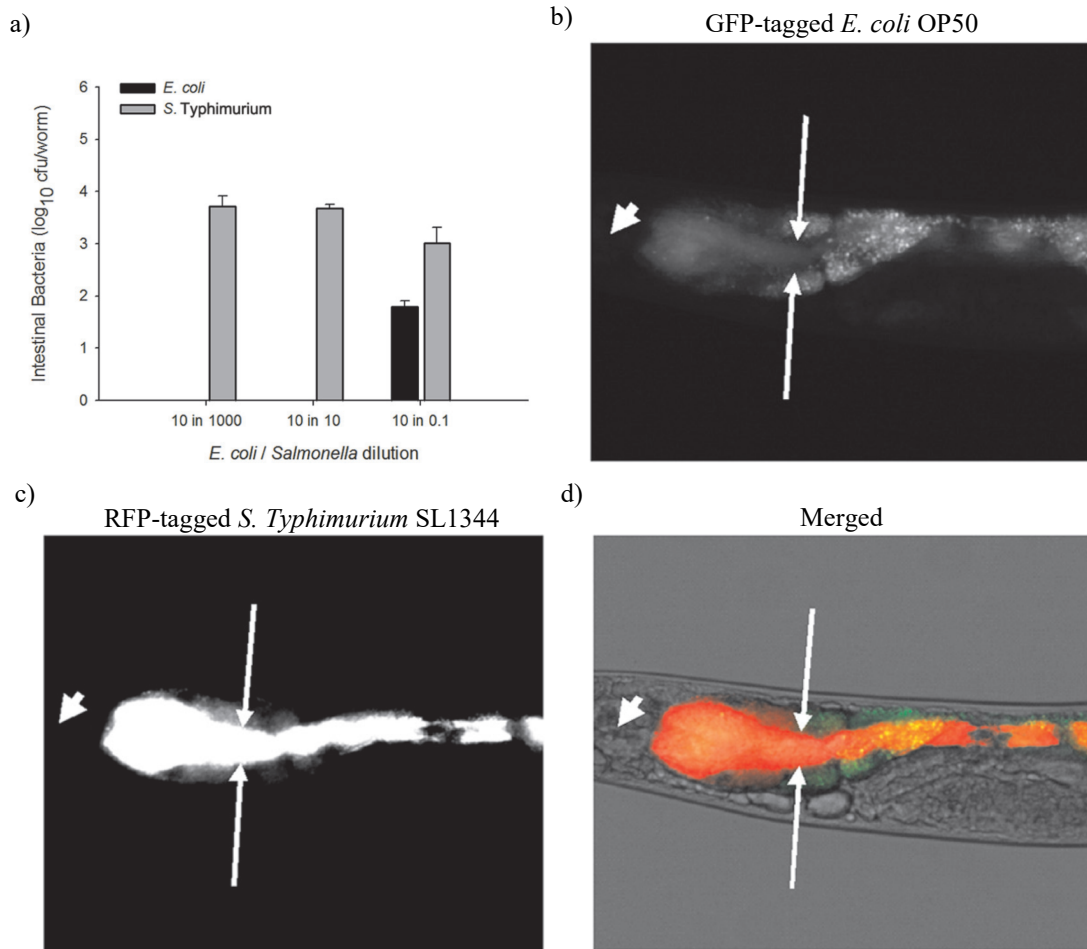


Figure 1-1- (a) An example of a competition assay in which worms fed on lawns with different ratios of streptomycin-resistant *E. coli* OP50 to *S. Typhimurium* SL1344 (10:1,000, 10:10, 10:0.1) for 6 h. The intestinal bacterial load was measured after 24 hours of feeding on a streptomycin-susceptible *E. coli* OP50. (b), (c) and (d) Fluorescence imaging of worms after feeding for 12 hours on a mixed lawn of *E. coli* OP50-pGB5 and *S. Typhimurium* SL1344-pRZT3 at a ratio of 10:0.1 (100-fold *E. coli* excess). Reproduced from [51].

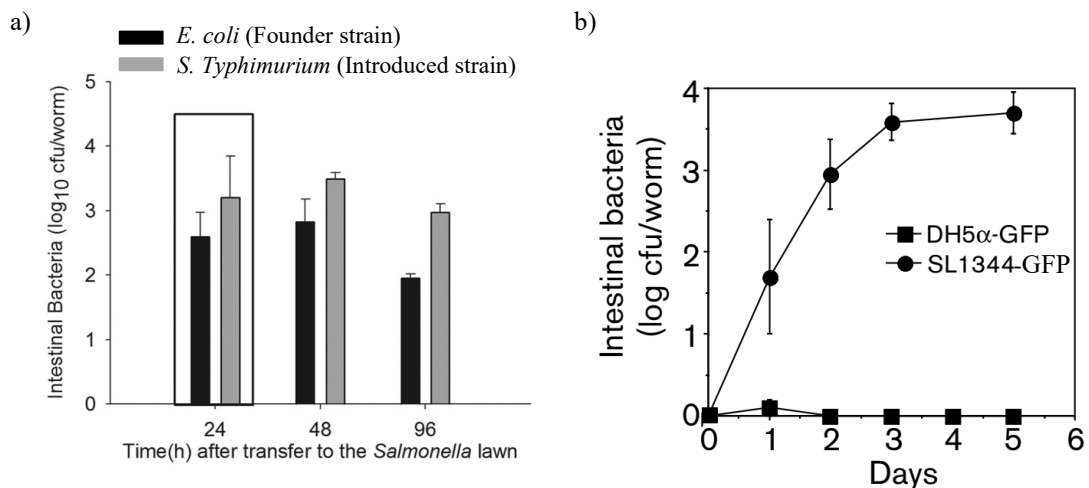


Figure 1-2- (a) Variation in shifting assays showing the persistence of *E. coli* OP50 colonies in the intestine of the worms after they were transferred from an *E. coli* OP50 lawn to a *S. typhimurium* SL1344 lawn. The bacterial levels in the intestine are shown after 24, 48 and 96 hours of feeding on *S. typhimurium* SL1344 lawn. Reproduced from [51]. (b) Young adult worms fed for 5 hours either on a mixed lawn of *S. typhimurium* SL1344-GFP and *E. coli* DH5α at ratio of 1:1000 or on plates containing only *E. coli* DH5α-GFP. Afterwards, they were transferred to a *E. coli* OP50 lawns and the bacterial levels in the intestine were measured every 24 hours. Reproduced from [54].

However, in this case, it is not clear whether the change in the CFU over time is due to mere accumulation of ingested bacteria in the gut, bacterial proliferation in the gut or both at the same time.

Staphylococcus aureus (*S. aureus*) is a gram-positive bacterium and versatile human opportunistic pathogen that can cause a variety of diseases such as severe skin infections and life-threatening infections such as sepsis and pneumonia and endocarditis [17], [55]. The majority of *S. aureus* strains have been shown to be capable of killing the worm through intestinal colonization within 5 days. Even the strains that are not efficient in killing L4 stage and adult worms, can easily kill the worm when it is in earlier developmental stages [55]. During the first 16 to 20 hours of exposure to *S. aureus* lawns, the nematode motility and pharyngeal pumping remains unaffected [55]. Within 24 to 48 hours of exposure, the motility of the worms and the rate of pharyngeal pumping gradually declines, until the worms stop moving and die [55]. Concurrently, after 24 hours of feeding on this pathogenic bacterium, the intestine becomes distended and bacterial accumulation throughout the digestive tract can be observed via fluorescence microscopy [55]. To understand whether continuous exposure to *S. aureus* for 48 hours is required for worm killing, the worms were fed on *S. aureus* for different periods of time and were afterwards moved to lawns seeded with nonpathogenic bacteria [55]. Interestingly, it was observed that worms could completely recover from the exposures to *S. aureus* that lasted less than 8 hours and appeared to be capable of removing this bacterium from their intestine. However, the effects of exposures lasting more than 18 hours were lethal to the worms as the majority of worms would die within 70 hours of being moved to a plate with nonpathogenic bacteria.

In a more recent work, the cytopathology of *S. aureus* infection was examined using Transmission Electron Microscopy (TEM) to obtain a clearer picture of the intestinal damage caused by this pathogenic bacterium (Figure 1-3) [56]. After 12 hours of exposure to this pathogen (Figure 1-3b), the microvilli in the intestine of worms are significantly shortened as evident by comparison to heat-killed non-pathogenic *E. coli* OP50-fed worms (Figure 1-3a). In agreement with previous reports, intestinal accumulation of this pathogenic bacterium could be observed and intestinal distention due to drastic loss of intestinal epithelial cell volume was apparent. Additionally, intestinal cell lysis and considerable plasma membrane blebbing on the apical surface of the intestinal cells could be also seen. After 24 hours (Figure 1-3d) of exposure to *S. aureus*, the microvilli are essentially destroyed and after 36 hours (Figure 1-3e), they have completely disappeared. Concurrently after 36 hours of exposure, further reduction in the volume of the intestinal epithelial cell and increased intestinal cell lysis was observed. Additionally, a few dead *C. elegans* worms could also be observed whose organs were entirely damaged. These observations suggest a toxin-mediated killing of the *C. elegans* worms and helps to clarify why worms cannot recover from a sufficiently long exposure to this pathogen.

Pseudomonas aeruginosa (*P. aeruginosa*) is another gram-negative pathogenic bacterium capable of causing diseases in a wide range of organisms, including plants, insects, and vertebrates. This bacterium is the first human pathogen that was studied using *C. elegans* in 1998 and has been subjected to extensive research ever since [52], [57]–[67]. Over time, it was discovered that *P. aeruginosa* is capable of killing the worm through 5 different mechanisms depending on the culturing

media and incubation conditions [64]. In what follows, we will discuss the two of the five killing mechanisms, namely, the slow-killing and the fast-killing.

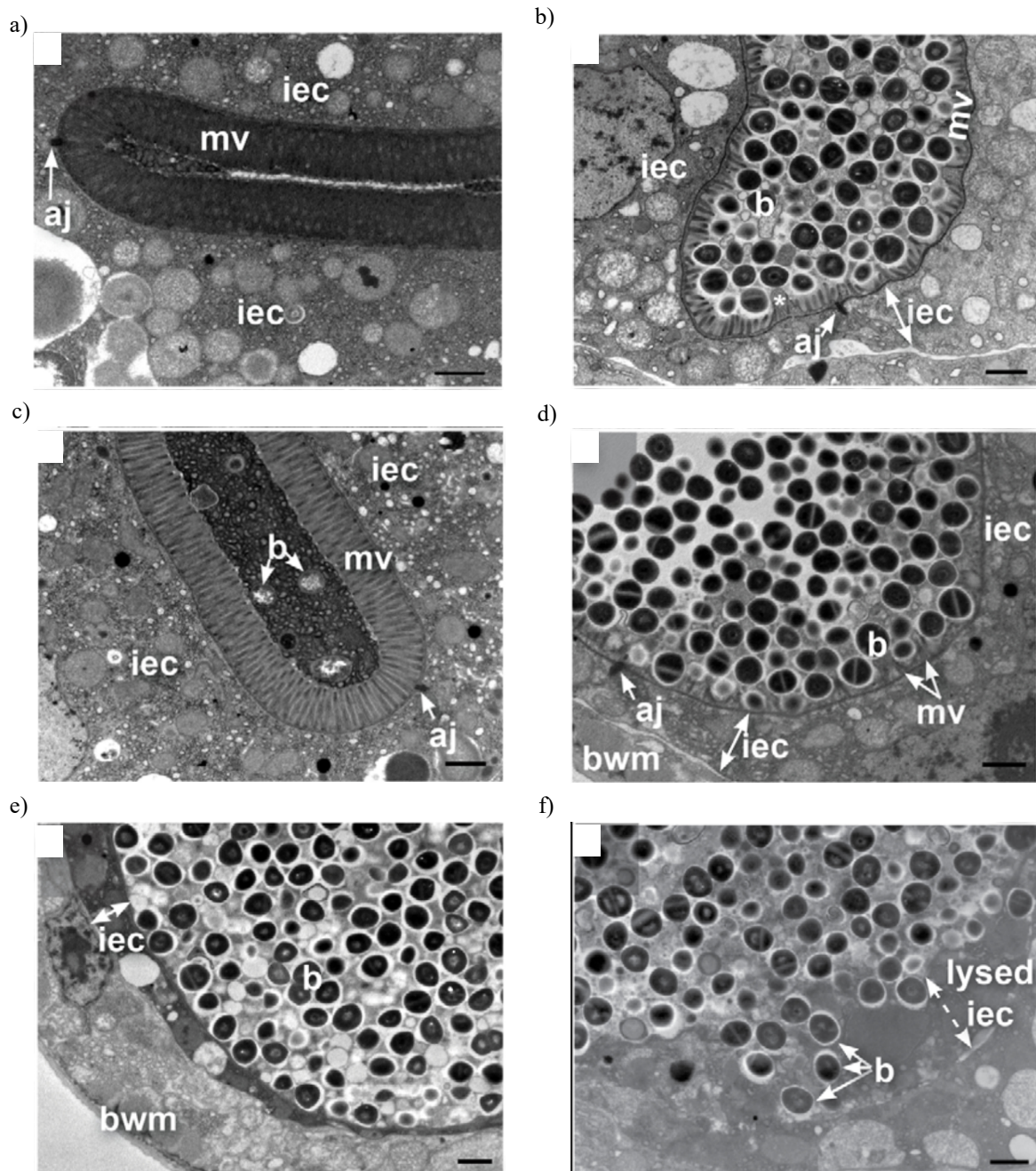


Figure 1-3- TEM micrographs of midbody cross-sections of worms fed on heat-killed *E. coli* OP50 (a, c, e) and *S. aureus* NCTC8325 (b, d, f) for 12 (a, b), 24 (c, d) and 36 h (e, f). Scale bar = 1 μm. iec, intestinal epithelial cell; mv, microvilli; b, bacterial cell; bwm, body wall muscle; aj, apical junctions, asterisk in b indicates membrane blebbing. Reproduced from [56].

In the early works on *P. aeruginosa* pathogenesis in *C. elegans*, it was shown that the bacterium is capable of slowly killing the worm via intestinal colonization (referred to as the slow-killing) as well as rapidly killing the worm via phenazine toxins (referred to as the fast-killing) [57], [68]. The type of killing depended on the composition of the agar plate used for culturing *P. aeruginosa* [69]. In the case of fast-killing a high-osmolarity peptone-glucose-sorbitol PGS agar plate is utilized while in the case of

slow-killing a modified NGM plate was used. *P. aeruginosa* PA14 as the most lethal strain of *P. aeruginosa*, was capable of killing L4 and adult worms within 2.5 to 3 days in the slow-killing condition [58]. In contrast, in the fast-killing condition, *P. aeruginosa* PA14 was capable of killing L4 worms within 4-24 hours [58]. The rate of fast-killing of 1-day-old adult worms was considerably slower. Interestingly, while the slow-killing required the consumption of live bacteria, the fast-killing still occurred at the same frequency even when the worms were fed heat-killed bacteria that were cultured under fast-killing conditions. This observation suggested that the fast-killing relies partly on heat-stable toxins produced *P. aeruginosa* PA14 [58].

C. elegans worms were used to screen the mutants of *P. aeruginosa* PA14, which had mutations in known and hitherto unknown virulence factors, under slow and fast killing conditions [58]. The results of the screening suggested that the underlying mechanisms used by the bacterium for fast-killing and slow-killing of *C. elegans* worms are distinct [58]. Further investigations showed that *P. aeruginosa* PA14 mutants that have reduced pyocyanin (a well-known phenazine) production were drastically less capable of fast-killing the worms [68]. This implies that pyocyanin or in general phenazines are at least one class of toxins that contribute to fast killing [68]. The cytotoxicity of pyocyanin is in part ascribed to its ability to produce reactive oxygen species (ROS) and peroxide [68]. To test whether this mechanism of action contributes to the fast-killing process, three mutants of *C. elegans* worms, one of which (*age-1 (hx546)* mutant) is resistant to ROS while the two others (*mev-1* and *rad-8* mutants) are susceptible to it, were employed in fast-killing assays [68]. As expected, the *age-1 (hx546)* mutant showed significant resistance to fast-killing compared to wild-type worms, whereas, *mev-1* and *rad-8* mutants showed enhanced susceptibility to fast-killing compared to wild-type worms. These observations strongly suggest that the harmful impact of pyocyanin on the worm is at least in part through oxidative stress. The discussion here shows how the genetic tractability of the bacteria and the host helps to clarify and better understand the underlying mechanisms of bacterial pathogenesis.

To better understand the slow-killing process of the worms, they were subjected to further observations and experiments [58]. Monitoring of the L4 worms within the first 18 to 24 hours of exposure to *P. aeruginosa* PA14 showed that the rate of pharyngeal pumping and defecation are not considerably dissimilar to worms fed on *E. coli* OP50. However, during an exposure window of 24 to 48 hours, the rate of pharyngeal pumping as well as the motility of the worms progressively decrease until the worms stop moving and die. In the majority of cases, the animals die to internal hatching of embryos. Nevertheless, *P. aeruginosa* PA14 was capable of killing male mutants and sterile hermaphrodite, albeit at a lower, under slow-killing conditions implying that the internal hatching of embryos is not the only mechanism of worm killing. To determine whether exposure to *P. aeruginosa* PA14 leaves long-lasting detrimental effect on the health of the worms, they were exposed to *P. aeruginosa* PA14 for different time windows before being transferred to plates seeded with *E. coli* OP50. Worms could survive exposures to *P. aeruginosa* PA14 that lasted less than 12 hours. However, exposures longer equal to 18 hours and longer results in the death of at least 25% of the initial population in the next 60 hours of feeding on *E. coli* OP50. These experiments show that similar to *S. aureus* infection, a long enough exposure leaves severe detrimental effects on the health of the worm. To establish whether slow-killing is concomitant with bacterial accumulation in the gut, after 48 hours

of feeding on fluorescent *P. aeruginosa* PA14, *C. elegans* worms were observed using fluorescence microscopy which revealed the presence of high-intensity bacteria derived fluorescence signal in the intestinal lumen. As expected, in worms fed on *P. aeruginosa* PA14 mutants with attenuated virulence phenotype, the bacterial accumulation in the intestine after 48 of feeding was not significant.

Using TEM, the cytopathology of *P. aeruginosa* PA14 intestinal infection under slow-killing condition was investigated [56]. After the 8 hours of exposure (Figure 1-4b) to *P. aeruginosa* PA14, bacterial accumulation in the intestine is limited but the intestine itself is significantly distended. The apical surface of the brush border is covered with a thin layer of Electron-dense ExtraCellular Matrix (EECM). This is EECM is also present around the few bacterial clusters. However, neither the role nor the origin of this EECM is known; it might be one of the defensive mechanisms of either the *P. aeruginosa* PA14 or the intestine of the worm. Furthermore, *P. aeruginosa* PA14-derived putative outer membrane vesicles (OMVs), which are involved in pathogenesis, were present in large numbers around the bacteria and in contact with the EECM. In contrast, the intestine of worms fed on *E. coli* OP50 (Figure 1-4a) appeared healthy and no signs of pathogenesis as described above were present. After 24 hours of exposure (Figure 1-4d), the infection progresses further. The intestinal distension is increased and a larger number of bacteria clusters covered by the EECM can be observed. The microvilli in the intestine still retain their normal length but are now covered deeply with the EECM. Again, as before, none of the described signs of intestinal infection are present in *E. coli* OP50-fed worms (Figure 1-4c).

At 48 hours of exposure (Figure 1-4e and f), the intestinal infection becomes worse. The intestine is now greatly distended and more and more bacteria are present in lumen of the intestine. However, the majority of the present bacteria are distanced from the intestinal microvilli, which are now shorter in length, by a thick layer of the EECM. Intercellular invasion is present in 21% of the cross sections and there are even cases that reveal the ability of the *P. aeruginosa* PA14 bacterial cell to invade tissues that lie beyond the intestine. Lastly, a larger number of autophagosomes either in their early formation stage or in an aberrant multivesicular form is observed. These observations are in agreement with the previous report on rescuing the worms from *P. aeruginosa* PA14 (via shifting to *E. coli* OP50 lawns) that showed the inability of the worms to recover from exposures lasting 18 hours or longer.

The cytopathology of *P. aeruginosa* PA14-infected worms (under slow-killing condition) revealed the participation of autophagosomes as one of the host's defense mechanisms. In a further study, the role of autophagy and the signaling pathway required for the activation of this defense mechanisms was examined [62]. Generally speaking, autophagy allows the organism, the *C. elegans* worm in this case, to eliminate intracellular pathogens such as *P. aeruginosa* PA14. Using transgenic worms that have GFP-tagged indicators of autophagy, it was shown that *P. aeruginosa* PA14 triggers an autophagy response. Additionally, the induction of autophagy response was confirmed by measuring the levels of autophagy-involved proteins via Western blotting. Life span and bacterial colonization assays on autophagy-deficient worms (via RNAi of *bec-1* autophagy gene) showed that while these mutant worms have levels of intestinal bacterial accumulation similar to wild-type worms, they are more susceptible to *P. aeruginosa* PA14 as indicated by the increased killing rate. Measuring the level of autophagy-involved proteins and life spans of worms with loss-of-function mutations in different

innate immunity pathways showed that autophagy activation occurs via the extracellular signal-regulated kinase (ERK) pathway. This observation was further confirmed by increased phosphorylation of ERK as measured by Western blotting in worms exposed to *P. aeruginosa* PA14.

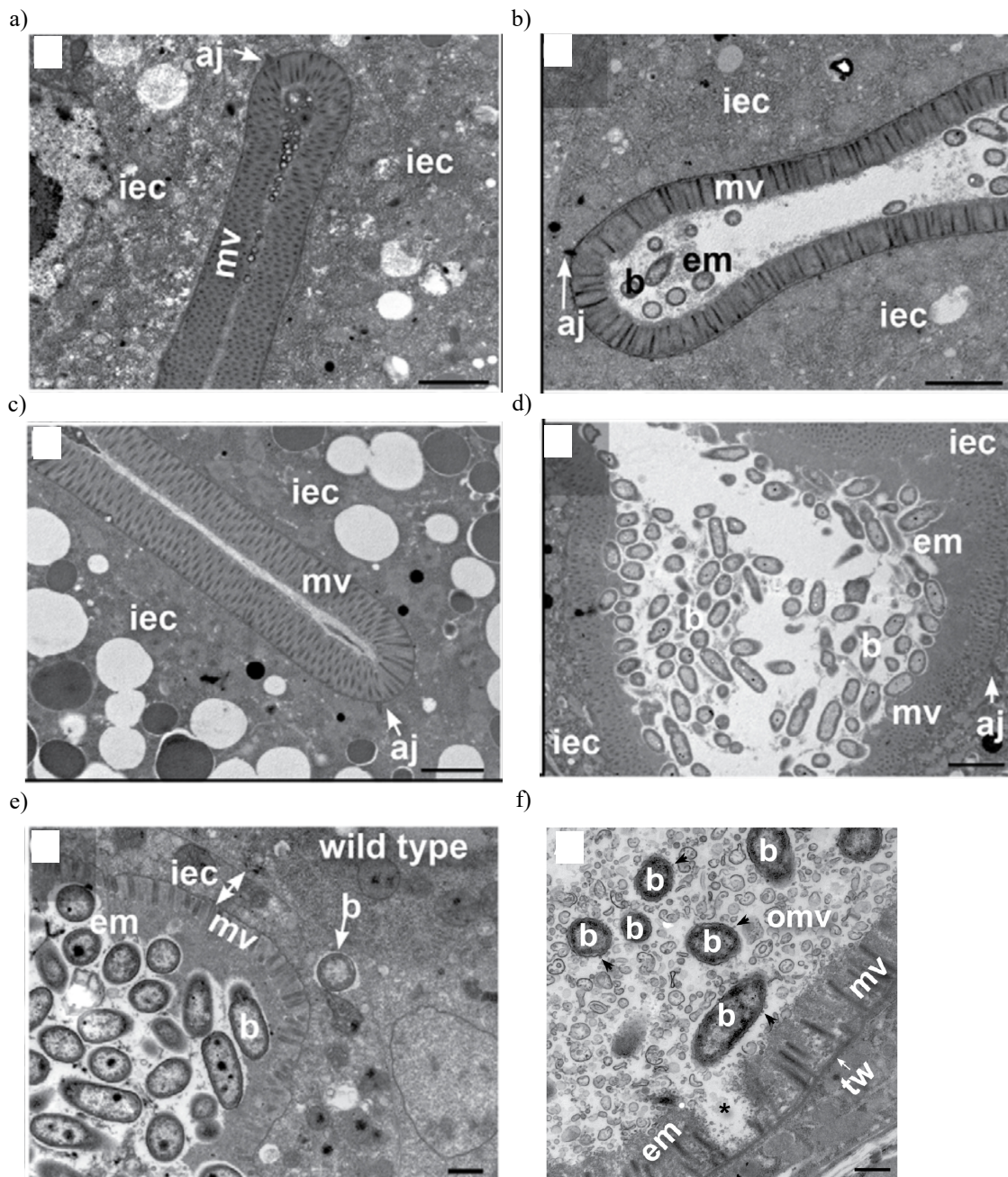


Figure 1-4- TEM micrographs of midbody cross-sections of worms fed on *E. coli* OP50 (a, c) and *P. aeruginosa* PA14 (b, d, e, f) for 8 (a, b), 24 (c, d) and 48 h (e, f). Black asterisk and arrowheads highlight the disruption of the microvilli and OMV shedding from the bacterial cells, respectively, in f. Scale bar in a-d, 2 μ m; in e, 1 μ m; in f, 0.5 μ m. iec, intestinal epithelial cell; mv, microvilli; b, bacterial cell; bwm, body wall muscle; aj, apical junctions; em, extracellular material. Reproduced from [56].

To understand how autophagy protects the worms, autophagy-deficient mutants exposed to *P. aeruginosa* PA14 were studied. Differential interference contrast (DIC) images showed an enlarged vacuolar morphology which is typically seen in necrotic intestinal cells. Staining analysis revealed lysosomal injury, leakage of cathepsins (enzymes that degrade proteins) and significant loss of

intestinal nuclei. These observations suggest that the main role of autophagy is preventing *P. aeruginosa* PA14 bacteria from inducing necrosis in the intestine of the worms. Indeed, it was also demonstrated that inhibition of necrosis pathways and thus necrosis-mediated death of worms, increases the life span of infected autophagy-deficient worms.

The interaction of *P. aeruginosa* PA14 with *C. elegans* worms in slow-killing condition is also mediated by the mucus layer covering intestinal epithelium [63]. Generally speaking, the mucus layer, secreted by mucosal epithelial cells, is a physical barrier with antimicrobial properties. The viscous nature of the mucus layer originates from mucins which are heavily glycosylated proteins with high-molecular weight. Despite the general understanding of the antimicrobial role of the mucus layer, it has been shown that *P. aeruginosa* PA14 is able to exploit the mucin for intestinal colonization [63]. One of the mucin-related genes upregulated by *P. aeruginosa* PA14 infection is *mul-1*. Remarkably, *mul-1* mutants (loss-of-function mutation in *mul-1* gene) could survive the exposure *P. aeruginosa* PA14 for a longer time compared with wild-type worms. To explain this unexpected observation, the intestinal bacterial load in mutants and wild-type worms were measured, and it was found that *P. aeruginosa* PA14 is considerably less successful in colonizing the intestine of mutants. To better understand how mucin MUL-1 affects the slow-killing capability of *P. aeruginosa* PA14, those monosaccharides that are known to make up mucin MUL-1 were added as supplements to life span studies of *mul-1* mutant worms exposed to *P. aeruginosa* PA14. It was found that N-acetyl-galactosamine and N-acetylglucosamine monosaccharides, added as supplements, could enhance the pathogenicity of *P. aeruginosa* PA14 in *mul-1* mutants. Further experiments show that N-acetyl-galactosamine enhances biofilm formation while N-acetylglucosamine increases pyocyanin production which as we discussed earlier is a toxin which is involved in killing of *C. elegans* worms under fast-killing condition. Further experiments showed that these monosaccharides also augment the ability of *P. aeruginosa* PA14 to bind to human lung epithelial cells. Perhaps these two monosaccharides also provide binding sites that required *P. aeruginosa* PA14 intestinal infection in worms.

2 *State of the art*

2.1 The need for devices enabling high-throughput and high-resolution studies

As we saw in chapter 1, the interactions between the worm and pathogenic bacteria have many different facets and can be extremely complex. At the same time, understanding the mechanisms governing these interactions requires the generation and screening of many different worms and bacteria strains. Even though simple life span assays can determine which genetic mutation affects the interaction between the worm and the bacteria, they still require a considerable amount of manual labor due the sheer number of genetic mutations possible and the typical control experiments and repetitions involved such assays. Especially, in the case of studies involving adult worms, as they need to be moved to fresh agar plates on a daily basis to avoid overcrowding by progenies. Additionally, a life span assay is very limited in clarifying how a given genetic mutation is affecting the interaction between bacteria and the worm. This is especially true when the mutations are introduced in genes whose functions are not known. To alleviate this issue, in addition to life span studies, different bacterial colonization assays are also performed to better characterize the dynamic relationship between the worm and bacteria. However, these assays, in principle, can only report an average number of viable bacteria that is typically obtain from a group of 10 or more worms. Moreover, as the bacterial proliferation/accumulation in the intestine is of exponential nature, the presence of a single worm with very high intestinal bacterial accumulation can greatly bias the average number of viable bacteria and thus result in misinterpretations. Additionally, all the bacterial colonization assays involve mechanically disrupting the worms and thus it is not possible observe the intestinal bacterial load of a single worm over time. There were instances where worms were fed fluorescent bacteria and afterwards fluorescent microscopy was used to investigate whether the bacterium is capable of colonizing the gut. However, these were never done in systematic manner and did not include quantitative analysis. Additionally, high-resolution imaging of worms require immobilization which typically involves the use drugs or glues. The drugs affect the biochemical state of the worm while glues irreversibly immobilize the worms [70]. Consequently, long-term high-resolution imaging of a single worm is not possible. Gene-expression was measured via Western blotting or Quantitative Real-Time Polymerase Chain Reaction (qRT-PCR) analysis also involved killing the worms and as result these methods do not allow long-term observation of a single worm. There were attempts to monitor gene-expression via transgenic worms in which the gene of interest has a fluorescent tag. However again, these were not carried out in a systematic and quantified manner. Additionally, other phenotypes such as motility and the rate of development (measured through change in area and length), pharyngeal pumping, intestinal peristalsis, defecation and egg laying rate are instrumental in obtaining a complete picture of the interaction between the worms and bacteria. Therefore, there is a need for high-throughput devices that can enable rapid screening of the generated mutant worms and bacteria via simple assays such as life span, motility and developmental

rate. Furthermore, there is also a need for devices that enable high-resolution long-term studies on mutant worms and bacteria of interest so that the multifaceted interactions between the worm and bacteria can be studied thoroughly. As we will see in the following sections, microfluidic devices can greatly facilitate high-throughput and high-content screening studies as well as long-term high-resolution studies of *C. elegans*.

2.2 A brief overview of microfluidic devices for *C. elegans* studies

Microfluidic devices as the name suggest are devices for manipulating liquids at the micro scale. In their simplest form, they are an arrangement of interconnected micro-sized channels with the same height but different profiles (in terms width and length) which can be used to displace microliters of liquids [71]. As the fluid flows at low Reynolds number, a precise control can be exerted over flow and shear rates and concentration gradients [72]. Additionally, as the cross-section of channels are micro-sized, small volumes of samples or reagents are needed and heat and mass transfer occur at a fast rate [72]. Microfluidic devices have a wide-ranging application including but not limited to chemical analysis, disease diagnosis, cell manipulation and cellular analysis, nucleic acid analysis, synthesis of nanomaterials [73], [74]. Microfluidic devices can be manufactured using different methods and materials [75], however, most commonly they are based on molding a soft, biocompatible and transparent polymer called Polydimethylsiloxane (PDMS). Briefly stated, through conventional soft-lithography techniques, a structural photoresist named SU-8 is patterned according the design of the microfluidic device to obtain a mold. Afterwards PDMS in its liquid state is poured in the mold and takes its shape. Afterwards the mold is heated and PDMS transforms into a solid elastomer through a heat-assisted crosslinking process. The solid PDMS is afterwards separated from the mold and subsequently is bonded to glass substrate to form the channels. The mold itself is quite durable and can be used to replicate many PDMS microfluidic chips.

The earliest reported microfluidic devices for studying *C. elegans* dates back to 2007. Hulme et al. reported for the first time a microfluidic device for immobilization and imaging of *C. elegans* worms. The device featured a network of 128 tapered channels that allow automated distribution and reversible immobilization of 100 worms within 15 minutes by using a constant pressure to drive the liquid flow in the channels [70]. Shortly after, Chronis et al reported two microfluidic devices for studying behavior at the neuronal level [76]. The first chip featured a single tight channel that trapped a single worm and enabled the monitoring of its neuronal activity and locomotion through fluorescence imaging. The second microfluidic device also featured a tight channel to trap a single worm and via the operation of 4 other channels, exposed to the worm a chemosensory stimulus. As the worms were immobilized in the trap, the activity of their chemosensory neurons could be observed via fluorescence imaging. These two publications were followed by further research on developing novel microfluidic devices for *C. elegans* studies and until today numerous microfluidic devices covering a wide range of applications have been reported [72], [77]–[80].

To understand the appeal and the interest in the development of microfluidic devices applied to *C. elegans* studies, we briefly highlight the advantages this approach provides [72]: (i) facile manipulations of a large number of worms thus enabling high-throughput screening studies; (ii) precise and easy control over the experimental conditions, examples of which are the customization of the feeding protocol as required in specific host-microbiota studies and the possibility of introducing stimuli in a controlled manner; (iii) ease of doing long-term studies as the maintenance of the worms and imaging can be in principle automated; (iv) reversible immobilization which, in particular, is needed for high-resolution imaging; (v) laser microsurgery, typically required in nerve regeneration studies.

Devices for high-throughput screening and long-term high-resolution studies have opposing design and operation considerations and as a result, it is very challenging to have a microfluidic device that is excellent in terms of both screening throughput and the capability for long-term high-resolution studies. In what follows, given our interest, we will highlight the state-of-the-art devices for long-term high-resolution imaging studies.

2.3 Long-term high-resolution imaging in microfluidic devices

While it is possible to limit the movement of the worms by placing them inside small chambers and rely on high-frame rate imaging to monitor them, such an approach is inherently limiting, as the exposure times should be short which reduces the signal-to-noise ratio and imaging is restricted to low or moderate magnifications. Therefore, long-term high-resolution imaging of worms on a microfluidic chip unavoidably depends on immobilizing the worm sufficiently, without harming it. Generally speaking, there are three common approaches to achieve immobilization in microfluidic devices: (i) traps with certain geometry that restrict the movement of the worm, typically used in one-layer devices [81]–[84], (ii) membranes that deform upon application of pressure either via liquid or air preventing the movement of the worm [85]–[87], (iii) thermo-sensitive hydrogels that go through a reversible sol-to-gel transition within the physiological temperature range of the worm [88]–[92]. Rarely, there are also devices that incorporate the first two approaches [93]. We will briefly review a selection of microfluidic devices featuring each of the approaches to show the evolution of on-chip immobilization and imaging and to highlight the-state-of-the-art devices.

We begin with discussing trap-based immobilization in microfluidic devices. Hulme et al reported a microfluidic chip for lifelong observation of *C. elegans* worms [81]. The chip featured an array of 16 chambers each measuring 1.5 mm in diameter and leading into a tapered channel for immobilization and imaging purposes (Figure 2-1a and c). The presence of pre-fabricated screw valves allowed the chambers to be loaded sequentially with a single L4-stage worm which can be subsequently monitored during its life span (Figure 2-1b). It should be however mentioned that the loading of the worm in chambers and their immobilization via the clamps needed manual interventions. While it was demonstrated that the life-span of the worms maintained on the chip is similar to those maintained on NGM plates, no systematic study involving high-resolution imaging was performed to show the

degree of immobilization afforded by the chip. Rather, the studies were mostly involved measuring the volume and the motility of the worms.

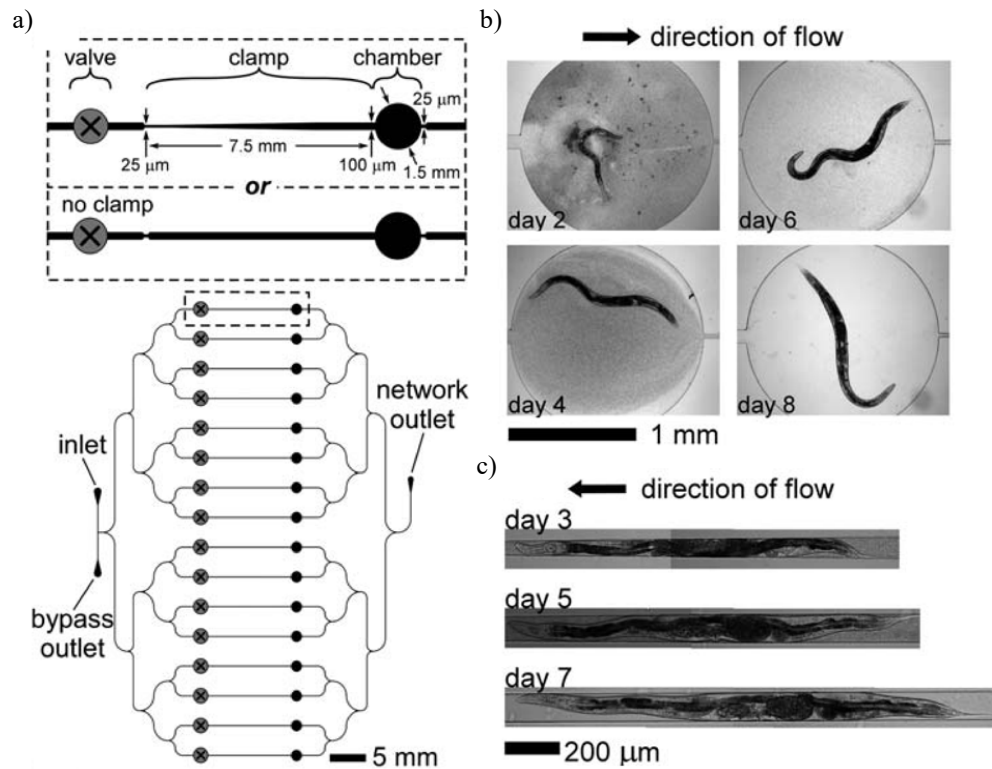


Figure 2-1- (a) An array of chambers and tapered channels (clamps) for on-chip lifespan studies and imaging of *C. elegans* worms. (b) Culturing of *C. elegans* worms in the chambers. (c) Brightfield images of worms immobilized in tapered channels. Reproduced from [81].

Kopito and Levine reported a microfluidic device named WormSpa that enable long-term confinement and monitoring of individual adult worms, while maintain their identities, in array of 32 or 64 chambers (Figure 2-2) [82]. The hydrodynamic resistivity of the distribution networks leads to facile distribution of worms between those chambers such that within 15 minutes 80% of the chambers contain a single adult worm. Within each chamber, the movement of the worms are limited by a set of pillars but not totally constrained ensuring that the worms are not harmed/stressed (Figure 2-2a). The worms are also able to lay eggs which are afterwards collected in a designated area. The microfluidic chip also allows the incorporation of a step module or gradient module to provide temporal stimuli or stimulus concentration profile (across the chambers), respectively (Figure 2-2b and c). Worms that had spent 24 hours on the WormSpa and were later transferred to NGM plates, had lifespans that were similar to worms that were maintained at all times on NGM plates, indicating that WormSpa does not stress or harm the worm.

The rate of egg laying of worms maintained on chip was measured in an automated way and found to be similar to the rate of egg laying of worms that were maintained on NGM plates (Figure 2-2d). The device was also used to monitor pharyngeal pumping rate, indicating a general decline at the population level but also revealing a subset of worm population that had increased pharyngeal pumping rate. Lastly, the device allowed the monitoring of the stress response to starvation by

fluorescence imaging of a transgenic worm in which the DAF-16 protein expresses green fluorescence (DAF-16::GFP) (Figure 2-2e and f).

Atakan et al reported a microfluidic device for automated on-chip culturing and high-content phenotyping of *C. elegans* worms starting from L1 stage and for a duration of 100 hours [83]. The device featured 8 lanes each of which had 4 chambers that could accommodate up to 3 worms (Figure 2-3a). Each chamber has a culture area where the worms freely move and feed and an immobilization area where the worms can be reversibly immobilized using an array of tapered channels. Feeding, immobilization, imaging and video-recording protocols were established and were executed in automated fashion. Images of immobilized worms were analyzed in an automated fashion to monitor the growth-related parameters, motility and expression of the fluorescence in two different worm strains (the mitochondrial unfolded protein response reporter *hsp-6::gfp* strain and the Huntington disease model *p_{unc-54}::Q40::YFP*) (Figure 2-3b, c and d).

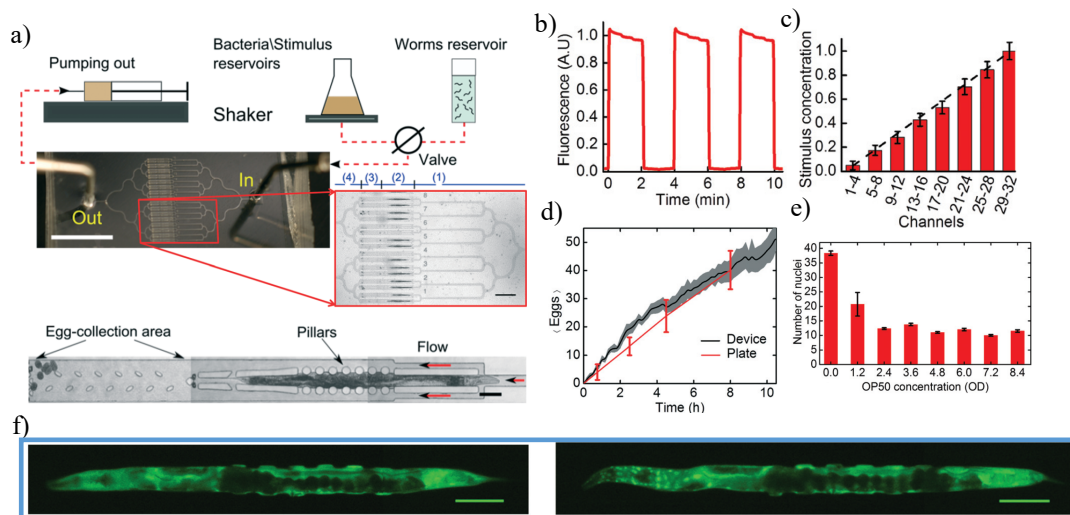


Figure 2-2- (a) Wormspa microfluidic device for automated long-term monitoring of *C. elegans* worms while maintaining the identity of individual worms. The worms are confined within traps and thus their movement is restricted. (b) a step module allows enables a fast exchange of the media (c) a concentration gradient allows the delivery of different doses to 32 channels. (d) Tracking of eggs released by worms cultured on chip through automated imaging and image analysis shows that worms maintained on chip and NGM plates have similar egg release rate. (e) Food restriction-induced nuclear localization of DAF-16::GFP captured through fluorescence imaging. (f) Diffusive pattern of DAF-16::GFP in a well-fed worm (left) in contrast to the localized expression of DAF-16::GFP in the nuclei of cells in the head of starved worms (right). Reproduced from [82].

Similarly, video-recordings of freely moving worms were analyzed in automated fashion to extract motility-related parameters. While the devices we discussed so far allow long-term imaging of *C. elegans* worms, they have not explored the high-resolution imaging potential afforded by traps that mechanically limit the movement of the worm.

Gokce et al reported a single layer microfluidic that featured traps that allowed immobilization of 20 worms via traps for laser axotomy and high-resolution imaging using an oil-immersion 63x objective (Figure 2-4) [84].

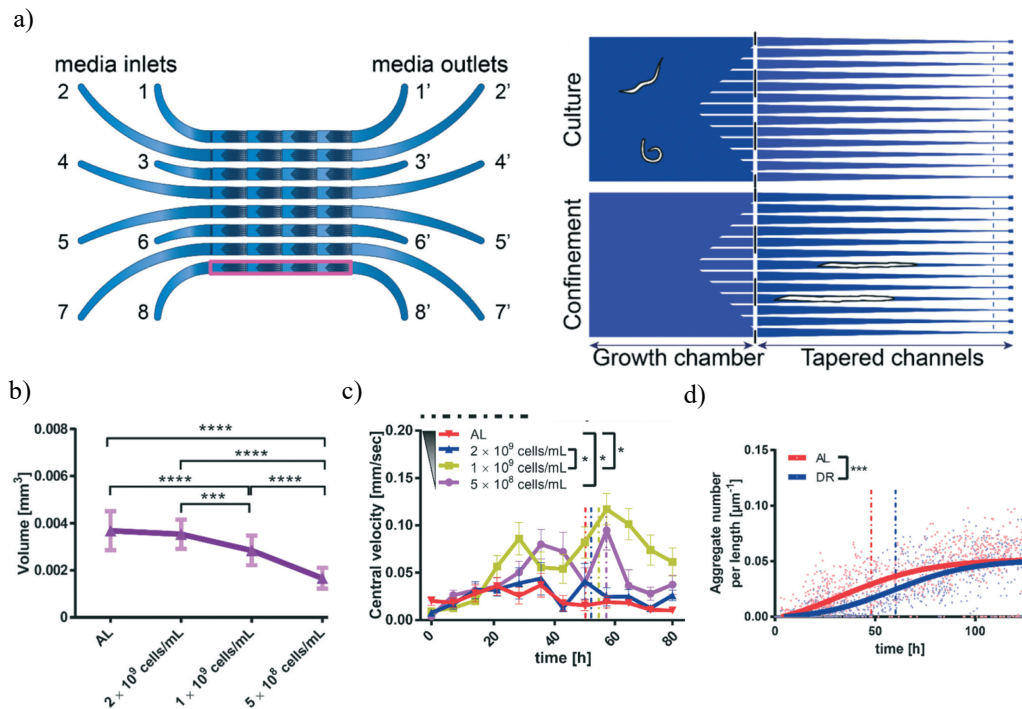


Figure 2-3- Microfluidic device for automated high-content phenotyping of *C. elegans* worms. (a) Design of the microfluidic device. Automated long-term monitoring of (b) the volume and (c) the motility of *hsp-6::gfp* worms in different feeding conditions. (d) Automated fluorescence imaging and analysis yielding the number of fluorescent protein aggregates in *unc-54::Q40::YFP* worms fed under *ad libitum* (AL) and diet restriction (DR) conditions. Reproduced from [83].

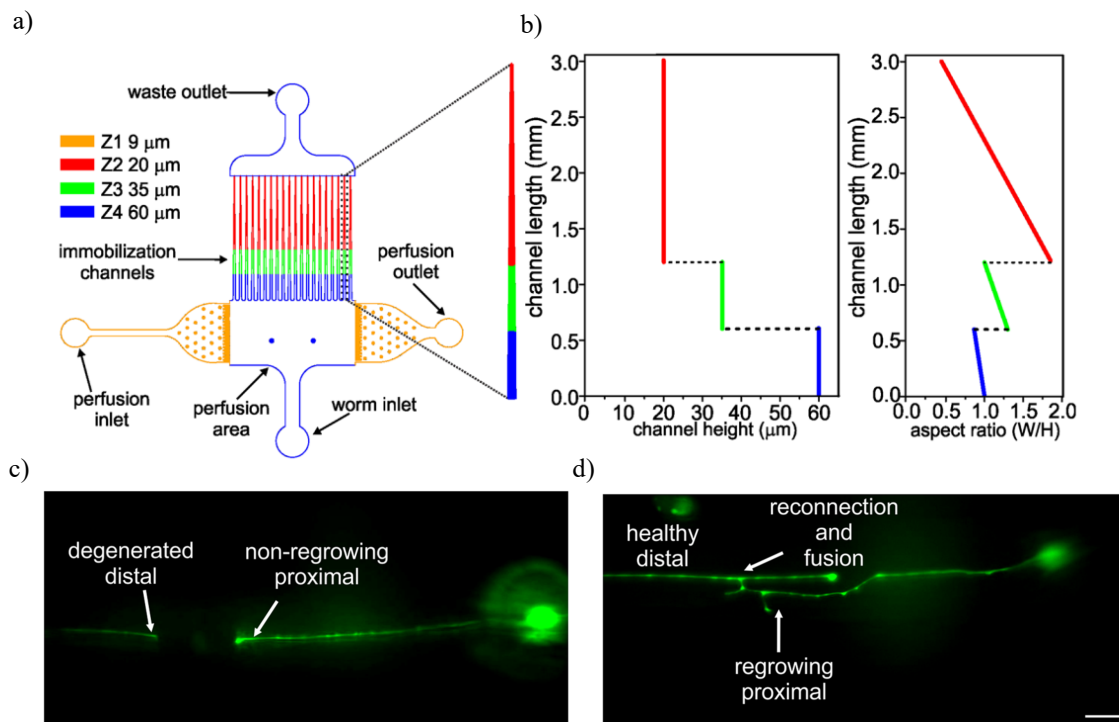


Figure 2-4- Microfluidic device for laser axotomy and longitudinal studies of nerve regeneration in *C. elegans* worms. (a) The design of the microfluidic device. (b) The profile of the 3D-tapered channel; the width and the height of the channel both change across the length of the channel. High-resolution fluorescent image of (c) a non-regrowing PLM neuron in an *egl-20* mutant and (d) regrowing PLM neuron in a *zdl5* mutant. Scale bar = 10 μm . Reproduced from [84].

The traps used in this work was a more sophisticated variation of the typical tapered channels we have seen so far. The main difference was that in addition to the typical lateral narrowing of channel, the height of the channel was also reduced in several steps to ensure that the worms remains in the later orientation which is more suitable for laser surgery (Figure 2-4a and b). The device also featured a perfusion area that the worms could reside in for 24 hours to recover from the laser surgery (Figure 2-4a). After the 24 hours recovery period was passed, the worms were again pushed towards the traps to be immobilized and imaged at a high resolution for nerve regeneration studies (Figure 2-4c and d). It should be also mentioned that while this device was capable of high-resolution imaging, due to lack of dedicated chambers for individual worms, it cannot track individual worms over time.

Having discussed microfluidic devices featuring traps for immobilization, we will now review devices that use deformable membranes for immobilization. Guo et al reported a microfluidic device for performing on-chip laser axotomy and studying nerve regeneration (Figure 2-5) [87]. The microfluidic device was based on 2 layers, namely, a flow layer and a control layer that were bonded together to form a 40 μm membrane. The flow layer included a trapping area for performing laser axotomy and time-lapse imaging and 3 feeding chambers for the recovery of operated worms (Figure 2-5a and b).

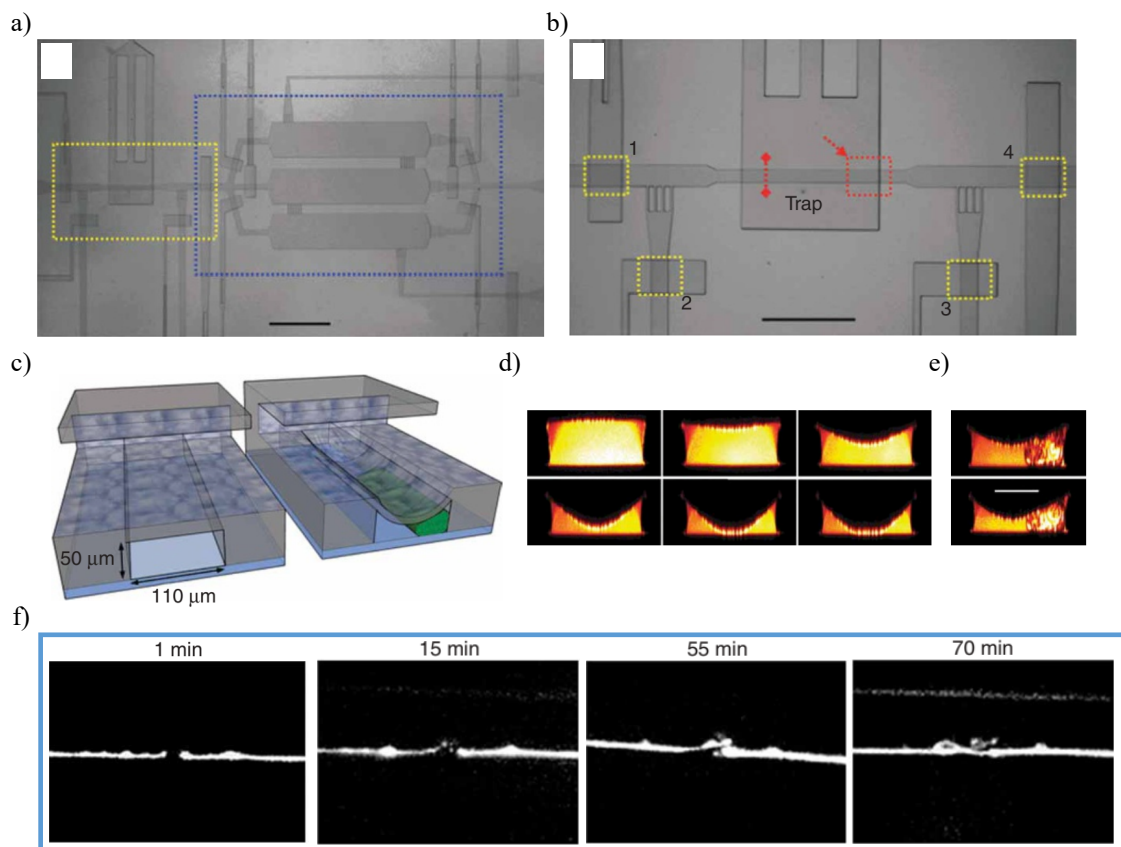


Figure 2-5- a 2-layer microfluidic chip for laser axotomy and nerve regeneration studies. (a) Overview of the microfluidic device in which the trap area (for immobilization and surgery) is shown with a yellow rectangle while the three recovery chambers are delineated by a blue rectangle (b) Magnified view of the trap area; 4 valves (indicated by the yellow rectangles) are used to enable regulation of the inlet flow (1), fine positioning of the worm (2, 3) and transfer to the recovery chambers (4). (c) 3D view of the red rectangle in (b) showing how the pressure-mediated deformation of the membrane immobilizes the worm (in green) for imaging and surgery. (d) Two-photon imaging characterizing the deformation profile of the membrane at different air pressures ranging from 0 to 35, 70, 105, 140 and 175 kPa. (e) Two-photon imaging displaying an immobilized worm at 105 and 140 kPa. (f) Time-lapse imaging of nerve regeneration. Reproduced from [87].

Pressurizing the control layer resulted in the deformation of the membrane (Figure 2-5c and) and thus immobilization of the worm (Figure 2-5e) which was required for nanosurgery and high-resolution imaging (Figure 2-5f). Using this device, the axotomy process took 1 min compared to 10 min that is required for performing the same operation using conventional methods. Additionally, it was demonstrated that the use of anesthetics in conventional methods prolongs the nerve regeneration process by several hours.

Gokce et al reported a complex 2-layer microfluidic device that allowed performing laser axotomy in a fully automated manner (Figure 2-6) [86]. A dedicated staging area was designed that allowed reliable loading of a single worm to the trapping area at a high throughput. This was made possible by the use of two valves (based on the pressure-mediated deformation of membranes) and a narrow channel which only permitted the entry of a single worm. In this device the immobilization of the worm is achieved by the pressure-mediated deformation of a membrane. To immobilize the worm reliably and precisely in a predefined location, the device also included two additional components: (i) a T-shaped trapping area where the worm was pushed against a fine filter structure (sieve) via the application of a flow while being immobilized by the deformed membrane (Figure 2-6 and Figure 2-7a); (ii) two completely sealing valves (only possible in channels with hemispherical cross-section) (Figure 2-7b). The realization of completely sealing valves without compromise in imaging resolution required the inclusion of 3D interconnects (Figure 2-7b). The immobilization allowed imaging at a high resolution using a 63x oil immersion objective. The authors also developed an image processing pipeline for the automated detection and targeting of the neuron of interest in immobilized worms for laser axotomy. This image processing pipeline could also evaluate the success of each laser surgery. The developments in both device design and image processing enabled this device to perform laser axotomy in a fully automated manner at a rate of 17 s/worm.

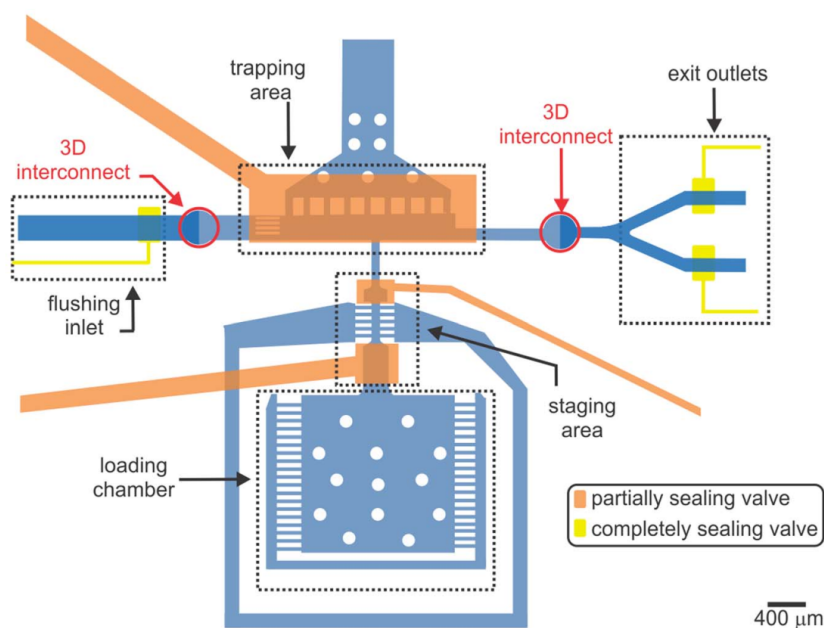


Figure 2-6- The design of the microfluidic device for fully automated on-chip laser axotomy. Reproduced from [86].

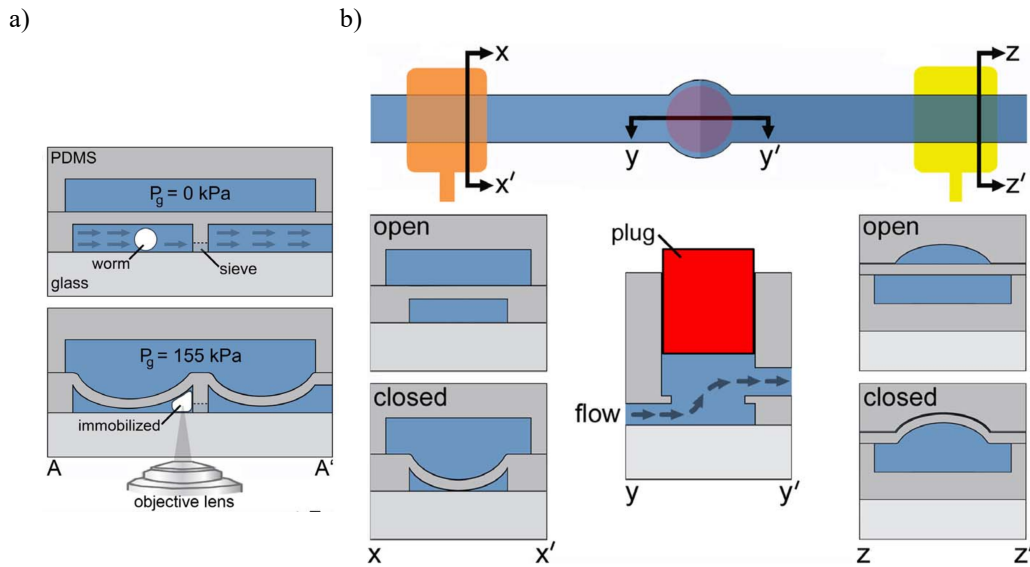


Figure 2-7- (a) In the trapping area, the worm is pushed against the sieve structure and afterwards is immobilized via the pressure-mediated deformation of the membrane (b) Two types of valves. A partially sealing valve on the left and the completely sealing valve on the right. The presence of a 3D interconnect (middle) in the microfluidic device allows the implementation of a completely sealing valve in 2-layer device which is required for fine positioning of the worm during immobilization. In this implementation, only a thin cover slip lies in between the worm and the microscope objective and thus optical distortions are reduced to a minimum. Reproduced from [86].

Keil et al reported a 2-layer microfluidic device for studying developmental processes in *C. elegans* worms from larval stages until adulthood at a high spatial and temporal resolution [85]. The device featured 10 lanes, in each of which a circular chamber with a diameter of 400 μm capable of accommodating a single worm from L1 stage till adulthood is present (Figure 2-8a and b). Worms regardless of their age can be immobilized frequently by the pressure-mediated deformation of the membrane without being harmed/damaged in the process (Figure 2-8c and d). The microfluidic device was used to study cell-fate specification, cell death and transdifferentiation during the larval stages using time-lapse z-stack multichannel fluorescence and Nomarski microscopy. A widefield microscope equipped with a (40x, 1.3NA) oil immersion objective coupled with a 0.63x camera adaptor (except when studying transdifferentiation processes) was used to capture the entire chamber in one frame. Additionally, they implemented a pipeline for automated image registration that was used to monitor PVD neuron arborization.

Berger et al developed a single-layer microfluidic device which used traps and valves together to fully immobilize the worms, thereby enabling long-term high-resolution z-stack multichannel fluorescence imaging using a (60x, NA 1.2) water immersion objective (Figure 2-9) [93]. Microfluidic chips with channel heights of 15 μm , 20 μm and 50 μm and specific trap geometries were designed to accommodate worms in the L3, L4 and adult stages, respectively. Interestingly, as the device is composed of one layer of PDMS, the valve is implemented laterally and is used to close the channels leading to/ leaving the worm trapping area (Figure 2-9 a-e). As the worms are immobilized in a straight line, tracking of complex spatiotemporal processes is simpler in this device. The authors were able to study developmental process such anchor cell invasion, distal tip cell migration and germ cell apoptosis using this device.

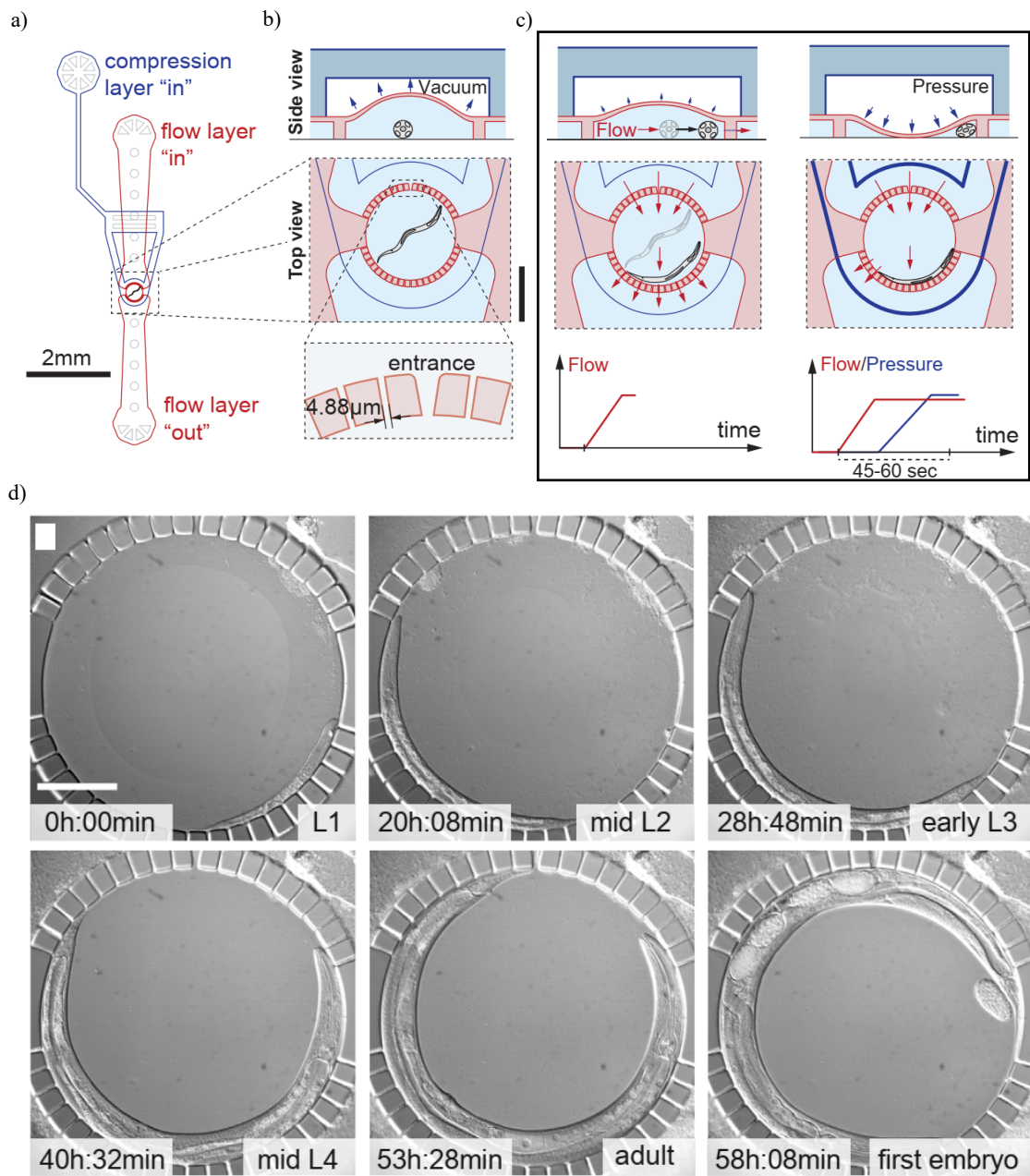


Figure 2-8-(a) The design of the 2-layer microfluidic device where the flow layer and the compression layer are shown with red and blue colors, respectively. (b) The magnified view of the circular chamber and its cross-section. As the height of the flow layer is only $20\ \mu\text{m}$, the compression layer is kept in vacuum to increase the height of the chamber to accommodate worms from L1 stage till the onset of egg laying. Scale bar = $250\ \mu\text{m}$. (c) The immobilization principle: a flow in the flow layer first pushes the worm toward the filters and, afterwards, the pressurization of the compression layer deforms the membrane and gently immobilizes the worm against the filters. (d) The device can support the development of the worm from the L1 stage till the onset of egg laying. The pressure-mediated deformation of the membrane can immobilize the worms regardless of their age. Scale bar = $100\ \mu\text{m}$. Reproduced from [85].

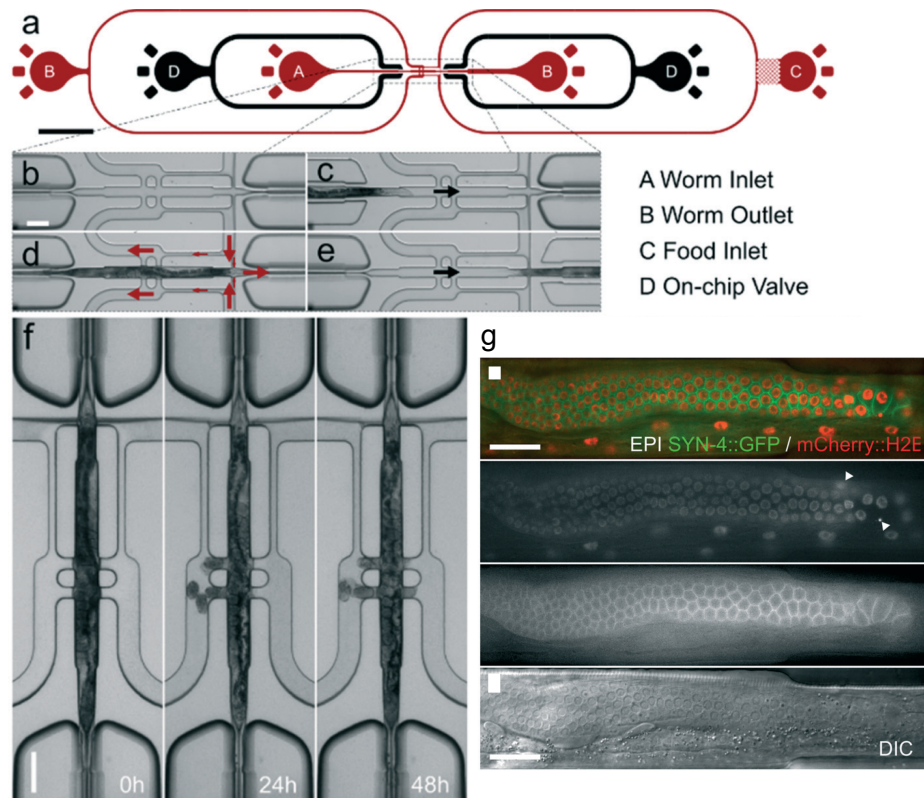


Figure 2-9- A single-layer microfluidic device featuring traps and valves for the long-term immobilization and high-resolution imaging of *C. elegans*. a) The design of the microfluidic devices. Scale bar = 1000 μm . b-e) The worm loading sequence. Scale bar = 100 μm . b) empty chamber. c) The first valve (on the left) is opened to allow the entry of the worm to the trap while the second valve (on the right) remains closed. d) The worm is immobilized by keeping both valves closed. The immobilized worm can still feed and release eggs. (e) Unsuitable worms can be released by opening the second valve. f) An adult worm maintained on the device for 48 hours. g) High-resolution fluorescence and DIC imaging of the germ cells using a 60x/NA 1.2 objective. The germ cell nuclei and cell membranes can be identified via fluorescently-labelled histone (*mCherry::H2B*) and t-SNARE transgenes (*syn-4p::GFP*), respectively. Scale bar = 25 μm . Reproduced from [93].

Lastly, we review a number of devices that immobilize worms using thermos-sensitive hydrogels that undergo reversible thermogelling within the physiological temperature range of the worm [88]–[90]. Pluronic F127 (PF127) hydrogel is one of such hydrogels that are used in microfluidic devices and the three devices that we review here make use of this hydrogel for immobilization [88]–[90]. PF127 is a biocompatible triblock copolymer that can be dissolved in water and the resulting aqueous solution is a viscous liquid at low temperatures and forms a gel when it is heated and reaches its critical gelation temperature [89]. The critical gelation temperature and the viscosity of this hydrogel can be tuned by modifying the concentration of PF127 in the solution which allows the immobilization of the worm within safe temperatures [94].

Krajniak and Lu reported a 2-layer microfluidic device for developmental studies on *C. elegans* starting from L1 stage [89]. The flow layer of the device contains 8 chambers which are divided into 2 groups of 4 such that each group can be controlled independently (Figure 2-10a). The second layer (heating layer) is used to deliver a hot liquid from a bath that is maintained at a temperature of 85 $^{\circ}\text{C}$. The hot liquid is used to heat up the PF127, trigger thermogelling and thus immobilize the worms (Figure 2-10b). In this work a PF127 solution with a concentration of 25% w/v was used. The worms were maintained at 19 $^{\circ}\text{C}$ and the PF127 solution became a gel when the temperature was raised to 21 $^{\circ}\text{C}$.

The heating layer also includes valves that are used to control the flow in the flow layer and trap animals within the chambers (Figure 2-10b). They showed that PF127 solution has no negative impact on the development of the worms and that PF127 gel can limit the movement of the worm to less than 0.5 μm for a duration of 10 seconds and thus enable high-resolution z-stack imaging. An example of the immobilization and imaging sequence is shown in Figure 2-11.

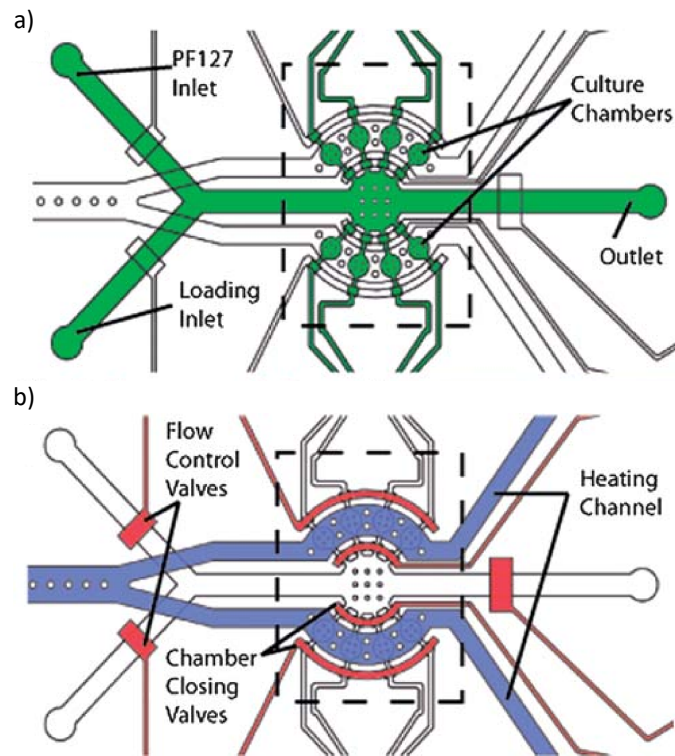


Figure 2-10- The design of the 2-layer microfluidic device for developmental studies on *C. elegans*. (a) The design of the flow layer, where the loading inlet (for worms and bacterial solution), PF127 inlet, chambers and the waste outlet are highlighted. (b) The design of the heating layer showing the heating channels which deliver the hot liquid required for the thermogelling of PF127 solution. Additionally, the valves controlling the flow layer inlets and valves for keeping the worms in the chambers are shown. Reproduced from [89].

Aubry et al developed a hydrogel-droplet microfluidic device for manipulating, high-resolution imaging, and sorting of *C. elegans* larvae [90]. In this device, the worms are suspended in a PF127 solution and injected in the device along with two other immiscible oils. PF127 droplets containing worms could be generated and to prevent the coalescence of these PF127 droplets, they were separated by spacer droplets (Figure 2-12a). The PF127 droplets containing worms are then stored in a serpentine channel and once enough number of them are present, the microfluidic chip is unplugged and taken to a microscope for imaging (Figure 2-12b). As the imaging takes place at 22 $^{\circ}\text{C}$, the PF127 solution becomes a gel and immobilizes the worms. Once the imaging is finished, the chip is cooled down again and the imaged worms can be sorted via two different outlets (Figure 2-12c).

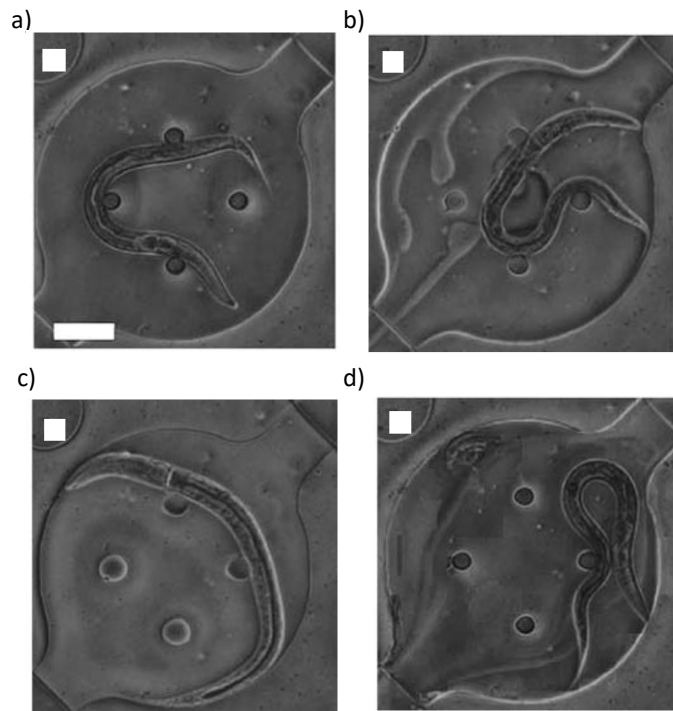


Figure 2-11- Imaging procedure. (a) During the culturing period, the chamber is filled with M9 buffer containing *E. coli* OP50. (b) To acquire images, the M9 buffer is first replaced with the PF127 solution. (c) The chambers are then heated to trigger the sol-to-gel transition in PF127 solution which immobilizes the worms for imaging. (d) Once the images are acquired, the heating is stopped and the PF127 becomes a liquid again which can be then removed from the chamber. Scale bar = 60 μm . Reproduced from [89].

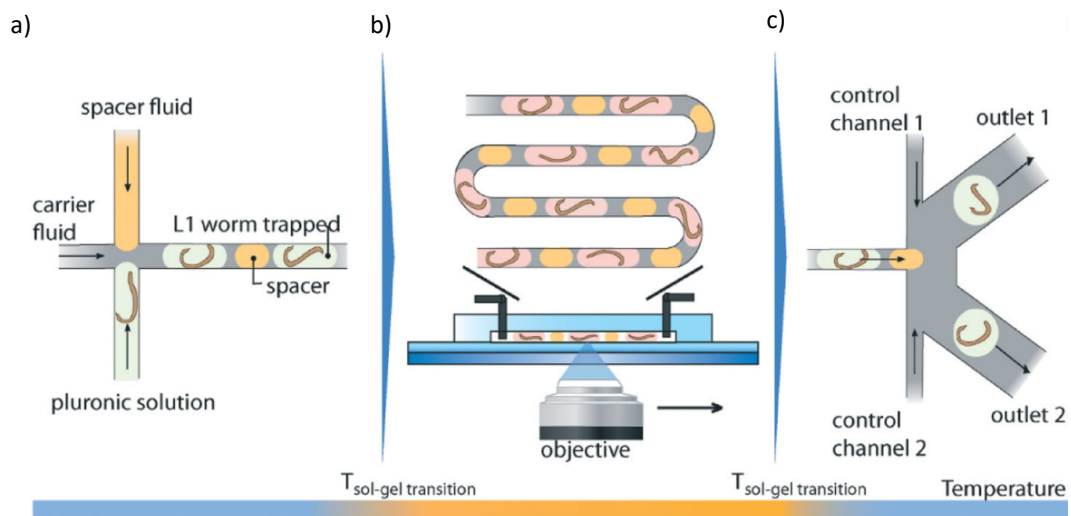


Figure 2-12- Different modules of a hydrogel-droplet microfluidic device for manipulation, high-resolution imaging and sorting of *C. elegans* worms. (a) Droplet production. (b) Storage and immobilization in a serpentine channel for imaging. (c) Sorting. Reproduced from [90].

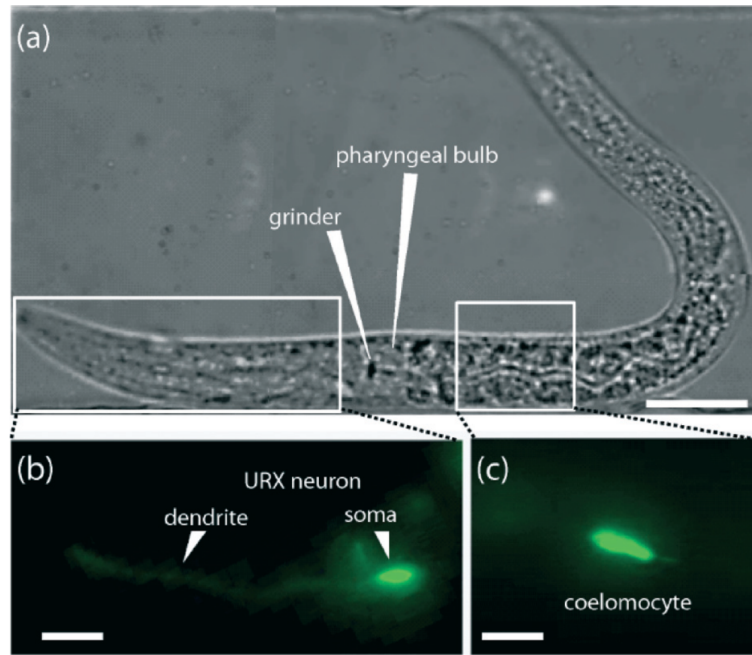


Figure 2-13- High-resolution images of L1 worms immobilized in PF127 droplets obtained utilizing a 63x objective. (a) Brightfield image. Scale bar = 25 μm . Fluorescent images of (b) a URX neuron in the head and (c) a coelomocyte. Scale bars = 12 μm in (b) and (c). Reproduced from [90].

Cornaglia et al reported a microfluidic platform for automated studies on neurodegenerative diseases (Figure 2-14) [88]. The microfluidic device allowed long-term culturing and monitoring of worms in dedicated chambers (Figure 2-14dii), thereby enabling tracking of each worm for the duration of study. The microfluidic platform included a Peltier module and a PID controller for temperature control. Such a temperature control system allowed the automation of the temperature regulation in the microfluidic device (Figure 2-14b). Therefore, when needed, they could heat up and cool down the 25 % w/v PF127 solution for high-resolution imaging and washing steps, respectively. Using this device, they monitored protein aggregation in *C. elegans* models for neurodegenerative diseases such as amyotrophic lateral sclerosis (ALS) (Figure 2-15) and Huntington disease (HD) through fluorescence and brightfield imaging. Low-resolution imaging for screening purposes could be carried out without immobilizing the worms. However, high-resolution imaging required the worms to be immobilized first before they could be imaged.

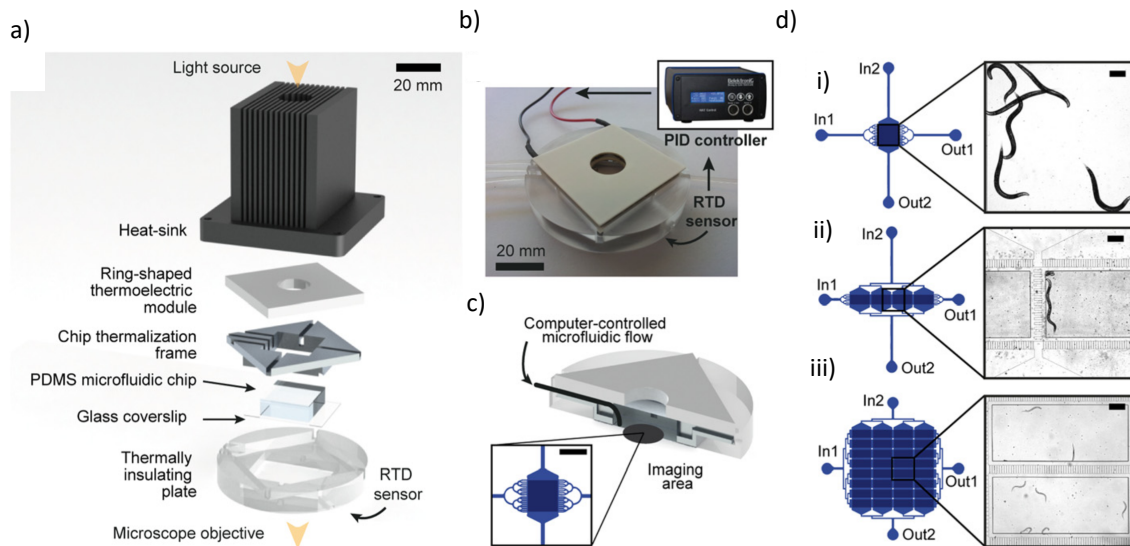


Figure 2-14- (a) The main elements of the microfluidic platform. (b) Photograph of the device and the schematic picture of the temperature control system. (c) Cross-section view of the assembled device. The inset shows the part of the microfluidic chip that can be observed from the imaging area. Scale bar = 2 mm (d) Different designs of microfluidic chips with (i) 1, (ii) 4 and (iii) 32 culture chambers. Scale bars = 200 μm . Reproduced from [88].

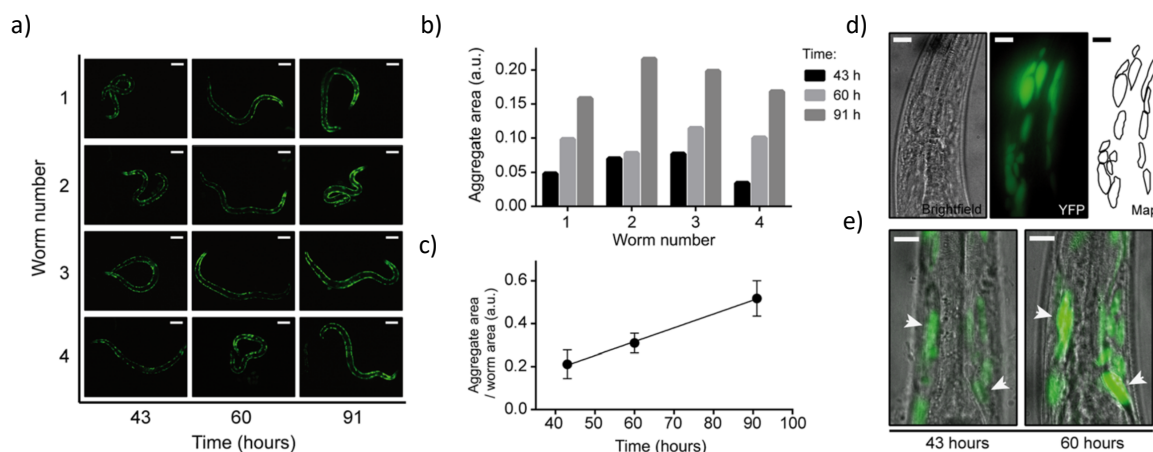


Figure 2-15- Time-lapse fluorescence imaging of four ALS model worms immobilized using PF127. These are transgenic worms (strain AM725) which express mutated human SOD1-YFP fusion proteins in the body wall muscle cells. Scale bar = 100 μm . (b) Growth rate of SOD1-YFP aggregates in each worm. (c) Average protein aggregate area per worm area over time. (d) High-resolution brightfield and fluorescent images of worm 1 acquired 91 hours after the worm was loaded on the device using a 63x/1.4 NA oil immersion objective. The morphology of the aggregates can be mapped. (e) Superimposed high-resolution brightfield and fluorescent images of worm 4 acquired 43 and 60 hours after the worm was loaded on the chip. The arrow heads point at the specific SOD1-YFP aggregates which can be tracked over time. Scale bars = 20 μm . Reproduced from [88].

2.4 Microfluidic devices for host-microbiota studies

In section 2.3, we gave an overview of a number of microfluidic devices for a variety of applications. We also showed the evolution of long-term high-resolution imaging using microfluidic devices. However, very few microfluidic devices for studying host-microbiota interactions can be found in the literature. Yang et al reported a microfluidic device for exposing worms to pathogenic bacteria and evaluating the effectiveness of natural antimicrobial compounds for treatment of the infected worms

[95]. The microfluidic device features a central reservoir that is used to introduce young adult worms to the 32 radially-distributed chambers. There are four Concentration Gradient Generators (CGG), each providing a unique group consisting of 8 chambers with 8 different concentrations of a chosen antimicrobial compound (Figure 2-16a).

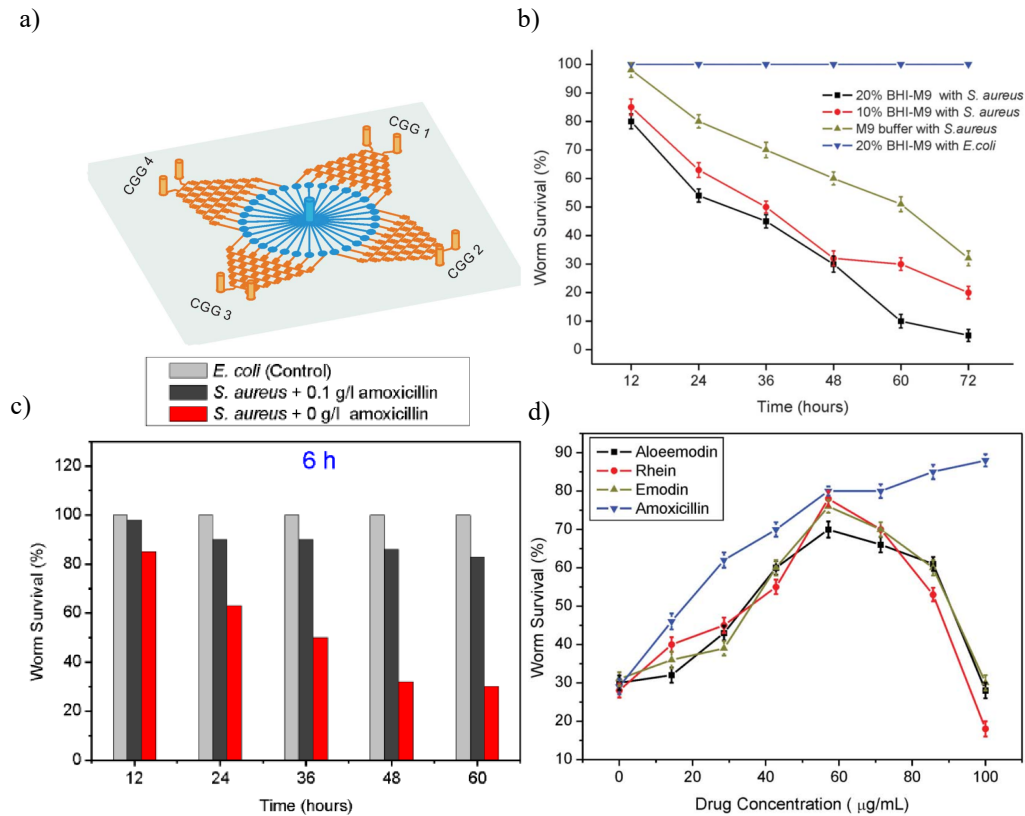


Figure 2-16- The First microfluidic device reported for, exposing worms to pathogenic bacteria and their subsequent treatment with antimicrobial compounds. (a) 4 CGGs supplying 8 unique chambers with different concentration of antimicrobials compounds. Worms and subsequently pathogenic bacteria are loaded in the chambers from the central inlet. (b) Survival of worms exposed to *S. aureus* or *E. coli* in different media (c) The survival of worms that were initially exposed to *S. aureus* for 6 hours and were subsequently treated with amoxicillin. (d) The effect of the antimicrobial compound and its dose on the survival of infected worms (exposed to *S. aureus* for 6 hours). Reproduced from [95].

To carry out an infection assay using this device, 10-15 worms were first introduced in each chamber and were subsequently exposed to a pathogenic bacterium (*S. aureus* in this case) for a set duration. Afterwards, the pathogenic bacterium was flushed out and the worms were treated with different doses of different antibiotics as supplied by the four CGGs. The survival rate of the worms was used to evaluate the effectiveness of the treatment. Using this platform, they could show the effect of the liquid culture media and the duration of exposure to pathogenic bacteria (*S. aureus* in this case) on the survival of the worms (Figure 2-16b). To confirm that the worm killing is via bacterial colonization of the intestine, they performed fluorescence imaging, albeit at a relatively low-magnification and not in a systematic manner. Interestingly, they also demonstrated that worms exposed to *S. aureus* for 9 hours or more could not recover even when treated with antibiotics. Similarly, they could also show that only after 6 hours of exposure, antibiotic treatment is required and the optimum duration for treatment is 48 hours (Figure 2-16c). Lastly, using the CGGs, they could compare the dose-dependent effectiveness of a variety of natural antimicrobial compounds with amoxicillin (Figure 2-16d).

Lee et al reported a microfluidic chip for studying the interactions between pathogenic bacteria and *C. elegans* in an automated fashion [96]. The device featured 10 large chambers within each an adult worm population (20-30 worms) could be introduced (Figure 2-17a). The chambers had a hexagonal array of pillars which allowed the worms to move freely as they do on agar plates. Once the chambers were loaded with adult worm population, a suspension containing the pathogenic bacterium of interest (in this case *P. aeruginosa* PA14) was introduced to chambers. In this work, the survival of the worms (Figure 2-17b), the expression of the infection response gene (*irg-1::GFP*) (Figure 2-17c) and their motility (Figure 2-17d) were monitored via automated low-resolution brightfield and fluorescence imaging throughout the duration of infection until all the worms had died. The resulting images were also analyzed in an automated manner by first detecting the pixels corresponding to each worm and subsequently extracting the parameters of interest.

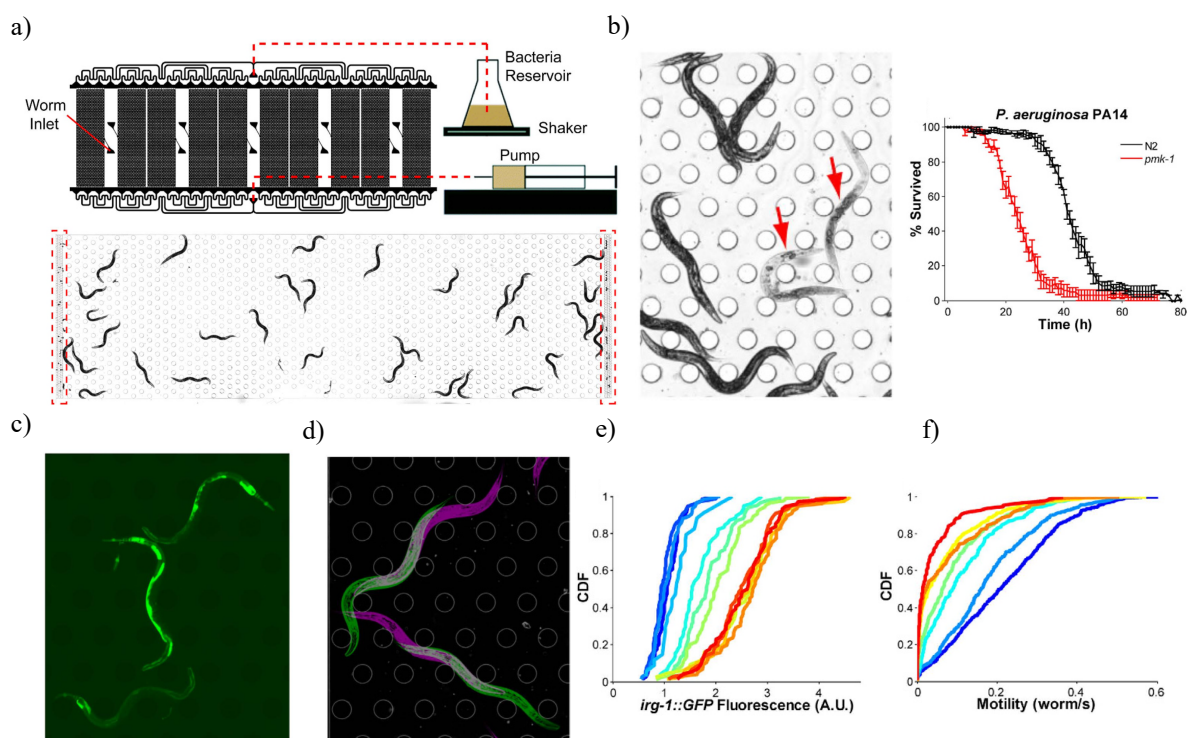


Figure 2-17- HandKAchip, a microfluidic device enabling automated killing assays using *C. elegans*. (a) The design of the microfluidic device. (b) The low contrast of dead worms with respect to the background allows the automated monitoring of worm survival over time. (c) The infection gene response (*irg-1::GFP*) monitored through fluorescence imaging. (d) The displacement of the worms between two acquired frames yields the motility of the worms. Single-worm resolution analysis represented through the cumulative distribution function (CDF) of (e) infection gene response (*irg-1::GFP*) and (f) motility. Reproduced from [96].

In the case of worm survival, a threshold value for opacity was used to determine whether the worms are alive or dead, as dead worms become rapidly transparent. The motility was obtained by measuring the displacement of the worms between two images that are acquired 1 second apart. Lastly, to obtain the response of the worm to *P. aeruginosa* infection, the fluorescence signal intensity of the *irg-1::GFP* gene throughout the entire body of the worm was extracted. The algorithm for automated image analysis was also capable of distinguishing single worms in cases where a group of worms were in contact with each other (Figure 2-17e and f). While the imaging and analysis framework allowed

longitudinal monitoring of worms at single-worm resolution, it was not capable of maintaining the identity of the worms through time.

Viri et al reported a microfluidic device for studying the dynamics of bacterial transition in *C. elegans* worms in an automated fashion [97]. The device featured 4 lanes and in each lane 5 chambers, for growth and immobilization of worms were arranged consecutively (Figure 2-18a). Each chamber could accommodate 1 to 3 worms (in the L4 stage and at adulthood) and included a large free space where the worms could freely move and feed on bacteria (in this case, fluorescent *E. coli*). Additionally, within each chamber, an array of tapered channels for worm immobilization could be also found. Low-resolution time-lapse fluorescent images were acquired from the worms while they were freely moving and feeding on fluorescent *E. coli* OP50 (Figure 2-18b) and when they were immobilized (Figure 2-18b). These images were then analyzed to acquire the spatio-temporal evolution of the bacteria-derived fluorescence signal within the intestine of the worm (Figure 2-18c). The analysis and imaging of GFP-tagged *E. coli* HT115 fed-worms while they were freely moving and eating in the chambers showed that a feeding cycle, starting from the ingestion of bacteria until the clearance of bacteria from the intestine takes about 70 s. Similar analysis was performed on immobilized worms (Figure 2-18d).

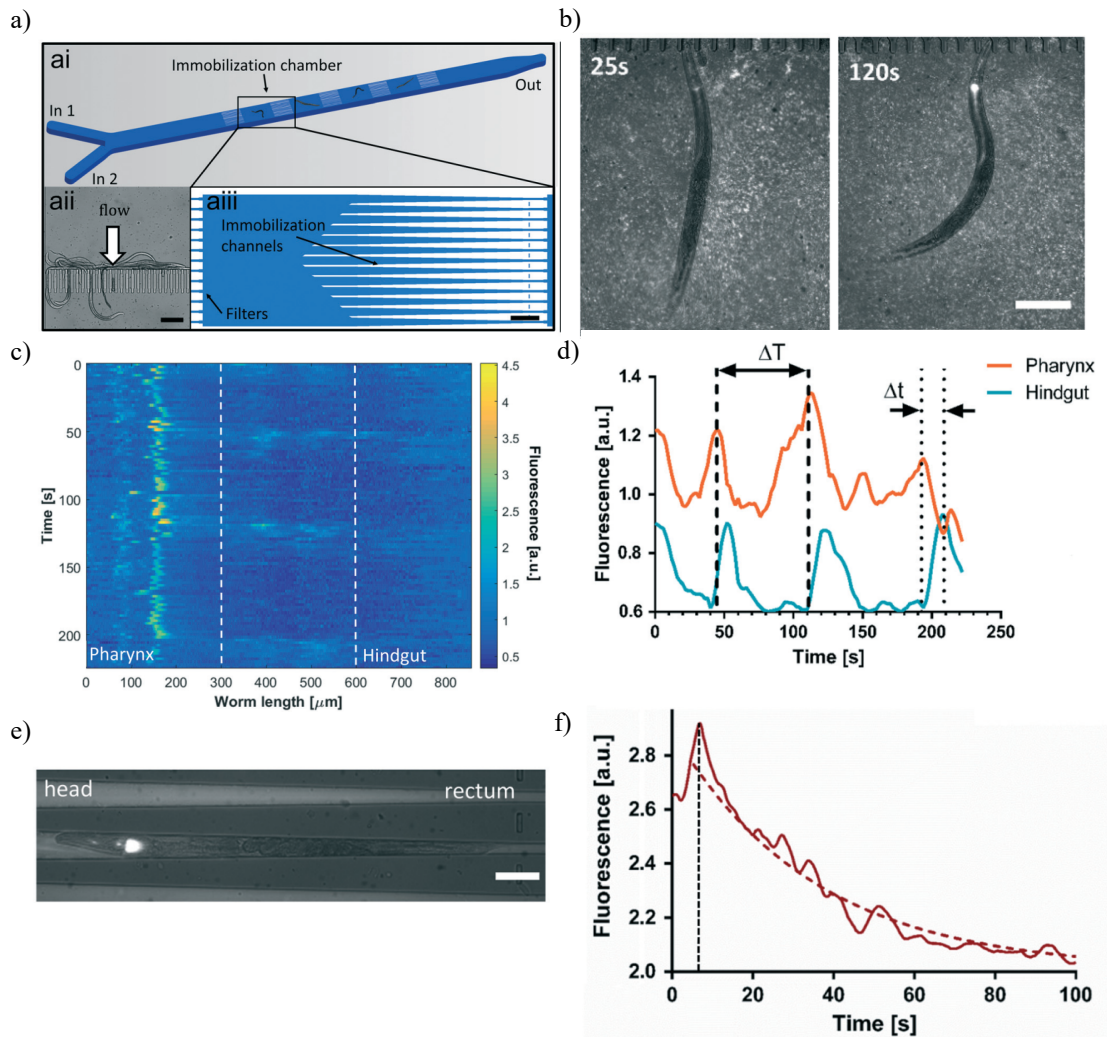


Figure 2-18- Microfluidic device for automated studies on bacterial transit in *C. elegans* worms. (a) The design of microfluidic device. (b) Two example images from time-lapse fluorescence imaging of freely-moving worms feeding on GFP-tagged *E. coli* HT115. (c) Analyzing the time-lapse fluorescent images (in b) yields the spatiotemporal evolution of bacterial load in the body of worms. Spatial averaging over the first third and the last third of the worm body yields the bacterial load in the pharynx and hindgut, respectively. (d) Time-evolution of bacterial load in pharynx and hindgut of worms fed on GFP-tagged *E. coli* HT115. (e) One example image from time-lapse fluorescence imaging of immobilized worms. (f) Time-evolution of bacterial load in the pharynx of immobilized worms. Reproduced from [97]

It should be noted that, once the worms are immobilized, they are incapable of ingesting further bacteria and thus analysis of bacterial load in these worms reveals the bacteria transit time constant. Using these two types of analysis, they could show the effect of worm age, the rate of pharyngeal pumping, and drugs on the dynamics of bacterial transit processes.

Viri et al improved on their previous work and reported a new microfluidic device with enhanced immobilization for studying bacterial load dynamics and digestion in an automated way [98]. The device featured 4 chambers each located in a channel (Figure 2-19a). Similar to the previous device, each chamber included an area where the worms could freely move and feed. However, the main difference is the presence of carefully designed geometric traps that can safely immobilize a single worm for 30 hours and yet allow the worm to freely feed on bacteria and lay eggs (Figure 2-19b and

c). As immobilizing the worms in this device did not stop them from feeding, the dynamics of bacterial transit and digestion could be studied at a higher resolution through fluorescence imaging using a widefield microscope equipped with a 50x objective. In particular, the higher resolution made it possible to distinguish disrupted bacteria from intact ones by applying an intensity threshold (Figure 2-19d-g). Analyzing the time evolution of the disrupted bacteria-derived fluorescence signal yielded a bacterial digestion time constant of 14 ± 4 s (Figure 2-19h and i).

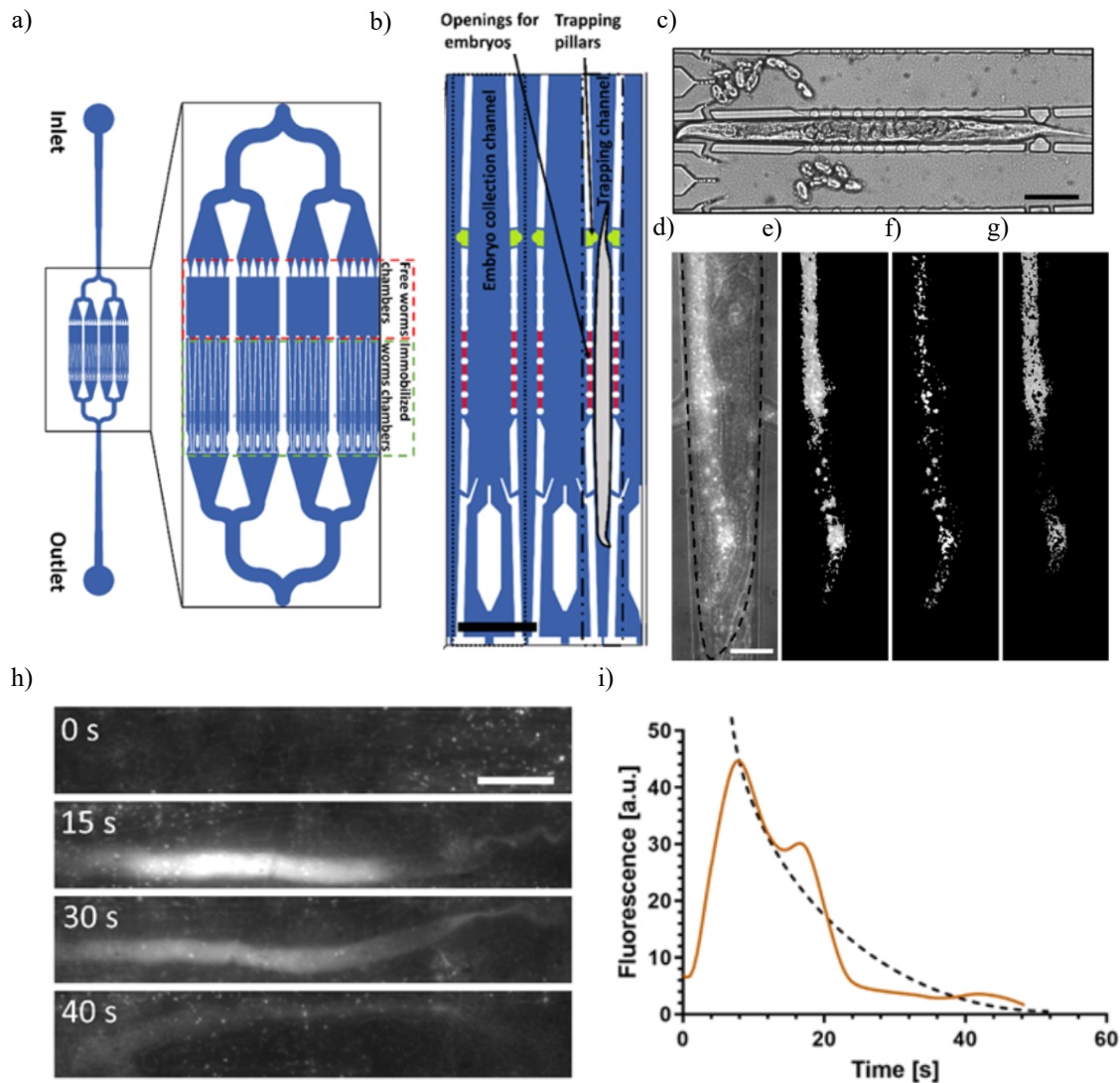


Figure 2-19- Microfluidic device for automated studies on bacterial load dynamics and digestion. (a) The design of the microfluidic devices. (b) The worms are immobilized within a trapping channel. (c) Example of an immobilized adult worm. (d) High-resolution brightfield/fluorescent images of intestinal bacteria. (e-g) Using a brightness level thresholding protocol, the total fluorescence intensity (e) and the fluorescence intensity of intact (f) and disrupted bacteria (g) can be extracted from d. (h) Time-lapse high-resolution images of bacteria in the hindgut of an immobilized worm fed RFP-labelled *E. coli* OP50. (i) The time evolution of the intensity of disrupted bacteria (extracted from h according to the protocol described in e-g) was used to estimate a bacterial digestion time constant of 14 ± 4 s. Reproduced from [98].

2.5 Imaging modalities for *C. elegans* studies

While adequate immobilization is crucial to high-resolution imaging of *C. elegans* worms, the microscopy techniques involved also play an important role in the resolution and the contrast of the resulting images, especially when the obtained images will be later subjected to quantitative analysis. Widefield fluorescence microscopy remains as one of the oldest and most routine techniques for observing transgenic *C. elegans* worms [99]. However, the adult *C. elegans* worms can have diameters that reach up to 80 μm and observing such an organism using widefield microscopy is not ideal. This is because in widefield microscopy, the entire sample is being illuminated and the light originating from out-of-focus planes reduces the contrast and blurs the image (Figure 2-20a) [100]–[102].

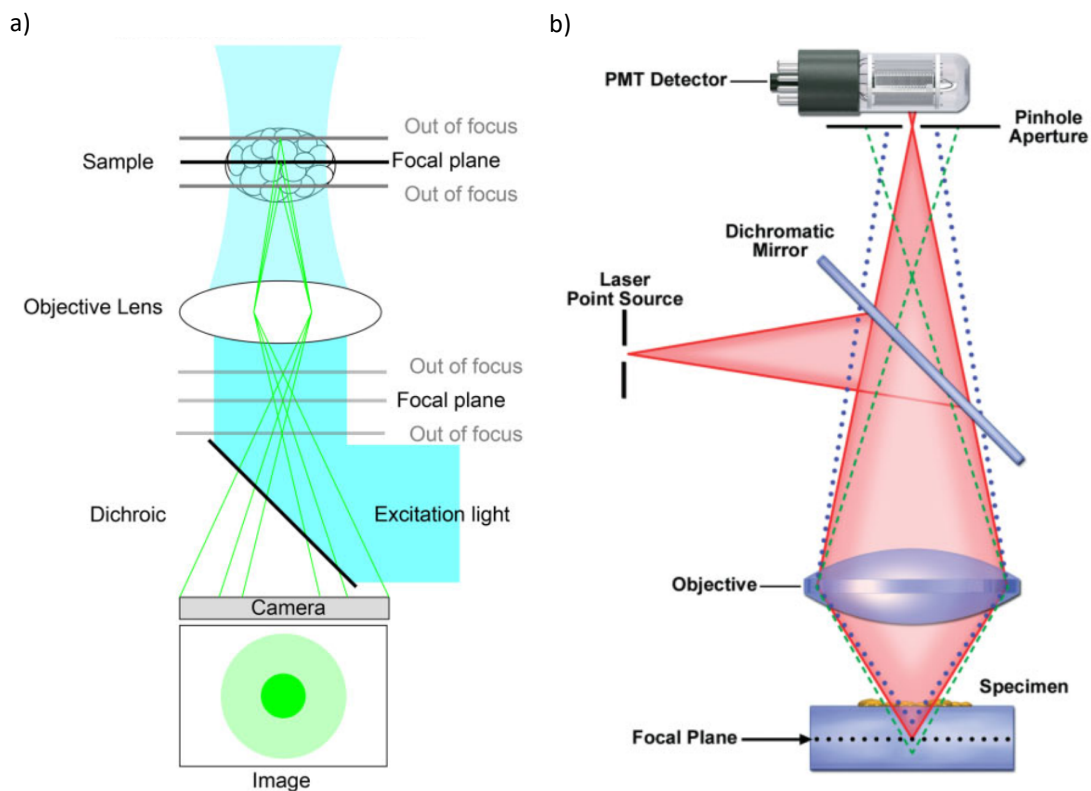


Figure 2-20- Simplified schematics demonstrating the principle of operation in (a) widefield fluorescence microscopy and (b) Laser Scanning Confocal Microscopy (LSCM). (a) In widefield epifluorescence microscopy, the out-of-focus light is collected by the camera resulting in a blurry image with reduced contrast. Reproduced from [99]. (b) In LSCM, most of the out-of-focus light (blue and green dashed line) is blocked by the pinhole while the in-focus light (red solid line) passes through the pinhole and is collected by the PMT. For the sake of simplicity, the galvanometer mirror for the scanning of the excitation laser beam is not shown. Reproduced from [103].

One way to remove the out-of-focus light is to use an image processing procedure called deconvolution which relies on acquiring z-stack images of sample of interest and the point spread function of the optical system to remove the out-of-focus light in thick samples and restore the contrast and increase the signal-to-noise ratio [100]. Alternatively, it is also possible to use microscopy techniques that are capable of removing the out-of-focus light or in words others capable of acquiring optical sections of the (thick) sample [101], [104]–[106].

One of the common microscopy techniques capable of this feat is the Laser Scanning Confocal Microscopy (LSCM). In this technique, a small single spot of laser beam is scanned over the sample using galvanometer mirrors and the fluorescent signal emitted by the sample is collected by a PhotoMultiplier Tube (PMT) through a pinhole placed at the conjugate plane (Figure 2-20b) [105]. This pinhole serves to block most of the out-of-focus light emitted by the sample since the fluorescent light that is emitted by parts of the sample that lie above or below the plane of focus will converge to a point either before or after the pinhole (Figure 2-20b). Additionally, it is possible to have better axial and lateral resolutions in LSCM compared to widefield microscopy by using smallest possible pinhole [103], [105]. However, in practice, such an approach is exercised with caution as reducing the size of the pinhole also limits the amount of in-focus light and as a result reduces the signal-to-noise ratio [103], [105]. LSCM can be used to image both live and fixed samples, but care must be taken to avoid inducing photobleaching and phototoxicity during imaging due to high excitation intensities used when compared to widefield fluorescence microscopy [101], [103]. One of the disadvantages of LSCM is the slow imaging speed (as the sample needs to be illuminated long enough to have sufficient signal-to-noise ratio and the focused laser spot needs to be scanned across the sample) and therefore multiplexing schemes such as Spinning Disk Confocal Microscopy (SDCM) can mitigate the lack of imaging speed [99], [103], [107].

In SDCM, the sample is illuminated through a spinning disk that has pinholes all having the same dimensions that are arranged spirally across the disk (Figure 2-21a) [108]. In this way, the sample is being illuminated through multiple pinholes and as a result the imaging procedure is parallelized and the dwelling time (the time spent exciting the fluorophores sample) can be increased to have better signal-to-noise ratio [99], [107]. Additionally, in this technique, as the sample experiences less peak intensity compared to the LSCM, the risk of phototoxicity and photobleaching is reduced [99], [109]. In earlier implementation of the SDCM, only a small portion (4 to 6%) of the light passed through the spinning disk, and as a result the sample was not well illuminated. However, this issue is solved in the Yokogawa implementation of the spinning disk where the micro lenses focus the light into the pinholes and consequently the light throughput is in range of 40 to 60% (Figure 2-21a) [107], [108]. In SDCM, the pinhole crosstalk can reduce the axial resolution (in particular, when imaging thicker samples) as the light that is scattered or originates from structures present in regions removed from the focal plane can still arrive at the sensor via adjacent pinholes [102], [105]. Overall, the SDCM has lower axial resolution and optical sectioning capability compared to LSCM and in return, it offers better imaging speed and signal-to-noise ratio with lower risks of photobleaching and phototoxicity [102], [103].

Another microscopy technique capable of acquiring optical sections is Light Sheet Fluorescence Microscopy (LSFM) also known as single plane illumination microscopy (SPIM) in which the sample is illuminated using a sheet of light that is parallel to the imaging plane [99]. In this manner, only a thin layer of the sample is being illuminated and as a result the fluorophores present in planes that are out of focus are not excited and thus do not contribute to the image formation (Figure 2-21b) [100]. Furthermore, since an entire plane of the sample is being illuminated at once, the images can be acquired at a much faster rate when compared to LSCM [110]. Additionally, as only a thin layer of the sample is being excited at a given time, the risk of photobleaching and phototoxicity is significantly

reduced in this technique [110]. As a result, this imaging modality is suitable for long-term imaging of organisms in the range of several days. Despite these advantages, the available commercial products are generally less mature and the mounting of *C. elegans* worms and embryos are challenging and require creativity and training [99], [106], [111].

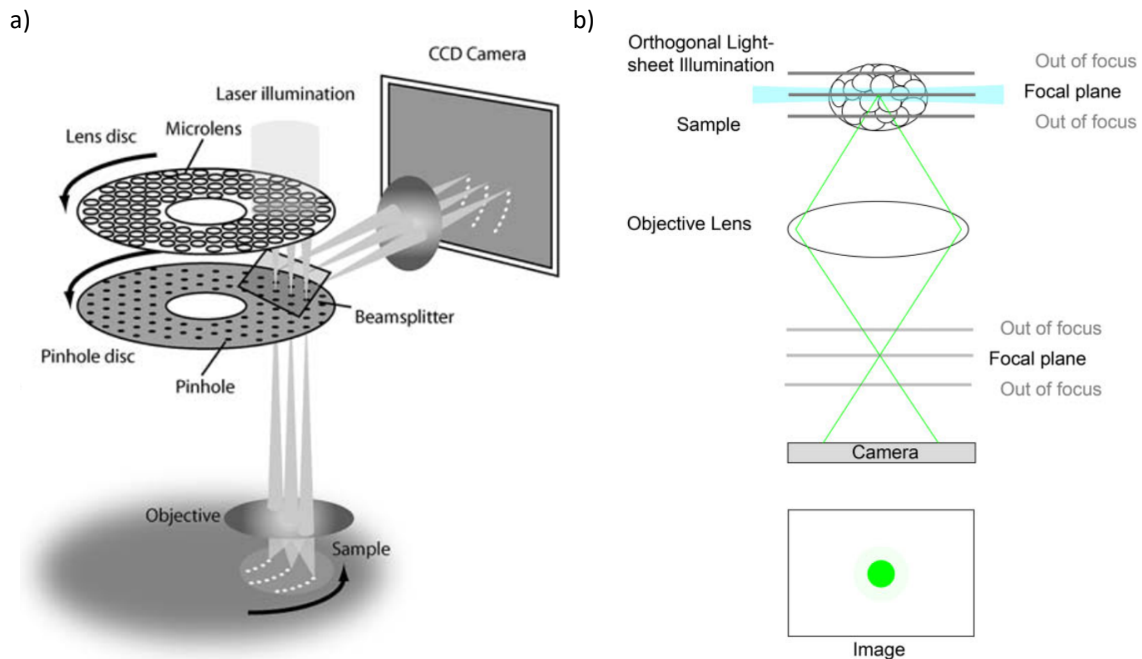


Figure 2-21- (a) Schematic drawing of the Yokogawa implementation of SDCM featuring an array of micro lenses to increase the illumination throughput. Reproduced from [107]. (b) A simplified schematic demonstrating the principle of operation in light sheet microscopy. Optical sectioning capability is acquired by illuminating only a thin layer of the sample. Reproduced from [99].

In summary, SDCM offers a good compromise between axial resolution, optical sectioning capability, imaging speed, signal-to-noise ratio, photobleaching and phototoxicity when compared to LSCM [102], [103], and benefits from the maturity of commercial products available and the ease of sample mounting when compared to LSFM [99], [106], [111].

2.6 Immobilization strategies for high-resolution *in vivo* imaging of intestinal bacteria

In section 2.4, we reviewed a number of microfluidic devices for host-microbiota studies. Among those devices [95]–[98], the (more recent) one by Viri et al [98] affords the highest imaging resolution. In this work, fluorescence imaging was carried out using a widefield microscope. However, observing a thick sample such as a *C. elegans* worm using widefield fluorescence microscopy is not ideal due to the contribution of the out-of-focus light to image formation. As discussed in section 2.5, one way to solve this problem is to acquire z-stack images and perform de-convolution to eliminate the out-of-focus light and thus increase image contrast and the signal-to-noise ratio [100]. However, In the work by Viri et al [98], no attempts were made to acquire z-stack fluorescent images. Alternatively, it is

possible to rely on optical sectioning microscopy techniques such as SDCM to remove the out-of-focus light [107]. Furthermore, high-resolution z-stack fluorescent images acquired using SDCM (or in general any optical sectioning technique) can be assembled to create 3D representations of the observed samples which in this case (considering the work of Viri et al [98]) is the fluorescent bacteria in the intestines of the worms [103]. To the best of our knowledge, there are no reports in the literature on the 3D representation of intestinal bacteria in *C. elegans* worms obtained via high-resolution z-stack fluorescence imaging.

In vivo high-resolution z-stack imaging of the worm crucially depends on immobilizing the worm without harming it. To better understand the suitability of different immobilization strategies for high-resolution host-microbiota studies, we will evaluate the state-of-the-art microfluidic devices that enable *in vivo* high-resolution z-stack imaging of the worm, regardless of the type of study carried out. In addition, we will also highlight the general design considerations for host-microbiota studies. Among the microfluidic devices we reviewed in section 2.3, the devices reported by Gokce et al [84], Berger et al [93], Keil et al [85] and Cornaglia et al [88] are most relevant to our discussion.

Studies on the bacterial colonization of the intestine in *C. elegans* involve monitoring the worm, at least for a few days starting from L4 stage. We should also keep in mind that the adult worms grow and reach a length of ~ 1 mm and a diameter of $80 \mu\text{m}$ [112]. These circumstances impose additional restrictions for the design of a microfluidic device targeting host-microbiota studies. Considering the device reported by Gokce [84] in the light of these requirements above shows that the device has been not tested for on-chip maintenance of the worm for more than 24 hours. At the same time, due to the lack of dedicated culturing areas, the identities of the worms cannot be maintained. Most importantly, the traps are designed for immobilizing L4 and young adult worms and as such they cannot accommodate adult worms as their diameter reach $80 \mu\text{m}$. As a result, the already sophisticated trapping channels, the fabrication of which involved four lithography steps, may not be suitable for the immobilization of adult worms. In principle, for any trap to restrict the movement of the worm without harming it, its dimensions should be adapted to the size of the worm. Considering that the diameter of the worm changes from $29.5 \mu\text{m}$ at L4 stage and reaches up to $80 \mu\text{m}$ in adulthood [112], [113], an even more geometrically complex trap is required to be able to adequately and safely immobilize the worm during these stages. It should also be noted that the trapping efficiencies of the traps in this device depended on the age of the worms to be immobilized: $94 \pm 1.1\%$ for L4 worms and $83.3 \pm 2.0\%$ for young adult worms. This further shows another consideration in the design of the traps, as the automation of the imaging procedure depends on the consistency of trapping.

Similar to the device above, the single-layer microfluidic devices developed by Berger et al [93] leveraged traps with carefully adjusted dimensions and valves to immobilize the worms for long-term high-resolution z-stack fluorescence imaging. Since adequate immobilization of the worms requires the adaptation of the dimensions of the traps to the sizes of the worms, three separate microfluidic devices each featuring a specific trap geometry were designed to enable immobilization of the worm at L3 and L4 stages and during adulthood. Unlike the device reported by Gocke [84], the current devices did not include a culture area where the worms could feed and swim freely; rather, the worms were kept immobilized within the trap at all times. While this simplifies the tracking of individual

worms during the course of experiments, this raises concerns with regards to the potential negative impact of immobilization on the health of the worm. While the authors claimed that the continuous immobilization had no detrimental effect on the health of the (adult) worms, the lifetime reported for the immobilized adult worms in this device was ~50% of the reported lifetimes of worms moving freely in a previously reported microfluidic device [81].

The 2-layer microfluidic device developed by Keil et al [85] uses valves to immobilize worms inside circular chambers and thereby enable long-term high-resolution z-stack fluorescence imaging. The device supports the development of the worms from L1 stage until the onset of egg laying in adulthood but not beyond it as the progenies will gradually accumulate in the chamber. Consequently, this device is not suitable for studying host-microbiota interactions as such studies require monitoring the worms during adulthood. The worms are allowed to move and feed freely in the chamber, and when needed, the pressure-mediated deformation of the membrane can safely immobilize the worms, regardless of their age. Automation of the imaging process at a high resolution crucially depends on immobilizing the worm in a pre-defined location- a consequence of the limited field of view at high magnifications- which is not possible in this device due to the simple implementation of valve-based immobilization. However, the authors overcame this shortcoming by using a combination of demagnifying camera adapter and a camera sensor with sufficient number of pixels to capture the entire chamber in a single frame, albeit at the cost of resolution.

The microfluidic device reported by Cornaglia et al [88] relies on the sol-gel transition of PF127 to immobilize worms and image them at a high resolution . Additionally, this device allows long-term culturing of the worms which is essential for host-microbiota studies. However, in this device, similar to the device reported Keil et al [85], there is no control over the location of the immobilized worms. As a result, the automation of high-resolution imaging, and in particular, z-stack imaging is out of reach. Furthermore, the use of PF127 solution for immobilization increases the risk of clogging in the channels, especially when long-term studies are concerned.

In summary, there is no perfect approach for the immobilization of worms for high-resolution host-microbiota studies. Any immobilization approach relying on traps should take into account the change in the size of worms from the L4 stage until and during adulthood, because this change affects the efficiency of trapping, the degree of immobilization, and the health of the worm. On the other hand, the immobilization approaches that rely on a deformable membrane should address the lack of precise control over the location of immobilized worms. Similarly, devices that make use of a PF127 solution for immobilization suffer from the same issue and in addition, a higher risk of clogging in channels in long-term studies.

3 High-resolution imaging and analysis of the intestinal bacterial load of *Caenorhabditis elegans* during early adulthood

We study the presence within the worm *Caenorhabditis elegans* (*C. elegans*) of a fluorescent strain of the worm's bacterial food (*Escherichia coli* (*E. coli*) OP50) during early adulthood. Use of a microfluidic chip based on a thin glass coverslip substrate allows investigating the intestinal bacterial load using a Spinning Disk Confocal Microscope (SDCM) equipped with a high-resolution objective (60x). High-resolution z-stack fluorescent images of the gut bacteria in adult worms, which were loaded in the microfluidic chip and subsequently fixed, were analyzed using IMARIS software and 3D reconstructions of the intestinal bacterial load in the worms were obtained. We present an automated bivariate histogram analysis of the volumes and intensities of the bacterial spots for each worm and find that, as the worms age, the bacterial load in their hindguts increases. We could show the advantage of single-worm resolution automated analysis for bacterial load studies and anticipate that the methods described in our work can be easily implemented in existing microfluidic solutions to enable thorough studies of bacterial proliferation.

This chapter is a copy of the following publication:

- **Farzad Rezaeianaran (F.R.)** and Martin A. M. Gijs (M.G.), "High-resolution imaging and analysis of the intestinal bacterial load of *Caenorhabditis elegans* during early adulthood," *RSC Advances*, vol. 13, no. 25, pp. 17230–17243, 2023, doi: 10.1039/D3RA02934D. Creative Commons license: <https://creativecommons.org/licenses/by-nc/3.0/>. Authors contribution: **F.R.** and M.G. conceptualized the research project. **F.R.** designed the platform and experiments and fabricated the microfluidic chip. **F.R.** performed the experiments, carried out the image analysis and analyzed the data. **F.R.** wrote the original draft. M.G. reviewed and edited the original draft. This work is supported by the Swiss National Science Foundation (Grant No. 205321-179021).

3.1 Introduction

The nematode *C. elegans* is a bacterivorous organism with considerable genetic similarity to humans and is used as a model for studying the relation between microbiota and aging and health/diseases [1], [2], [8], [15]–[18]. In particular, this roundworm, owing to its genetical tractability and evolutionary conserved innate immunity is an established model organism for the investigation of virulence mechanisms of pathogens [17].

In order to discover the virulence determinants, different mutants of a pathogen of interest as well as the worms are generated and the interactions between the bacteria and the host (worm) is studied through survival curves and bacterial colonization assays. However, these assays typically cannot capture the interactions between the host and the bacteria on a microscopic scale. For example, the bacterial colonization itself can only measure the number of viable bacteria and it cannot determine whether the bacteria are merely accumulating in the gut or if they are proliferating there. Additionally, this assay cannot reveal the spatio-temporal dynamics of bacterial colonization in the gut as this requires real-time *in vivo* fluorescence imaging of the gut. Furthermore, the impact of pathogenic bacteria on the worm is not limited to the colonization of the gut. For example, it has been reported that both *Salmonella typhimurium* (*S. typhimurium*) and *Pseudomonas aeruginosa* (*P. aeruginosa*) reduce the motility and the rate of pharyngeal pumping of the worm over the course of infection [54], [57]. Intestinal infection with *Serratia marcescens* (*S. marcescens*) leads to the lysis and vacuolation of intestinal cells and a reduction of the volume of the epithelium [33]. Therefore, a complete description of bacterial pathogenesis also requires imaging, to extract the relevant phenotypes, and the use of/designing of specific assays that target a certain interaction between the host and the pathogen (e.g., using competition and shifting assays to investigate whether a certain pathogen is capable of establishing a persistent infection[51], [54]). While we mainly discussed the requirements for studying bacterial pathogenesis in the worm, it should be noted that the same requirements apply when it comes to investigating the beneficial aspects of commensal and probiotic bacteria or the role of the worm's native microbiome.

Based on the analysis above, it can be seen that a comprehensive characterization of the host-microbiota interactions, if done manually, is extremely laborious. However, this is exactly what makes microfluidics such a powerful approach. Microfluidic devices offer [72]: (i) precise control over experimental conditions, (ii) facilitating manipulations of worms permitting high throughput screening studies, (iii) ease-of-doing long-term studies, (iv) reversible immobilization for both low- and high-resolution imaging, (v) laser microsurgery [84], [86], [87]. As a result, the use of microfluidics for studying *C. elegans* has been extensively practiced [78] and different devices for low-throughput long-term studies at single-worm resolution [81]–[83], [85], [93] as well as high-throughput and high-content screening studies have been reported [77], [79], [114].

However, only a few microfluidic devices have been reported for studying the interactions between bacteria and *C. elegans* [95]–[98]. Yang et al., [95] fabricated a microfluidic chip featuring 32 chambers arranged radially and 4 concentration gradient generators for evaluation of *in vivo* antimicrobial

activity of several compounds. Each concentration generator supplies 8 unique chambers with 8 different concentrations of a given antibiotic. The device enables on-chip establishment of an infection model (in this case *Staphylococcus aureus* after 6 hours) and antibiotic treatment of the infection (in this case amoxicillin and some natural compounds for 48 hours) and, compared to conventional methods, requires less analysis time and less reagent consumption. However, the evaluation of antimicrobial activity was mostly limited to survival curves (within a 72-hours period). Fluorescence imaging of the worms was feasible but, since each chamber contained around 10 worms that were not immobilized, neither high-resolution imaging nor single-worm resolution analysis were possible.

In another study by Lee et al., [96] a microfluidic chip for implementing a *C. elegans* killing assay was reported. The chip featured large chambers where the worm and the pathogen of interest (in this case *P. aeruginosa*) could be loaded. Survival curves were obtained with high accuracy and reproducibility. Due to lack of an immobilization mechanism on the chip, only low-resolution imaging could be performed. Imaging in the brightfield channel was used for the automated detection of dead worms and motility analysis, while fluorescence imaging was implemented for measuring the expression of *irg-1::GFP* (infection response gene 1). Since, the worms were freely moving in the chamber without any compartments, they could not be differentiated from each other, and thus individual worms could not be monitored over the entire course of the experiment.

In the more recent works by Viri et al., [97], [98] the dynamics of bacterial transition, load and absorption in the gut of the worms are studied in an automated fashion through fluorescence imaging. The first microfluidic device [97] contained 4 channels, each of which comprised 5 consecutive chambers, separated by filter structures. These chambers, which could hold 1-3 worms, included a culturing area where the worms could freely move and feed on fluorescent *E. coli* and tapered traps that immobilize the worm and stop it from eating (due to the application of strong fluid flow required for immobilization). Low-resolution fluorescence imaging over the entire body of the worms was performed, while they were freely moving and feeding on the fluorescent bacteria. Analyzing the resulting image sequence yielded the spatio-temporal distribution of the bacteria in the gut, albeit at a low resolution. In addition, the duration of a full cycle of bacterial ingestion until intestinal clearance was determined. Similar imaging and analysis were also performed while the worms were immobilized. In this case, the time constant of the transition of recently ingested bacteria could be obtained (as the worms could not eat while they were immobilized).

The second microfluidic device [98] was similar in scope to the first one but had a different design. The device still consisted of 4 channels, but each channel had 4 parallel chambers instead. As before, these chambers included a culturing area where the worms were free to move and feed but the design of the trapping structure was modified so that the worm could continue eating while it was immobilized. As a result, the dynamics of bacterial load and digestion could be studied on immobilized worms using fluorescent bacteria at relatively higher imaging resolution. The higher resolution made it possible to distinguish the ingested intact bacteria from the ingested disrupted ones and as a result, and the time constant for food digestion was determined. As the immobilization could be maintained for 30 hours, long-term studies at single-worm resolution were also possible. While the newly improved immobilization and imaging procedure allows the spotting of intact bacteria, the bacterial

dynamics load assay described was not capable of answering questions on bacterial colonization of the gut. Granting that the intact bacteria are indeed viable and have the potential to forming colonies, it is by no means guaranteed that this effectively happens in the gut; it is very much possible that the viable bacteria merely accumulate in the gut and do not proliferate.

Therefore, in this work, we intend to bring the analysis of intestinal bacteria to a higher level, by acquiring for the first time high-resolution z-stack fluorescent images of fluorescent *E. coli* bacteria in the gut of fixed worms using a SPDM. The resulting images are subsequently imported in IMARIS software to allow visualization bacterial load of the gut in 3D. Such a representation facilitates the investigation of eventual bacterial colonization of the gut. We could study whether there are preferential regions in the gut for colonization and how intestinal bacterial load advanced with time.

3.2 Materials and methods

3.2.1 Chip materials and chemicals

4 inch 550 μm Si wafers, 5-inch Chromium/soda–lime glass masks, polydimethylsiloxane (PDMS) Sylgard 184 (Dow[®]) and trimethylchlorosilane (TMCS) (Sigma-Aldrich) were obtained from the Center of MicroNanoTechnology (CMi) at EPFL (Lausanne, Switzerland). Kayaku Advanced Materials (KAM) SU-8 3050 was purchased from Micro Resist Technology GmbH (Berlin, Germany). 45 mm \times 70 mm glass coverslips with a thickness of 170 μm were purchased from Biosystems Switzerland AG (Muttens, Switzerland). Saint-Gobain Tygon[™] ND 100-80 Tubing (inner diameter and thickness of 0.02 inch and outer diameter of 0.06 inch) was bought from Fisher Scientific (Reinach, Switzerland). Nematode growth medium (NGM) plates were ordered from the Solution Preparation Facility at EPFL. S-basal was prepared by first dissolving 5.85 g of NaCl, 6 g of KH_2PO_4 and 1 g of K_2HPO_4 in H_2O until a final volume of 1 l was reached. The resulting solution was then autoclaved, and, once it cooled down, 1 ml of cholesterol solution (5 mg ml^{-1} in ethanol) was added aseptically to obtain S-basal. S-medium was obtained by adding aseptically 500 μl of 1 M potassium citrate (pH 6), 500 μl of trace metals solution, 150 μl of 1M CaCl_2 and 150 μl of 1M MgSO_4 to 50 ml of S-basal. The materials involved in the preparation of S-basal and S-medium, lysogeny broth (LB) for bacteria culture and tetracycline were ordered from Sigma-Aldrich Chemie GmbH (Buchs, Switzerland). 4% paraformaldehyde (PFA) solution in phosphate buffered saline (PBS) for the fixation of *C. elegans* was purchased from Fisher Scientific (Reinach, Switzerland).

3.2.2 Worm and bacteria culture and preparation

C. elegans wild-type (WT) Bristol N2 strain were maintained 22 °C on NGM plates (55 mm in diameter) seeded with *E. coli* OP50. In order to synchronize the worm populations for experiments, gravid adult worms are suspended in S-medium in a falcon tube overnight. During this period, the adults lay eggs which will hatch into L1 larvae. Due to the absence of food, the hatched L1s will enter developmental

arrest resulting in a synchronized L1 population. The next day, L1s were aspirated from the falcon tube and thus separated from dead adults (as the adults sediment while the L1s remain floating in S-medium) and were placed inside 1.5 ml Eppendorf tubes to be centrifuged for 4 min at 2000 RPM. Afterwards, the L1s were aspirated from the bottom of the Eppendorf tube and about 100 of them were dispensed on NGM plates seeded with *E. coli* OP50.

E. coli OP50 was grown overnight in LB at 37 °C on a shaker. *E. coli* OP50 expressing Red Fluorescent Protein (RFP) was provided by the *C. elegans* Ageing Laboratory at the University College London. *E. coli* OP50 was transformed with plasmid *pRZT3::dsRED* to construct RFP-expressing *E. coli* OP50. The plasmid also contains genes for tetracycline resistance. As a result, RFP-expressing *E. coli* OP50 was grown in LB containing 10 µg/ml of tetracycline overnight at 37 °C on a shaker.

3.2.3 Fabrication of the microfluidic chip

The layout of the microfluidic device was designed with Clewin 4.0 (WieWeb software, Hengelo, The Netherlands) and then transferred to a chromium/soda-lime glass mask using standard mask fabrication processes. Afterwards, the mask was employed in standard soft photolithography processes to fabricate a 75 µm high SU-8 mold on a Si wafer. Next, the SU-8 mold was treated with TMCS to promote the detachment of PDMS from SU-8. Subsequently, PDMS with base-to-curing agent ratio of 10:1 was casted onto the mold and cured at 80 °C for 2 hours. Afterwards, the cured PDMS device was cut and separated from the SU-8 mold and punched to create inlets and outlets. Next, the PDMS device was bonded to a 45 mm × 70 mm coverslip with a thickness of 170 µm using oxygen plasma. To enhance the bonding between the PDMS device and the cover slide, the microfluidic chip was kept on a hotplate at 80 °C for 10 minutes. Lastly the tubing for the inlet and outlet were connected.

3.2.4 Image processing and statistical analysis

IMARIS (version 9.9.1) was used to process the raw optical microscopy images. The results of image analysis by IMARIS were extracted to datasheets which were further processed in MATLAB (version 2022a) and Graphpad Prism (version 9.5.0) software. MATLAB was used for basic arithmetic operations on the datasets and in particular, to create histograms in an automated fashion. Furthermore, MATLAB was also used to extract certain quantitative results and prepare them for further processing for GraphPad Prism. GraphPad Prism was mainly used to elaborate on the statistical variation and the statistical significance of the data. The number of worms analyzed for each experiment is shown by the parameter “n”. Since the processed data did not follow a Gaussian distribution, we employed the Mann-Whitney test to determine statistical significance. Furthermore, based on previous studies, we expected specific trends in different experimental conditions. Consequently, we utilized the one-tailed Mann-Whitney test.

3.2.5 Microscopy platform and the imaging parameters

Two different microscopes were used in our experiments. A Zeiss Axio Imager.M2 with a 2.5X Zeiss objective was used in brightfield mode to prepare the microfluidic chip for the experiment and to load and fix worms on the chip. We used a Visitron CSU-W1, an SDCM for high-resolution fluorescence imaging. It was equipped with a Hamamatsu ImagEMX2 electron-multiplying CCD (EMCCD) camera. The different lasers used for the excitation of the fluorophores for imaging in the RFP and the Green Fluorescent Protein (GFP) channels were operating at wavelengths 561 nm and 488 nm, respectively. We used Chroma Technology (Vermont, USA) ET605/70m and ET525/50m emission filters for the RFP and GFP channels, respectively. Lastly an Olympus U PLAN S APO 60X/1.42 NA objective was employed for high-resolution imaging. The imaging was done with the following parameters: exposure time: 60 ms, laser power for both the RFP and the GFP channels: 50%, gain of the EMCCD camera: 200, pinhole size: 50 μm , z-stack imaging: 50 μm range with step size of 0.2 μm .

3.3 Experimental

3.3.1 Operation of the microfluidic device

We have designed our microfluidic device (Figure 3-1a) such that we can load an adult worm population of interest on the device, contain them within an area in the channel and fix them for the purpose of high-resolution imaging with an SDCM. The device comprises 5 lanes where each lane is 2 cm in length, 1300 μm wide and 75 μm high. This height was chosen since the diameter of a young adult worm is on average 48 μm and can reach up to 80 μm during adulthood. Each lane also features 2 sets of filter structures, the purpose of which is to keep the worms on the right side of the channel while a fluid flow towards the inlet is maintained. Figure 3-1b shows an example of the fabricated microfluidic chip. The filters are each 20 μm wide and the spacing between them is 15 μm , except in the middle area where it is 30 μm instead (Figure 3-1c). As the worms are compressible, especially if high flow rates are used, the filter sizes should be smaller than the diameter of the worms so that the worms cannot squeeze through the filters.

Before a worm population of interest can be loaded on the chip, the channels should be filled by S-medium. The chip therefore is placed on the stage of the Zeiss Axio Imager.M2 equipped with a 2.5x Zeiss objective to be observed in brightfield mode. To introduce S-medium in the chip, we connect its inlet tube to a neMESYS syringe pump (CETONI GmbH, Korbußen, Germany) where a 1 ml BD I Luer-Lok syringe containing S-medium is present. When the chip is filled with S-medium for the first time, bubbles of air are bound to form in the channel. To remove the air bubbles, the tube of the outlet is clipped, 10 μl of S-medium is dispensed in the channel which pressurizes the air bubbles and thus facilitates their disappearance via the outward diffusion of air through the PDMS. In our case, the debubbling process takes around 15-20 minutes. Next, the worms suspended in S-medium (inside an Eppendorf tube) can be placed at the outlet of the chip and by aspirating with a flow rate of 500 nl s-

1, the worms are loaded in the chip (Figure 3-1d). It is preferred to have around 10-15 worms in the channel. In the case of overcrowding/undercrowding, further aspirations/dispensing of S-medium can be performed to adjust the number of worms present in the channel. In order to fix the worms, a 4% PFA solution is placed at the outlet and by aspiration with a flow rate of 80 nl s^{-1} , it is introduced inside the channel. We use a relatively low flow rate to avoid excessive pushing of the worms against the filters. The worms are fixed within 5-10 minutes of being in contact with the 4% PFA solution. At this point, the inlet and outlet tubing are cut and clipped, and the worms are ready for high-resolution imaging.

It should be noted that while mounting already fixed worms on agarose pads is an option, we opted for conducting the fixation process and imaging on a microfluidic chip. This approach enables simultaneous fixation and imaging of all the worms while demonstrating its compatibility with various microfluidic devices for investigating host-microbiota interactions.

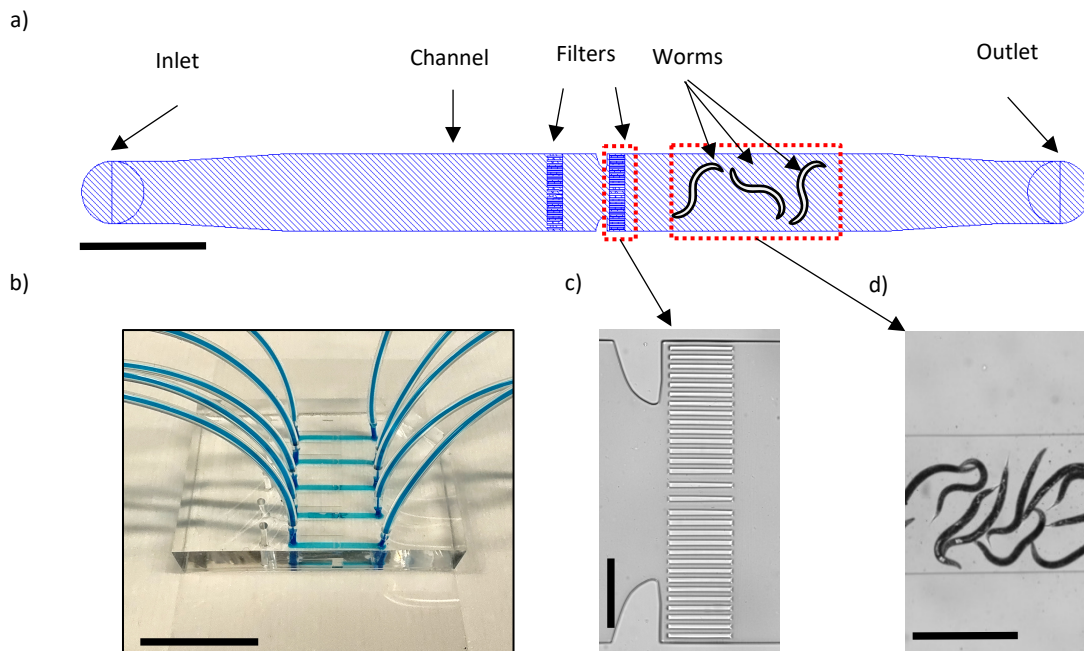


Figure 3-1-Microfluidic device for high-resolution imaging of *E. coli* OP50 in the *C. elegans* gut. (a) Schematic representation of one of the five lanes in each device. The lanes are $1300 \mu\text{m}$ wide and $75 \mu\text{m}$ high. The filters serve to contain the worms in the channel. Scale bar = 2 mm . (b) Image of a fabricated microfluidic chip where the channels are filled with a blue dye. Scale bar = 2 cm . (c) Brightfield image of the filter structures. Scale bar = $300 \mu\text{m}$. (d) Brightfield image of the worms in the channel. Scale bar = 0.8 mm

3.3.2 Experimental planning

The aim of our experiment is to observe the bacterial presence in the intestine of the worm for young adult worms of different ages via high-resolution fluorescence imaging. Figure 3-2 shows the steps involved in our experiment. To obtain a synchronized L1 population, an adult population of wild-type *C. elegans* is suspended overnight in S-medium in a 50 ml falcon tube. During this period, the adults lay eggs that will hatch into L1 larvae. Due to lack of food, these larvae will be in a state of developmental arrest resulting in a synchronized population. The day after, ~ 100 hatched L1s were

placed on an NGM plate seeded with *E. coli* OP50 (Figure 3-2a and b). The L1s are cultured on these plates until they reach adulthood (46 hours at 22 °C) and afterwards, they are transferred to an NGM plate seeded with RFP labelled *E. coli* OP50. Before this transfer takes place, the number of *E. coli* OP50 present in the S-medium is reduced to a minimum by serial dilutions (1:10¹⁰ total dilution) (Figure 3-2 c).

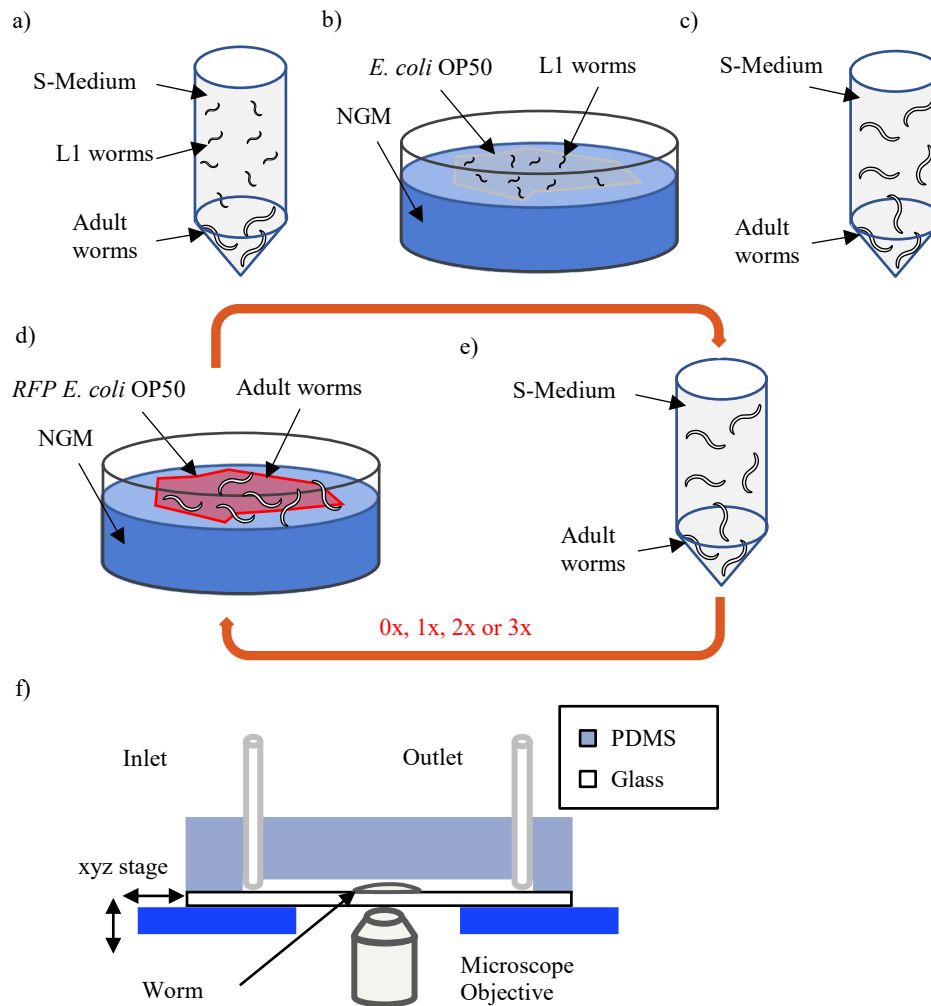


Figure 3-2- The experimental steps involved in high-resolution imaging of fluorescent *E. coli* in the *C. elegans* gut. a) Suspending adult worms in S-medium overnight yields numerous synchronized L1s in developmental arrest the next day. b) ~100 synchronized L1s are transferred to an NGM plate seeded with *E. coli* OP50 and kept there until they become adults (46 hours at 22 °C). c) The adult worms are taken from the NGM plate and are washed in S-medium in a 1.5 ml Eppendorf tube; since adults naturally sediment at the bottom of the tube, the supernatant is removed (1:10 dilution) and the process is repeated until the number of *E. coli* OP50 present is reduced to a minimum (a total of 1:10¹⁰ dilution). d) The adults are now transferred to an NGM plate seeded with *E. coli* OP50 expressing RFP and kept there for 24 h. e) To remove the progenies of the adult worms, every 24 h, the adults are taken from the plate and are suspended in S-medium and a total of 1:10¹⁰ dilution is performed (similar to “step c”). Afterwards, the adult worms are transferred to new NGM plates seeded with *E. coli* OP50 expressing RFP. Given the number of the days, adult worms are planned to be fed on *E. coli* OP50 expressing RFP (1 day, 2 days, 3 days and 4 days), steps d and e are repeated as many times as required (0x, 1x, 2x and 3x for 1 day, 2 days, 3 days and 4 days feeding, respectively). Once the last repetition of “step e” is done, the worms are instead kept in the Eppendorf tube containing S-medium for one hour to ascertain that recently ingested bacteria are fully processed. f) The worms are loaded on the microfluidic chip and are fixed with a 4%PFA solution. Afterwards, the tubings are cut and clipped and the microfluidic chip is transferred to an SDCM for high-resolution imaging of the gut bacteria.

This allows us to safely assume that, after the transfer, the adult population is only feeding on RFP-expressing bacteria (Figure 3-2d). The transfer is done after the worms become adults because the

bacterial colonization of the gut starts in adulthood. We plan to image the adult worms that have fed on RFP labelled bacteria for 1, 2, 3 and 4 days. Since our imaging relies on fixing the worms to enable the highest possible resolution, it's not possible to follow an identical worm at different times. In our case, for each experimental condition (1, 2, 3 and 4 days of feeding on RFP-expressing bacteria), we used separate worm populations fed over variable times with RFP-labelled *E. coli* OP50. Since we are using WT worms in our experiment, naturally the adults will lay eggs over time. This will cause two problems, namely, the fast depletion of food on the plates and a confusion in selecting the original adult worms (and not their progenies) for imaging. Therefore, only the adults should be transferred to a new plate seeded with RFP-labelled *E. coli* OP50 every 24 hours (Figure 3-2e). The transfer process is done in the same way as explained earlier (Figure 3-2c), however, the main aim is instead removing the L1 progenies floating in S-medium by serial dilutions. Furthermore, before the adult worms are loaded on the chip for fixation and imaging, progenies and in particular, RFP-labelled *E. coli* OP50 should be reduced to a minimum. Therefore, considering these two aspects, steps in Figure 3-2d and e should be repeated in this manner: 0x, 1x, 2x and 3x for 1 day, 2 days, 3 days and 4 days of feeding, respectively (0 meaning that steps in Figure 3-2d and e are performed once). After the worms have spent the required time feeding on RFP-labelled *E. coli* OP50 and before they are loaded on chip to be imaged, the worms must stay in the Eppendorf tube containing S-medium (Figure 3-2e) for an hour. Based on the work by Viri et al., [97] in WT worms the time interval between bacterial ingestion and intestinal clearance is about 70 to 90 s. Therefore, it is reasonable to assume that after one hour of starving the worms, any bacteria present in the gut which are observed by fluorescence microscopy may be at least persistent and eventually are colonizing the intestine. The chip is prepared for worm loading as explained in the materials and methods section, one day before the experiment. As the starvation time approaches 1-hour, the worms are loaded on the chip where they are fixed. Afterwards the tubings are cut and clipped and the chip is ready to be taken to an SDCM for high-resolution imaging. The RFP-labelled *E. coli* OP50 was previously used in lifespan and ageing studies and there were no mentions of potential effects of the fluorescent tag on the worm [115]–[117]. As a result, we expect in good faith, that the RFP-labelled *E. coli* OP50, other than being fluorescent, is identical to the unlabelled *E. coli* OP50. Consequently, no control experiments were conceived.

3.3.3 Imaging procedure and analysis

Figure 3-3a shows a typical brightfield image of fixed worms that have fed on RFP-labelled *E. coli* OP50. In order for the worms to be properly imaged in the fluorescence channel, overcrowding of the worms should be avoided, as it can cause two problems. The first problem is the overlapping of the worms on top of each other, which makes it impossible to distinguish the signals originating from each worm. The second problem is fluorophore photobleaching that takes place during fluorescence imaging [118]. When the channel is overcrowded, the worms might not be overlapping, but instead, they are merely touching each other. In such cases, during the fluorescence imaging of one worm, the worm next to it is also being exposed and thus subjected to photobleaching. Despite our best efforts, such cases were present during imaging and therefore, we imaged only one of such worms to prevent our results from getting biased by photobleaching. Our previous observations (not shown here) revealed

that the hindgut is most often the location where bacterial presence is seen and, thus, we limit our observations to the hindgut (Figure 3-3a). High-resolution brightfield images, RFP channel and GFP channel images are shown in Figure 3-3b, c and d, respectively. The imaging parameters (as mentioned in the Materials and Methods section) have been optimized such that signal/noise ratio is high enough in the fluorescence channels, photobleaching is limited and signal saturation is avoided. The z-range of the z-stacks (50 μm) is also large enough to cover the intestine entirely. We use the brightfield mode (Figure 3-3b) to avoid photobleaching while locating the hindgut and adjusting the center of focus for z-stack imaging; afterwards fluorescence imaging is performed (Figure 3-3c and d).

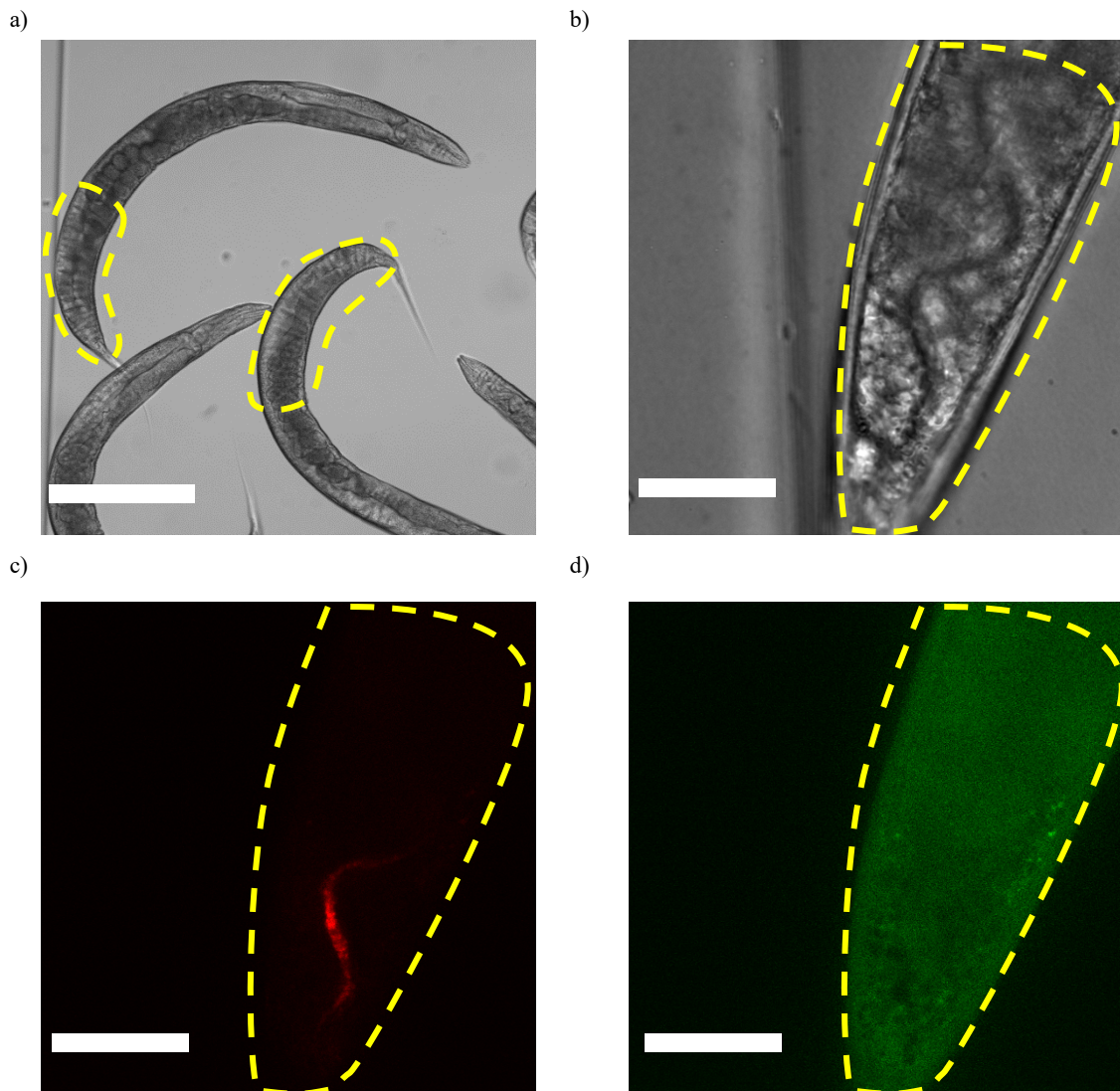


Figure 3-3- Imaging of typical fixed worms that have fed on RFP *E. coli* OP50 (for 1 day in a and 4 days in b, c and d). a) Brightfield image of fixed worms, in which, the hindgut, as area of interest, is delineated. High-resolution b) Brightfield image, c) RFP channel image where the bacteria in the hindgut can be seen and d) GFP channel image where the worm autofluorescence can be observed. (a: 10x objective, scale bar = 250 μm ; b, c and d: High-resolution imaging using an oil-immersive 60x objective, scale bar = 40 μm)

The presence of fluorescent bacteria in hindgut can be clearly observed in Figure 3-3c while the worm autofluorescence that originates mainly from the intracellular lysosome-derived granules within the intestinal cells [119] is seen in Figure 3-3d. As the field of view allows only a length of 150 μm of the worm to be imaged at a time, each worm needs to be imaged twice to observe the entire hindgut. In

our case, the region closest to the tail was imaged first and it was followed by imaging the second half of the hindgut which is further away from the tail.

We can see in Figure 3-4 several slices from z-stack fluorescence imaging of a typical fixed worm that has fed on RFP labelled *E. coli* OP50 for 4 days.

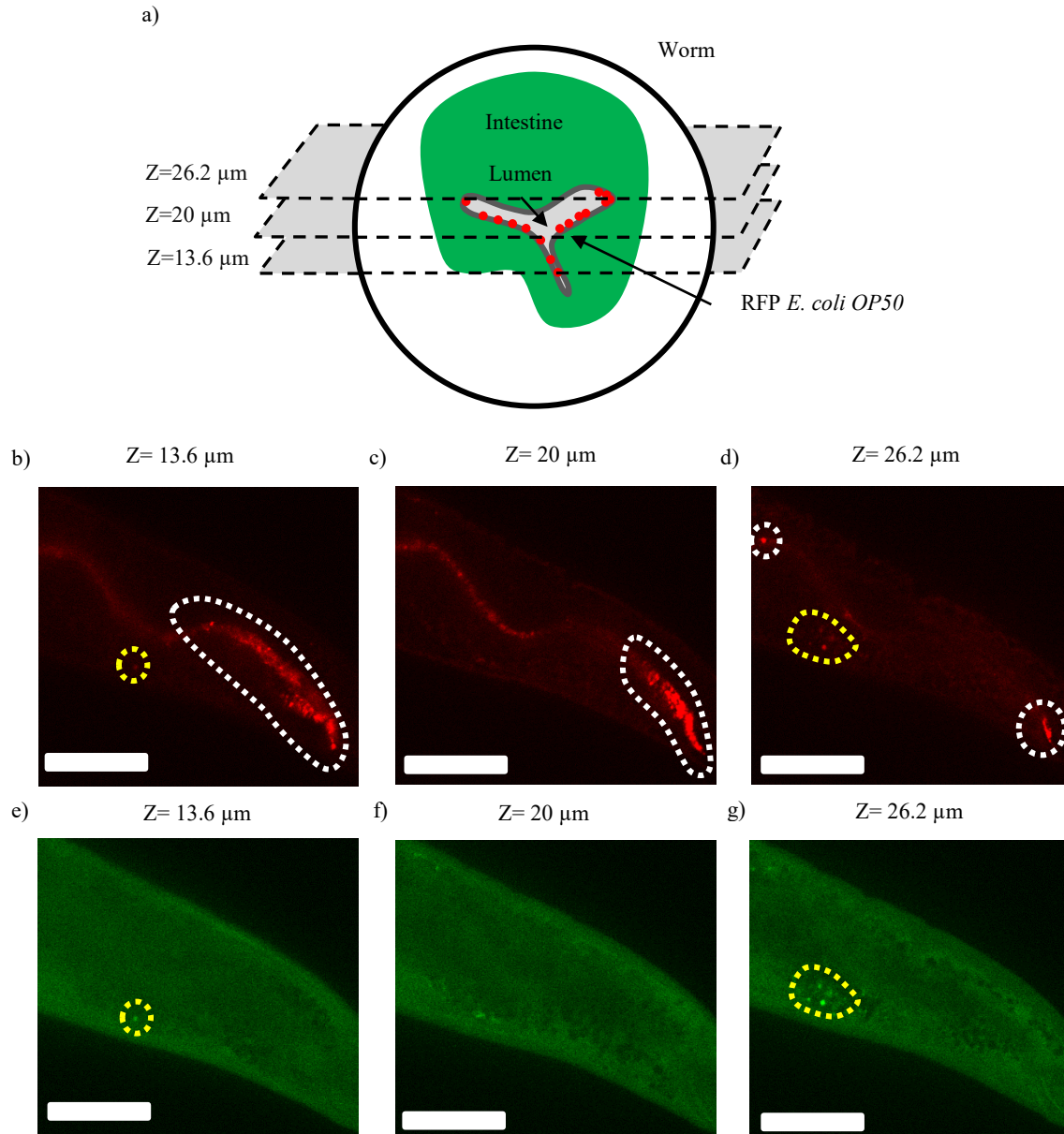


Figure 3-4- Z-stack fluorescence imaging of typical fixed worms that have fed on RFP *E. coli* OP50 for 4 days. The z-stacks are taken using a 60X oil-immersion objective in both RFP and GFP channels. They include 250 slices with a step size of 200 nm and total focal range of 50 μm . a) The three example slices with their associated planes of focus, positioned relative to a schematic worm cross-section. Typical images acquired at these slices are shown both in the RFP channel (b, c and d) and the GFP channel (e, f and g), where the z numbers of images e, f and g are the same as those of images b, c and d, respectively.) Focusing reveals RFP *E. coli* OP50 in the different regions of the hindgut, as highlighted by the white dashed lines in b-d). The signal in the GFP channel originates from autofluorescence in the adult worms. In the presence of strong autofluorescence, the latter signal can also be observed in the RFP channel, as delineated by the yellow dashed lines in (b and e) and (d and g). In these cases, the RFP signal present in the yellow dashed line-limited area in (b and d) should not be attributed to the existence of bacteria and therefore should be omitted from any visualization/analysis pertaining to bacterial load. (Scale bar = 40 μm)

As shown schematically in (Figure 3-4a), the bacteria can be present in different focal planes (z numbers) within a cross-section of the intestinal lumen of the worm. In conventional widefield microscopy the light is received from many focal planes some of which are out of focus and thus leading to blurry image with reduced signal-to-noise ratio and contrast [100], [102]. In contrast, in an SDCM, the pinholes block most of the signal from out-of-focus planes and as a result the bacteria in each focal plane are resolved [107]. Figure 3-4b, c and d are slices with certain z numbers in the RFP channel, where each focal plane reveals the presence of bacteria in different positions (not only in plane but also along the z-axis) within the hindgut. Furthermore, while individual bacterial spots can be observed in Figure 3-4a and c, in Figure 3-4b, the bacteria appear to form clusters having high density. Figure 3-4e, f and g show the same slices (the z numbers of e, f and g are the same as b, c and d, respectively) imaged in the GFP channel. It can be seen that, in the presence of strong worm autofluorescence, the signal appears both in the GFP (Figure 3-4e and g) channel and the RFP channel (Figure 3-4b and d). As a result, in these cases the latter RFP signals should be omitted from bacterial load analysis.

We use IMARIS for visualization and processing of our raw z-stack fluorescent images. IMARIS assembles all the slices belonging to the same channel (e.g. the RFP channel) of a given raw image and thereby creates a 3D image. In our case, since our raw images have two channels, namely, the RFP and the GFP channel, IMARIS creates two 3D images from each raw images-stacks. We can also display the two 3D images at the same time as shown in Figure 3-5a. In this image, a worm that has fed on RFP *E. coli* OP50 for 3 days is displayed. The green signal originates from the autofluorescence of the worm, while the orange signal is due to RFP *E. coli*. A magnified view of the purple rectangle is shown in Figure 3-5b. We can now observe more clearly the orange spots. We also see 3 yellow spots, as indicated by the white arrows, that are due to strong autofluorescence. The strong autofluorescence leads to the presence of signals both in the GFP and the RFP channels. The overlap of the stronger signal in the GFP channel with the weaker signal in the RFP channel results in the yellow spots. These signals should be omitted from our bacterial analysis.

By using the built-in spot detection algorithm of IMARIS, we can detect bacterial spots and obtain their sizes and intensities in a consistent manner. The algorithm begins with setting the RFP channel as the channel of interest for spot detection. Afterwards, we need to provide an initial estimate for the smallest spot size. Based on our observation of bacterial spots across different slices of the raw z-stack fluorescent images, we found the smallest bacteria spot to be 1 μm in the “X” and the “Y” directions. We assumed the bacterial spots to be spherical but due to the point spread function (PSF) of the microscope, the spherical spots become elongated in the “Z” direction and turn into ellipsoids. We thus used 2 μm in the “z” direction to account for the effect of PSF. IMARIS then uses the spot size estimation together with an internal parameter called “Quality” to detect spots. The “Quality” parameter is related to the intensity at the center of a spot in the RFP channel while including correction for the background intensity around that spot. This parameter sets a threshold on the detected spots, meaning spots with lower values are discarded and the spots with higher value are accepted. Based on one typical image, we optimized the value of this parameter such that the vast majority of the spots that we observe (in that one image) are detected by IMARIS and no false positives

are present. We found the optimized value for the “Quality” to be 150 and we used this value for the detection of the spots in all the images to make sure that the detection of spots is consistent (i.e. the results obtained from different images can be meaningfully compared).

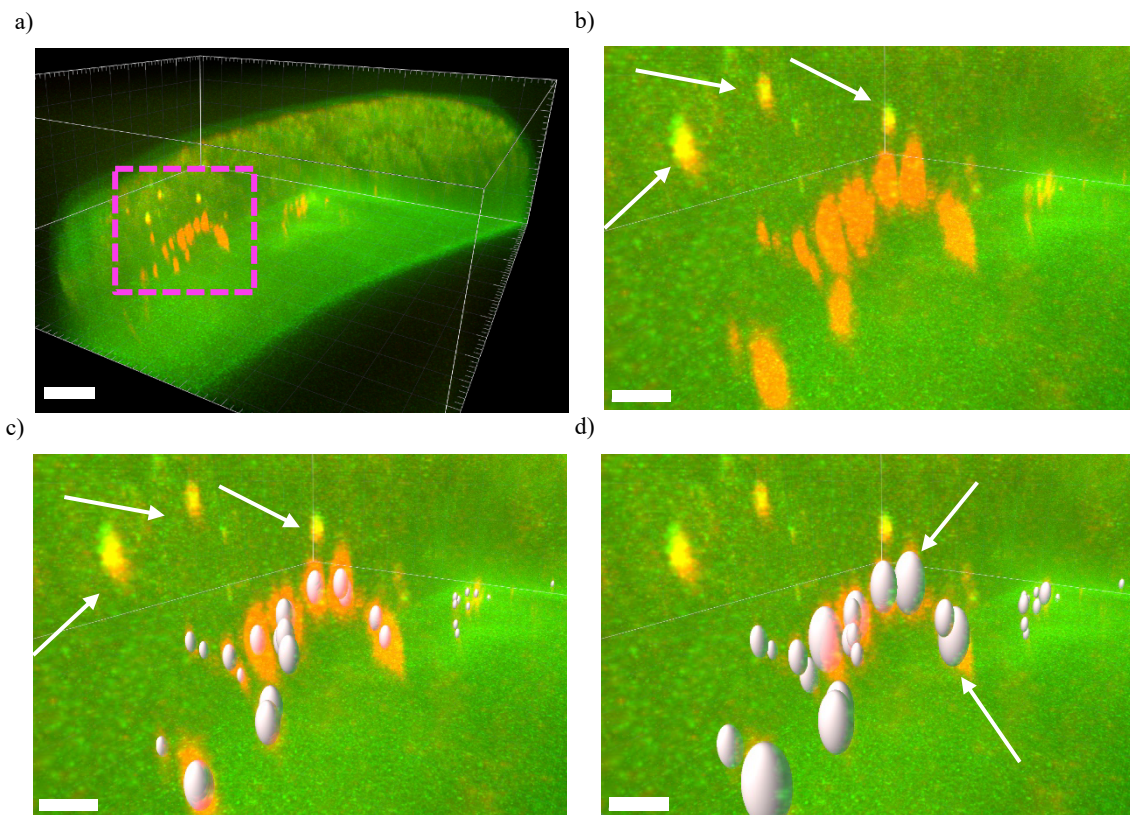


Figure 3-5- Visualization and processing of z-stack fluorescent images in IMARIS. a) 3D presentation of a z-stack image by assembling all the slices from each channel together (RFP and GFP) and displaying both channels at the same time. In this case, a worm that has fed on RFP *E. coli* OP50 for 3 days is being shown. Scale bar = 15 μm b) *E. coli* OP50 are seen as orange spots, while the yellow spots originate from the worm’s autofluorescence. Since the worm’s autofluorescence is strong in these spots, the signal is present both in the GFP channel and the RFP channel and thus the spots appear yellow (as shown by the arrows) due to the overlap of the green color and the red color. A proper bacterial spot detection procedure should identify the orange spots and ignore the yellow ones. Scale bar = 10 μm . c) The spot detection relies on an estimated of the smallest spot size and an IMARIS parameter called “Quality”. In our case, we used 1 μm in x and y directions and 2 μm in z direction. The parameter “Quality” is related to the intensity at the center of a spot while including corrections for the background intensity around that spot. This parameter acts as threshold and thus only spots with higher intensities than this threshold value will be accepted. The optimized “Quality” parameter value was 150 and it was such that the detected spots matched the actual spots we could observe, and no false positives were present. In addition, a threshold limit (3500-4000) was also set on the intensity of the GFP channel to reject the spots that originate from the worm autofluorescence. The white ellipsoids shown are the spots detected using the above-mentioned parameters. It should be noted that at this stage, all the spots are assumed to have the same size that is set by the smallest spots size we used for the spot detection algorithm. It’s only due to the perspective projection that the farther spots are seen smaller. Scale bar = 10 μm . d) The centers of the detected spots are used as seeds and by using a “local contrast” method the spot size is determined. In this approach, the intensity distribution around the center of the detected spot is first adjusted by subtracting from it the intensity of the background in the vicinity of that spot. After this correction, only the region that has intensity higher than a threshold value is considered to be a part of the spot. The optimized threshold value was 80.4 and at this value the finalized spots matched visually to the actual spots. The white ellipsoids seen are the finalized detected spots. Since an actual bacterial region may not be always ellipsoid, the size determination algorithm uses the volume of this region to construct an ellipsoid that has the same volume as this region. Therefore, there is not always a perfect overlap between the actual bacterial spot and the finalized detected spot (as shown by the arrows in d). Scale bar = 10 μm .

The spot detection algorithm also allows the additional filtering of the detected spots by other parameters such as the central intensity of the spots in the GFP channel. This is extremely useful, since, by setting an upper limit (3500-4000, depending on the image) for the central intensity we can discard those spots (in the RFP channel) that originate from the strong autofluorescence of the worm. Figure 3-5c shows the detected spots after applying the said constraints (i.e. estimation of smallest spot size, “Quality” factor, and central intensity in the GFP channel). As it can be seen, all the bacterial spots are detected while the yellow spots, as shown by the white arrows, are discarded from further analysis.

It should be noted that, at this step, only for the purpose of representation, the algorithm assigns to all the detected spots the same ellipsoid that we defined when we provided the dimensions of the smallest spot size. More importantly, it should be emphasized that up to this step, IMARIS treats these detected spots merely as seed points, meaning that it is only the centers of the spots that are meaningful, while their sizes still need to be determined in a consistent manner. The reason that those ellipsoids appear to have different sizes in Figure 3-5c is due to the perspective projection.

Next, we used the “local contrast” method in IMARIS to find the spot size. In this method, the intensity distribution in the region around the center of a detected spot is first adjusted by subtracting from it the intensity of the background in the vicinity of that spot. After the adjustment, only the region around the center of that spot that has an intensity higher than a certain threshold value is considered to be belonging to the spot. If this threshold value is too low, the finalized detected spot will be larger than the actual bacterial spot while if the threshold value is too high, the finalized detected spot will be smaller than the actual bacterial spot. Based on analyzing typical images, we found the optimized value threshold value to be 80.4 in order that the finalized detected spot matched the actual bacterial spot. Figure 3-5d shows the finalized detected spots where the sizes of the detected spots now match the size of the actual bacterial spots. The fine-tuning of this threshold value is subjective, as it is somewhat arbitrary to exactly determine where the border of the actual bacterial spot is and in turn how large the finalized detect spot should be. In addition, sometimes the actual bacterial spot is not perfectly ellipsoidal, which makes it impossible to have a perfect overlap between the actual bacterial spot and the finalized detected spot (Figure 3-5d). As a result, in these cases, it is harder to find the exact value for the threshold parameter. In fact, in all cases, the diameters of the finalized spots are calculated such that the volumes of the finalized detected spots are equal to the volumes of the regions around the center of the spots that have higher intensity than the chosen threshold value. Despite these slight difficulties, we used the same threshold value (80.4) for all the images to ensure that the spot sizes are determined in a consistent manner.

3.4 Results

Figure 3-6 shows an example of extracted data after image analysis by IMARIS, and the post-processing performed to visualize the volume distribution and the intensity distribution of the bacterial spots within the hindgut of the worm. In this example, the data from a single worm that has fed on RFP

labelled *E. coli* OP50 for 4 days is shown. This particular worm was chosen because its hindgut contained only a few bacteria and thus is suitable for illustration purposes. The first two columns of the table (“Vol” and “Int”) in Figure 3-6a are the raw outputs obtained from image analysis in IMARIS. “Vol” is the volume of each spot while “Int” is its average intensity in the RFP channel. To account for the change in background intensity across different experiments (2780-2965 arbitrary units (au)), we modified the average intensity by subtracting from it the background intensity to obtain “C. Int”. The background intensity was obtained by averaging the intensities over an area where the worm is not present. In this case the background intensity was 2900 au. The total bacterial load in the worm is proportional to the sum of the product of “C. Int” and “Vol” ($\text{Vol} \cdot \text{C. Int}$) across all the bacterial spots.

The volume and the average intensity distribution across all the bacterial spots can be presented with histograms (Figure 3-6b, c and d). While the histograms in Figure 3-6b and c are simpler and easier to grasp, in principle, they exclude the possibility of revealing any trends or correlation between the volumes of the bacterial spots and their average intensities. Therefore, we prefer to use a bivariate histogram (Figure 3-6d) to visualize the data in a more precise manner.

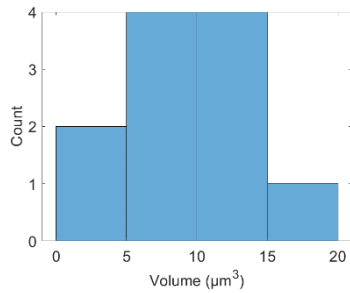
This method of post-processing can be applied to each worm within an experiment to obtain single-worm resolution statistics of the bacterial presence within the hindgut. Additionally, the volumes and the average intensities of all the bacterial spots from all the worms belonging to one experiment, e.g., all the worms that have fed on RFP labelled *E. coli* OP50 for 4 days, can be pooled together. These data can be then visualized with a bivariate histogram normalized by the number of worms in that particular experiment (Figure 3-7d). This bivariate histogram thus shows an average distribution of the volumes and the average intensities of the bacterial spots of worms in one experiment. Additionally, normalizing the sum of $\text{Vol} \cdot \text{C. Int}$ across all the pooled bacterial spots by the total number of worms in the experiment yields the average bacterial load per worm (Figure 3-7e).

a)

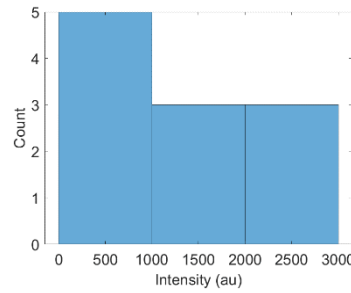
Vol* (μm^3)	Int** (au)	C. Int*** (au)	Vol · C. Int ($\mu\text{m}^3 \cdot \text{au}$)
16.54	3503	603	9980
12.34	3598	698	8617
6.42	3523	623	3999
5.53	3399	499	2757
13.59	4395	1495	20316
7.18	3357	457	3284
11.34	5068	2168	24595
13.01	4909	2009	26139
2.12	5108	2208	4683
3.65	4862	1962	7162
5.89	4806	1906	11233
Total Bacterial Load $\propto \sum \text{Vol} * \text{C. Int}$		1.228E+05 $\mu\text{m}^3 \cdot \text{au}$	

*Vol: Volume **Int: Average intensity ***C. Int: Average intensity corrected for background

b)



c)



d)

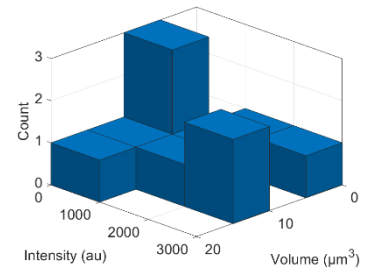


Figure 3-6- Analysis of the detected bacterial spots in a single worm that has fed on RFP labelled *E. coli* OP50 for 4 days. a) The table contains the volume (Vol) and the average intensity of the detected bacterial spots (Int), as extracted from IMARIS. C. Int is the average spot intensity corrected for the background. The product of the volume and the corrected average intensity of each spot (Vol · C. Int) is proportional to the number of bacteria within that spot. The summation of (Vol · C. Int) over all the bacteria spots in one worm is proportional to the total bacterial load in that worm. b) Histogram of the volume of the detected bacterial spots. c) Histogram of the average intensity of the detected bacterial spots. d) The bivariate histogram showing the distribution of the volume and the average intensity of the bacterial spots.

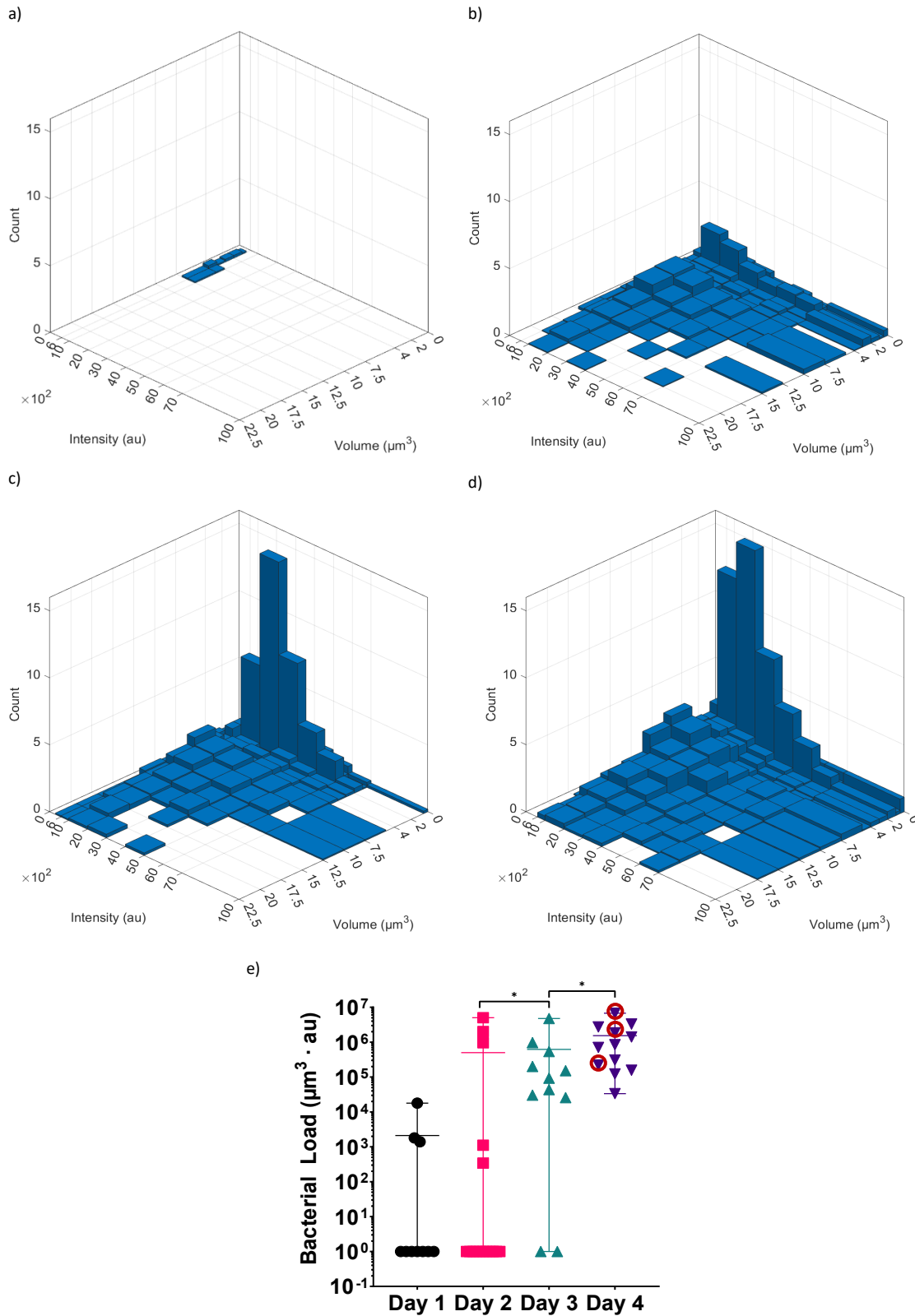


Figure 3-7- Bivariate histograms displaying the average distribution of the volumes and the average intensities of the bacterial spots in the hindgut of worms that have fed on RFP-labelled *E. coli* OP50 for a) one day (n = 10), b) two days (n = 16), c) three days (n = 11) and d) four days (n = 12). e) The total bacterial load of each worm after each day of feeding on fluorescent bacteria. The horizontal bar shows the average total bacterial load for each day while the error bars represent the range of bacterial load in each day. * $p \leq 0.05$.

It can be seen that, as the worms age, the bacterial load in their hindguts increases (Figure 3-7). This is in agreement with the general dynamics of intestinal bacterial load of the worm with age [34]. It is known that the function of the grinder in the pharynx and the innate immunity of the worm decline with age and that older worms have less control over the number of bacteria present in their intestine, thus this trend is to be expected [34]. Furthermore, over time, the number of bacterial spots, their sizes and their average intensity also increase. Therefore, not only there are more bacterial spots within the hindgut of the worm, but also each bacterial spot contains more bacteria. This suggests that there are preferential places in the hindgut where the bacteria accumulate over time, or it may also be possible that the ingested bacteria colonize the gut and proliferate there. It should be emphasized that these two phenomena are not mutually exclusive. Additionally, we can observe a significant increase in the number of small bacterial spots (volume ranging from 0 to $2 \mu\text{m}^3$) in day 3 and day 4. Perhaps due to the weakening of the innate immune system [50] and the loss of function in the grinder in the pharynx [120] in older worms, it becomes easier for the recently ingested bacteria to accumulate in the gut. As before, another possible explanation would be that, in older worms, due to the weakening of the immune system, the bacteria can more easily proliferate and spread in the gut.

The bacterial load in each individual worm in each day can be seen in Figure 3-7e. A bacterial load of 1 was attributed to the worms for which no bacteria could be detected, so that the bacterial load can be displayed using a logarithmic axis. It can be seen that the average load in the hindgut of the worms is increasing with the age of worm similar to what was observed with the bivariate histograms. Even though the average bacterial load can be useful for identifying general trends, it does not provide an accurate representation of all the worms involved in a given experiment and in fact can be quite misleading. Additionally, by using average values to represent the entire population, the subpopulations that exhibit a significantly different phenotype (than the average of the entire population) will remain undiscovered. For example, while the average bacterial load for day 2 is quite high and comparable to that of day 3 and day 4, the large majority of the worms at day 2 have no or very little bacterial in their hindguts. Similar representation problems can also exist for the worms in day 1 and day 3. Even in the case of worms of day 4, which have the least worm-to-worm variations, the worm with highest bacterial population has 200 times more bacteria in hindgut than the one with the lowest bacterial population.

Previous studies done via conventional techniques on agar plates are affected by the same issue [34], [51], [54], [121]. In these studies, 10 worms were taken from a given experiment, washed, mechanically disrupted and number of colony forming bacteria were determined by culturing them on suitable agar plates. Therefore, this method inherently pools together the bacteria of all the worms and as a result can only provide an average bacterial load to represent the state of bacterial colonization in the gut of the worms. Moreover, the few worms with bacterial load that are greatly different from the majority of the worms (e.g. in day 2 the worms having bacterial load measuring around 10^6 - 10^7 compared with the majority that have few or no bacteria) cannot be simply discarded a priori. The experiments therefore need to be repeated and, in case of persistence of the “outlying” results, further systematic investigations should take place to discover causal relations/correlations.

Lastly, considering the bacterial loads in individual worms, there seems to be a saturating limit for the number of bacteria present in the hindgut. If the bacteria are simply accumulating in the gut, it is possible that the accumulation becomes balanced with defecation. In the case of proliferation, perhaps the bacterial population reaches an equilibrium with the immune system of the worm and/or with the hindgut milieu. Regardless of the exact explanation, this saturating limit has been previously reported by Portal and Blaser [51].

Based on the discussions above, we also plotted the bivariate histograms (Figure 3-8) of selected worms that have fed on RFP-labelled *E. coli* OP50 for 4 days (highlighted by red circle in Figure 3-7e).

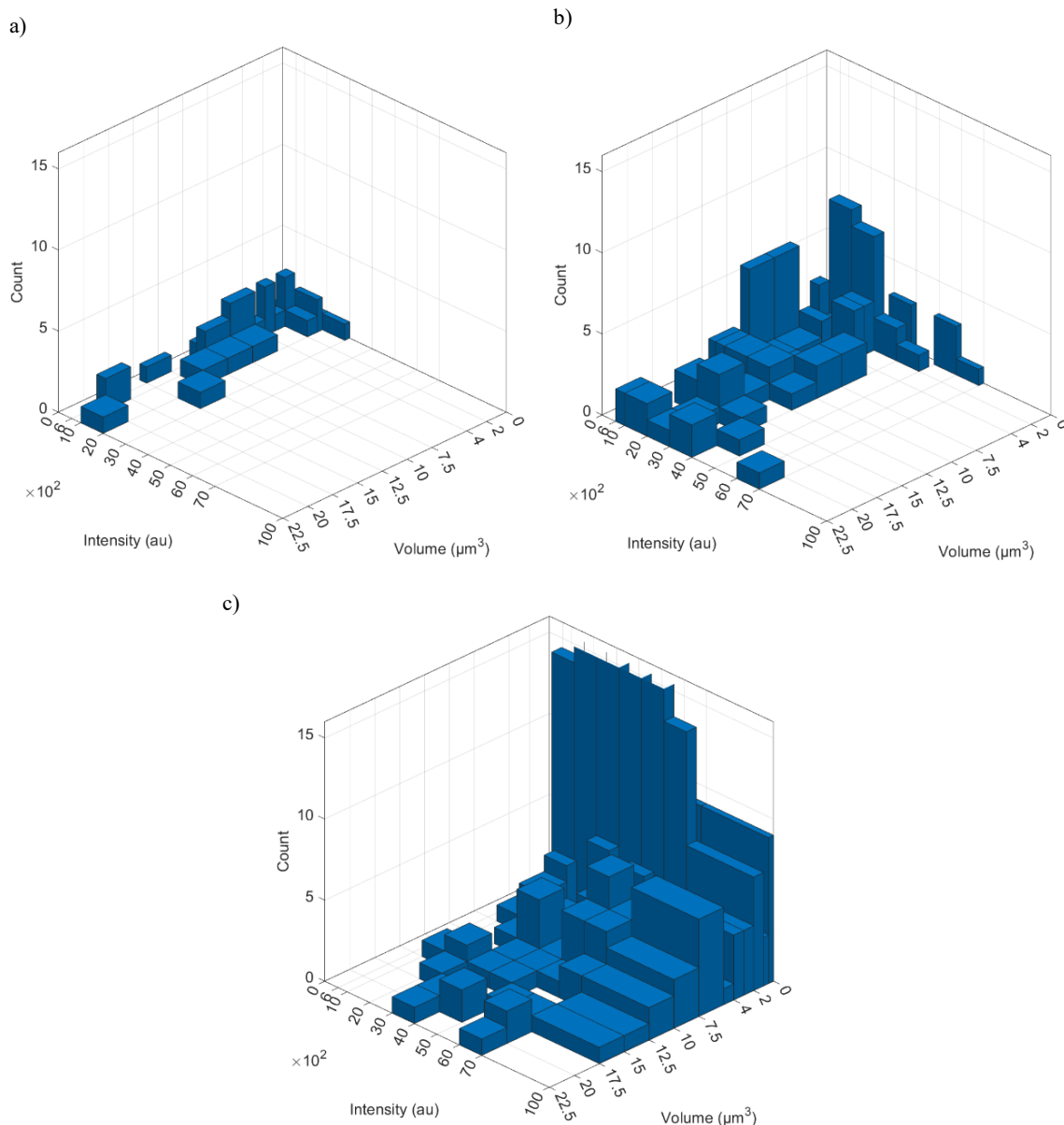


Figure 3-8-Bivariate histograms of 3 selected worms that have fed on RFP-labelled *E. coli* OP50 for 4 days. The total number of bacterial spots is a) 31, b) 100 and c) 422. The total bacterial load is a) $2.2042\text{E}+05 \mu\text{m}^3 \cdot \text{au}$ b) $1.8478\text{E}+06 \mu\text{m}^3 \cdot \text{au}$ and c) $6.7720\text{E}+06 \mu\text{m}^3 \cdot \text{au}$.

It can be seen in Figure 3-8 that the volumes, the intensities and the number of the bacterial spots in the gut are low, which implies a relatively small bacterial load. However, considering the worms in

Figure 3-8b and Figure 3-8c, the increase in bacterial load is accompanied by the formation of larger bacterial spots with higher intensities and the appearance of numerous small bacterial spots. Similar observations could be made in the worm populations at day 2 and day 3. An adequate explanation of the variation observed among the worms with the same feeding conditions requires further investigation.

3.5 Discussion

C. elegans, as a genetically tractable organism with evolutionary conserved pathways of innate immunity, is an interesting model for understanding bacterial pathogenesis. In the conventional methods of studying bacterial pathogenesis, mutant worms and bacteria are generated. Afterwards the interaction between these two is observed by culturing the mutant worms on the mutant bacteria and obtaining the survival curves and the average numbers of colony-forming bacteria. However, survival curves cannot provide a complete description of the said interactions. As mentioned earlier, the average number of colony-forming bacteria does not necessarily represent the state of all the worms and one may miss subpopulations that have few or no bacterial load. Additionally, this measurement cannot determine whether the viable bacteria are merely accumulating in the intestine or that they are actively proliferating within the gut and as a result shifting assays using fluorescent and non-fluorescent bacteria can be utilized to tackle this issue. For example in the study by Aballay et al., [54] WT adults were fed on a mixed lawn containing GFP-tagged *S. typhimurium* SL1344 and *E. coli* DH5 α with a ratio of 1:1000 for 5 hours. Afterwards, the worms are washed and transferred to *E. coli* OP50 plates and every day, 10 of these worms are randomly selected and the number of *S. typhimurium* SL1344 bacteria was determined. It was observed that the number of *S. typhimurium* SL1344 bacteria increased a few bacteria in day 0 (day the transfer took place) to around 10^4 in day 4. This clearly shows that *S. typhimurium* SL1344 can persist and proliferate in the intestine. Additionally, since *S. typhimurium* SL1344 is fluorescent, in principle, it is possible to follow its proliferation dynamics.

The effect of the bacteria on the host is not only limited to the colonization of the gut. For example, *P. aeruginosa* and *S. typhimurium* reduce the motility and the rate of pharyngeal pumping of the worm overtime. Both of these phenotypes can be tracked *in vivo* using microfluidic solutions [83], [98]. Moreover, infection with bacteria can also damage the intestinal cells. For example, it has been reported that *S. marcescens* is a pathogen of the worm that over time causes vacuolation of the intestinal cells and reduces the volume of the intestinal epithelium [33]. Overall, these examples show that interactions between the worm and the bacteria can have various aspects that need to be monitored.

In this work, for the first time to the best of our knowledge, we have carried out high-resolution z-stack imaging of fluorescent *E. coli* OP50 bacteria using an SDCM. Utilizing IMARIS, we constructed a 3D representation of the bacteria within the hindgut of each worm and managed to identify their sizes and their (fluorescent) intensities in an automated way. We showed that the number of bacterial

spots, their sizes and their intensities increase as the worm ages, in agreement with previous studies [8], [34]. Interestingly, our single-worm bacterial analysis showed that the conventional sampling method for evaluating the bacterial presence within the gut of the worms may be less adequate and can be misleading in some cases. While the main innovation in our work is the establishment of a high-resolution imaging and analysis pipeline, our work also demonstrated that on-chip high-resolution imaging of intestinal bacteria is not hindered by the optical distortions that the PDMS layer and the liquid media can potentially introduce. Consequently, the methods we developed in this work can be readily implemented in existing microfluidic chips that are aimed at studying host-microbiota interactions.

To better highlight the novelty of our approach and the new possibilities offered by our imaging and analysis pipeline, we briefly compare our work with the previously reported microfluidic devices applied to host-microbiota interactions. The first reported microfluidic only considered the life span of the bacteria-infected worms that were being treated on-chip with antimicrobial compounds [95]. The imaging possibilities were only briefly explored and were limited to fluorescence imaging at low magnifications. The HandKAchip microfluidic device for on chip hands-free killing assay improved on the previous work [96]. Brightfield and fluorescent images, albeit with low resolution and acquired at a low-magnification, were used to monitor the life span of the worms as well as their motility and infection response (*irg-1::GFP*) in an automated manner. However, similar to the imaging and analysis pipeline we presented in this work, the identities of the worms were lost in the analysis stage and therefore it was not possible to track and monitor the worms over an extended period of time. The latest microfluidic device for host-microbiota interactions allowed *in vivo* fluorescence imaging of *C. elegans* worms immobilized via traps at a moderate resolution for a duration of 30 hours while maintaining the identities of the worms [98]. However, the immobilization is not sufficient to allow high-resolution z-stack fluorescence imaging. Indeed, in this study, a widefield microscope was used to perform time-lapse fluorescence imaging and no z-stack imaging was performed. However, widefield microscopes are not ideal for imaging thick specimens such as *C. elegans* worms since the light signals from out-of-focus planes blur the image and reduces the contrast. This, in particular, is noticeable when bacterial cells are present in the intestine at high densities, which is typically the case in older worms. As a result, intact fluorescent bacteria in densely populated bacterial clusters will appear as diffusive fluorescent background when imaged using a widefield microscope and consequently, will be mistakenly interpreted as disrupted bacteria. This shows the necessity of utilizing an SDCM to acquire optical sections which can be then used to accurately analyze the bacterial colonies present in the intestine.

As an outlook, a simple way to further improve the functionality of our chip would be to include traps for aligning the worms before performing fixing. This would allow us to not only to identify the bacterial spots but also to systematically characterize their positions within the gut and discover any preferential place for colonization. Our group has previously designed a microfluidic device that enables *in vivo* extraction of phenotypes such as length, area, motility and first egg release time in an automated fashion [83]. The imaging analysis involved for the determination of these phenotypes could be modified such they can be used in the new device. Additionally, our group has also reported

microfluidic devices for *in vivo* studying of bacterial load dynamics and absorption (e.g. measurement of the pharyngeal pumping rate, and the time evolution of bacterial load in the worm gut) [98]. The functions exhibited by the latter device could be complemented with image analysis techniques of the former device and combined with the ideas expressed in this work (high-resolution fluorescent z-stack imaging, fixing the worms on chip, shifting assays using fluorescent and non-fluorescent bacteria) to result in a more complete picture of bacterial proliferation and/or pathogenesis within the worm.

3.6 Conclusions

We have performed high-resolution z-stack fluorescence imaging of the gut bacteria in *C. elegans*. We were able to automatically construct a 3D representation of the bacteria in the intestine using IMARIS and characterized the bacterial load of the worm (the sizes and the fluorescence intensities of the bacterial spots) during early adulthood. Our analysis showed that the conventional sampling and averaging method for determining the number of bacteria in the gut is not always representative for all the worms and in some cases can be misleading. Our ideas on high-resolution imaging, on-chip fixing and shifting assays can complement currently existing microfluidic solutions providing a step forward towards a complete description of bacterial pathogenesis in *C. elegans*.

4 Difference in intestine content of *Caenorhabditis elegans* when fed on non-pathogenic or pathogenic bacteria

We investigated the bacterial food digestion and accumulation in wild-type adult *Caenorhabditis elegans* (*C. elegans*) worms that have fed on either non-pathogenic RFP-expressing *Escherichia coli* *E. coli* OP50 or pathogenic RFP-expressing *Pseudomonas aeruginosa* (*P. aeruginosa*) PAO1 during the first 4 days of adulthood. Once the worms had completed their planned feeding cycles, they were loaded on microfluidic chips, where they were fixed to allow high-resolution z-stack fluorescence imaging of their intestines utilizing a Spinning Disk Confocal Microscope (SDCM) equipped with a high-resolution oil-immersion objective (60x). IMARIS software was used to visualize and analyze the obtained images, resulting in the production of three-dimensional constructs of the intestinal bacterial load. We discovered two distinct patterns for the bacteria-derived fluorescence signal in the intestine: (i) individual fluorescent spots, originating from intact bacteria, were present in the fluorescent *E. coli* OP50-fed worms, and (ii) we observed individual fluorescent spots (originating from intact bacteria) dispersed in large regions of diffuse fluorescence (RDF), originating from disrupted bacteria, in fluorescent *P. aeruginosa* PAO1-fed worms. We performed a semi-automated single-worm-resolution quantitative analysis of the intestinal bacterial load, which showed that the intestinal bacterial load generally increases with age of the worms, but more rapidly for the fluorescent *P. aeruginosa* PAO1-fed worms.

This chapter is a copy of the following publication:

- **Farzad Rezaeianaran (F.R.)** and Martin A. M. Gijs (M.G.), “Difference in intestine content of *Caenorhabditis elegans* when fed on non-pathogenic or pathogenic bacteria,” *Micromachines*, vol. 14, no. 7, Art. no. 7, Jul. 2023, doi: 10.3390/mi14071386. Creative Common license: <https://creativecommons.org/licenses/by/4.0/>. Authors contribution: **F.R.** and M.G. conceptualized the research project. **F.R.** designed the platform and experiments and fabricated the microfluidic chip. **F.R.** performed the experiments, carried out the image analysis and analyzed the data. **F.R.** wrote the original draft. M.G. reviewed and edited the original draft. This work is supported by the Swiss National Science Foundation (Grant No. 205321-179021).

4.1 Introduction

Host-microbiota interactions have a profound and wide-ranging impact on the health, ageing and diseases in humans [1]–[5]. The microbiota can affect the development and the health of central nervous systems [11], [122], possibly play a causal role in diseases such as diabetes and obesity [16], mediate drug action [8] and fight against toxins and pathogens in the intestine [5], [8]. However, these studies are mostly based on correlations, as discovering the underlying mechanisms through which the gut microbiota exerts such influence is extremely complicated due the diversity of human genomes and the bacterial species present in the intestine [1], [14].

The *C. elegans* nematode is a genetically tractable model organism for studying host-microbiota interactions and in particular, bacterial pathogenesis, innate immunity, and ageing [17]. As the genome of this nematode bears considerable similarity to the genome of humans, the discoveries made using this organism are also relevant to health and diseases in humans [15], [17], [22]. The millimeter-sized transparent organism relies on consumption of bacteria for its development and reproduction [8], [16]. In laboratories, the nematode is often maintained on Nematode Growth Medium (NGM) plates containing a single type of bacteria (mostly *E. coli*) [123]. The relationship between the worm and *E. coli* is dynamic and changes over time. In the larval stages, the bacteria are thought to be simply a food source, which are killed by the pharyngeal grinder and thus no live bacteria in principle reach the intestine. In young adult worms, few intact bacteria manage to pass through the pharyngeal grinder without being damaged and form a community in some areas in the intestine and thus establish a commensal relationship with the worm [8]. As the worm gets older however, the decline in the effectiveness of the pharyngeal grinder in killing bacteria, innate immunity, ingestion and defecation leads to excessive proliferation of bacteria which can become mildly pathogenic to the worm [8], [34].

The interaction between the bacteria and the worm are often characterized in terms of TD_{50} (the time after which 50% of the worms feeding on a bacterial lawn are dead, obtained from survival/lifespan curves), average number of colony-forming bacteria per worm at a given time point and gene expression of the worm that is measured either through fluorescence microscopy, blotting techniques or quantitative real-time polymerase chain reaction (qRT-PCR) analysis. We can use TD_{50} as a simple way to compare the pathogenicity of different bacteria assuming that the considered bacteria support the worm adequately from a nutritional standpoint. For example, an adult wild-type worm population feeding on pathogenic *P. aeruginosa* PAO1 has a $TD_{50} = 2.84$ days [57], while the same population fed on *E. coli* OP50 has a $TD_{50} = 12.93$ days [34]. Both of these bacteria have been shown to provide adequate nutrition to the worm, but also cause its demise through intestinal colonization [36], [57], [123]. However, the much shorter lifespan of worms fed *P. aeruginosa* PAO1 shows that this bacterium exhibits a higher degree of pathogenicity compared to *E. coli* OP50. Despite the extensive research on non-pathogenic *E. coli* OP50 [34]–[36], [51] and pathogenic *P. aeruginosa* [52], [57]–[65], which reveals and discusses the innate immunity pathways of the worm and the virulence mechanism of

pathogenic *P. aeruginosa*, little is known about the impact of the bacterial food source on the digestion/absorption of bacterial material by the worm through its intestine.

The use of microfluidics for studying *C. elegans* is reported for the first time in 2007 [70] and, since then, the field has grown considerably and devices for different purposes have been proposed [72], [77]–[80]. The main advantages of microfluidics are the ease in handling large worm populations and reversible immobilization that enables high-resolution imaging [72]. Generally speaking, microfluidic devices can either enable high-throughput at low imaging resolution [77], [114] or low-throughput studies at a high imaging resolution [81]–[84], [86], [87], [93]. The vast majority of host-microbiota studies have been and are still carried out using conventional techniques and despite the great potential of microfluidic devices, there are very few microfluidic devices that are designed for such studies.

The first microfluidic device for implementing a *C. elegans* infection assay was proposed by Yang et al [95] in 2013. The device comprised 32 chambers that were divided into 4 groups. In each group, different doses of a given antimicrobial compound could be administered to the 8 chambers through concentration gradient generators. Worm populations were infected on-chip with *Staphylococcus aureus* and, afterwards, the efficacies of the antibiotic compounds as a function of their doses were assessed through survival curves. As a result, this device is mostly suitable for *in vivo* antibiotic compound screening. Lee et al [96] reported a microfluidic device for performing *C. elegans* killing assays. The worm and the pathogen of interest could be loaded in a large chamber, where the motility and survival of the worms and the expression of *irg-1::GFP* could be monitored *in vivo* through low-resolution imaging. However due to lack of compartments, the identities of the worms could not be tracked over time.

Viri et al [97] reported a microfluidic device for *in vivo* study of the bacterial transit in *C. elegans*. The device featured 4 separate lanes each of which comprised 5 compartments. 1 to 3 worms were loaded into each compartment where they were fed fluorescent-tagged bacteria. Through low-resolution fluorescence imaging and subsequent image analysis, the spatio-temporal evolution of intestinal bacterial load of the freely moving worms could be obtained. In this way, the periodic behavior associated with ingestion of bacteria and its clearance from the intestine was monitored and its temporal periodicity was determined. The worms could also be immobilized in the tapered structures present in the compartment, which rendered them incapable of feeding. Afterwards, low-resolution fluorescent images were acquired from these worms to obtain the time constant of the bacterial transition. In a subsequent work, Viri et al [98] improved the design of their previous device [97] such that worms could be immobilized in individual traps for up to 30 hours while being able to feed on fluorescent bacteria. This device could replicate the previous results and the improved immobilization enabled relatively high-resolution fluorescence imaging. Thus, in the fluorescent images of the immobilized worms, the intact bacteria which appeared as individual fluorescent spots could be distinguished from the disrupted ones which appeared as diffuse fluorescence. This allowed the observation of the digestion process and, as a result, the associated time constant was determined. It should be mentioned that in their work [98], they used a widefield microscope for fluorescence imaging. When a thick specimen such as a *C. elegans* worm is imaged with a widefield microscope, the

fluorescence signal is received from many focal planes including those that are out of focus. Consequently, despite their usage of a 50x objective for fluorescence imaging, the fluorescence signals originating from intact bacteria that lie in the out-of-focus planes reduce the contrast and blur the image [100], [105]. This effect, in particular, is pronounced in areas of high bacterial density and ultimately poses an insurmountable obstacle for the correct determination of the source of an eventual diffuse fluorescence signal from the intestine (as the fluorescent signal originating from bacteria could originate from the diffuse-fluorescence of disrupted bacteria present in the plane of focus, or spot-like intact bacteria present in out-of-focus planes), and thus for distinguishing the intact bacteria from the disrupted ones.

In contrast to widefield microscopes, SDCMs are capable of acquiring optical sections by incorporating pinholes that block most of the light signal from out-of-focus planes leading to improved contrast and signal-to-noise ratio, and reduced blur [105]. Therefore, to improve upon the previous works by Viri et al [97], [98], we aim to use an SDCM for high-resolution z-stack fluorescence imaging of intestinal bacteria. By performing advanced image analysis techniques on the acquired optical sections, we can improve the visualization of the intestinal bacteria and carry out more accurate quantitative analysis. To achieve this, we relied on loading the worm population of interest on a simple microfluidic chip where the worms could be subsequently fixed for high-resolution imaging. We preferred this approach to the more conventional method whereby previously anesthetized worms are mounted on an agarose pad before they are observed [124], [125]. While anesthetics such as levamisole could be used to immobilize the worm, we are not sure if they would also stop the intestinal peristaltic motion. For our advanced image analysis to be accurate, even movements as little as 5-10 μm should be avoided, especially if they occur frequently and in a periodic manner. This is to prevent any unwanted alteration in the size and the intensity distribution of the detected bacterial spots. Alternatively, these movements can also lead to the appearance of new but illusory bacterial spots. While it is also possible to mount previously fixed worms on agarose pads, we preferred to carry out the fixation procedure and imaging on a microfluidic chip. This allows us to fix and image all the worms at the same time and also shows that our approach can be applied to any existing microfluidic device for host-microbiota studies.

4.2 Materials and methods

4.2.1 Materials and chemicals

4 inch 550 μm Si wafers, 5-inch Chromium/soda-lime glass masks, polydimethylsiloxane (PDMS) Sylgard 184 (Dow®) and trimethylchlorosilane (TMCS) (Sigma-Aldrich) were acquired from the Center of MicroNanoTechnology (CMi) at EPFL (Lausanne, Switzerland). Kayaku Advanced Materials (KAM) SU-8 3050 was bought from Micro Resist Technology GmbH (Berlin, Germany). 45 mm \times 70 mm \times 170 μm glass coverslips were obtained from Biosystems Switzerland AG (Muttens, Switzerland). Saint-

Gobain Tygon™ ND 100-80 Tubing (inner diameter and thickness of 0.02 inch and outer diameter of 0.06 inch) was purchased from Fisher Scientific (Reinach, Switzerland). NGM plates were ordered from the Solution Preparation Facility at EPFL. In order to prepare S-basal, 5.85 g of NaCl, 6 g of KH₂PO₄ and 1 g of K₂HPO₄ were first dissolved in H₂O until a final volume of 1 l was realized. This solution was subsequently sterilized via autoclaving and, afterwards, 1 ml of cholesterol solution (5 mg ml⁻¹ in ethanol) was added using sterile technique to obtain S-basal. In order to make S-medium, 500 µl of 1 M potassium citrate (pH 6), 500 µl of trace metals solution, 150 µl of 1M CaCl₂ and 150 µl of 1M MgSO₄ were added using sterile technique to 50 ml of S-basal. The materials required for the preparation of S-basal and S-medium, lysogeny broth (LB) for bacteria culture, tetracycline was purchased from Sigma-Aldrich Chemie GmbH (Buchs, Switzerland). 4% paraformaldehyde (PFA) solution in phosphate buffered saline (PBS) used for the fixation of *C. elegans* and was kindly provided by the Laboratoire des Polymères (LP) at EPFL (Lausanne, Switzerland).

4.2.2 Worm and bacteria culture and preparation

We used *C. elegans* wild-type (WT) Bristol N2 strain in our experiments. The worm populations were synchronized by suspending gravid adult worms (that can have slightly different ages) overnight inside a 50 ml falcon tube containing 8 ml of S-medium. During this time, due to lack of food, the L1s that hatch from the eggs laid by the adults undergo developmental arrest [126] and thus a synchronized L1 population is obtained on the next day. Afterwards, the dead adults that naturally settle at the bottom of the falcon tube are removed via aspiration and the remaining synchronized L1 population is transferred to multiple 1.5 ml Eppendorf tubes to be centrifuged for 4 mins at 2000 RPM. ~100 L1s are aspirated from the bottom of one of the Eppendorf tubes and are spread on NGM plates seeded with *E. coli* OP50 and maintained there for 46 hours at 22 °C until they become adults and thus ready for the experiments.

E. coli OP50 was cultured overnight in LB at 37 °C on a shaker. Red Fluorescent Protein (RFP)-labelled *E. coli* OP50 was kindly provided by the *C. elegans* Ageing Laboratory at the University College London. Plasmid *pRZT3::dsRED*, which also contained genes for tetracycline resistance, was used to transform *E. coli* OP50 and produce the RFP-labelled *E. coli* OP50. RFP-labelled *E. coli* OP50 was cultured in LB containing 10 µg/ml of tetracycline overnight at 37 °C on a shaker. RFP-labelled *P. aeruginosa* PAO1, which was kindly provided by Laboratoire des Polymères (LP), constitutively express mCherry (*attTn7::miniTn7T2.1-Gm-GW::PA1/04/03::mCherry*) in the bacterial cytoplasm. RFP-labelled *P. aeruginosa* PAO1 was cultured overnight in LB at 37 °C on a shaker.

4.2.3 Fabrication of the microfluidic chip

The microfluidic chip was designed in Clewin 4.0 (WieWeb software, Hengelo, The Netherlands) and through standard mask fabrication techniques, the designed layout was then transferred to a chromium/soda-lime glass mask. Next, the mask was used to create a 75 µm high SU-8 mold on a Si wafer using standard soft photolithography techniques. To facilitate the separation of the

polydimethylsiloxane (PDMS) chip from the SU-8 mold, the mold was treated with trimethylchlorosilane (TMCS) and, afterwards, PDMS with base-to-curing agent ratio of 10:1 was cast onto the mold and cured for 2 hours at 80 °C inside an oven. Once the PDMS cured and cooled down, it was cut according to the design of the device and the resulting PDMS block was removed from the mold. Afterwards, using a biopsy punch, inlets and outlets were made in the PDMS block. The PDMS block and a glass coverslip measuring 45 mm × 70 mm × 170 μm were bonded together, utilizing oxygen plasma surface activation, to create the microfluidic device. The microfluidic chip was then placed on a hotplate for 10 minutes at 80 °C to improve the bonding strength.

4.2.4 Image processing and statistical analysis

Raw z-stack fluorescent images are processed in IMARIS (version 9.9.1). The software constructs three dimensional (3D) images from z-stack fluorescent images which can be further analyzed using the built-in toolkits. The results of image analysis by IMARIS are exported to excel files that are processed in an automated fashion in MATLAB software (version 2022a). The processing involves the selection of the data of interest and performing basic arithmetic operations on them. The processed data can be then easily imported in GraphPad Prism software (version 9.5.0) to be plotted and tested for statistical significance. As the processed data did not have a Gaussian distribution, we utilized the Mann-Whitney test to establish statistical significance. Additionally, based on previous studies in the literature, we expected specific trends in different experimental conditions. As a result, we used the one-tailed Mann-Whitney test.

4.2.5 Microscopy platform and the imaging parameters

We utilized two different microscopes in our experiments. A Zeiss Axio Imager.M2 operated in brightfield mode and equipped with a 2.5X Zeiss objective was used for the preparation of the microfluidic chip, loading worms on the chip and their subsequent fixing. High-resolution z-stack fluorescence imaging was realized using Visitron's CSU-W1, a spinning disk confocal microscope equipped with: (i) two laser light sources for fluorescence imaging in the RFP and the Green Fluorescent Protein (GFP) channels, running at wavelengths 561 nm and 488 nm, respectively, (ii) an Olympus U PLAN S APO 60X/1.42 NA oil immersion objective, (iii) emission filter cubes ET605/70m and ET525/50m, by Chroma Technology (Vermont, USA), for the RFP and the GFP channels, respectively and (iv) a Hamamatsu ImagEMX2 electron-multiplying CCD (EMCCD) camera. The imaging was carried out with the following parameters: exposure time of 60 ms, laser power for both the RFP and the GFP channels of 50%, gain of the EMCCD camera set to 200, pinhole size of 50 μm, z-stack imaging in a 50 μm range with a step size of 0.2 μm.

4.3 Experimental

4.3.1 The design and operation of the microfluidic chip platform

Our microfluidic chip consists of 5 identical lanes, the layout of which can be seen in Figure 4-1a. Our device allows on-chip fixation and subsequent high-resolution imaging of adult worms.

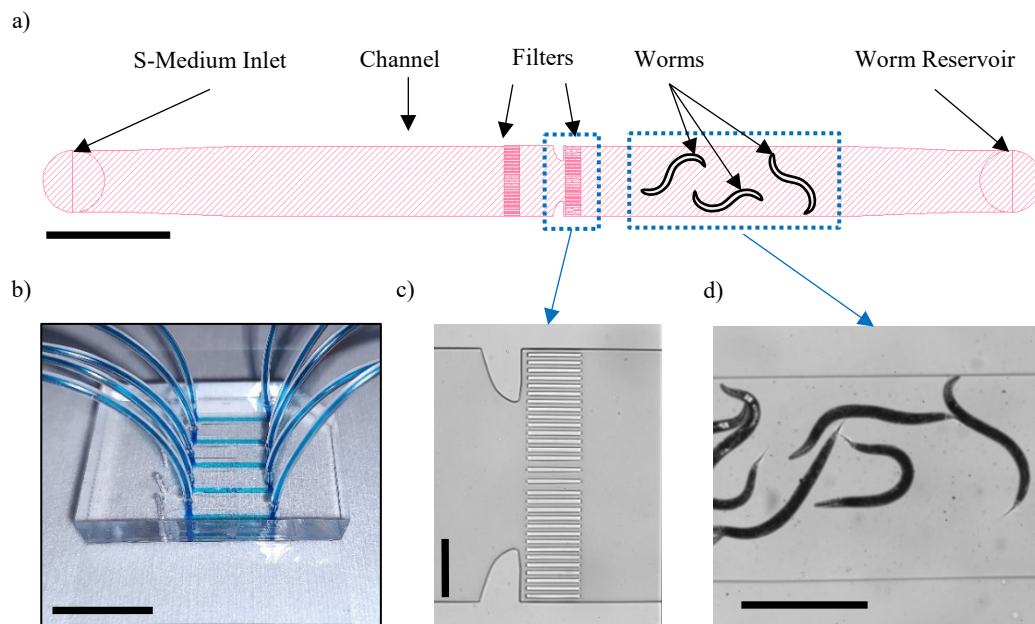


Figure 4-1- Microfluidic chip for high-resolution imaging of bacteria in the intestine of *C. elegans*. a) The schematic shows the typical design of the lanes in the device. Every device has 5 lanes that are 1300 μm wide and 75 μm high. The worms are contained in the channel by the filters. Scale bar = 2 mm. b) Photograph of a fabricated microfluidic device. The tubing and the channels of the device are filled with a blue dye for better visibility. Scale bar = 2 cm. c) Brightfield image showing the filter structures. Scale bar = 300 μm . d) Brightfield image showing the worms that are loaded in the microfluidic chip. Scale bar = 0.8 mm

The lanes are 2 cm long, 1300 μm wide and 75 μm high, the last of which makes the device capable of accommodating adult worms. Furthermore, each lane features two filter structures whose functions are to confine the loaded worms to the right side of the channel and provide control over the number of worms present on the chip. An example of a fabricated microfluidic device is shown in Figure 4-1b. The filter structure, which is shown with more details in Figure 4-1c, consists of rows of 20 μm -wide PDMS slabs that are spaced 15 μm apart except in the middle where the spacing is 30 μm . The spacings have been chosen such that even upon the application of relatively high flow rates which results in adult worms being compressed against the filter structures, no adult worm passes through the filter structures.

The microfluidic chip is operated while being observed in the brightfield mode using a Zeiss Axio Imager.M2 equipped with A 2.5x Zeiss objective. Before worms can be loaded on the chip to be fixed and imaged, a chip initialization step should take place. Therefore, S-medium is first injected from the

inlet to the channels using a neMESYS syringe pump (CETONI GmbH, Korbußen, Germany). However, as the air in the channels is being replaced by S-medium, some bubbles of air are bound to form. To eliminate these, the outlet tubing is clipped and the channel is pressurized by injecting 10 μl of S-medium through the inlet. The increased pressure promotes the outward diffusion of air through PDMS and thus the channel is cleared from air bubbles within 15-20 minutes. Afterwards, the outlet tubing is unclipped and is placed inside an Eppendorf tube containing the adult worms of interest suspended in S-medium. The worms can be then loaded on the chip (Figure 4-1d) by using the neMESYS syringe pump to aspirate the S-medium with a flow rate of 500 nl s^{-1} . Once around 10-15 worms are present in the channel, an Eppendorf tube containing a 4% PFA fixation solution is placed at the outlet and by aspirating with a flow rate of 80 nl s^{-1} , the fixation solution is introduced in the channel. The worms become fixed by staying in contact with the fixation solution for about 5 to 10 minutes, after which, the inlet and outlet tubings are cut and fastened and the microfluidic chip can be taken to an SDCM for high-resolution z-stack fluorescence imaging.

4.3.2 Experiment planning

We wish to study the bacterial food digestion and accumulation in wild-type adult *C. elegans* worms that have fed on either RFP-labelled *E. coli* OP50 or *P. aeruginosa* PAO1 during the first 4 days of adulthood via high-resolution z-stack fluorescence imaging (Figure 4-2). First, we synchronize the worm population (Figure 4-2a) by suspending an adult worm population in a falcon tube containing S-medium overnight, during which the adult worms lay eggs. The next day, a large number of synchronized L1s will be present in the falcon tube since the lack of food causes the hatched larvae to undergo developmental arrest [126]. About a 100 of these synchronized L1s are then transferred to an NGM plate seeded with *E. coli* OP50 where they will be kept for 46 hours at 22 °C until they reach adulthood (Figure 4-2b). At this point, the adult worms can be fed either the RFP-labelled *E. coli* OP50 or the RFP-labelled *P. aeruginosa* PAO1. However, when the adult worm population is to be taken to an NGM plate seeded with either one of these two fluorescent bacteria, it must be ensured that ideally no unlabeled *E. coli* OP50 is transferred with it. Therefore, after adult worms are washed off the NGM plate using S-medium, they are placed inside a 1.5 ml Eppendorf tube where they naturally sink to its bottom. This facilitates the gradual elimination of *E. coli* OP50 through the replacement of the supernatant with fresh S-medium (dilution of 1:10). This procedure is repeated 10 times (1:10¹⁰ total dilution) and thus the number of *E. coli* OP50 present in S-medium is extremely reduced (Figure 4-2c). The adult worms can now be safely placed on NGM plates seeded with either RFP-labelled *E. coli* OP50 or *P. aeruginosa* PAO1 to feed for 1, 2, 3 and 4 days (Figure 4-2d). As high-resolution imaging at each time point of interest (i.e., after 3 days of feeding on RFP-labelled *E. coli* OP50) requires fixation, the same worms cannot be studied at different time points. Additionally, while the adult worms are feeding (on either of the fluorescent bacteria), they also lay eggs which hatch into L1s. These L1s not only mix with the adult population, which later can become a source of confusion, but they can also rapidly deplete the NGM plate of bacterial food. Therefore, every 24 hours, the adult worms are separated from L1s through serial dilutions (Figure 4-2e) which is carried out in a manner similar to Figure 4-2c with a total dilution of 1:10¹⁰.

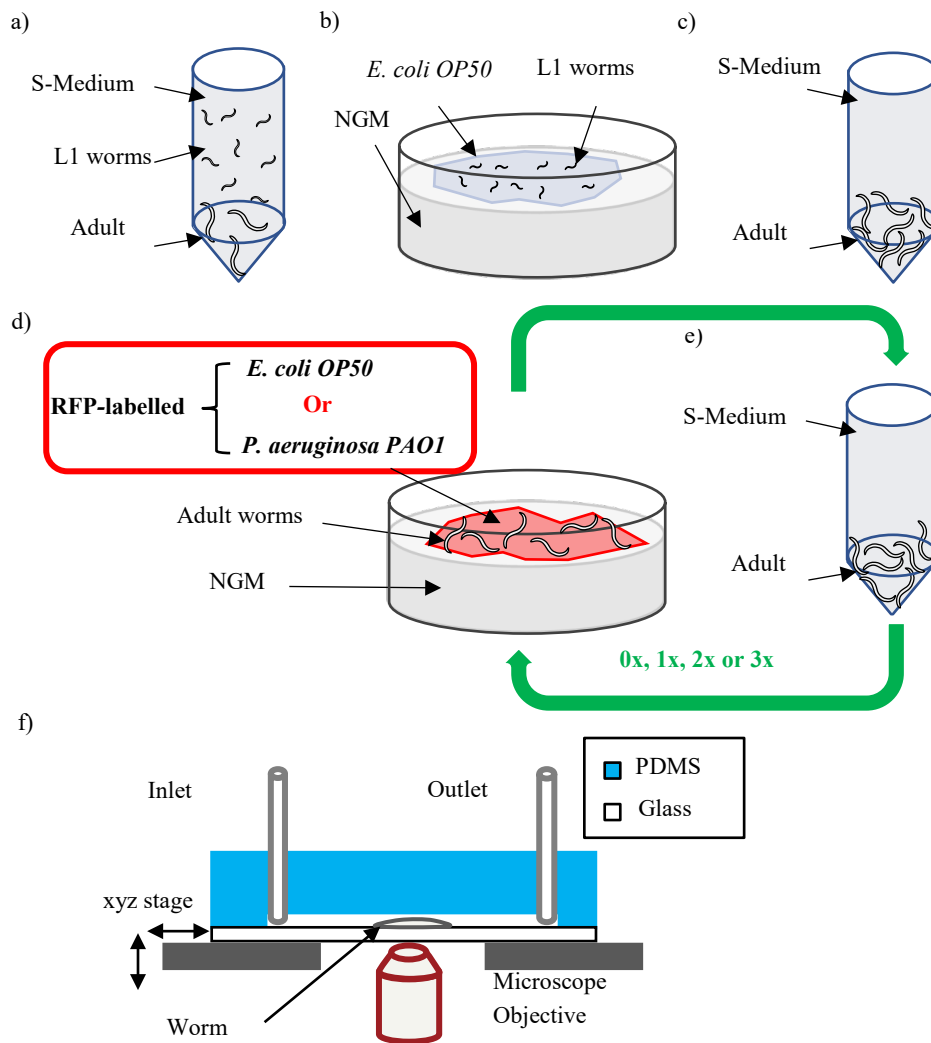


Figure 4-2- Protocol and experimental planning for high-resolution imaging of fluorescent *E. coli* and *P. aeruginosa* in the intestine of *C. elegans*. a) An adult population of worms are suspended overnight in S-medium to obtain a multitude of synchronized L1s in developmental arrest the following day. b) ~100 synchronized L1s are placed on an NGM plate seeded with *E. coli* OP50 and grown there for 46 hours at 22 °C until they reach adulthood. c) Using S-medium, the adult worms are removed from the NGM plate and are placed inside a 1.5 ml Eppendorf tube, where they naturally settle at its bottom. This allows the removal of *E. coli* OP50 through the replacement of the supernatant with fresh S-medium (dilution of 1:10). This procedure is repeated 10 times (1:10¹⁰ total dilution) to drastically reduce the number of *E. coli* OP50 present. d) The adults are then fed for 24 hours by being placed on an NGM plate, that depending on the experiment to be performed, is either seeded with RFP-labelled *E. coli* OP50 or RFP-labelled *P. aeruginosa* PAO1. e) To prevent the progenies from overcrowding the plates and mixing with the adult population, every 24 hours the adults along with their progenies are washed off the plate using S-medium and are placed inside a 1.5 ml Eppendorf tube. As the L1 progenies remain suspended in S-medium, similar to “step c”, a total of 1:10¹⁰ dilution is carried out to remove them and the remaining adults are then moved to a new NGM plate seeded with the same bacteria as before (e.g., if the adult worms were feeding on RFP-labelled *E. coli* OP50, the new NGM plate is also seeded with this bacteria). Steps d and e are repeated according to the number of days the adult worms are planned to be fed on either RFP-labelled *E. coli* OP50 or RFP-labelled *P. aeruginosa* PAO1 (0x, 1x, 2x and 3x of repetitions for 1 day, 2 days, 3 days and 4 days of feeding, respectively). After the last iteration of “step e”, the worms stay for an hour within the Eppendorf tube containing S-medium to ensure the complete digestion of recently eaten bacteria. f) The worms are then transferred to the microfluidic device where they are fixed using a 4% PFA solution. Shortly after, the tubings are cut and fastened with clips and the microfluidic device is moved to an SDCM, where high-resolution imaging of the intestinal bacteria is carried out.

Afterwards, the adult worms are transferred to a fresh NGM plate (Figure 4-2d) seeded with the same bacteria as before (e.g., if the adult worms were feeding on RFP-labelled *E. coli* OP50, the new NGM

plate is also seeded with this bacteria). It follows naturally that the steps described in Figure 4-2d and e should be repeated in a cyclic manner depending on the number of days the worms are to feed on fluorescent bacteria. This translates to 0x, 1x, 2x and 3x of repetitions for 1 day, 2 days, 3 days and 4 days of feeding, respectively, with 0x meaning that the steps described in Figure 4-2d and e are performed once. After the step in Figure 4-2e is carried out for the last time, the worms should remain suspended in S-medium (Figure 4-2e) and thus be starved for 1 hour before their intestines can be imaged. As the starvation period of 1 hour is considerably longer than 70s to 90 s time interval between bacterial ingestion and intestinal clearance in wild-type adult worms (70 to 90 s as reported by Viri et al [97]) and 60 to 110 s as reported by Ghafouri and McGhee [127]), it is safe to assume that any recently ingested non-pathogenic bacterium has the possibility to be completely digested before fluorescence imaging is carried out. Therefore, any bacteria that still will be imaged via fluorescence microscopy can be thought to have at least a persistent presence in the gut if not colonizing it. When the worms have starved for an hour, they are loaded on the microfluidic chip and subsequently undergo the fixation procedure (Figure 4-2f). Afterwards, the tubings are cut and fastened and the microfluidic chip is taken to a SCDM for high-resolution z-stack fluorescence imaging. Regarding the fixation of RFP-labelled *P. aeruginosa* PAO1, it should be mentioned that the lab (Laboratoire des Polymères, EPFL,) that provided us this bacterium used a 4% PFA solution as per their fixation protocol and hence in good faith, we followed the same protocol.

4.3.3 Imaging procedure and analysis

We start the imaging procedure with a low-magnification brightfield image (Figure 4-3a) to first locate the hindguts of the worms. We avoid imaging the worms that are overlapping or whose hindguts are merely touching each other. In the former case, the fluorescence signal of the two overlapping worms cannot be simply differentiated. In the latter case, when one of the worms is being imaged, the other worm that is very close to it, is also being exposed and thus subjected to potential fluorophore photobleaching [118]. Thus, the worm that is imaged second, will always have its fluorescence signal intensity skewed towards a lower value.

Once the hindguts of the worms of interest are identified, we carry out high-resolution imaging of the hindguts in the brightfield mode, the RFP and the GFP channel, an example of which is shown Figure 4-3b, c and d, respectively. Figure 4-3b is a brightfield image of the hindgut used to set the field of view more accurately and to determine the center of focus for the z-stack fluorescence imaging. Afterwards, we perform z-stack fluorescence imaging in the RFP channel (Figure 4-3c) to observe the fluorescence signal originating from either disrupted (the case in Figure 4-3c) or intact bacteria. The parameters used for the fluorescence imaging are previously discussed in the “Microscopy Platform and the Imaging Parameters” section. We optimized these parameters to have a decent signal-to-noise ratio, minimize the fluorophore photobleaching and avoid the saturation of the fluorescence signal in the camera. Furthermore, we have chosen a sufficiently large range of focus (50 μm) to image the intestine across its height. However, since the 60 \times objective used for high-resolution imaging affords a limited field of view (140 μm \times 140 μm), the hindgut needs to be imaged twice. Thus, we first

imaged the part of hindgut which is closest to the tail of the worm and afterwards imaged the other part which lies further away from the tail.

The adult wild-type worms exhibit autofluorescence, which at least partly originates from the intracellular lysosome-derived granules within the intestinal cells [119], [128]. This autofluorescence signal can be observed in the Blue Fluorescent Protein (BFP), GFP and RFP channel [119]. The exact chemical makeup for the fluorescent species responsible for the autofluorescence is not known [119]. It has been reported that the spatial overlap between the autofluorescence in the GFP and RFP channel is limited [119]. This suggests that the fluorescent species responsible for the GFP and RFP signal may be biologically distinct. Based on our observations, the autofluorescence signal originating from the RFP species (in the intestine of the worm) were negligible compared to the bacteria-derived RFP signal. However, in some of our observations, the autofluorescence signal originating from the GFP species (in the intestine of the worm) could also appear in the images acquired in the RFP channel (as suggested by the total spatial overlap of the signal in the RFP and the GFP channel). An example of the autofluorescence in the GFP channel in the hindgut of an adult worm is shown in Figure 4-3d. The purpose of these types of images is to ensure that the fluorescence signal observed in the RFP channel (Figure 4-3c) is not due to autofluorescence of GFP species present in the intestine of the worm (Figure 4-3d). In the event that an overlap between fluorescence signal in the RFP and GFP channel is observed, the fluorescence signal in the RFP channel should not be attributed to the presence of either intact or disrupted bacteria.

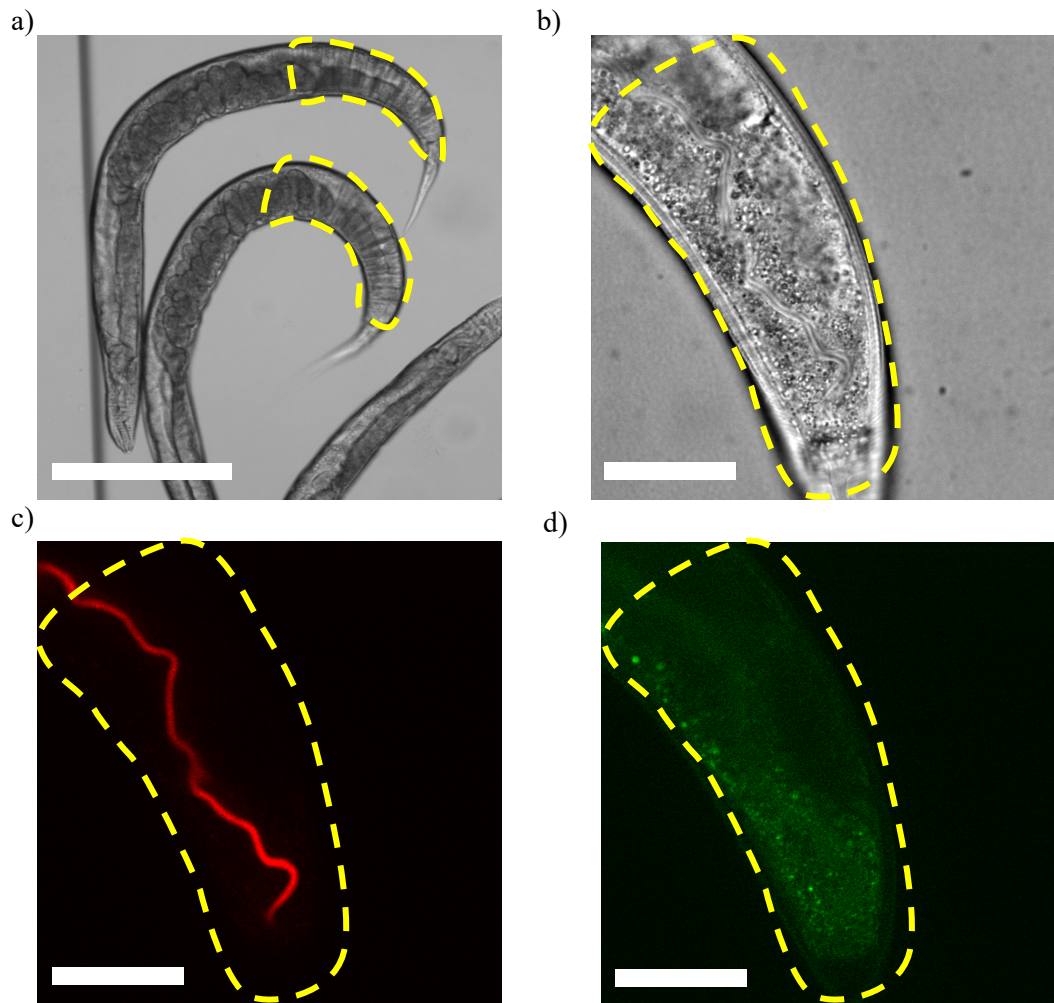


Figure 4-3- Imaging of representative fixed worms that had RFP-expressing *P. aeruginosa* PAO1 as their food source (duration of feeding is 1 day in figure a and 2 days in figures b, c and d). a) Brightfield image of the fixed worms where the hindgut, as the key area for high-resolution imaging, is marked. High-resolution b) Brightfield image, c) RFP channel image showing the diffuse fluorescence originating from the disrupted bacteria and d) GFP channel image showing the worm's autofluorescence. Lack of overlap in the fluorescence signal in figure c and d, indicates that fluorescence in the RFP channel is not due to the worm's autofluorescence. r (a: 10x objective, scale bar = 250 μm ; b, c and d: High-resolution imaging using an oil-immersive 60x objective, scale bar = 40 μm)

High-resolution z-stack fluorescent images of the intestine of the worms fed on either RFP-expressing *E. coli* OP50 or *P. aeruginosa* PAO1 revealed two distinct patterns for the bacteria-related fluorescence signal (Figure 4-4a).

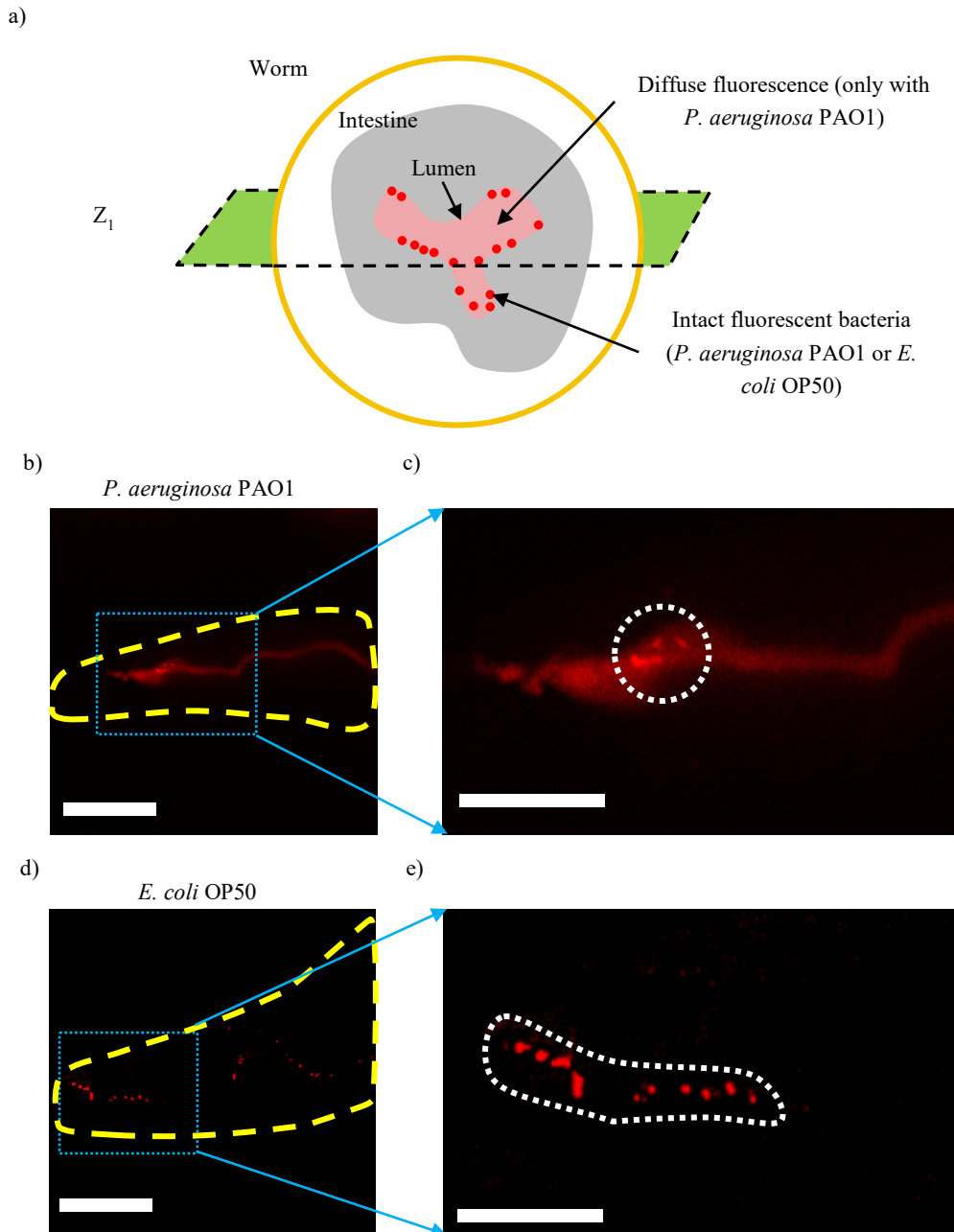


Figure 4-4- High-resolution z-stack fluorescence imaging (in the RFP channel) of representative fixed worms that had RFP-labelled bacteria (*P. aeruginosa* PAO1 or *E. coli* OP50) as their food source for 4 days. a) An illustration of the worm cross-section where individual fluorescent spots originating from intact fluorescent bacteria (*P. aeruginosa* PAO1 or *E. coli* OP50) and diffuse fluorescence, originating from disrupted bacteria, that is present only in fluorescent *P. aeruginosa* PAO1-fed worms, can be observed in one of the slices (Z_1). Z-stack imaging is required to capture all fluorescence signals across the height of the intestine. Example slices from the z-stack images (in the RFP channel) of worms that have fed on fluorescent *P. aeruginosa* PAO1 (b) and *E. coli* OP50 (d). c) Magnified view of the blue rectangle in “b” which shows diffuse fluorescence and individual fluorescent spots (marked by the white circle) in fluorescent *P. aeruginosa* PAO1-fed worms. The presence of diffuse fluorescence from disrupted *P. aeruginosa* PAO1 does not exclude the presence of intact *P. aeruginosa* PAO1. e) Magnified view of the blue rectangle in “d”, in which individual fluorescent spots (delineated by the white dashed line) originating from intact fluorescent *E. coli* OP50 can be clearly observed. b and d: scale bar = 40 μm . c and d: scale bar = 20 μm .

In the case of RFP-labelled *P. aeruginosa* PAO-fed worms, diffuse fluorescence originating from disrupted bacteria and individual fluorescent spots originating from intact bacteria can be observed (Figure 4-4b and c). It should be emphasized that the presence of diffuse fluorescence from disrupted

P. aeruginosa PAO1 does not rule out the presence of intact *P. aeruginosa* PAO1, and that the fluorescence signal from the latter eventually can be obscured by the fluorescence signal from the former. In marked contrast, in the case of RFP-labelled *E. coli* OP50-fed worms, only individual fluorescent spots originating from intact bacteria can be seen (Figure 4-4d and e).

We use IMARIS software to enhance the visualization and analysis of the raw z-stack fluorescent images. IMARIS constructs a 3D image by putting together all the slices belonging to the same channel, which in our case is the RFP channel. Figure 4-5 a and b show representative examples of such 3D images. In agreement with our discussion earlier regarding Figure 4-4, in the fluorescent *E. coli* OP50-fed worms, the pattern of the fluorescence signal takes the form of individual spots which are spread through the volume of the intestine (Figure 4-5a), while in the case of fluorescent *P. aeruginosa* PAO1-fed worms, it takes the form of individual spots which are dispersed in a region with diffuse fluorescence (RDF) (Figure 4-5b). This observation prompts us to employ different methods for the analysis of the bacterial load between the fluorescent *E. coli* OP50-fed worms and the fluorescent *P. aeruginosa* PAO1-fed ones.

In a previous work [129], we have expounded on the detection and analysis of fluorescent spots in IMARIS. As the procedure is applicable here, but only to the fluorescent *E. coli* OP50-fed worms (Figure 4-5 a), we also briefly explain it here. The fluorescent spot detection begins with providing an estimate for the smallest spot size. In our case, we used 1 μm in the “x” and the “y” directions and 2 μm in the “z” direction to account for the point spread function of the microscope. The smallest spot size together with an IMARIS internal parameter called “Quality”, which is related to the local background-corrected fluorescence intensity at the center of spots, control the detection of spots. If the “Quality” is set too low, it leads to false positives and if set too high, it leads to false negatives. Therefore, the “Quality” parameter should be chosen such that the detected spots match the actual spots and in our case a value of 150 satisfied this requirement. The spot detection procedure also makes it possible to correct for the contribution of worm autofluorescence to bacterial load. It should be first emphasized that there is no spatial overlap between the autofluorescence signal and bacteria-derived signal. Additionally, for every spot that is detected in the RFP channel by IMARIS, we also check whether the same spot also appears in the GFP channel. If the spot is also present in the GFP channel, the spot is assumed to originate from the worm autofluorescence and is discarded from the analysis. At this point, the spots are detected, however their sizes are yet to be determined through the “local contrast” method in IMARIS. In this method, a local background correction is applied to the intensity distribution around each spot. Afterwards, only the region around the center of each spot that has an intensity higher than a certain threshold (local contrast threshold) is deemed to be part of that spot. Consequently, the threshold should be set (80.4 in our case) such that the sizes of the finalized detected spots match visually with those of the actual spots (Figure 4-5c). To ensure that the detection of spots and their sizes is consistent across all the fluorescent *E. coli* OP50-fed worms, the values for the estimation of smallest spot size, “Quality” parameter and the local contrast threshold were kept the same for all the said worms. Once the procedure for the detection of fluorescent spots is completed, the volumes and the average intensities of the finalized detected spots can be exported to excel datasheets for the purpose bacterial load analysis.

The approach used for fluorescent *E. coli* OP50-fed worms, however, is not applicable to the fluorescent *P. aeruginosa* PAO1-fed worms as the intensity of RDF is too high to be ignored. Additionally, as mentioned earlier, the fluorescence signal originating from the intact fluorescent *P. aeruginosa* PAO1 bacteria can be masked by the signal from the disrupted fluorescent *P. aeruginosa* PAO1 bacteria and thus a bacterial load analysis based on separating these two types of fluorescence signal will not be entirely meaningful. Consequently, we decided to consider the RDF in its entirety, including the fluorescent spots that are spread within it, as one object for analysis (Figure 4-5b). In IMARIS, this can be achieved by using the “Surface” functionality. A surface can be defined such that its fluorescence signal intensity is equal to a given threshold value.

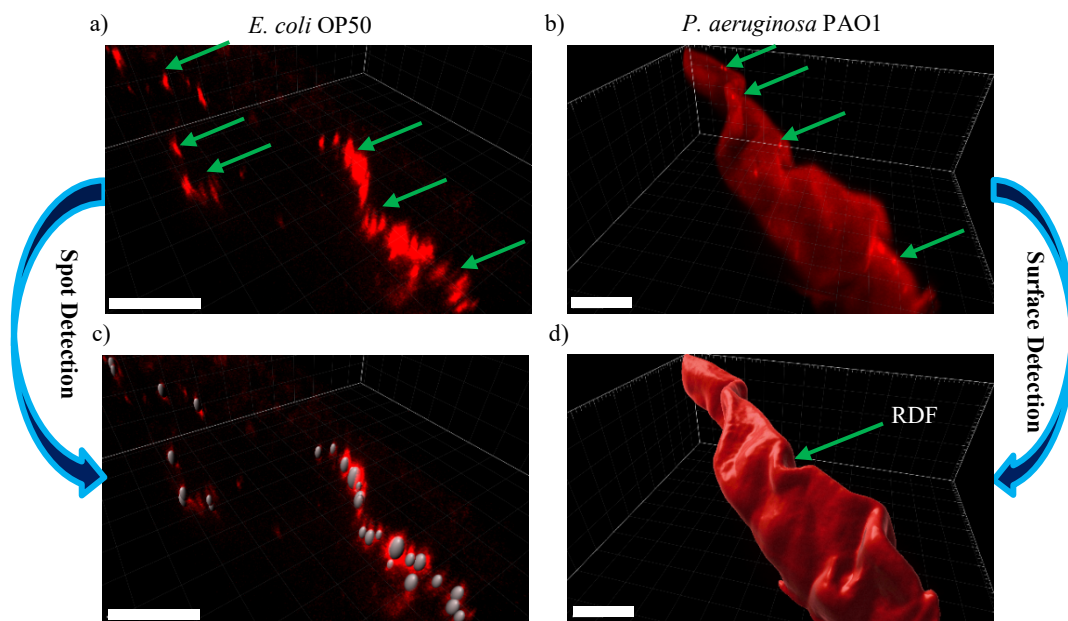


Figure 4-5- Visualization and analysis of the raw z-stack fluorescent images in IMARIS. 3D images of representative worms fed on either fluorescent *E. coli* OP50 (for 3 days) or fluorescent *P. aeruginosa* PAO1 (for 2 days) are constructed by assembling all the slices of the z-stack fluorescent images in the RFP channel. a) Individual fluorescence spots (as shown by green arrows) originating from intact bacteria spread through the intestine of RFP-labelled *E. coli* OP50-fed worms. b) Individual fluorescent spots dispersed (as shown by green arrows) in a region of diffuse fluorescence (RDF) in the intestine of fluorescent *P. aeruginosa* PAO1-fed worms. As the pattern of the fluorescence signal is different in a and b, two different methods are used to analyze the bacterial load. c) Spot detection is governed by an estimation of the smallest fluorescent spot size as well as the threshold value for the local background-corrected intensity at the center of the spots, which is referred to as the "Quality" parameter in IMARIS. We chose the value of the "Quality" parameter such that detected spots match the actual spots and false positives were not present. Once the spots are detected, their sizes still need to be determined through the IMARIS "local contrast" method in which only the region around the center of the spot that has an intensity higher than a certain threshold, is considered to be part of the spot. It should be mentioned that the perceived spot size is affected by the perspective projection that is used to display the 3D image. d) Surface detection in IMARIS is done by setting a threshold value for the fluorescence intensity that can be then used to define a surface. In our case, we set this value such that it is always 600 higher than the average background noise in each set of experiments. Afterwards, using this surface one can define the RDF as the volume within which the fluorescence intensity exceeds the threshold value. Scale bar = 20 μm

In our case, in each set of experiments, for example for worms that have fed on RFP-labelled *P. aeruginosa* PAO1 for 1 day, we measured the background noise (measuring the intensity where no worm is present), which ranged from 2770 to 2900 across all the experiments. The threshold value used for defining the surface was set 600 higher than the background noise and thus ranged from

3370 to 3500. This surface can be then used to define RDF as the volume within which the fluorescence intensity is higher than the threshold value (Figure 4-5d). Once the RDF, defined in this manner, is calculated by the software, its average intensity and volume can be extracted for bacterial load analysis. As the quantification of the bacterial load relies on measuring the volume and the intensity of the RDF, the worm autofluorescence can potentially bias the results. However, based on our observations (Figure 4-6), the contribution of the worm autofluorescence (from either the GFP or RFP species present in the intestine of the worm) to the RFP signal is dwarfed by the bacteria-derived RFP signal and thus in practice the worm autofluorescence can be safely ignored.

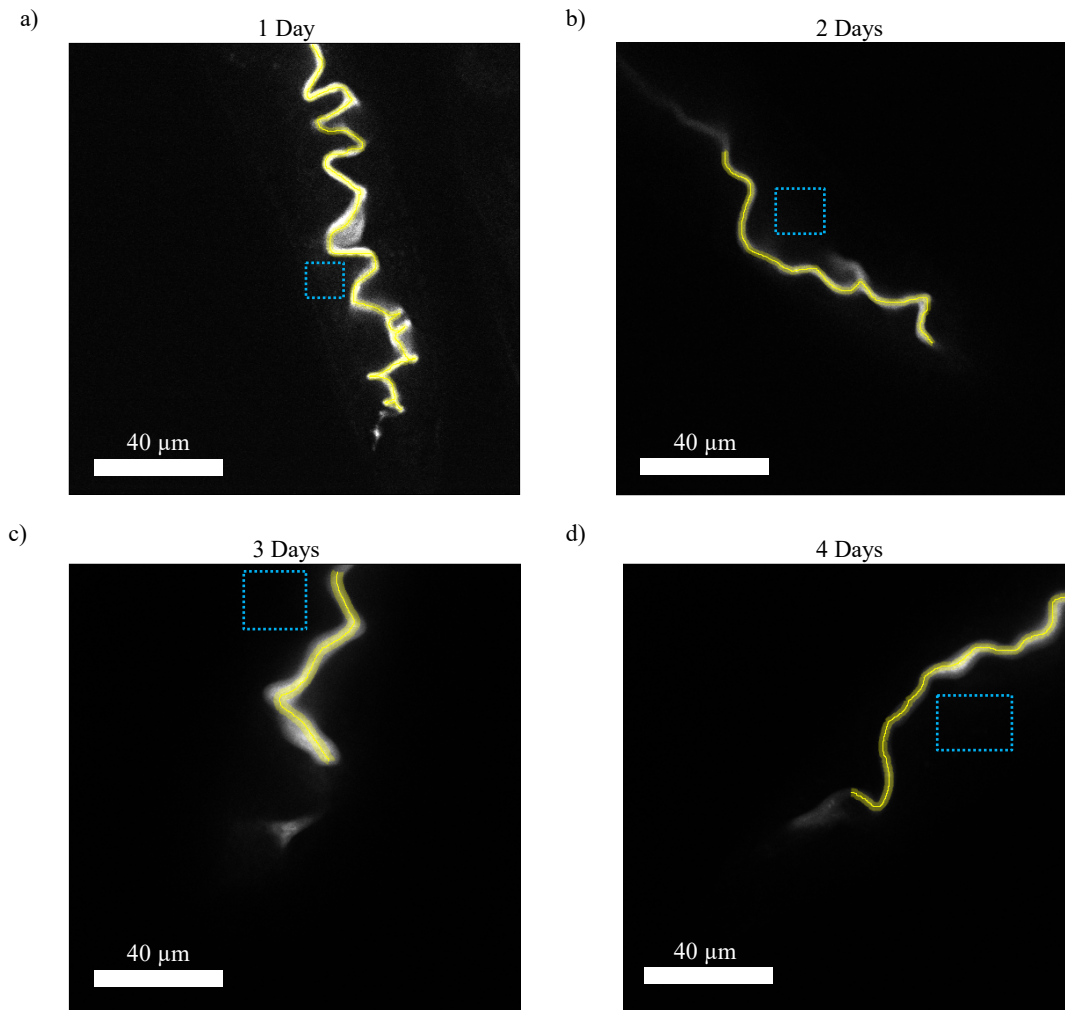


Figure 4-6 High-resolution fluorescent images acquired in the RFP channel of representative fixed worms that have fed on RFP-expressing *P. aeruginosa* PAO1 for different durations. The ratio of the background-corrected average signal intensity in the intestinal lumen (as indicated by the yellow ribbon) to the background-corrected average signal intensity of an area outside of the intestinal lumen (as shown by blue rectangle) is equal to (a) 14, (b) 26, (c) 52 and (d) 30.

4.4 Results

The image analysis by IMARIS allows us to analyze the intestinal bacterial content with single-worm resolution. In the case of worms that have fed on RFP-labelled *E. coli* OP50, IMARIS provides datasheets containing the volumes and the average intensities of every fluorescent spot in each worm.

These datasheets are then imported in MATLAB software to be processed using basic arithmetic operations. For each worm we determine the total volumes of the fluorescent spots. Additionally, we apply a background correction to the average intensities of the fluorescent spots by subtracting from them the background noise intensity. Afterwards a volume-weighted average of the background-corrected average intensities of all the fluorescent spots in each worm (referred to as “AVG Intensity”) is calculated. Thus, the bacterial load in every worm is proportional to the multiplication of the total volume and the “AVG Intensity” of the fluorescent spots. In the case of worms that have fed on RFP-labelled *P. aeruginosa* PAO1, IMARIS provides datasheets containing the volumes and the average intensities of the RDF in each worm which are similarly imported and processed using MATLAB. However, it must be remembered that in the case of RFP-labelled *E. coli* OP50-fed worms, the bacterial load describes the total number of intact bacteria, while in the case of RFP-labelled *P. aeruginosa* PAO1-fed worms, the bacterial load describes the Sum of Intact and Disrupted Bacteria (SIDB). Regardless, in both cases, the processed data is plotted in GraphPad yielding Figure 4-7 where single-worm-resolution analysis of intestinal bacterial load can be seen.

Figure 4-7a shows the total volume of fluorescent spots in worms that have fed on RFP-labelled *E. coli* OP50. As there is a large variation in the data points, the use of a log plot is necessary. As a result, no data points can be shown for worms whose intestines are free of bacteria (since $\log(0)$ is undefined). Instead, the number of worms devoid of bacteria at each day is mentioned inside the plot alongside the data points of the respective day. The absence of a number indicates the absence of worms devoid of bacteria in the respective day. This convention has been applied to plots in Figure 4-7a, b, e and f. We can observe in Figure 4-7a that the hindguts of almost all the worms that have fed on RFP-labelled *E. coli* OP50 are devoid of fluorescent spots and thus intact bacteria in the first two days. Nonetheless, there are 3 worms on the second day in which the total volume of the fluorescent spots is significantly large. This shows the importance of single-worm resolution analysis since considering the average of the total volume of the fluorescent spots alone would imply the presence of a significant volume of fluorescent spots in all the worms. On the third day, there is a sharp increase in the number of worms whose intestines contain significant volumes of fluorescent spots and at day 4, the intestines of all the worms contain significant volumes of fluorescent spots. Similar observations can be made when the “AVG Intensity” fluorescent spots is considered in Figure 4-7c. It should be noted that an AVG Intensity of zero indicates worms whose intestines are devoid of bacteria (similar convention also applies to Figure 4-7d). Additionally, we can further observe that the fluorescent spots grow in intensity between day 3 and 4 which shows that the density of intact bacteria within the bacterial spot is increasing. It must be mentioned that the worm-to-worm variation in the total volume of the fluorescence spots for each day (Figure 4-7a) is larger than that in the “AVG Intensity” of the fluorescent spots for the same day (Figure 4-7c), as evident from the use of the log axis in the former. Consequently, the plot representing the total number of intact bacteria within the intestine, (Figure 4-7e) which is obtained by the multiplication of Figure 4-7a and c, mostly resembles the former. This means that the intestinal bacterial load increases through the spread of intact bacteria in the intestine, rather than the formation of very dense bacterial clusters. Overall, it can be understood that until day 2, most of the worms are devoid of any intact bacteria and it is at day 3 and 4 where significant number of intact bacteria are found in the intestine of every worm. However, considering the upper and lower limits of

bacterial load variation among the worms in day 3 and day 4, it seems that the number of intact bacteria is approaching a saturation limit.

Figure 4-7b shows the volume of the RDF in the worms that have fed on RFP-labelled *P. aeruginosa* PAO1. It can be seen that at day 1, in about half of the worms, the total volume of the RDF is significantly large and only in 25% of the worms, the total volume of the RDF is very small (in fact for two worms the total volume of the RDF is zero but due to using log axis, a value of 1 was assigned instead). On day 2, there is an increase in the total volume of RDF and through comparison of intrapopulation variations among day 2, 3 and 4, it can be inferred that the volume of the RDF has already reached a saturation limit. Figure 4-7d shows the AVG intensity of the RDF, representing the density of the sum of intact and disrupted bacteria, for different feeding periods. On day 1, except in two worms, AVG intensity of the RDF is significant. On day 2, the AVG intensity of the RDF is higher than day 1 and has already reached a saturation limit as suggested by comparing intrapopulation variations among day 2, 3 and 4. Considering the use of a log axis in Figure 4-7b and a linear axis in Figure 4-7d, we can observe that for a worm population of each day, there is a larger intrapopulation variation in terms of the total volume of the RDF than in terms of "AVG Intensity". Therefore, the plot representing the SIDB (Figure 4-7f), which is the result of multiplying Figure 4-7b and d, mostly resembles the former. This implies that the increase in bacterial load is through the spread of bacteria within the intestine rather than the formation of high-density but small RDFs. Based on Figure 4-7b, we can observe that at day 1, out of 13 worms, two worms have a SIDB of 0 (due to use of log scale, they were assigned a value of 1), 6 worms have a significantly high SIDM, while the rest of the worms are in between these two extremes. However, on day 2, all the worms have a significantly high SIDM and comparing their intrapopulation variation to those of worms at day 3 and 4 suggests that the SIDM has already reached a saturation limit after 2 days.

We must stress that we have used two different methods for the quantification of bacterial load in RFP-labelled *E. coli* OP50-fed worms and RFP-labelled *P. aeruginosa* PAO1-fed worms. Moreover, in the former case, the bacterial load is proportional to the number of intact bacteria, while in the latter case, it is proportional to SIDB. Additionally, we have not measured the fluorescence signal intensity per unit of either (intact) bacteria. As a result, direct quantitative comparison between the two groups should be avoided. Nevertheless, it is reasonable to assume that when the intestine of the worm is filled with either of the two bacteria, as indicated by reaching a saturation limit in Figure 4-7e and f, the number of intact RFP-labelled *E. coli* OP50 and *P. aeruginosa* PAO1 bacteria present in the intestine are similar. This assumption allows us compare the rate of bacterial colonization in the intestine of worms. In the case of RFP-labelled *P. aeruginosa*-fed worms, already at day 1, half of the worms contain bacterial load similar to those of worms at day 4. However, in the case of RFP-labelled *E. coli* OP50-fed worms, this takes place sometime between day 2 and day 3.

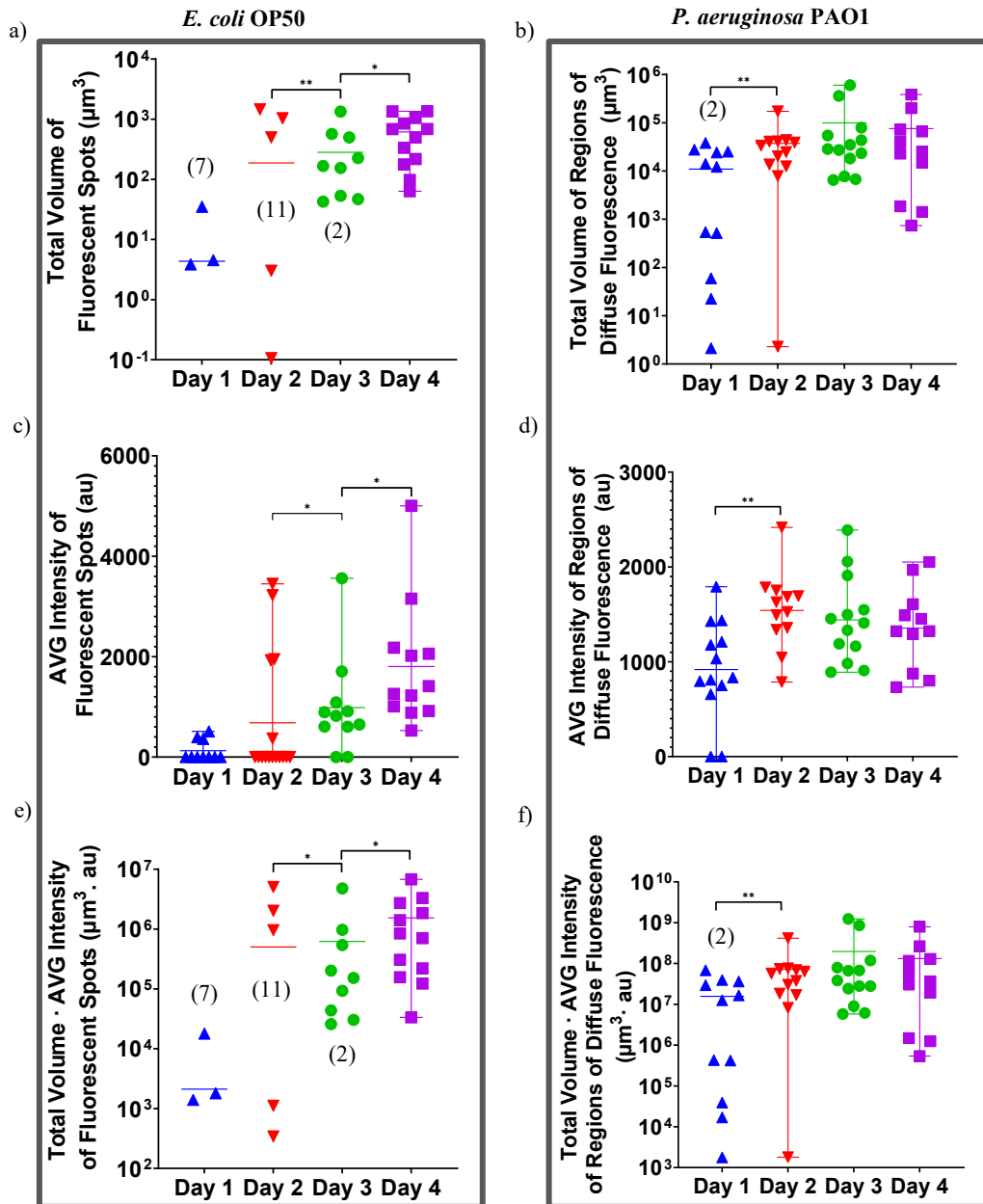


Figure 4-7-. Single-worm-resolution analysis of bacterial load in adult worms that have fed on RFP-labelled bacteria for 1, 2, 3 and 4 days. Each data point is calculated for a single worm. The horizontal bars denote the average value and the error bars (where applicable) show the range of the data. The number of worms devoid of bacteria at each day is mentioned inside the plot alongside the data points of the respective day (applicable to a, b, e and f). An AVG intensity of zero indicates worms whose intestines are devoid of bacteria (applicable to c and d). a) The total volume of fluorescent spots, c) the background-corrected average intensity of fluorescent spots and e) the multiplication of a and c which is proportional to the total number of intact bacteria. a, c and e are obtained from fluorescent *E. coli* OP50-fed worms with worm sample size of 10, 16, 11 and 12, for day 1 to day 4, respectively. b) The total volume of RDF, d) the average intensity of RDF and f) the multiplication of the b and d which is proportional to the SIDM. b, d and f are obtained from fluorescent *P. aeruginosa* PAO1-fed worms with worm sample size of 13, 12, 13 and 11 for day 1 to day 4, respectively. * $p \leq 0.05$, ** $p \leq 0.01$.

The faster spread of RFP-labelled *P. aeruginosa* is also evident by the fact that after 2 days, the bacterial load reaches saturation while for RFP-labelled *E. coli* OP50, the saturation can be thought to occur at earliest on day 4. Therefore, in both cases, the intestinal bacterial load generally increases with the age of the worm, albeit more rapidly for worms fed on RFP-labelled *P. aeruginosa* PAO1.

4.5 Discussion

C. elegans is a versatile model organism for studying bacterial pathogenesis and evolutionary-conserved innate immunity pathways [17], [51]. *E. coli* OP50, a non-pathogenic bacterium, is used as a food source for the general maintenance of *C. elegans* worms [123]. However, despite being a seemingly innocuous bacterium in the larval stages, as the worm ages past the L4 stage, due to the general decline in the functioning of the pharyngeal grinder and innate immunity, *E. coli* OP50 colonizes the intestine of the worm and thus becomes mildly pathogenic [8]. On the other hand, *P. aeruginosa* is a known pathogenic bacterium, which is capable of killing the worm through different means, and in particular, intestinal colonization [52], [57]–[65]. The average lifespan of worms fed on *P. aeruginosa* PAO1 is about 20% of those fed on *E. coli* OP50, which reflects the stark difference in the degree of pathogenicity [34], [57].

Despite the extensive research on *P. aeruginosa* infection in *C. elegans* via intestinal colonization, there are no systematic studies on the feeding behavior and the digestion in infected worms. We do know, however, that within 8 hours of feeding on *P. aeruginosa* PA14, a more virulent strain compared to PAO1 we used in our study, the intestine becomes distended, containing few intact bacteria which are the source of putative Outer Membrane Vesicles (OMVs) that are also present in the intestine [56]. Additionally, an unknown Extracellular Material (EM) covers the intact bacteria as well as the apical surface of the intestine's brush border [56]. Unfortunately, it is not known whether the EM is produced by the bacteria or the worms [56]. After 24 hours of feeding, the intestine becomes more distended, the numbers of intact bacteria and OMVs increase, and a thicker layer of EM covers the microvilli, which still retain their normal length [56]. At 48 hours of feeding, the intestine becomes even more distended, and the increased number of intact bacteria are mostly separated from the now shortened microvilli by a thick layer of EM and intercellular invasion by the bacteria can be seen [56]. Similar pathogenesis has been observed in worms feeding on *P. aeruginosa* PAO1 [130] but worms fed on *E. coli* showed no such signs [56].

Whether and how the symptoms seen in *P. aeruginosa*-fed worms are related to the accumulation of disrupted bacteria we observed in Figure 4-4c is not established. It has been previously reported that worms fed on *P. aeruginosa* PAO1 have shorter body lengths compared to those fed on *E. coli* OP50 [131], indicative of a reduced metabolism. Probably, feeding on *P. aeruginosa* PAO1 reduces the rate of bacterial material absorption and/or defecation in the worms, which then results in the accumulation of nutrients/waste originating from disrupted bacteria in the gut. This hypothesis can be evaluated in future works, by observing how the time gap between the last feeding event and the fixation of the worms affects the pattern of the bacteria-derived fluorescence signals. In the present study, the time gap was 1 hour, which was sufficient for *E. coli* OP50-fed worms to fully digest the bacteria but not enough for *P. aeruginosa*-fed worms. Imaging the worms that are fixed with different time gaps (e.g., 15, 120 and 180 minutes) can eventually reveal the dependency of the digestion dynamics on the bacteria used as the food source.

Previous studies on worms fed on either *E. coli* OP50 or *Salmonella typhimurium* (*S. typhimurium*) SL1344 show that the number of colony-forming bacteria in the intestine generally increases with the age of the worm until it reaches a saturation limit, albeit earlier in the case of the more pathogenic *S. typhimurium* SL1344 [34], [51]. We obtained similar results and found that the bacterial load in worms fed on RFP-labelled *E. coli* OP50 seem to approach a saturation limit at day 4, while for those fed on RFP-labelled *P. aeruginosa* PAO1, the saturation limit is reached at day 2. This observation can be at least partially explained, as we alluded to earlier, by the reduced metabolism in the worms fed on *P. aeruginosa* PAO1.

Even though we used a simple microfluidic device in this work, the methods described in this work can be readily implemented in other types of microfluidic devices. Our group has already developed automated image and video processing techniques that can be used for *in vivo* extraction of phenotypes such as area, length, egg release rate and motility from the worms that are studied via microfluidic devices [83]. As discussed earlier, phenotypes such as length and area can help clarify the impact of bacterial food source on the development of the worm. Furthermore, our group has also reported devices dedicated to studying bacterial load dynamics and digestion [97], [98]. The high-resolution imaging of the gut bacteria afforded by the methods described here can extend the capabilities of such devices and thus provide a better understanding of the interactions between bacteria and the worm.

4.6 Conclusion

We have demonstrated the potential of on-chip high-resolution z-stack fluorescence imaging and advanced image analysis for elucidating the bacterial food digestion and accumulation in *C. elegans* worms. We discovered that bacteria-derived fluorescence signals in the intestines of the worms fed on RFP-labelled *P. aeruginosa* PAO1 uniquely included a diffuse fluorescent background in addition to individual fluorescent spots that are also present in worms that were fed on RFP-labelled *E. coli* OP50. This observation indicates an intestinal accumulation of disrupted bacteria exclusive to RFP-labelled *P. aeruginosa* PAO1-fed worms, which, when understood in the context of previous studies, hints at a reduced metabolism in such worms compared to those fed on RFP-labelled *E. coli* OP50. Furthermore, our single-worm resolution analysis showed that with both diets, the bacterial load in the intestine generally increases with age until it reaches a saturation limit. However, in the case of RFP-labelled *P. aeruginosa* PAO1-fed worms, this limit was reached in 2 days compared to 4 days for RFP-labelled *E. coli* OP50, which further suggests a reduced metabolism in the former worms. The methods described here can readily be used to complement the scopes of existing microfluidic technologies.

5 High-resolution in vivo imaging of bacteria in the C. elegans gut

In sections 3 and 4, we discussed a framework for high-resolution imaging and analysis of ingested bacteria, which relied on worm fixation. Here we attempted to reproduce the same level of imaging and analysis *in vivo* using microfluidic devices featuring valves for the reversible immobilization of the worms. Although we were able to sufficiently immobilize the worms for high-resolution imaging of the gut bacteria, we could not reliably control the sites where the worms were immobilized, which is essential for automating the imaging procedure. More importantly, the bacteria present in the intestine constantly move due to the intestinal peristalsis. As a result, z-stack imaging, which is required for obtaining 3D representation of intestinal bacteria, was out of reach. Overall, our investigation shows that high-resolution z-stack imaging of the gut bacteria in an automated fashion in living worms is extremely challenging.

5.1 Introduction

As we saw in chapter 1, and sections 3.1 and 4.1, *C. elegans* is a powerful model organism for studying host-microbiota interactions and in particular, host-pathogen interactions [1], [2], [8], [15]–[19]. This nematode has been used to discover evolutionary-conserved innate immunity pathways as well as bacterial virulent mechanisms [17]. These studies involve the generation of different bacteria and worm strains whose interactions are studied using a variety of assays. In the simplest of assays, the lifetime of the worms feeding on a given bacteria can be measured as an indicator of the pathogenicity of the bacteria. The nutritional value of the bacteria is also evaluated by observing the development of the worms and their fecundity. Additionally, the motility of the worm, the rate of pharyngeal pumping and defecation are also indicators of the worm's health which can be monitored. To quantify the number of bacteria present in the intestine, bacterial colonization assays are performed on a group of typically 10 worms to obtain the average number of colonies forming units (CFU) of bacteria. When necessary, the ability of a given bacterium to establish persistent intestinal infection is studied using shift and competition assays. It is also possible to visualize the presence of intestinal bacteria using fluorescent microscopy. Additionally, the host response to bacteria can be monitored by measuring the host's gene expression via fluorescence microscopy, blotting techniques or quantitative real-time polymerase chain reaction (qRT-PCR) analysis. Overall, the interactions between the worm and bacteria is complex and multi-faceted and numerous assays should be carried out to completely exhaust the different aspects of these interactions.

Consequently, microfluidic devices are promising platforms for the investigation and discovery of host-microbiota interactions. In general, there is a spectrum with two extremes for the development of microfluidic devices for research on *C. elegans*, namely, high-throughput screening applications and long-term high-resolution imaging applications [72], [77], [79]. While numerous microfluidic devices for studies involving *C. elegans* have been reported thus far, only a handful of devices are applied to host-microbiota interactions [95]–[98]. The devices reported by Lee et al [96] and Yang et al [95] are efforts toward high-throughput killing-assays using *C. elegans* while the devices reported by Viri et al aim at long-term high-resolution imaging of bacterial load dynamics and absorption [97], [98]. In the more recent work by Viri et al [98], the microfluidic device enabled long-term high-resolution fluorescence imaging and tracking of individual immobilized worms fed fluorescent bacterium. While the worms were imaged at a high resolution, the imaging was carried out using a widefield microscope equipped with 50×/NA 0.55 objective. The widefield microscope suffers from reduced contrast and image blur due to the collection of out-of-focus light and there were no attempts to acquire z-stack fluorescent images and perform de-convolution to achieve confocal-like imaging quality [100]. Alternatively, it is also possible to acquire z-stacks using optical sectioning microscopy techniques such as SDCM [107]. Therefore, microfluidic devices applied to host-microbiota interactions can be still improved in terms of imaging.

In vivo high-resolution z-stack imaging of the worm crucially depends on immobilizing the worm without harming it. We have already carried out a detailed analysis of potential immobilization

strategies for high-resolution host microbiota studies in section 2.6. Based on our analysis, we prefer a valve-based immobilization strategy, as it allows high-resolution imaging of the worms during L4 stage and adulthood, the period most relevant to host-microbiota interactions, in a single microfluidic device. Additionally, compared to hydrogel-based immobilization techniques, the risk of clogging in the channels in long-term studies is lower. However, it should be emphasized that the automation of the imaging process is essential for longitudinal studies with the highest spatiotemporal resolution. Therefore, the microfluidic device should also include novel elements that enable the immobilization of the worm in predefined locations. Having these considerations in mind, we fabricated 2-layer microfluidic devices with different designs and evaluated their performances for automated high-resolution imaging of *C. elegans* worms and in particular of their intestinal bacteria. We start by detailing the design, fabrication and performance of our first device and use it as a basis to describe how design variations affected the performance of our microfluidic devices.

5.2 Design and fabrication of microfluidic devices

We have designed and fabricated 2-layer microfluidic devices featuring valves for the immobilization of the worms. Figure 5-1a and b show the initial design of a single lane in our devices, where the blue and green color represent the superimposed flow and the control layers, respectively. Every device features five identical lanes, each having four identical chambers, where, in an ideal distribution scenario, single worms can be cultured and imaged for long-term studies at high spatiotemporal resolution. The chambers are equipped with filters that consist of 20 μm wide array of slabs that are uniformly spaced apart with a spacing (Figure 5-1b) based on the age of the starting worm population (L4 stage or young adult). The spacing is small enough such that it prevents the worms of interest from leaving the chambers on their own (in the absence of a strong fluid flow) and yet is large enough such that their progenies can be periodically removed by applying a moderate fluid flow. Pressurizing the control layer with deionized (DI) water deforms the membrane, which immobilizes the worm (Figure 5-1c). We attempted to immobilize the worm in a predefined location by starting the immobilization procedure with applying a flow in the flow layer for a duration of T_w to push the worms towards the filters. Afterwards, while maintaining the flow in the flow layer, the control layer is pressurized gradually to gently immobilize the worm. We define the critical pressure (in the control layer) as the pressure at which the worm is sufficiently immobilized. Once this critical pressure is achieved, the flow rate in the flow layer is reduced while the flow in the control layer is stopped, and the worm can be now imaged.

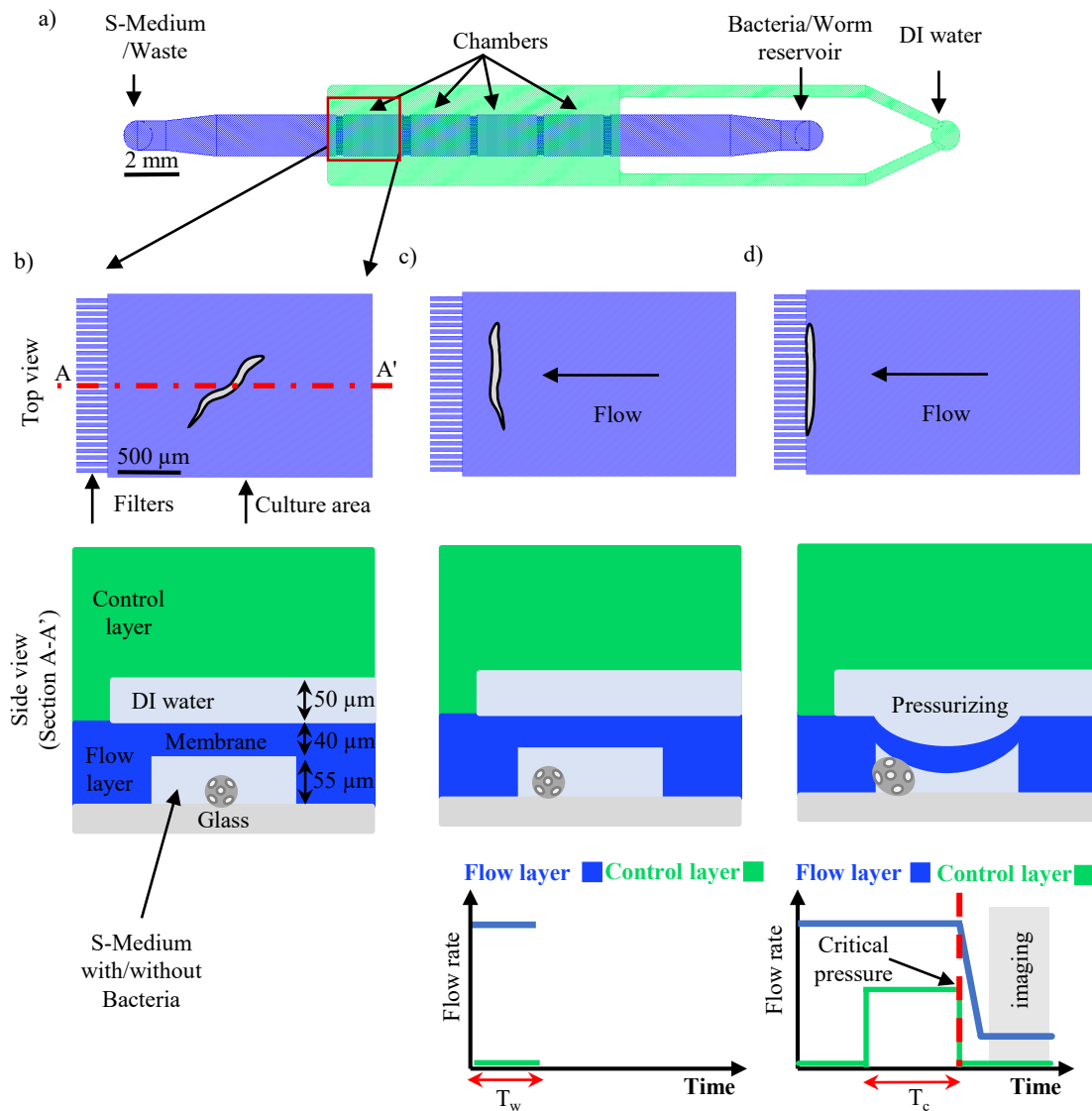


Figure 5-1- The initial design of the microfluidic device and the immobilization procedure. (a) The design of a single lane featuring the flow (blue) and the control (green) layers. (b) An enlarged top view (control layer not shown) of the leftmost chamber and its cross-section. Notice that since the cross-section of the leftmost chamber is displayed, the control layer is enclosed only on the left side. The chambers are 2.1 mm long and 1.4 mm wide and are used for culturing and imaging the worms. (c) The immobilization procedure. (c) A fluid flow in the flow layer pushes the worm towards the filter structure for a duration of T_w . (d) Afterwards, while maintaining the same flow rate in the flow layer, the control layer is gradually pressurized by applying a constant flow rate in the control layer. The pressure-mediated deformation of the membrane gradually and gently immobilizes the worm. Once sufficient immobilization is achieved (at a critical pressure resulting from maintain the flow rate for a duration of T_c), the flow rate in the control layer is brought to zero and the flow rate in the flow layer is reduced, and imaging can be carried out.

We used the Clewin software to prepare the layout of the microfluidic device according to the design described above (Figure 5-1). The layout was then used to pattern a chromium/soda-lime glass mask (Cr/glass mask for brevity) (Figure 5-2). Cr/glass mask is first spin-coated with a thin layer of a positive photoresist (PR for brevity). Subsequently, the Cr/glass mask is exposed to UV light in a direct laser writer machine according to the designed layout. Afterwards, the exposed PR is developed, the Cr/glass mask is etched using solution consisting of ceric ammonium nitrate $(\text{NH}_4)_2[\text{Ce}(\text{NO}_3)_6]$: Perchloric acid (HClO_4) : water $(\text{H}_2\text{O}) = 10.9\% : 4.25\% : 84.85\%$ and the fabrication of the Cr/glass mask is completed by stripping the remaining PR and rinsing the Cr/glass with DI water.

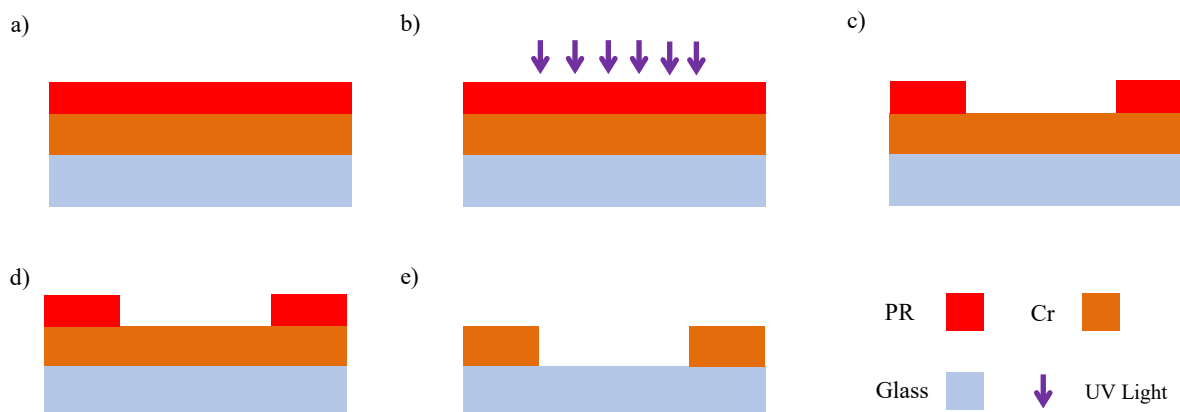


Figure 5-2- Patterning of Cr/glass masks. (a) Spin-coating of PR. (b) UV exposure of PR using a direct laser writer. (c) Development of PR. (d) Etching of Cr (e) PR stripping and rinsing.

The fabricated Cr/glass mask is afterwards used to fabricate a SU-8 (a negative structural photoresist) mold on a silicon wafer (Si wafer for brevity) substrate (Figure 5-3 a-c). The Si wafers are first cleaned using an oxygen plasma oven. Afterwards, SU-8 is spin-coated on the Si wafer to obtain the desired thickness (which also defines the height of channels in the final microfluidic device). We chose a thickness of 55 and 50 μm for the flow and the control layers, respectively. Next, the SU-8/ Si wafer goes through a (soft) baking step to evaporate the solvent and increase the adhesion of SU-8 to the substrate. Subsequently, the SU-8/Si wafer is exposed to UV light through the previously fabricated Cr/glass mask. After the exposure the SU-8/Si wafer is baked a second time (referred to as the post-exposure bake) to drive the crosslinking reaction in the exposed area of the SU-8. After a relaxation period, the SU-8/Si wafer is developed and thus SU-8 is patterned according to the designed layout. Lastly, the patterned SU-8/Si wafer goes through a third baking step (referred to as hard bake) to enhance the structural integrity of SU-8.

Before the SU-8 mold can be used for PDMS molding (Figure 5-3d), its surface must be treated to reduce its adhesion to PDMS. This is accomplished by exposing the SU-8 mold to Trimethylchlorosilane (TMCS) vapors for 30 minutes inside a desiccator. The Sylgard 184 PDMS kit consists of two components, namely, the base and the curing agent (both liquids) and typically a base-to-curing agent ratio of 10:1 is used. This ratio can be modified with lower base-to-curing agent ratios (higher relative amount of curing agent) resulting in stiffer PDMS due to increased cross-linking [132]. We added the base and the curing agent with a ratio of 10:1 and blended them together until a homogenous mixture was obtained. The blending process creates bubbles of air in the mixture which are eliminated by placing the mixture in a vacuum desiccator. Depending on the design of the PDMS device, the mixture can be applied to the mold in two different ways. The mixture can be simply casted unto the mold with some rough control over the thickness of the final device (from a few mms to ~ 1.5 cm) which was the approach for the fabrication of the control layer (Figure 5-3e). However, if a very thin membrane is needed (ranging from a few tens of microns to a few hundreds), the mixture is spin-coated on the mold. Consequently, the flow layer was obtained by spin-coating the liquid PDMS at 500 RPM for 60 which resulted in 100 μm PDMS layer (since the channel is 55 μm high and the membrane is 45 μm thick) (Figure 5-3e).

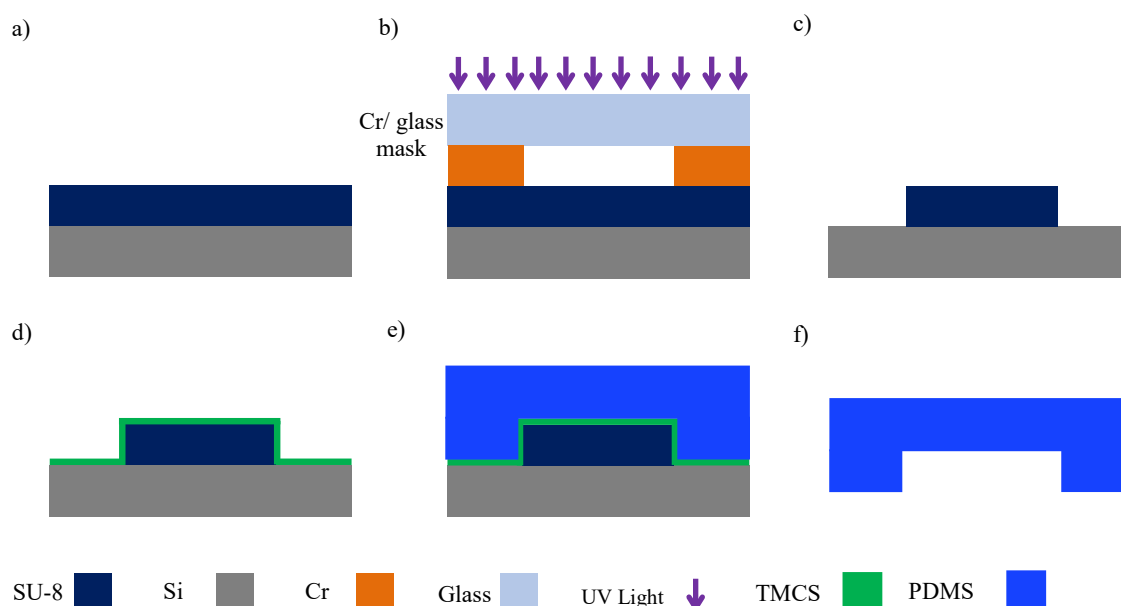


Figure 5-3- SU-8 molds for PDMS molding. (a) Spin-coating of SU-8 followed by a soft bake step. (b) Exposure of SU-8 followed by a post-exposure bake and a relaxation step. (c) Development of SU-8 followed by a hard-bake step. (d) TMCS surface treatment. (e) Spin-coating or casting of degassed liquid (uncured) PDMS followed by a second degassing step before curing process can take place. (f) casted PDMS can manually detached from the mold.

Once, the PDMS mixture is applied to the mold, the mold is placed inside a vacuum desiccator to help remove the air bubbles trapped between the fine SU-8 structures and thus allow the PDMS mixture to completely fill the SU-8 mold. Afterwards, the mold is placed inside an oven for 2 hours at 80 °C during which the cross-linking process takes place (curing) and the PDMS becomes rigid.

The casted control layer can be easily and manually removed from the mold (Figure 5-3f) but the thin spin-coated flow layer is very fragile and cannot be manually manipulated as easily. As a result, the control and the flow layers undergo oxygen plasma surface activation and afterwards are manually aligned and bonded together under a microscope (Figure 5-4a). The combined layers (flow and control layers) are then first placed on a hot plate for 80 °C for 4 hours to enhance the bonding and afterwards can be safely removed from the SU-8 mold (Figure 5-4a).

A biopsy punch is used for creating the inlets and outlets on the combined layers. Afterwards, the combined layers and a glass slide are bonded together via oxygen plasma surface activation. Lastly, the fabrication of the microfluidic chip is completed by placing it on a hotplate at 80 °C for 4 hours to enhance the bonding between the glass slide and the flow layer. It must be noted that since the membrane extends for a length of 8.4 mm without any support from the control layer, it is highly likely that the flow layer has deformed towards the empty channel in the control layer. If the combined layers are bonded the glass slide at this state, there will be areas along the flow layer that do not come into contact with the glass and thus no bond will form in these areas (Figure 5-4b). Therefore, before bonding the combined layers to the glass slide, we pressurize the control layer to flatten the flow layer to ensure the proper bonding of the flow layer and the glass slide.

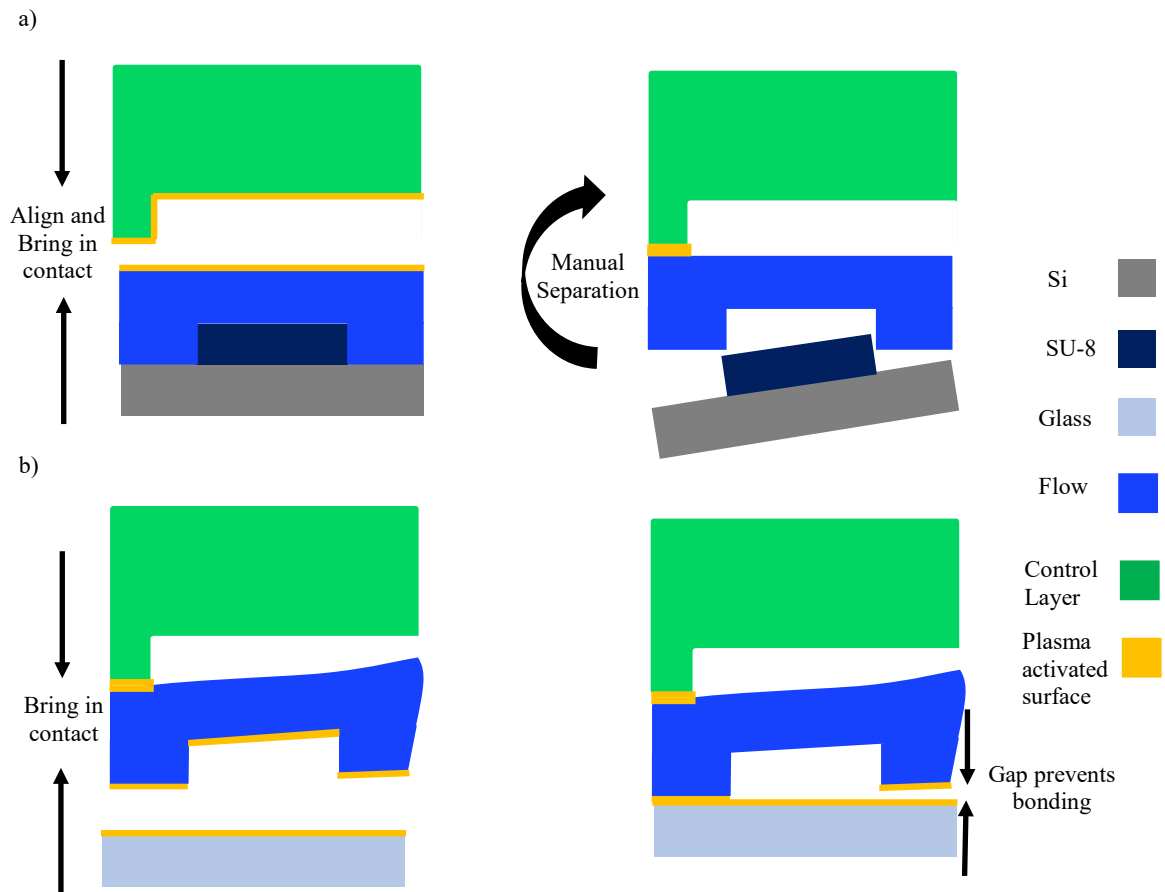


Figure 5-4- (a) Detaching the spin-coated flow layer from the respective SU-8 mold. (b) Potential bonding issue between the flow-layer and the glass substrate due to the deformation of the flow layer after removal from the SU-8 mold

5.3 High-resolution *in vivo* imaging of intestinal bacteria

To evaluate the performance of our chips in terms of immobilization and high-resolution imaging, we loaded adult wild-type *C. elegans* worms on the chip and fed them RFP-labelled *E. coli* OP50. We then acquired high-resolution time-lapse fluorescence and brightfield images of immobilized worms using a Zeiss Axio Imager 2, an upright widefield microscope equipped with a 50×/0.55 NA objective. We observed that while it was not possible to immobilize the worms consistently near the filter structures as initially intended (Figure 5-5a and b), it was still possible to immobilize them and have control over the degree of immobilization. When moderate pressures are used for immobilization, the movements of the worms are limited but not totally restricted. We could see the pumping of the pharynx in brightfield images (Figure 5-6a), and bacteria moving in the pharynx and the anterior section of intestine (near the pharyngeal-intestinal valve) in the fluorescent images (Figure 5-6b). If required, the movement of the worm can be further suppressed by using very high pressures for immobilization but it disrupts the eating behavior of the worm. We observed that the pumping of pharynx took place with extreme difficulty and no new bacteria seemed to be entering the pharynx. Similarly, the intestinal peristalsis seemed to be hindered but it was not completely stopped as several bacteria were seen moving through the intestine. This is problematic as the movement of bacteria due to the intestinal

peristalsis prevents acquiring z-stack images which are essential for obtaining 3D representations of intestinal bacteria.

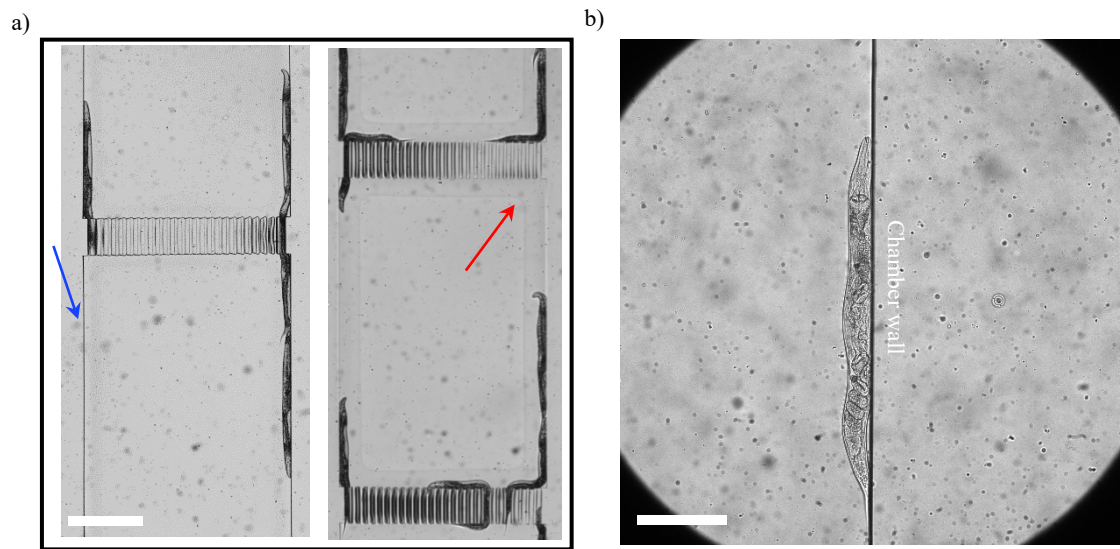


Figure 5-5- (a and b) Brightfield images of worms becoming immobilized near the chamber walls. (a) The blue and red arrows show the chamber wall and the faint outline of the deformed membrane, respectively. Scale bar = 500 μm . (b) Scale bar = 250 μm

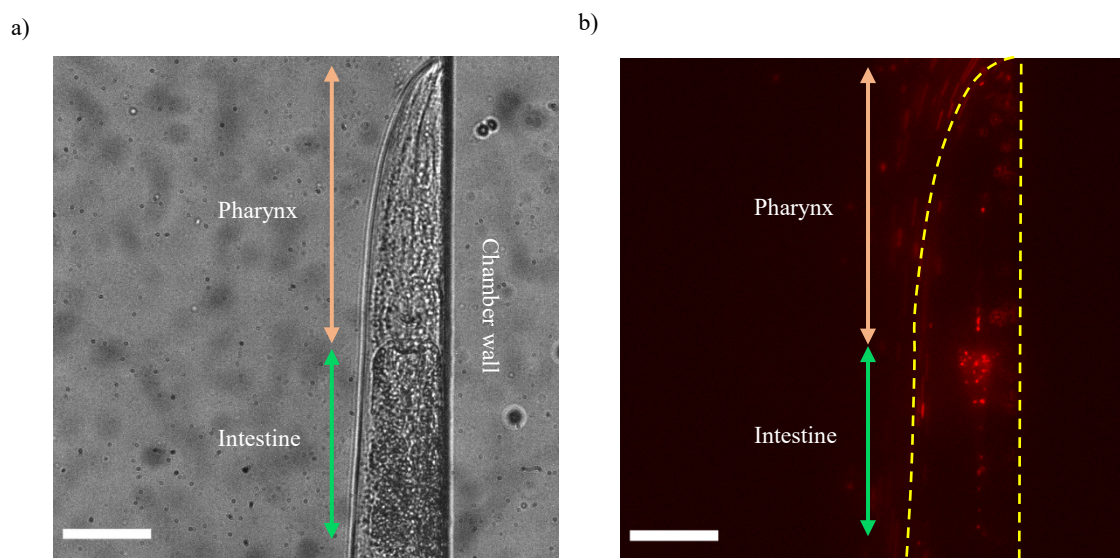


Figure 5-6- Brightfield and fluorescence microscopy images of a moderately immobilized adult wild-type worm shortly after being fed RFP-labelled *E. coli* OP50. (a) Brightfield and (b) fluorescent image of the worm in the RFP channel; bacteria can be seen both in the grinder and just after the pharyngeal-intestinal valve. Contrary to our intention, the worm is immobilized next to the chamber wall instead of the filters. Scale bar = 50 μm

Regardless, we still attempted to acquire high-resolution images of the bacteria present through the intestine of the worm. In Figure 5-7(a), we can see a strong fluorescence signal coming from a group of bacteria at the pharynx. In addition, single bacteria in the intestine as well as in the channel are also resolved. However, since the channel is 55 μm high, only the bacteria in the plane of focus are resolved. Similar observations can be made Figure 5-7 (b) and, in addition, the intestine seems to emit a uniform fluorescence signal which originates from disrupted bacteria. Figure 5-7 (c) and (d) show

the bacteria in the intestine of worm; however, resolving a single bacterium is only possible when the bacteria are sparsely-packed as seen in Figure 5-7(c). We were also able to see the movement of the bacteria within the intestine of the worm through time-lapse imaging.

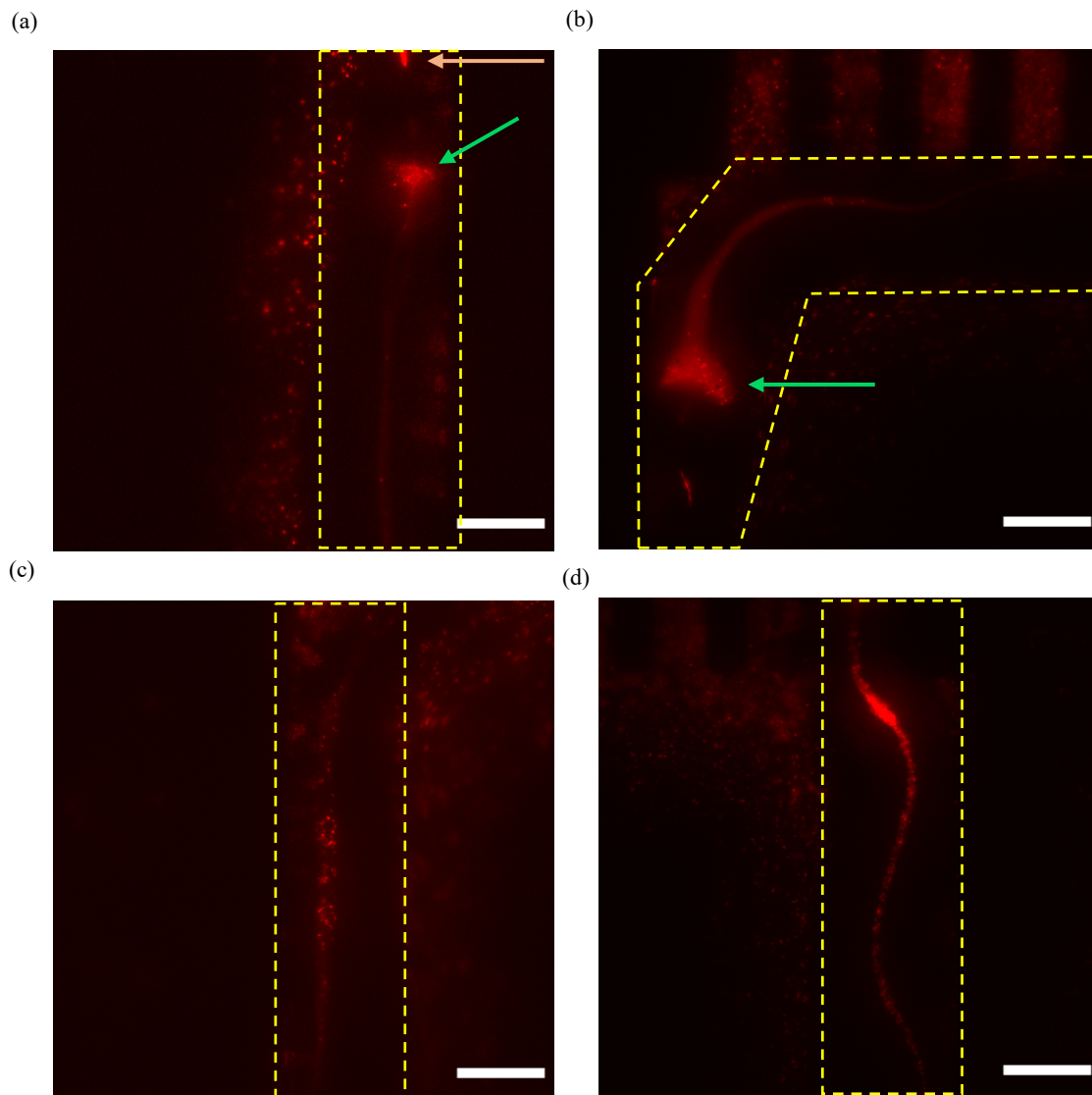


Figure 5-7- Fluorescence microscopy of adult wild-type *C. elegans* fed with RFP-labelled *E. coli* OP50 bacteria. The dashed lines and the greens arrows, respectively, show the outline of worm and the beginning of the intestine. (a) The orange arrow shows a group of bacteria in the pharynx; single bacteria can be resolved both in the intestine and the microfluidic channel. (b) The intestine gives a uniform fluorescence signal. (c) Single bacteria in the intestine can be resolved. (d) Single bacteria cannot be resolved when having a tightly-packed group of bacteria. Scale bar = 50 μm

As we were still interested in high-resolution imaging of the intestinal bacteria, we made several variations in the design of the microfluidic device to be able to consistently immobilize the worms in a predefined location. We changed the design of the filters to facilitate the distribution of the worms in the chambers and also to prevent the worms being trapped within the openings in the filters during immobilization. We also added traps not only to limit the movement of the tails and the heads of the worms but also to help immobilize the worms near the filter structure. Additionally, we also varied, the length, width and height of the chambers to be able to accommodate worms over the entire adulthood. Lastly, we also varied the fluidic protocols to improve the reliability of the location of

immobilization. Despite our best efforts, we were not able to consistently immobilize the worms in the intended location, which is essential for an automated imaging procedure. As a result, due this shortcoming of our microfluidic devices as well as the movement of the bacteria due to intestinal peristalsis, we decided, instead, to load the worms on already-fabricated microfluidic chips and rely on a fixation procedure for the immobilization and high-resolution imaging of the worms (as was reported in chapters 3 and 4).

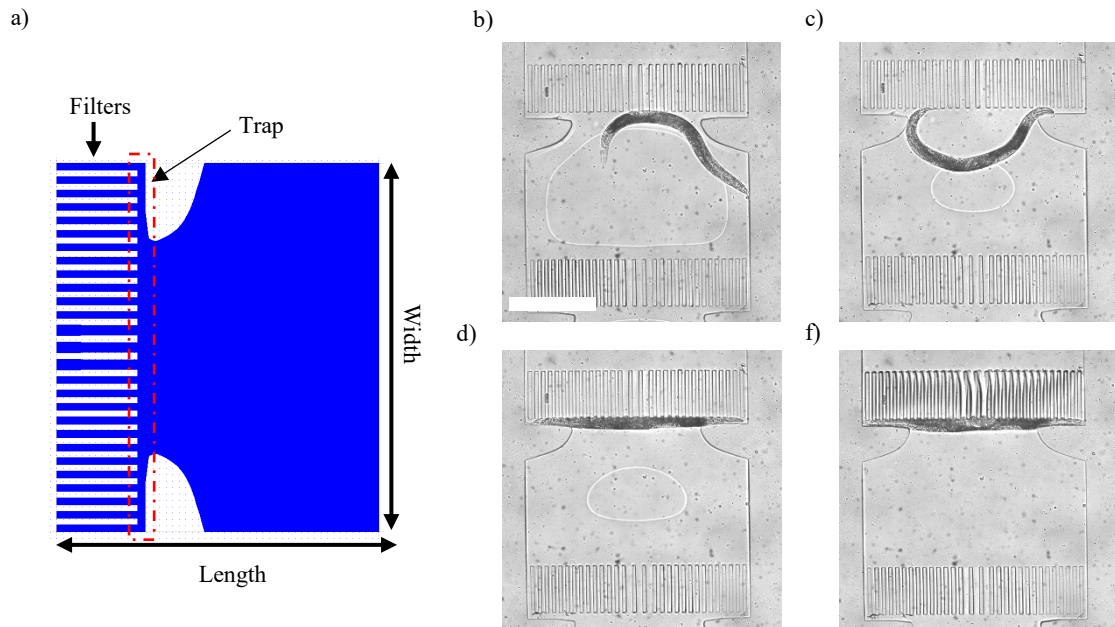


Figure 5-8-(a) Variations in the design of the chambers (filters, trap, width, length and height) to enable immobilization of the worm in the area delineated by the red dashed line. (b-f) An example of a successful sequence of worm immobilization. Scale bar = 500 μm

5.4 Conclusions

We made ambitious attempts to carry out high-resolution *in vivo* imaging of the gut bacteria in *C. elegans* worms. We fabricated microfluidic devices featuring valves for the immobilization of the worm. While it was possible to immobilize the worms sufficiently for high-resolution imaging, the lack of control over the location of immobilization prevented the automation of the imaging procedure. More importantly, the intestinal peristalsis displaces the bacteria within the intestine, which makes it impossible to acquire z-stack images which are essential for obtaining 3D representations of intestinal bacteria. These results lead us to using fixation as an immobilization method to study the intestinal bacteria, as seen in chapters 3 and 4.

6 Studying symmetry breaking in one-cell stage C. elegans embryos using PDMS microwell arrays

Symmetry breaking as a fundamental feature of living systems has been extensively studied using *C. elegans* embryos. These studies are typically based on time-lapse z-stack fluorescence imaging of one-cell stage embryos that are placed horizontally on agarose pads. As symmetry breaking starts at the future posterior pole of the embryo, it is preferred to image the embryos vertically from the future posterior pole. Therefore, we fabricated PDMS microwells with different dimensions and shapes and evaluated their suitability for the vertical placement of the embryos and imaging of symmetry breaking from the posterior pole. While cylindrical microwells with a depth of 50 μm and diameters ranging from 34-36 μm seemed to be more suited, overall, we found that it is not possible to reliably place the embryos inside the microwell at a vertical orientation. An alternative approach worth considering is to image the embryos horizontally and develop an image analysis framework or use currently available image analysis software to visualize and study the symmetry breaking and polarity establishment from the posterior pole.

This mini chapter is based on a collaborative work with the lab of Prof. Pierre Gönczy. The project involved, Ella Muller (E.M.) (from the lab of Prof. Gönczy), **Farzad Rezaeianaran (F.R.)**, Pierre Gönczy (P.G.) and Martin A. M. Gijis (M.G.). The contribution of each individual is as follows:

P.G. and M.G. conceptualized the research project. **F.R.** designed and fabricated the PDMS microwell arrays. E.M. designed and performed the experiments and carried out the image analysis. E.M., **F.R.**, P.G. and M.G. performed the formal analysis. **F.R.** wrote the original draft of the mini chapter. E.M. and M.G. reviewed and edited the original draft.

6.1 Introduction

One mechanism by which cells acquire different fates during their development is asymmetric division [133]. Early *C. elegans* embryos undergo five asymmetric divisions, which results in the generation of six founder cells whose descendants afterwards produce specific cell types. It is also during these divisions that three body axes, namely, the anterior-posterior (AP) axis, the dorso-ventral-axis (DV) and left-right (LR) axis are formed in the order they were mentioned [133]. The formation of the AP axis takes place in the one-cell stage embryo and involves three stages, namely, symmetry breaking, establishment of AP polarity and maintenance of this polarity [134]. Symmetry breaking is a fundamental aspect of any living organism, and as such has been extensively studied using *C. elegans* embryos [134]. However, the underlying physical and molecular mechanisms required for the symmetry breaking to occur in a coordinated manner are not still fully understood.

Based on the current understanding of symmetry breaking in one-cell stage *C. elegans* embryos, centrosomes provided by the sperm are essential for symmetry breaking which leads to cortical flows and asymmetric distribution of partitioning-defective PAR proteins [135]. Fertilization occurs with the fusion of a mature oocyte and sperm cell combine and then the resulting zygote completes female meiosis. By the end of the meiosis II, PAR-3 and PAR-6 proteins and the atypical protein kinase PKC-3 (collectively referred to as the anterior PAR complex) are enriched in the cortex while PAR-2 and PAR-1 proteins (also known as posterior PAR proteins) are uniformly cytoplasmic (Figure 6-1a) [136]. Meanwhile, the maternal nucleus and the paternal nucleus and the pair of centrosomes donated by the sperm occupy opposing poles of the embryo. At the same time, the entire actomyosin network in the cell cortex is under uniform contraction which requires the activity of the non-muscle myosin II heavy chain (NMY-2) (Figure 6-1a) and the associated non-muscle myosin light chain 4 MLC-4 [136], [137]. The activity of NMY-2 itself is regulated positively by the activity of Rho family GTPase RHO-1 (Figure 6-1a) and the Rho-binding kinase LET-502 [138]–[140]. At this point, the symmetry breaking event can be initiated through two partially redundant pathways [136], [141]: (i) anterior-directed cortical flows caused by the local interruption of the contractility in the actomyosin, and (ii) PAR-2 dependant pathway. In what follows we will focus on the first pathway.

The centrosomes carry a cue (the protein AIR-1) that triggers a local relaxation in the nearby actomyosin cortex at the paternal pole [135], [141]. The local cessation of the cortical contractions involves the local inactivation of RHO-1 (and thus in turn NMY-2, Figure 6-1b) whose activity is positively regulated by guanine-nucleotide-exchange factors (GEFs) [139]. Indeed, the RHO-1 GEF ECT-2 has a uniform distribution throughout cortex before symmetry breaking but is absent locally from the newly non-contractile cortex located in the vicinity of the approaching centrosomes [139], [140]. The pole at which the cortical weakening has occurred is referred to as the posterior while the opposite pole is referred to as the anterior. The cortical weakening at the posterior leads to an anterior-directed cortical flow that transports PAR-3, PAR-6, and PKC-3, initially enriched throughout the cortex, towards the anterior side (Figure 6-1b and c) [142] which is why these PAR proteins referred to as the anterior PAR complex. At the same time, PAR-1 and PAR-2, initially present in the

cytoplasm, are loaded on the posterior cortex, the latter of which inhibits the accumulation of NMY-2 in the posterior pole [142], [143] and as a result they are referred to as the posterior PAR proteins (Figure 6-1b and c). The established polarization is afterwards maintained through the antagonistic interactions of the posterior and anterior domains [134].

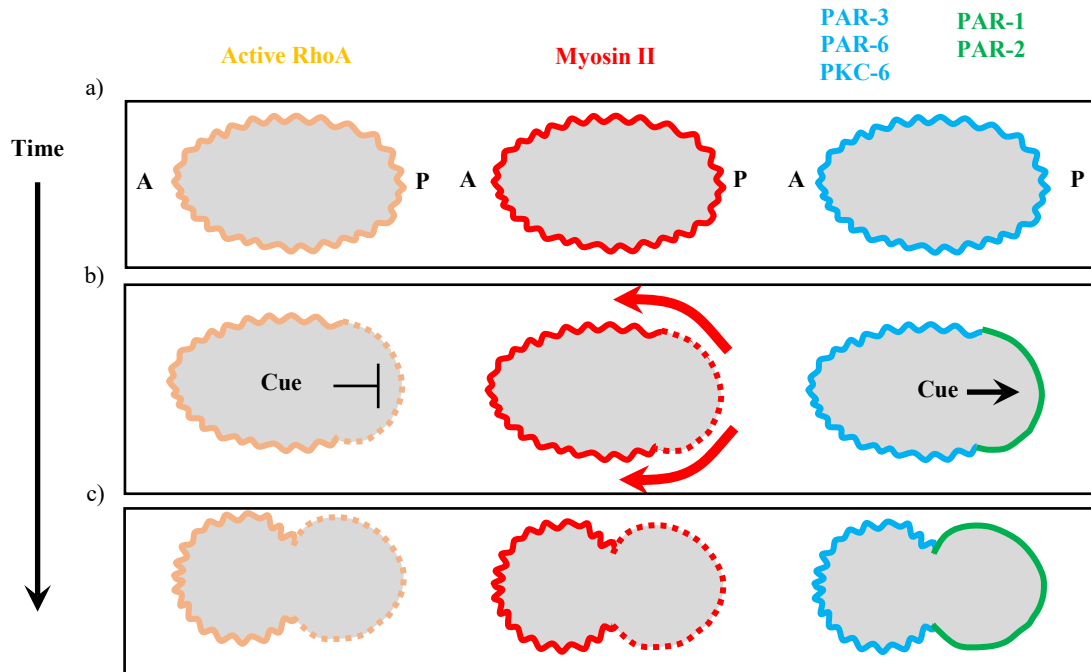


Figure 6-1- Establishment of polarization in one-cell stage *C. elegans* embryo. Anterior (A) and Posterior (P) poles are on the left and right side of the embryo, respectively. (a) Initially, active RhoA, Myosin II and anterior PAR complex are enriched on the cortex, while the posterior PAR proteins are present uniformly throughout the cytoplasm (not shown). (b) and (c) During polarity establishment, the sperm-derived centrosomes locally inhibit the activity of RhoA in the posterior pole which results in the anterior-directed actomyosin flows. These flows lead to the presence of anterior PAR complex on the posterior pole of the embryo and at the same time, the posterior PAR proteins are loaded on the posterior pole.

Symmetry breaking and polarization studies typically are based on time-lapse z-stack fluorescence imaging of early embryos that are laid horizontally on agarose pads. As we saw earlier, symmetry breaking starts at the posterior pole and therefore it is preferable to image the early embryos vertically from that pole (Figure 6-2). This allows us to better monitor the spatiotemporal relationship between cortical activity, PAR-2 loading onto the posterior cortex and the centrosomes positions during symmetry breaking event under different conditions. Therefore, we have fabricated PDMS microwells with different diameters, depths and spacings and evaluated their suitability for vertical imaging of symmetry breaking. In particular, using the PDMS microwells, we attempted to investigate the pattern of actomyosin relaxation during symmetry breaking and the formation of PAR-2 domain with respect to the onset of actomyosin flows.

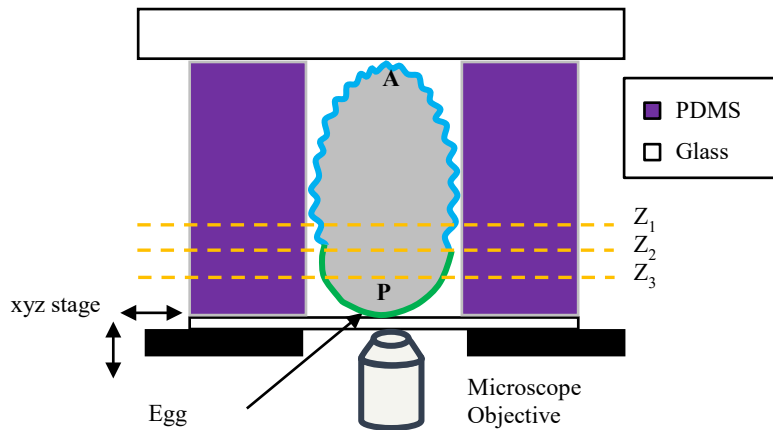


Figure 6-2- Z-stack time-lapse imaging of symmetry breaking and polarization from the posterior pole.

6.2 Materials and methods

6.2.1 Materials and chemicals

4 inch 550 μm Si wafers, 5-inch Chromium/soda–lime glass masks, polydimethylsiloxane (PDMS) Sylgard 184 (Dow®) and trimethylchlorosilane (TMCS) (Sigma-Aldrich) were obtained from the Center of MicroNanoTechnology (CMi) at EPFL (Lausanne, Switzerland). Kayaku Advanced Materials (KAM) SU-8 3050 was purchased from Micro Resist Technology GmbH (Berlin, Germany). 25 x 75 x 1 mm (with ground edges 45°) glass slides were acquired from DWK Life Sciences. Cover glasses measuring 22 x 40 mm x 170 μm were purchased from VWR.

To extract the embryos for *ex utero* imaging, gravid hermaphrodites were dissected in the osmotically balanced buffer Shelton's growth medium [144] prepared as follows: 1 ml of 5 mg ml⁻¹ inulin (acquired from Sigma-Aldrich), 50 mg of Polyvinylpyrrolidone (obtained from Sigma-Aldrich), 100 μl of 100x BME Vitamin (bought from Chemie Brunschwig AG), 100 μl of chemically defined lipid concentrate (acquired from) and 100 μl of 10mg ml⁻¹ Penicillin-Streptomycin (obtained from BioConcept AG) were added to 9 ml of Schneider's *Drosophila* medium (bought from Gibco). The resulting solution was then mixed with heat-inactivated fetal bovine serum (acquired from Gibco) with a volume to volume ratio of 65/35.

6.2.2 Worm strains

The *C. elegans* strain used for the experiments expressed endogenously tagged GFP::PAR-2, GFP::SAS-7 and RFP::NMY-2 (GZ: 1476). Exact genotype of the strain is as follows: *nmy-2(ges6(nmy-2::RFP-T+unc-119(+)))I; par-2(it328[gfp::par-2]) sas-7(or1940[gfp::sas-7])III*. Nematodes were maintained on *E. coli* OP50 bacteria at 20–24°C according to standard protocols [123].

6.2.3 Design and fabrication of the PDMS microwells

We designed a number of microwells with different shapes, diameters, depth and spacings in Clewin 4.0 (WieWeb software, Hengelo, The Netherlands). The simplest design consists of an array of cylindrical microwells (Figure 6-3a). We envisaged that the lack of an outlet for the buffer solution might prevent/impede the entry of the embryos into the microwells. As a result, we also prepared variations that had two or four outlets (Figure 6-3b and c). The outlets were made as narrow as possible (8 μm and 5 μm wide in Figure 6-3b and c, respectively) to prevent the deformation of the embryos into the outlets but not too narrow to avoid fabrication issues. Microwells with different spacings (10, 15 and 20 μm) were included in the designs to facilitate the placement of the embryos within the microwells. Lastly, for each design (microwell shape and spacing), different microwell diameters (30, 32, 34 and 36 μm) and depths (45 μm and 50 μm) were considered. All the design variations mentioned above (except the depth which is determined by the thickness of spin-coated SU-8 layer) could be fit into a single 5-inch mask. We thus transferred the designed layout through standard mask fabrication processes to a chromium/soda-lime glass mask.

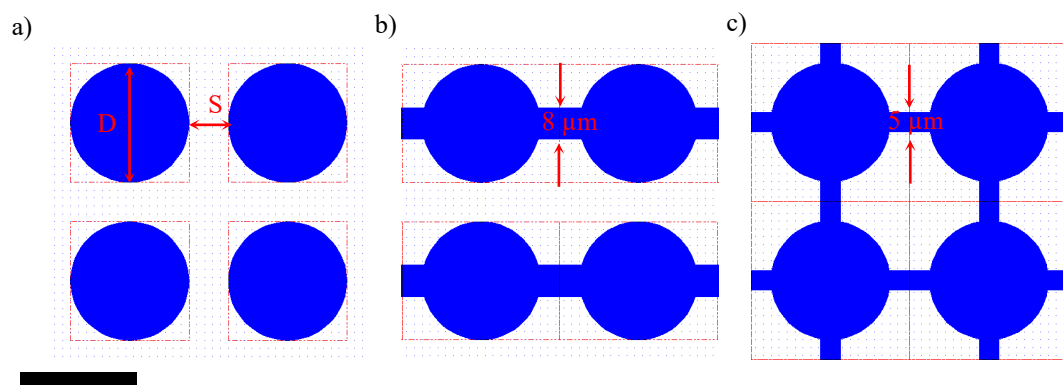


Figure 6-3- Design of the PDMS microwells. An array of cylindrical (a) microwells, (b) microwells with two outlets and (c) microwells with four outlets. D and S represent the diameters of the circular cross-section and the distance (spacing) between the microwells, respectively.

Afterwards, we used the mask in standard soft photolithography processes to fabricate two SU-8 molds with thicknesses of 45 and 50 μm on a Si wafer. The SU-8 molds were treated with TMCS to ease the separation of the PDMS from the mold. PDMS with base-to-curing agent ratio of 10:1 was cast onto the mold and cured for 2 hours at 80 $^{\circ}\text{C}$ inside an oven. Once the PDMS cured and cooled down, it was cut, according to the designed layout to 9 blocks (2.3 x 2.3 cm). Lastly, the resulting PDMS blocks were removed from the mold and were bonded on the reverse side (i.e. the flat side lacking any features), using oxygen plasma surface activation, to glass slides measuring 25 x 75 x 1 mm.

6.2.4 Evaluating the different PDMS microwell designs and the live imaging of symmetry breaking

Gravid hermaphrodites were dissected in the osmotically balanced buffer Shelton's growth medium to extract embryos. The extracted embryos were then transferred to the PDMS microwell using a mouth pipette. Afterwards, a cover slip was carefully placed on top of the PDMS microwells to push the embryos inside in the wells. When necessary, light pressure was manually applied to the cover slip to force embryos into the well.

The placement of the embryos in the PDMS microwells with different designs was evaluated through z-stack brightfield imaging using an inverted widefield microscope (Nikon Eclipse Ti-U) equipped with a 60x CFI Plan Apochromat Lambda/NA 1.4 objective and Andor Zyla 4.2 sCMOS camera. The height of the embryos in the PDMS devices were roughly estimated by identifying the z-range between the upper and lower focal planes. A binning of 2, light source power of 1% and exposure time of 50 ms were used for imaging.

Symmetry breaking was observed by time-lapse z-stack imaging in the brightfield, RFP and GFP channels using a spinning disk microscope (Visitron Spinning Disk CSU W1) equipped with an Olympus U PLAN S APO 60X/1.42 NA oil immersion objective and an Orca Flash 4.0 sCMOS camera. A binning of 2 was used for the brightfield and the fluorescent images. The time interval (between the images) was set to 14 s. The range of z-stacks and the step sizes were varied between 20-40 μm and 0.7-1 μm , respectively, to account for the difference in the orientation of eggs inside the microwells. For brightfield imaging, the LED power was set to 2.0 and an exposure time of 5 ms used. Fluorescence imaging in the GFP channel was carried out using a laser operating at 488 nm and set to 30% power with an exposure time of 300 ms. Fluorescent images in the RFP channel were acquired using a laser operating at 561 nm and set to 60% power with an exposure time of 150 ms.

The resulting images were analyzed using ImageJ. Brightness and contrast were adjusted using the inbuilt "auto" function to achieve an optimized visualization.

6.3 Results and discussions

Figure 6-4 shows the placement of the embryos within a number of PDMS microwells with different shapes and dimensions. To better evaluate the verticality of the placement of the embryos inside the microwells, the (optical) focus in Figure 6-4a-e, was on the top of the microwell. If an embryo is inserted perfectly vertical in the microwell, the center of the circular cross-section of the embryo coincides with the center of the microwell. We observed that changing the diameter of the microwells does not significantly affect the ease with which the embryos can be inserted into the microwells nor does it greatly affect their verticality (Figure 6-4a-d) as in all cases the embryos deviated from the vertical orientation. However, we still preferred to use microwells with larger diameters (34 – 36 μm) as the embryos could be inserted in those microwells slightly easier. The spacing between the

microwells also did not seem to affect the insertion of the embryos. In cases where embryos do not fall directly in the PDMS well, a gentle pressure is applied to the cover slip which forces the embryos to enter the closest microwell.

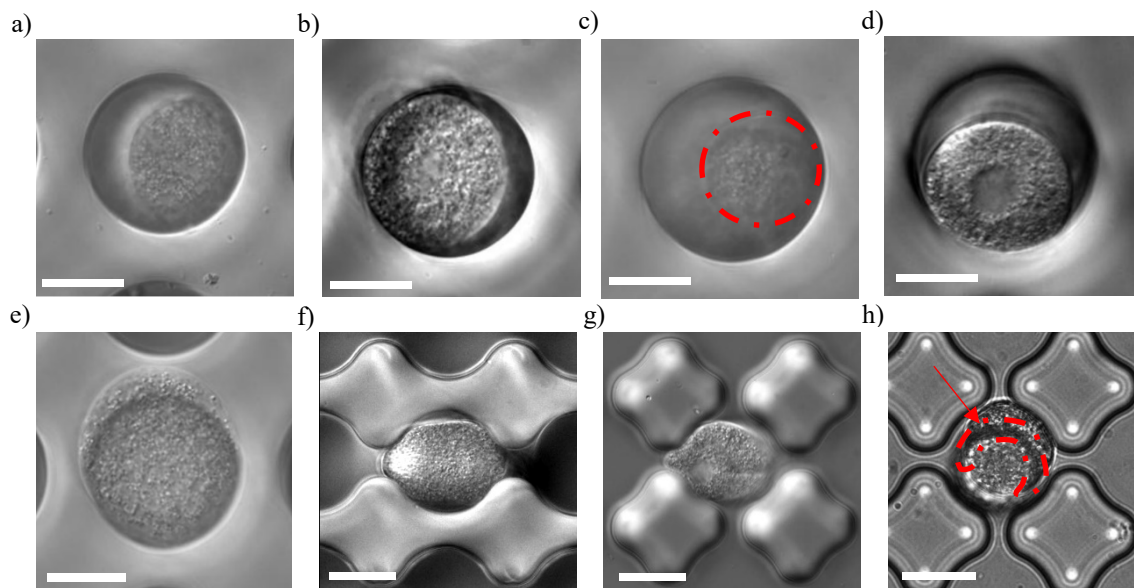


Figure 6-4- Screening of the PDMS microwells for the vertical placement of the embryos. Microwells with a depth of 50 μm and radii of (a) 30, (b) 32, (c) 34 and (d) 36 μm . The marked area in (c) highlights a region near the pole of the embryo. (e) A microwell with a depth of 45 μm in which one pole of the embryo is sticking out. In a-e, the topside of the well (near the coverslip) is in focus which enables the qualitative evaluation of the verticality of embryo placement. Microwells with (f) two and (g) four outlets. In f and g, the midsection of the embryo is in focus to better visualize the deformation of the embryos near the outlets. (h) Contortion (marked by the dashed line) in an embryo placed inside a microwell with four outlets. Scalebar: a-e, 15 μm and f-h, 20 μm .

Compared with microwells with the depth of 50 μm (Figure 6-4a-d), the microwells with the depth of 45 μm (Figure 6-4e) seemed to lead to more cases in which the embryos were either deformed or squeezed and thus we used the 50 μm deep microwells for vertical imaging. However, even with the 50 μm deep microwells, part of the embryo often sticks out of the microwell. The microwells with two or four outlets (Figure 6-4f and g, respectively) were not suitable as the embryos tended to deform and partially fill the outlets. Nonetheless, embryos seemed to fall inside the microwells with 4 outlets more easily compared to those lacking outlets. However, there were cases in which the viability of the embryos placed inside the microwells were compromised which seemed to be due to the compression-induced constriction effects on the cell (Figure 6-4h). We also investigated whether increasing the hydrophilicity of the surface of the PDMS microwells through oxygen plasma treatment [145] has an effect on the vertical placement of the eggs inside the microwells. We discovered that the wettability of the PDMS surface has no significant effect on the verticality of the inserted embryos. Overall, we found that it is very hard to control the orientation with which the embryos fall into the microwells. The embryos seem to be always somewhat tilted and often with part of them sticking out of the microwells.

Despite the observed shortcomings, we attempted to monitor the symmetry breaking process by z-stack time-lapse imaging of one-cell stage embryos placed in the PDMS microwells. Figure 6-5 shows the cortical activity (by monitoring RFP-tagged NMY-2) and the location of the centrosomes and PAR-

2 proteins (both tagged using a GFP label) at different time points around symmetry breaking. Initially ($t= 0^m 00^s$ and $2^m 48^s$ in Figure 6-5), the cortex should be uniformly contractile. As a result, based on our current understanding, we speculate that if an embryo is placed completely vertical, the signal originating from the RFP-tagged NMY-2 should resemble a ring that expands as we observe the z-planes that are further away from the posterior pole.

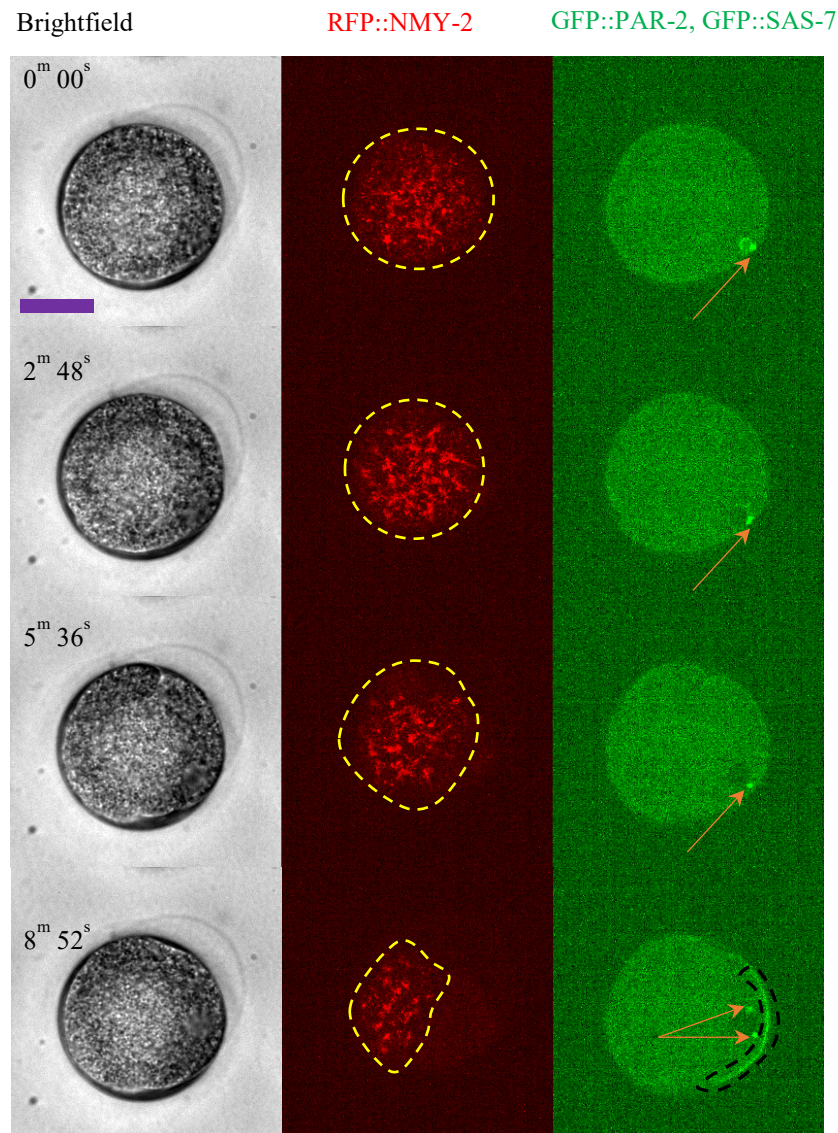


Figure 6-5-Time-lapse z-stack brightfield and fluorescence imaging of symmetry breaking and polarity establishment in a single-cell stage embryo placed inside a PDMS microwell. NMY-2, the activity of which is necessary for the contractility in the actomyosin network, is tagged with an RFP label while the PAR-2 protein and the centrosomes are tagged with a GFP label. To represent the fluorescent images in the RFP and in the GFP channels, a single plane with the best signal for each respective channel was chosen from the z-stack images. The yellow dashed lines delineate NMY-2. The orange arrows point at the centrosomes. The black dashed line delineates PAR-2 proteins. The local cessation in the contractility of the actomyosin network, and the loading of PAR-2 proteins on the cortex and in the vicinity of the centrosomes can be observed at $8^m 52^s$ which indicate that the symmetry breaking process has occurred. The actomyosin network-derived signal appearing as a circular area at $0^m 00^s$ and $2^m 48^s$, and the loading of PAR-2 proteins and the presence of centrosomes on the rightmost side of the embryo at $8^m 52^s$ indicate that the embryo is squeezed by the coverslip and is sitting inside the microwell with a tilted orientation. Scale bar (in purple) = $15\ \mu\text{m}$.

Instead, we observe that the fluorescence signal originating from RFP-tagged NMY-2 appears in a circular area (as shown by the yellow circles at $t= 0^m 00^s$ and $2^m 48^s$ in Figure 6-5) which indicates that

the embryo significantly deviates from the vertical orientation and is perhaps being squeezed by the cover slip. Despite sitting tilted in the microwell, the embryo does go through symmetry breaking and polarity establishment ($t = 5^m 36^s$ and $8^m 52^s$ in Figure 6-5). The NMY-2-derived fluorescence signal (delineated by the yellow dashed lines) starts to disappear from the right side ($5^m 36^s$) and afterwards is only present at the left side ($8^m 52^s$) which indicates a cortical flow from right to left, as opposed to a flow directed towards the anterior pole, going inside the plane, that could have been inferred from observing an embryo that is placed vertically (such flow could be deduced from observing the cortical activity across different z-planes at different time points after symmetry breaking). In agreement with the embryo being tilted, we also observe that the centrosomes (highlighted by the orange arrows) and the PAR-2 proteins (delineated by the black dashed line) are present on the rightmost side of the embryo at $8^m 52^s$. If the embryo was placed completely vertical, based on our speculations, the centrosomes should have appeared more or less close to the center while the PAR-2 proteins should have resembled rings whose centers coincide with the location of the centrosomes. Overall, these observations show that the embryos are squeezed by the coverslips and fall into the microwells with a tilted orientation (Figure 6-6b), instead of being placed in the microwells with a vertical orientation and without being deformed (Figure 6-6a).

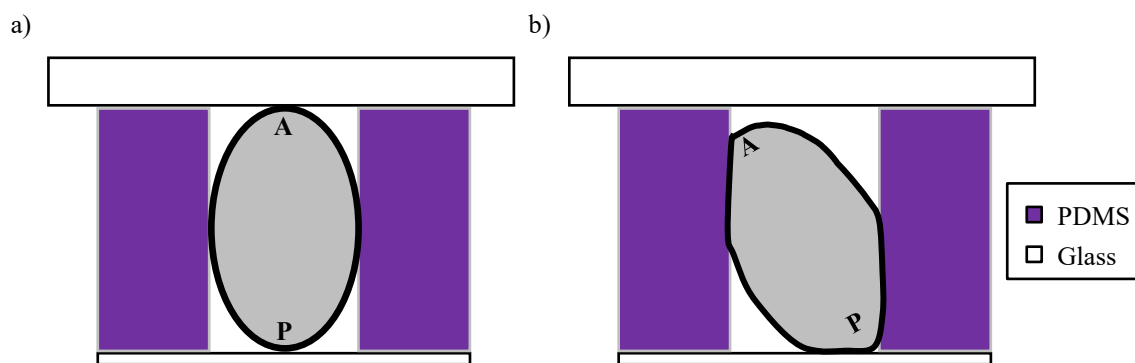


Figure 6-6- The placement of embryos inside the PDMS microwells. (a) An ideally placed embryo has a vertical orientation and does not experience any deformations. (b) In practice, the embryo is squeezed by the coverslip and has a tilted orientation.

6.4 Conclusions

We designed a number PDMS microwells with different shapes and dimensions to enable vertical imaging of symmetry breaking and polarity establishment in one-cell stage embryos from the future posterior pole. While the simple (lacking outlets) 50 μm deep microwells with the diameters of 34-36 μm appeared to be more suitable, overall, we found it very challenging to consistently place the embryos vertically inside the microwells. The embryos often deviated considerably from the ideal vertical orientation and could not be fully inserted in the microwells. An alternative avenue worth exploring is to acquire time-lapse z-stack fluorescent images from horizontally-placed embryos but instead develop image analysis pipelines or utilize the image analysis software available such as IMARIS to reconstruct the acquired images into either 2D images in the plane perpendicular to the AP

axis or 3D images. These reconstructed images can be then analyzed to study symmetry breaking and polarization establishment from the posterior pole, albeit at the cost of spatial resolution.

7 Conclusion and future perspectives

7.1 Achieved results

In this thesis, we developed, for the first time, a semi-automated framework for on-chip high-resolution imaging and analysis of intestinal bacteria in *C. elegans* worms. After being loaded on the chip, the worms are first immobilized via fixation and are subsequently imaged using a spinning disk confocal microscope (SDCM) equipped with an objective with high magnification and numerical aperture. The acquired high-resolution z-stack fluorescent images of the intestinal bacteria are then passed to IMARIS software for visualization and analyzing. The IMARIS software uses the raw z-stack images to construct a 3D image which represents the bacterial load in the intestine of the worm. By carefully adjusting the parameters of the built-in spot detection algorithm, the volumes and the intensities of the intestinal bacterial spots can be obtained. Finally, the distribution of the volumes and the intensities of bacterial spots of either an individual worm or the worm population of interest can be visualized using bivariate histograms.

We used our framework to monitor the intestinal bacterial load in worms that had fed on fluorescent *E. coli* OP50 during early adulthood. We found that the bacterial load in the hindgut generally increases with age, in agreement with previously reported studies. We also discovered that there can be considerable intrapopulation variations in the intestinal bacterial load of groups of worms that have fed on fluorescent bacteria for the same duration. This observation highlights the importance of single-worm resolution analysis, as the averaging of intestinal bacterial load, commonly done in conventional bacterial colonization assays, can potentially lead to inaccurate conclusions.

We also used our framework to investigate bacterial food digestion and accumulation in adult worms that had fed on either non-pathogenic fluorescent *E. coli* OP50 or pathogenic fluorescent *P. aeruginosa* PAO1 during early adulthood. We discovered that the pattern of the bacteria-derived fluorescence signal in fluorescent *E. coli* OP50-fed worms took the form of individual fluorescent spots that originated from intact (fluorescent *E. coli* OP50) bacteria. However, in the case of fluorescent *P. aeruginosa* PAO1-fed worms, the fluorescent signal appears as individual fluorescent spots (originating from intact fluorescent *P. aeruginosa* PAO1) dispersed in large regions of diffuse fluorescence, which are thought to originate from disrupted (fluorescent *P. aeruginosa* PAO1) bacteria. Furthermore, we also observed that, with both bacterial diets, the intestinal bacterial load generally increases with the age of the worms, while the rate of increase is faster in fluorescent *P. aeruginosa* PAO1-fed worms. These observations, when considered in the context of previous studies, hint at a reduced metabolism in worms fed fluorescent *P. aeruginosa* PAO1.

We also attempted to replicate the imaging and analysis above *in vivo* by using a microfluidic device that can immobilize the worm reversibly. We designed and fabricated a number of microfluidic devices, all of which utilized valves to enable the reversible immobilization of worms. While we succeeded in immobilizing the worms sufficiently for high-resolution imaging of intestinal bacteria, we

encountered challenges in reliably controlling their positions during immobilization, which is crucial for automating the imaging process. Moreover, the movement of bacteria within the intestinal lumen due to intestinal peristalsis made it impossible to acquire z-stack fluorescent images which are necessary for obtaining 3D representations of intestinal bacteria. Consequently, automated *in vivo* high-resolution z-stack fluorescence imaging of intestinal bacteria proved to be unattainable under these circumstances.

Lastly, we created several PDMS microwells with varying shapes and dimensions to enable the vertical placement of one-cell stage embryos and thus enable the time-lapse imaging of symmetry breaking and polarization establishment from the future posterior pole. Although the 50 μm deep microwells with diameters of 34-36 μm , which lacked outlets, seemed more suitable, we faced significant challenges in consistently placing the embryos vertically inside the microwells. The embryos frequently deviated from the desired vertical orientation and could not be fully inserted into the microwells.

7.2 Future perspectives

In this thesis, we developed a framework for high-resolution imaging and analysis of intestinal bacteria in *C. elegans*. We demonstrated the potential of our framework by characterizing the bacterial load of worms fed fluorescent *E. coli* OP50 during early adulthood in terms of the distribution of the intensities and the volumes of the bacteria-derived fluorescent spots. We also used our platform to study the digestion and accumulation of bacteria in worms fed with either a non-pathogenic fluorescent *E. coli* OP50 or pathogenic fluorescent *P. aeruginosa* PAO1. However, the capabilities of our framework were not fully exploited in our simple microfluidic chip. As the worms are immobilized via fixation in our framework, there are no specific restrictions for designing more sophisticated microfluidic devices. The imaging process can be automated by including tapered channels that help to straighten the worms and immobilize them (via fixation) in pre-defined locations. Moreover, we can benefit from designs that enable high-throughput screening and phenotyping of large worm populations with different conditions [77], [79]. This can be particularly useful considering that the fixation of the worm prevents the long-term monitoring of single worms. This shortcoming can be somewhat compensated by subjecting worm populations to the same conditions and acquire images at different time points in selected groups. For example, 200 adult worms are divided to 10 groups of 20 adult worms that are fed fluorescent *P. aeruginosa* PAO1 but are imaged at different time points (e.g., 2, 4, 6 and etc. hours of feeding).

In future works, we can use our framework together with more sophisticated microfluidic devices to shed light on how bacteria establish and maintain colonies in the intestine; We can identify if there are regions within the intestine where the bacteria prefer to establish colonies there. In cases where the worm is fed a mixture of bacteria (competition assays), how and if each bacterium establishes colonies in the intestine? How do these colonies interact with each other? In the case of a shifting assay, how the introduced bacterium interacts with the colonies consisting of founder bacteria. In

particular, we can investigate how pre-conditioning of the worm with probiotic bacteria affects the intestinal colonization by pathogenic bacteria. It is also possible to monitor the effect of antibiotic treatment on the probiotic and pathogenic bacteria present in the intestine.

More ambitiously, there is a lack of devices that allow lifelong high-resolution studies on host-microbiota interactions. One source of complication for these types of studies is the increase in the diameter of the worms as they grow from the young adult stage ($\sim 50 \mu\text{m}$) to adults ($80 \mu\text{m}$). As a result, devices that rely on traps for immobilization, such as the device reported by Viri et al [98], cannot enable studies that cover the entire adulthood. A less elegant solution would be to fabricate devices with different trap geometries that adapt to different stages of adulthood. Incidentally, in the case of device by Viri et al [98], the worms are not completely immobilized and perhaps the addition of a membrane can improve the immobilization and thus the imaging resolution. A more elegant solution would be to utilize microfluidic devices inspired by the work of Keil et al [85] and overcome the lack of control over the location of the immobilization via object detection. In this framework, initially a brightfield image at a low magnification is acquired and then processed to detect the outline of the worm and its location. Afterwards, the coordinates of the worm can be passed on to the microscope stage so that high-resolution images of the region of interest can be acquired.

Bibliography

- [1] K. V. Christensen, M. G. Morch, T. H. Morthorst, S. Lykkemark, and A. Olsen, "Microbiota, Probiotic Bacteria and Ageing," in *Ageing: Lessons from C. elegans*, A. Olsen and M. S. Gill, Eds., Cham: Springer International Publishing, 2017, pp. 411–429. doi: 10.1007/978-3-319-44703-2_18.
- [2] P. Dirksen *et al.*, "The native microbiome of the nematode *Caenorhabditis elegans*: gateway to a new host-microbiome model," *BMC Biology*, vol. 14, no. 1, Dec. 2016, doi: 10.1186/s12915-016-0258-1.
- [3] S. K. Mazmanian, C. H. Liu, A. O. Tzianabos, and D. L. Kasper, "An Immunomodulatory Molecule of Symbiotic Bacteria Directs Maturation of the Host Immune System," *Cell*, vol. 122, no. 1, pp. 107–118, Jul. 2005, doi: 10.1016/j.cell.2005.05.007.
- [4] J. K. Nicholson *et al.*, "Host-Gut Microbiota Metabolic Interactions," *Science*, vol. 336, no. 6086, pp. 1262–1267, Jun. 2012, doi: 10.1126/science.1223813.
- [5] C. G. Buffie and E. G. Pamer, "Microbiota-mediated colonization resistance against intestinal pathogens," *Nat Rev Immunol*, vol. 13, no. 11, Art. no. 11, Nov. 2013, doi: 10.1038/nri3535.
- [6] H. Tilg and A. R. Moschen, "Microbiota and diabetes: an evolving relationship," *Gut*, vol. 63, no. 9, pp. 1513–1521, Sep. 2014, doi: 10.1136/gutjnl-2014-306928.
- [7] M. Million, J.-C. Lagier, D. Yahav, and M. Paul, "Gut bacterial microbiota and obesity," *Clin Microbiol Infect*, vol. 19, no. 4, pp. 305–313, Apr. 2013, doi: 10.1111/1469-0691.12172.
- [8] F. Cabreiro and D. Gems, "Worms need microbes too: microbiota, health and aging in *Caenorhabditis elegans*: The *C. elegans* -microbe holobiont," *EMBO Molecular Medicine*, vol. 5, no. 9, pp. 1300–1310, Sep. 2013, doi: 10.1002/emmm.201100972.
- [9] L. H. Morais, H. L. Schreiber, and S. K. Mazmanian, "The gut microbiota–brain axis in behaviour and brain disorders," *Nat Rev Microbiol*, vol. 19, no. 4, Art. no. 4, Apr. 2021, doi: 10.1038/s41579-020-00460-0.
- [10] P. Bercik, S. M. Collins, and E. F. Verdu, "Microbes and the gut-brain axis," *Neurogastroenterology & Motility*, vol. 24, no. 5, pp. 405–413, 2012, doi: 10.1111/j.1365-2982.2012.01906.x.
- [11] Y. Wang and L. H. Kasper, "The role of microbiome in central nervous system disorders," *Brain, behavior, and immunity*, vol. 38, pp. 1–12, 2014.
- [12] P. W. O'Toole and I. B. Jeffery, "Gut microbiota and aging," *Science*, vol. 350, no. 6265, pp. 1214–1215, Dec. 2015, doi: 10.1126/science.aac8469.
- [13] M. J. Claesson *et al.*, "Gut microbiota composition correlates with diet and health in the elderly," *Nature*, vol. 488, no. 7410, pp. 178–184, Aug. 2012, doi: 10.1038/nature11319.
- [14] J. Zhang, A. D. Holdorf, and A. J. Walkout, "*C. elegans* and its bacterial diet as a model for systems-level understanding of host–microbiota interactions," *Current Opinion in Biotechnology*, vol. 46, pp. 74–80, Aug. 2017, doi: 10.1016/j.copbio.2017.01.008.
- [15] D. D. Shaye and I. Greenwald, "OrthoList: A Compendium of *C. elegans* Genes with Human Orthologs," *PLoS One*, vol. 6, no. 5, May 2011, doi: 10.1371/journal.pone.0020085.
- [16] L. S. Yilmaz and A. J. M. Walkout, "Worms, bacteria and micronutrients: an elegant model of our diet," *Trends Genet*, vol. 30, no. 11, pp. 496–503, Nov. 2014, doi: 10.1016/j.tig.2014.07.010.

- [17] C. D. Sifri, J. Begun, and F. M. Ausubel, "The worm has turned – microbial virulence modeled in *Caenorhabditis elegans*," *Trends in Microbiology*, vol. 13, no. 3, pp. 119–127, Mar. 2005, doi: 10.1016/j.tim.2005.01.003.
- [18] F. Zhang *et al.*, "Caenorhabditis elegans as a Model for Microbiome Research," *Frontiers in Microbiology*, vol. 8, Mar. 2017, doi: 10.3389/fmicb.2017.00485.
- [19] A. Kumar, A. Baruah, M. Tomioka, Y. Iino, M. C. Kalita, and M. Khan, "Caenorhabditis elegans: a model to understand host–microbe interactions," *Cell. Mol. Life Sci.*, vol. 77, no. 7, pp. 1229–1249, Apr. 2020, doi: 10.1007/s00018-019-03319-7.
- [20] S. Brenner, "The genetics of *Caenorhabditis elegans*," *Genetics*, vol. 77, no. 1, pp. 71–94, 1974.
- [21] J. Li and W. Le, "Modeling neurodegenerative diseases in *Caenorhabditis elegans*," *Experimental Neurology*, vol. 250, pp. 94–103, Dec. 2013, doi: 10.1016/j.expneurol.2013.09.024.
- [22] A. K. Corsi, B. Wightman, and M. Chalfie, "A Transparent Window into Biology: A Primer on *Caenorhabditis elegans*," *Genetics*, vol. 200, no. 2, pp. 387–407, Jun. 2015, doi: 10.1534/genetics.115.176099.
- [23] B. Leung, G. J. Hermann, and J. R. Priess, "Organogenesis of the *Caenorhabditis elegans* intestine," *Dev Biol*, vol. 216, no. 1, pp. 114–134, Dec. 1999, doi: 10.1006/dbio.1999.9471.
- [24] E. R. Troemel, M.-A. Félix, N. K. Whiteman, A. Barrière, and F. M. Ausubel, "Microsporidia are natural intracellular parasites of the nematode *Caenorhabditis elegans*," *PLoS Biol*, vol. 6, no. 12, pp. 2736–2752, Dec. 2008, doi: 10.1371/journal.pbio.0060309.
- [25] J. D. McGhee, "The *Caenorhabditis elegans* intestine," *WIREs Developmental Biology*, vol. 2, no. 3, pp. 347–367, 2013, doi: 10.1002/wdev.93.
- [26] H. Nakagawa *et al.*, "Effects and mechanisms of longevity induced by *Lactobacillus gasseri* SBT2055 in *Caenorhabditis elegans*," *Aging Cell*, vol. 15, no. 2, pp. 227–236, Apr. 2016, doi: 10.1111/acel.12431.
- [27] I. Y. Hwang *et al.*, "Engineered probiotic *Escherichia coli* can eliminate and prevent *Pseudomonas aeruginosa* gut infection in animal models," *Nat Commun*, vol. 8, no. 1, Art. no. 1, Apr. 2017, doi: 10.1038/ncomms15028.
- [28] M. R. Park *et al.*, "Probiotic *Lactobacillus fermentum* strain JDFM216 stimulates the longevity and immune response of *Caenorhabditis elegans* through a nuclear hormone receptor," *Scientific Reports*, vol. 8, no. 1, Dec. 2018, doi: 10.1038/s41598-018-25333-8.
- [29] V. Donato *et al.*, "*Bacillus subtilis* biofilm extends *Caenorhabditis elegans* longevity through downregulation of the insulin-like signalling pathway," *Nat Commun*, vol. 8, no. 1, pp. 1–15, Jan. 2017, doi: 10.1038/ncomms14332.
- [30] H. Jiang and D. Wang, "The Microbial Zoo in the *C. elegans* Intestine: Bacteria, Fungi and Viruses," *Viruses*, vol. 10, no. 2, Art. no. 2, Feb. 2018, doi: 10.3390/v10020085.
- [31] J. D. Meisel and D. H. Kim, "Behavioral avoidance of pathogenic bacteria by *Caenorhabditis elegans*," *Trends in Immunology*, vol. 35, no. 10, pp. 465–470, Oct. 2014, doi: 10.1016/j.it.2014.08.008.
- [32] C. Petersen, P. Dirksen, and H. Schulenburg, "Why we need more ecology for genetic models such as *C. elegans*," *Trends in Genetics*, vol. 31, no. 3, pp. 120–127, Mar. 2015, doi: 10.1016/j.tig.2014.12.001.
- [33] C. L. Kurz *et al.*, "Virulence factors of the human opportunistic pathogen *Serratia marcescens* identified by in vivo screening," *The EMBO Journal*, vol. 22, no. 7, pp. 1451–1460, Apr. 2003, doi: 10.1093/emboj/cdg159.

- [34] C. Portal-Celhay, E. R. Bradley, and M. J. Blaser, "Control of intestinal bacterial proliferation in regulation of lifespan in *Caenorhabditis elegans*," *BMC Microbiology*, vol. 12, no. 1, p. 49, 2012, doi: 10.1186/1471-2180-12-49.
- [35] M. D. McGee *et al.*, "Loss of intestinal nuclei and intestinal integrity in aging *C. elegans*: Intestinal changes in aging *C. elegans*," *Aging Cell*, vol. 10, no. 4, pp. 699–710, Aug. 2011, doi: 10.1111/j.1474-9726.2011.00713.x.
- [36] D. Garigan, A.-L. Hsu, A. G. Fraser, R. S. Kamath, J. Ahringer, and C. Kenyon, "Genetic Analysis of Tissue Aging in *Caenorhabditis elegans*: A Role for Heat-Shock Factor and Bacterial Proliferation," p. 12.
- [37] T. Bito, Y. Matsunaga, Y. Yabuta, T. Kawano, and F. Watanabe, "Vitamin B12 deficiency in *Caenorhabditis elegans* results in loss of fertility, extended life cycle, and reduced lifespan," *FEBS Open Bio*, vol. 3, pp. 112–117, Feb. 2013, doi: 10.1016/j.fob.2013.01.008.
- [38] B. Virk *et al.*, "Excessive folate synthesis limits lifespan in the *C. elegans*: *E. coli* aging model," *BMC Biology*, vol. 10, no. 1, p. 67, Jul. 2012, doi: 10.1186/1741-7007-10-67.
- [39] M. U. Austin, W.-S. Liao, K. Balamurugan, B. Ashokkumar, H. M. Said, and C. W. LaMunyon, "Knockout of the folate transporter *folT-1* causes germline and somatic defects in *C. elegans*," *BMC Developmental Biology*, vol. 10, no. 1, p. 46, May 2010, doi: 10.1186/1471-213X-10-46.
- [40] I. Lenaerts, G. A. Walker, L. Van Hoorebeke, D. Gems, and J. R. Vanfleteren, "Dietary restriction of *Caenorhabditis elegans* by axenic culture reflects nutritional requirement for constituents provided by metabolically active microbes," *J Gerontol A Biol Sci Med Sci*, vol. 63, no. 3, pp. 242–252, Mar. 2008, doi: 10.1093/gerona/63.3.242.
- [41] L. T. MacNeil, E. Watson, H. E. Arda, L. J. Zhu, and A. J. M. Walhout, "Diet-induced developmental acceleration independent of TOR and insulin in *C. elegans*," *Cell*, vol. 153, no. 1, pp. 240–252, Mar. 2013, doi: 10.1016/j.cell.2013.02.049.
- [42] F. Cabreiro *et al.*, "Metformin retards aging in *C. elegans* by altering microbial folate and methionine metabolism," *Cell*, vol. 153, no. 1, pp. 228–239, Mar. 2013, doi: 10.1016/j.cell.2013.02.035.
- [43] L. Avery, "The genetics of feeding in *Caenorhabditis elegans*," *Genetics*, vol. 133, no. 4, pp. 897–917, Apr. 1993, doi: 10.1093/genetics/133.4.897.
- [44] D. H. Kim, "Bacteria and the Aging and Longevity of *Caenorhabditis elegans*," *Annual Review of Genetics*, vol. 47, no. 1, pp. 233–246, Nov. 2013, doi: 10.1146/annurev-genet-111212-133352.
- [45] D. H. Kim *et al.*, "A Conserved p38 MAP Kinase Pathway in *Caenorhabditis elegans* Innate Immunity," *Science*, vol. 297, no. 5581, pp. 623–626, Jul. 2002, doi: 10.1126/science.1073759.
- [46] E. Mylonakis, F. M. Ausubel, J. R. Perfect, J. Heitman, and S. B. Calderwood, "Killing of *Caenorhabditis elegans* by *Cryptococcus neoformans* as a model of yeast pathogenesis," *Proceedings of the National Academy of Sciences*, vol. 99, no. 24, pp. 15675–15680, Nov. 2002, doi: 10.1073/pnas.232568599.
- [47] G. V. Mallo *et al.*, "Inducible antibacterial defense system in *C. elegans*," *Curr Biol*, vol. 12, no. 14, pp. 1209–1214, Jul. 2002, doi: 10.1016/s0960-9822(02)00928-4.
- [48] T. L. Gumienny and C. Savage-Dunn, "TGF- β signaling in *C. elegans*," in *WormBook: The Online Review of C. elegans Biology [Internet]*, WormBook, 2018. Accessed: May 30, 2023. [Online]. Available: <https://www.ncbi.nlm.nih.gov/books/NBK19692/>
- [49] R. Rae, H. Witte, C. Rödelsperger, and R. J. Sommer, "The importance of being regular: *Caenorhabditis elegans* and *Pristionchus pacificus* defecation mutants are hypersusceptible to

bacterial pathogens," *International Journal for Parasitology*, vol. 42, no. 8, pp. 747–753, Jul. 2012, doi: 10.1016/j.ijpara.2012.05.005.

[50] M. J. Youngman, Z. N. Rogers, and D. H. Kim, "A Decline in p38 MAPK Signaling Underlies Immunosenescence in *Caenorhabditis elegans*," *PLOS Genetics*, vol. 7, no. 5, p. e1002082, May 2011, doi: 10.1371/journal.pgen.1002082.

[51] C. Portal-Celhay and M. J. Blaser, "Competition and Resilience between Founder and Introduced Bacteria in the *Caenorhabditis elegans* Gut," *Infection and Immunity*, vol. 80, no. 3, pp. 1288–1299, Mar. 2012, doi: 10.1128/IAI.05522-11.

[52] D. A. Garsin *et al.*, "Long-Lived *C. elegans* *daf-2* Mutants Are Resistant to Bacterial Pathogens," *Science*, vol. 300, no. 5627, pp. 1921–1921, Jun. 2003, doi: 10.1126/science.1080147.

[53] C. Darby, *Interactions with microbial pathogens*. WormBook, 2005. Accessed: Dec. 29, 2019. [Online]. Available: <https://www.ncbi.nlm.nih.gov/books/NBK19779/>

[54] A. Aballay, P. Yorgey, and F. M. Ausubel, "Salmonella typhimurium proliferates and establishes a persistent infection in the intestine of *Caenorhabditis elegans*," *Current Biology*, vol. 10, no. 23, pp. 1539–1542, Nov. 2000, doi: 10.1016/S0960-9822(00)00830-7.

[55] C. D. Sifri, J. Begun, F. M. Ausubel, and S. B. Calderwood, "*Caenorhabditis elegans* as a Model Host for *Staphylococcus aureus* Pathogenesis," *Infection and Immunity*, vol. 71, no. 4, pp. 2208–2217, Apr. 2003, doi: 10.1128/IAI.71.4.2208-2217.2003.

[56] J. E. Irazoqui, E. R. Troemel, R. L. Feinbaum, L. G. Luhachack, B. O. Cezairliyan, and F. M. Ausubel, "Distinct Pathogenesis and Host Responses during Infection of *C. elegans* by *P. aeruginosa* and *S. aureus*," *PLOS Pathogens*, vol. 6, no. 7, p. e1000982, Jul. 2010, doi: 10.1371/journal.ppat.1000982.

[57] M.-W. Tan, S. Mahajan-Miklos, and F. M. Ausubel, "Killing of *Caenorhabditis elegans* by *Pseudomonas aeruginosa* used to model mammalian bacterial pathogenesis," *PNAS*, vol. 96, no. 2, pp. 715–720, Jan. 1999, doi: 10.1073/pnas.96.2.715.

[58] M.-W. Tan, L. G. Rahme, J. A. Sternberg, R. G. Tompkins, and F. M. Ausubel, "*Pseudomonas aeruginosa* killing of *Caenorhabditis elegans* used to identify *P. aeruginosa* virulence factors," *PNAS*, vol. 96, no. 5, pp. 2408–2413, Mar. 1999, doi: 10.1073/pnas.96.5.2408.

[59] L. A. Gallagher and C. Manoil, "*Pseudomonas aeruginosa* PAO1 Kills *Caenorhabditis elegans* by Cyanide Poisoning," *Journal of Bacteriology*, vol. 183, no. 21, pp. 6207–6214, Nov. 2001, doi: 10.1128/JB.183.21.6207-6214.2001.

[60] N. V. Kirienko, D. R. Kirienko, J. Larkins-Ford, C. Wählby, G. Ruvkun, and F. M. Ausubel, "*Pseudomonas aeruginosa* disrupts *Caenorhabditis elegans* iron homeostasis, causing a hypoxic response and death," *Cell Host Microbe*, vol. 13, no. 4, pp. 406–416, Apr. 2013, doi: 10.1016/j.chom.2013.03.003.

[61] B. Cezairliyan, N. Vinayavekhin, D. Grenfell-Lee, G. J. Yuen, A. Saghatelian, and F. M. Ausubel, "Identification of *Pseudomonas aeruginosa* Phenazines that Kill *Caenorhabditis elegans*," *PLOS Pathogens*, vol. 9, no. 1, p. e1003101, Jan. 2013, doi: 10.1371/journal.ppat.1003101.

[62] C.-G. Zou, Y.-C. Ma, L.-L. Dai, and K.-Q. Zhang, "Autophagy protects *C. elegans* against necrosis during *Pseudomonas aeruginosa* infection," *Proceedings of the National Academy of Sciences*, vol. 111, no. 34, pp. 12480–12485, Aug. 2014, doi: 10.1073/pnas.1405032111.

[63] C. L. Hoffman, J. Lalsiamthara, and A. Aballay, "Host Mucin Is Exploited by *Pseudomonas aeruginosa* To Provide Monosaccharides Required for a Successful Infection," *mBio*, vol. 11, no. 2, pp. e00060-20, Mar. 2020, doi: 10.1128/mBio.00060-20.

- [64] P. D. Utari and W. J. Quax, "Caenorhabditis elegans reveals novel Pseudomonas aeruginosa virulence mechanism," *Trends in Microbiology*, vol. 21, no. 7, pp. 315–316, Jul. 2013, doi: 10.1016/j.tim.2013.04.006.
- [65] C. T. O'Loughlin, L. C. Miller, A. Siryaporn, K. Drescher, M. F. Semmelhack, and B. L. Bassler, "A quorum-sensing inhibitor blocks Pseudomonas aeruginosa virulence and biofilm formation," *Proceedings of the National Academy of Sciences*, vol. 110, no. 44, pp. 17981–17986, Oct. 2013, doi: 10.1073/pnas.1316981110.
- [66] B. Vigneshkumar, S. Radhakrishnan, and K. Balamurugan, "Analysis of Pseudomonas aeruginosa PAO1 Lipid A Changes During the Interaction with Model Organism, Caenorhabditis elegans," *Lipids*, vol. 49, no. 6, pp. 555–575, Jun. 2014, doi: 10.1007/s11745-014-3898-3.
- [67] S. E. A. Christiaen, N. Matthijs, X.-H. Zhang, H. J. Nelis, P. Bossier, and T. Coenye, "Bacteria that inhibit quorum sensing decrease biofilm formation and virulence in Pseudomonas aeruginosa PAO1," *Pathogens and Disease*, vol. 70, no. 3, pp. 271–279, Apr. 2014, doi: 10.1111/2049-632X.12124.
- [68] S. Mahajan-Miklos, M.-W. Tan, L. G. Rahme, and F. M. Ausubel, "Molecular Mechanisms of Bacterial Virulence Elucidated Using a Pseudomonas aeruginosa–Caenorhabditis elegans Pathogenesis Model," *Cell*, vol. 96, no. 1, pp. 47–56, Jan. 1999, doi: 10.1016/S0092-8674(00)80958-7.
- [69] N. V. Kirienko, B. O. Cezairliyan, F. M. Ausubel, and J. R. Powell, "Pseudomonas aeruginosa PA14 Pathogenesis in Caenorhabditis elegans," in *Pseudomonas Methods and Protocols*, A. Filloux and J.-L. Ramos, Eds., in *Methods in Molecular Biology*, New York, NY: Springer, 2014, pp. 653–669. doi: 10.1007/978-1-4939-0473-0_50.
- [70] S. Elizabeth Hulme, S. S. Shevkopyas, J. Apfeld, W. Fontana, and G. M. Whitesides, "A microfabricated array of clamps for immobilizing and imaging C. elegans," *Lab on a Chip*, vol. 7, no. 11, pp. 1515–1523, 2007, doi: 10.1039/B707861G.
- [71] G. M. Whitesides, "The origins and the future of microfluidics," *Nature*, vol. 442, no. 7101, Art. no. 7101, Jul. 2006, doi: 10.1038/nature05058.
- [72] A. San-Miguel and H. Lu, *Microfluidics as a tool for C. elegans research*. WormBook, 2018. Accessed: Jan. 08, 2020. [Online]. Available: <https://www.ncbi.nlm.nih.gov/books/NBK174829/>
- [73] Y. Song, D. Cheng, and L. Zhao, *Microfluidics: Fundamentals, Devices, and Applications*. John Wiley & Sons, 2018.
- [74] X. (James) Li, C. Yang, and P. C. H. Li, *Multidisciplinary Microfluidic and Nanofluidic Lab-on-a-Chip: Principles and Applications*. Newnes, 2021.
- [75] S. M. Scott and Z. Ali, "Fabrication Methods for Microfluidic Devices: An Overview," *Micromachines (Basel)*, vol. 12, no. 3, p. 319, Mar. 2021, doi: 10.3390/mi12030319.
- [76] N. Chronis, M. Zimmer, and C. I. Bargmann, "Microfluidics for *in vivo* imaging of neuronal and behavioral activity in *Caenorhabditis elegans*," *Nature Methods*, vol. 4, no. 9, pp. 727–731, Sep. 2007, doi: 10.1038/nmeth1075.
- [77] M. Cornaglia, T. Lehnert, and M. A. M. Gijs, "Microfluidic systems for high-throughput and high-content screening using the nematode *Caenorhabditis elegans*," *Lab on a Chip*, vol. 17, no. 22, pp. 3736–3759, 2017, doi: 10.1039/C7LC00509A.
- [78] B. P. Gupta and P. Rezai, "Microfluidic Approaches for Manipulating, Imaging, and Screening C. elegans," *Micromachines*, vol. 7, no. 7, p. 123, Jul. 2016, doi: 10.3390/mi7070123.
- [79] D. Midkiff and A. San-Miguel, "Microfluidic technologies for high throughput screening through sorting and on-chip culture of C. elegans," *Molecules*, vol. 24, no. 23, 2019, doi: 10.3390/molecules24234292.

- [80] N. A. Bakhtina and J. G. Korvink, "Microfluidic laboratories for *C. elegans* enhance fundamental studies in biology," *RSC Advances*, vol. 4, no. 9, pp. 4691–4709, 2014, doi: 10.1039/C3RA43758B.
- [81] S. E. Hulme, S. S. Shevkoplyas, A. P. McGuigan, J. Apfeld, W. Fontana, and G. M. Whitesides, "Lifespan-on-a-chip: microfluidic chambers for performing lifelong observation of *C. elegans*," *Lab Chip*, vol. 10, no. 5, pp. 589–597, Mar. 2010, doi: 10.1039/B919265D.
- [82] R. B. Kopito and E. Levine, "Durable spatiotemporal surveillance of *Caenorhabditis elegans* response to environmental cues," *Lab Chip*, vol. 14, no. 4, pp. 764–770, 2014, doi: 10.1039/C3LC51061A.
- [83] H. B. Atakan, M. Cornaglia, L. Mouchiroud, J. Auwerx, and M. A. M. Gijs, "Automated high-content phenotyping from the first larval stage till the onset of adulthood of the nematode *Caenorhabditis elegans*," *Lab on a Chip*, vol. 19, no. 1, pp. 120–135, 2019, doi: 10.1039/C8LC00863A.
- [84] S. K. Gokce *et al.*, "A multi-trap microfluidic chip enabling longitudinal studies of nerve regeneration in *Caenorhabditis elegans*," *Scientific Reports*, vol. 7, no. 1, p. 9837, Aug. 2017, doi: 10.1038/s41598-017-10302-4.
- [85] W. Keil, L. M. Kutscher, S. Shaham, and E. D. Siggia, "Long-Term High-Resolution Imaging of Developing *C. elegans* Larvae with Microfluidics," *Developmental Cell*, vol. 40, no. 2, pp. 202–214, Jan. 2017, doi: 10.1016/j.devcel.2016.11.022.
- [86] S. K. Gokce *et al.*, "A Fully Automated Microfluidic Femtosecond Laser Axotomy Platform for Nerve Regeneration Studies in *C. elegans*," *PLoS ONE*, vol. 9, no. 12, p. e113917, Dec. 2014, doi: 10.1371/journal.pone.0113917.
- [87] S. X. Guo *et al.*, "Femtosecond laser nanoaxotomy lab-on-a-chip for in vivo nerve regeneration studies," *Nat. Methods*, vol. 5, no. 6, pp. 531–533, Jun. 2008, doi: 10.1038/nmeth.1203.
- [88] M. Cornaglia *et al.*, "Automated longitudinal monitoring of in vivo protein aggregation in neurodegenerative disease *C. elegans* models," *Molecular Neurodegeneration*, vol. 11, no. 1, p. 17, Feb. 2016, doi: 10.1186/s13024-016-0083-6.
- [89] J. Krajniak and H. Lu, "Long-term high-resolution imaging and culture of *C. elegans* in chip-gel hybrid microfluidic device for developmental studies," *Lab Chip*, vol. 10, no. 14, pp. 1862–1868, Jul. 2010, doi: 10.1039/c001986k.
- [90] G. Aubry, M. Zhan, and H. Lu, "Hydrogel-droplet microfluidic platform for high-resolution imaging and sorting of early larval *Caenorhabditis elegans*," *Lab on a Chip*, vol. 15, no. 6, pp. 1424–1431, 2015, doi: 10.1039/C4LC01384K.
- [91] J. Krajniak, Y. Hao, H. Y. Mak, and H. Lu, "C.L.I.P.—continuous live imaging platform for direct observation of *C. elegans* physiological processes," *Lab Chip*, vol. 13, no. 15, pp. 2963–2971, Jul. 2013, doi: 10.1039/C3LC50300C.
- [92] H. Hwang, J. Krajniak, Y. Matsunaga, G. M. Benian, and H. Lu, "On-demand optical immobilization of *Caenorhabditis elegans* for high-resolution imaging and microinjection," *Lab Chip*, vol. 14, no. 18, pp. 3498–3501, Aug. 2014, doi: 10.1039/C4LC00697F.
- [93] S. Berger *et al.*, "Long-term *C. elegans* immobilization enables high resolution developmental studies *in vivo*," *Lab on a Chip*, vol. 18, no. 9, pp. 1359–1368, 2018, doi: 10.1039/C7LC01185G.
- [94] L. Dong *et al.*, "Reversible and long-term immobilization in a hydrogel-microbead matrix for high-resolution imaging of *Caenorhabditis elegans* and other small organisms," *PLOS ONE*, vol. 13, no. 3, p. e0193989, Mar. 2018, doi: 10.1371/journal.pone.0193989.
- [95] J. Yang, Z. Chen, P. Ching, Q. Shi, and X. Li, "An integrated microfluidic platform for evaluating in vivo antimicrobial activity of natural compounds using a whole-animal infection model," *Lab on a Chip*, vol. 13, no. 17, pp. 3373–3382, 2013, doi: 10.1039/C3LC50264C.

- [96] K. S. Lee, L. E. Lee, and E. Levine, "HandKChip - Hands-free killing assay on a chip," *Sci Rep*, vol. 6, no. 1, pp. 1–9, Oct. 2016, doi: 10.1038/srep35862.
- [97] V. Viri, M. Cornaglia, H. B. Atakan, T. Lehnert, and M. A. M. Gijs, "An in vivo microfluidic study of bacterial transit in *C. elegans* nematodes," *Lab Chip*, vol. 20, no. 15, pp. 2696–2708, Jul. 2020, doi: 10.1039/D0LC00064G.
- [98] V. Viri, M. Arweiler, T. Lehnert, and M. A. M. Gijs, "An In Vivo Microfluidic Study of Bacterial Load Dynamics and Absorption in the *C. elegans* Intestine," *Micromachines*, vol. 12, no. 7, Art. no. 7, Jul. 2021, doi: 10.3390/mi12070832.
- [99] P. Shah, Z. Bao, and R. Zaidel-Bar, "Visualizing and quantifying molecular and cellular processes in *Caenorhabditis elegans* using light microscopy," *Genetics*, vol. 221, no. 4, p. iyac068, Aug. 2022, doi: 10.1093/genetics/iyac068.
- [100] P. J. Shaw, "Comparison of Widefield/Deconvolution and Confocal Microscopy for Three-Dimensional Imaging," in *Handbook Of Biological Confocal Microscopy*, J. B. Pawley, Ed., Boston, MA: Springer US, 2006, pp. 453–467. doi: 10.1007/978-0-387-45524-2_23.
- [101] J.-A. Conchello and J. W. Lichtman, "Optical sectioning microscopy," *Nat Methods*, vol. 2, no. 12, Art. no. 12, Dec. 2005, doi: 10.1038/nmeth815.
- [102] J. Jonkman and C. M. Brown, "Any Way You Slice It-A Comparison of Confocal Microscopy Techniques," *J Biomol Tech*, vol. 26, no. 2, pp. 54–65, Jul. 2015, doi: 10.7171/jbt.15-2602-003.
- [103] D. B. Murphy and M. W. Davidson, *Fundamentals of light microscopy and electronic imaging*. John Wiley & Sons, 2012.
- [104] S. Paddock, "Optical Sectioning-- Slices of Life," *Science*, vol. 295, no. 5558, pp. 1319–1321, Feb. 2002, doi: 10.1126/science.295.5558.1319.
- [105] A. D. Elliott, "Confocal Microscopy: Principles and Modern Practices," *Curr Protoc Cytom*, vol. 92, no. 1, p. e68, Mar. 2020, doi: 10.1002/cpcy.68.
- [106] D. Kromm, T. Thumberger, and J. Wittbrodt, "Chapter 5 - An eye on light-sheet microscopy," in *Methods in Cell Biology*, vol. 133, H. W. Detrich, M. Westerfield, and L. I. Zon, Eds., in *The Zebrafish*, vol. 133. , Academic Press, 2016, pp. 105–123. doi: 10.1016/bs.mcb.2016.01.001.
- [107] R. Gräf, J. Rietdorf, and T. Zimmermann, "Live cell spinning disk microscopy," *Adv Biochem Eng Biotechnol*, vol. 95, pp. 57–75, 2005, doi: 10.1007/b102210.
- [108] "ZEISS Microscopy Online Campus | Introduction to Spinning Disk Microscopy." Accessed: Oct. 03, 2023. [Online]. Available: <https://zeiss-campus.magnet.fsu.edu/articles/spinningdisk/introduction.html>
- [109] J. Oreopoulos, R. Berman, and M. Browne, "Chapter 9 - Spinning-disk confocal microscopy: present technology and future trends," in *Methods in Cell Biology*, vol. 123, J. C. Waters and T. Wittman, Eds., in *Quantitative Imaging in Cell Biology*, vol. 123. , Academic Press, 2014, pp. 153–175. doi: 10.1016/B978-0-12-420138-5.00009-4.
- [110] M. Weber, M. Mickoleit, and J. Huisken, "Chapter 11 - Light sheet microscopy," in *Methods in Cell Biology*, vol. 123, J. C. Waters and T. Wittman, Eds., in *Quantitative Imaging in Cell Biology*, vol. 123. , Academic Press, 2014, pp. 193–215. doi: 10.1016/B978-0-12-420138-5.00011-2.
- [111] J. J. Smith *et al.*, "A light sheet fluorescence microscopy protocol for *Caenorhabditis elegans* larvae and adults," *Frontiers in Cell and Developmental Biology*, vol. 10, 2022, Accessed: Sep. 27, 2023. [Online]. Available: <https://www.frontiersin.org/articles/10.3389/fcell.2022.1012820>

- [112] K. Palikaras and N. Tavernarakis, "Caenorhabditis elegans (Nematode)," in *Brenner's Encyclopedia of Genetics (Second Edition)*, S. Maloy and K. Hughes, Eds., San Diego: Academic Press, 2013, pp. 404–408. doi: 10.1016/B978-0-12-374984-0.00186-8.
- [113] L. Dong, M. Cornaglia, T. Lehnert, and M. A. M. Gijs, "Versatile size-dependent sorting of *C. elegans* nematodes and embryos using a tunable microfluidic filter structure," *Lab on a Chip*, vol. 16, no. 3, pp. 574–585, 2016, doi: 10.1039/C5LC01328C.
- [114] S. Mondal, E. Hegarty, C. Martin, S. K. Gökçe, N. Ghorashian, and A. Ben-Yakar, "Large-scale microfluidics providing high-resolution and high-throughput screening of *Caenorhabditis elegans* polyglutamine aggregation model," *Nature Communications*, vol. 7, p. 13023, Oct. 2016, doi: 10.1038/ncomms13023.
- [115] Y. Zhao *et al.*, "Two forms of death in ageing *Caenorhabditis elegans*," *Nat Commun*, vol. 8, no. 1, Art. no. 1, May 2017, doi: 10.1038/ncomms15458.
- [116] Y. Zhao, H. Wang, R. J. Poole, and D. Gems, "A *fln-2* mutation affects lethal pathology and lifespan in *C. elegans*," *Nat Commun*, vol. 10, no. 1, Art. no. 1, Nov. 2019, doi: 10.1038/s41467-019-13062-z.
- [117] Y. Zhao *et al.*, "Mutation of *daf-2* extends lifespan via tissue-specific effectors that suppress distinct life-limiting pathologies," *Aging Cell*, vol. 20, no. 3, p. e13324, 2021, doi: 10.1111/accel.13324.
- [118] G. Ball, R. M. Parton, R. S. Hamilton, and I. Davis, "Chapter Two - A Cell Biologist's Guide to High Resolution Imaging," in *Methods in Enzymology*, vol. 504, P. M. conn, Ed., in *Imaging and Spectroscopic Analysis of Living Cells*, vol. 504. , Academic Press, 2012, pp. 29–55. doi: 10.1016/B978-0-12-391857-4.00002-1.
- [119] Z. Pincus, T. C. Mazer, and F. J. Slack, "Autofluorescence as a measure of senescence in *C. elegans*: look to red, not blue or green," *Aging (Albany NY)*, vol. 8, no. 5, pp. 889–898, 2016, doi: 10.18632/aging.100936.
- [120] J. J. Collins, C. Huang, S. Hughes, and K. Kornfeld, "The measurement and analysis of age-related changes in *Caenorhabditis elegans*," *WormBook*, pp. 1–21, Jan. 2008, doi: 10.1895/wormbook.1.137.1.
- [121] S.-K. Ooi, T.-Y. Lim, S.-H. Lee, and S. Nathan, "*Burkholderia pseudomallei* kills *Caenorhabditis elegans* through virulence mechanisms distinct from intestinal lumen colonization," *Virulence*, vol. 3, no. 6, pp. 485–496, Oct. 2012, doi: 10.4161/viru.21808.
- [122] Q. Ma, C. Xing, W. Long, H. Y. Wang, Q. Liu, and R.-F. Wang, "Impact of microbiota on central nervous system and neurological diseases: the gut-brain axis," *Journal of Neuroinflammation*, vol. 16, no. 1, p. 53, Mar. 2019, doi: 10.1186/s12974-019-1434-3.
- [123] T. Stiernagle, "Maintenance of *C. elegans*. WormBook. The *C. elegans* research community," *WormBook*, 2006.
- [124] S. Shaham, "Methods in cell biology," *WormBook*, 2006, doi: 10.1895/wormbook.1.49.1.
- [125] A. S. Maddox and P. S. Maddox, "High-resolution imaging of cellular processes in *Caenorhabditis elegans*," *Methods Cell Biol*, vol. 107, pp. 1–34, 2012, doi: 10.1016/B978-0-12-394620-1.00001-1.
- [126] L. R. Baugh, "To Grow or Not to Grow: Nutritional Control of Development During *Caenorhabditis elegans* L1 Arrest," *Genetics*, vol. 194, no. 3, pp. 539–555, Jul. 2013, doi: 10.1534/genetics.113.150847.
- [127] S. Ghafouri and J. D. McGhee, "Bacterial residence time in the intestine of *Caenorhabditis elegans*," *Nematology*, vol. 9, no. 1, pp. 87–91, Jan. 2007, doi: 10.1163/156854107779969718.

- [128] A. Teuscher and C. Ewald, "Overcoming Autofluorescence to Assess GFP Expression During Normal Physiology and Aging in *Caenorhabditis elegans*," *BIO-PROTOCOL*, vol. 8, no. 14, 2018, doi: 10.21769/BioProtoc.2940.
- [129] F. Rezaeianaran and M. A. M. Gijs, "High-resolution imaging and analysis of the intestinal bacterial load of *Caenorhabditis elegans* during early adulthood," *RSC Advances*, vol. 13, no. 25, pp. 17230–17243, 2023, doi: 10.1039/D3RA02934D.
- [130] J. Zhu *et al.*, "Disarming *Pseudomonas aeruginosa* Virulence Factor LasB by Leveraging a *Caenorhabditis elegans* Infection Model," *Chemistry & Biology*, vol. 22, no. 4, pp. 483–491, Apr. 2015, doi: 10.1016/j.chembiol.2015.03.012.
- [131] S. T. Alam, T. A. N. Le, J.-S. Park, H. C. Kwon, and K. Kang, "Antimicrobial Biophotonic Treatment of Ampicillin-Resistant *Pseudomonas aeruginosa* with Hypericin and Ampicillin Cotreatment Followed by Orange Light," *Pharmaceutics*, vol. 11, no. 12, Art. no. 12, Dec. 2019, doi: 10.3390/pharmaceutics11120641.
- [132] Z. Wang, A. A. Volinsky, and N. D. Gallant, "Crosslinking effect on polydimethylsiloxane elastic modulus measured by custom-built compression instrument," *Journal of Applied Polymer Science*, vol. 131, no. 22, 2014, doi: 10.1002/app.41050.
- [133] P. Gönczy and L. S. Rose, "Asymmetric cell division and axis formation in the embryo," *WormBook*, pp. 1–20, Oct. 2005, doi: 10.1895/wormbook.1.30.1.
- [134] L. Rose and P. Gönczy, "Polarity establishment, asymmetric division and segregation of fate determinants in early *C. elegans* embryos," *WormBook*, pp. 1–43, Dec. 2014, doi: 10.1895/wormbook.1.30.2.
- [135] C. R. Cowan and A. A. Hyman, "Centrosomes direct cell polarity independently of microtubule assembly in *C. elegans* embryos," *Nature*, vol. 431, no. 7004, Art. no. 7004, Sep. 2004, doi: 10.1038/nature02825.
- [136] C. F. Lang and E. Munro, "The PAR proteins: from molecular circuits to dynamic self-stabilizing cell polarity," *Development*, vol. 144, no. 19, pp. 3405–3416, Oct. 2017, doi: 10.1242/dev.139063.
- [137] C. A. Shelton, J. C. Carter, G. C. Ellis, and B. Bowerman, "The Nonmuscle Myosin Regulatory Light Chain Gene *mlc-4* Is Required for Cytokinesis, Anterior-Posterior Polarity, and Body Morphology during *Caenorhabditis elegans* Embryogenesis," *Journal of Cell Biology*, vol. 146, no. 2, pp. 439–451, Jul. 1999, doi: 10.1083/jcb.146.2.439.
- [138] K. T. Kumfer *et al.*, "CGEF-1 and CHIN-1 Regulate CDC-42 Activity during Asymmetric Division in the *Caenorhabditis elegans* Embryo," *MBoC*, vol. 21, no. 2, pp. 266–277, Jan. 2010, doi: 10.1091/mbc.e09-01-0060.
- [139] F. Motegi and A. Sugimoto, "Sequential functioning of the ECT-2 RhoGEF, RHO-1 and CDC-42 establishes cell polarity in *Caenorhabditis elegans* embryos," *Nat Cell Biol*, vol. 8, no. 9, Art. no. 9, Sep. 2006, doi: 10.1038/ncb1459.
- [140] S. Schonegg and A. A. Hyman, "CDC-42 and RHO-1 coordinate acto-myosin contractility and PAR protein localization during polarity establishment in *C. elegans* embryos," *Development*, vol. 133, no. 18, pp. 3507–3516, Sep. 2006, doi: 10.1242/dev.02527.
- [141] K. Klinkert *et al.*, "Aurora A depletion reveals centrosome-independent polarization mechanism in *Caenorhabditis elegans*," *eLife*, vol. 8, p. e44552, Feb. 2019, doi: 10.7554/eLife.44552.
- [142] E. Munro, J. Nance, and J. R. Priess, "Cortical flows powered by asymmetrical contraction transport PAR proteins to establish and maintain anterior-posterior polarity in the early *C. elegans* embryo," *Dev Cell*, vol. 7, no. 3, pp. 413–424, Sep. 2004, doi: 10.1016/j.devcel.2004.08.001.

- [143] S. Zonies, F. Motegi, Y. Hao, and G. Seydoux, "Symmetry breaking and polarization of the *C. elegans* zygote by the polarity protein PAR-2," *Development*, vol. 137, no. 10, pp. 1669–1677, May 2010, doi: 10.1242/dev.045823.
- [144] C. A. Shelton and B. Bowerman, "Time-dependent responses to glp-1-mediated inductions in early *C. elegans* embryos," *Development*, vol. 122, no. 7, pp. 2043–2050, Jul. 1996, doi: 10.1242/dev.122.7.2043.
- [145] S. H. Tan, N.-T. Nguyen, Y. C. Chua, and T. G. Kang, "Oxygen plasma treatment for reducing hydrophobicity of a sealed polydimethylsiloxane microchannel," *Biomicrofluidics*, vol. 4, no. 3, p. 032204, Sep. 2010, doi: 10.1063/1.3466882.

Curriculum Vitae

Farzad Rezaeianaran

+41 78 794 90 44 | fdrezaeianaran@gmail.com

Ch. Plan-Soleil 3 – 1023 Crissier – Switzerland



Education

École Polytechnique Fédérale de Lausanne (EPFL)

PhD candidate in Microsystems and Microelectronics

Jan. 2019 – Current

- Developing microfluidic technologies for studying *Caenorhabditis elegans*

MSc in Materials Science and Engineering

Sept. 2015 – Jul. 2018

Specialization in Materials for Microelectronics and Microtechnology (GPA = 5.63/6)

Ranked 2nd among students graduating in Oct. 2018

Sharif University of Technology

Sept. 2011 – Jul. 2015

BSc in Materials Science and Engineering

Ranked 2nd among 55 students, GPA = 18.61/20.

Internships

Hitachi ABB Power Grids

Jul. 2016 – Apr. 2017

Intern in Photolithography area

Optimization of photoresist coating, developing and rework recipes to increase throughput and reduce costs.

Integration and qualification of a new coater/ developer and a stepper/scanner for production.

Experience with metrology tools such as CD SEM and IVS (CD and Overlay Measurement).

Research Experiences

Microfluidic devices for automated analysis of ingested bacteria in the *C. elegans* intestine (PhD Thesis)

Jan. 2019 – Current

[LMIS2](#), EPFL, Supervised by **Prof. Martin Gijs**

- Design and fabrication of SU-8 molds, process troubleshooting.
- Fabrication of PDMS chips and optimization of the processing parameters/fabrication protocols.
- Familiar with neMESYS and Kloehn syringe pumps for on-chip manipulating of worms.
- Spinning disk confocal microscopy for high-resolution imaging.
- 3D reconstruction and analysis of z-stack fluorescent images using IMARIS.
- Familiar with protocols for the maintenance of *Caenorhabditis elegans* and bacteria.
- Teaching assistant for bachelor's students' practical cleanroom sessions (photolithography and etching).
- Familiar with project planning, decision making, stress and time management.

Edge-Contacted Graphene with Slope Engineering by Stencil Lithography

Sept. 2018 – Nov. 2018

[LMIS1](#), EPFL, Supervised by **Prof. Jürgen Brugger**

- Gained familiarity with graphene, Its transfer process and characterization.
- Fabricated electrical contacts on the edge of the graphene using stencil lithography and measured the electrical contact resistance.

- Metallization Strategies for a Fired Passivating Contact in P-type PRC Solar Cells (Master's Thesis)** Feb. 2018 – Jul. 2018
PV-LAB, EPFL, Supervised by Prof. Christophe Ballif
- Investigation of novel firing-based approaches for simultaneous metallization and hydrogenation of hole-selective passivating contacts for upgrading the rear side of p-type PRC solar cells.
 - Thin film deposition, PL imaging, QSSPC and TLM measurements, SEM/EDX, AFM.
- Paving the Way for a Database of Piezoelectric Materials** Apr. 2017 – Jan. 2018
Theory and Simulation of Materials (THEOS), EPFL, Supervised by Prof. Nicola Marzari
- Gained a deep conceptual understanding of the modern theory of polarization and its implications for first-principles study of piezoelectricity in materials.
 - Developed a python-based script from scratch which by making use of python libraries such as ASE, SPGLIB, numpy and few others along with Quantum ESPRESSO simulation package can provide the full piezoelectric tensor of any 3D material starting from its crystal structure.
- New Set of Ionic Materials for Resistive Random-Access Memories** Feb. 2016 – Jul. 2016
Ceramics Laboratory (LC), EPFL, Supervised by Prof. Paul Muralt
- Microfabrication of RERAM devices (involving cleanroom activities such as thin film deposition, photolithography, dry etching techniques and electron and optical microscopy).
 - Systematic study on the effect of material processing and properties on electrical performance of fabricated RERAMs.
- Investigation and Control of Material Microstructure in Multi-Material Optoelectronic Fiber Devices** Sept. 2015 – Jan. 2016
Laboratory of Photonic Materials and Fiber Devices (FIMAP), EPFL, Supervised by Prof. Fabien Sorin
- Systematically investigated the impact of material microstructures on the performance of photodetecting fiber devices.
 - Simulated material treatment process using Comsol Multiphysics to improve control over material microstructure during treatment.
- Electrospinning and Characterization of Polymeric Nanofibers for Wound Dressing (Bachelor Thesis)** Sept. 2014 – Jul. 2015
Research Center for Nanostructured and Advanced Materials (CNAM), Sharif University of Technology, Supervised by Prof. Arash Simchi
- Successfully fabricated novel polymeric nanofibers using electrospinning and characterized their morphology as well as their physical, chemical and mechanical properties.

Publications

1. **Farzad Rezaeianaran** and Martin A. M. Gijs, “High-resolution imaging and analysis of the intestinal bacterial load of *Caenorhabditis elegans* during early adulthood,” *RSC Advances*, vol. 13, no. 25, pp. 17230–17243, 2023, doi: 10.1039/D3RA02934D.
2. **Farzad Rezaeianaran** and Martin A. M. Gijs, “Difference in intestine content of *Caenorhabditis elegans* when fed on non-pathogenic or pathogenic bacteria,” *Micromachines*, vol. 14, no. 7, Art. no. 7, Jul. 2023, doi: 10.3390/mi14071386.
3. **F. Rezaeianaran** and Martin A. M. Gijs, “High-resolution Imaging of Bacteria in the *Caenorhabditis elegans* Gut”, *NanoBioTech-Montreux Conference*, 2021
4. M. Mahdavi, N. Mahmoudi, **F. Rezaie Anaran**, and A. Simchi, “Electrospinning of Nanodiamond-Modified Polysaccharide Nanofibers with Physico-Mechanical Properties Close to Natural Skins,” *Mar. Drugs*, vol. 14, no. 7, Art. no. 7, Jul. 2016, doi: 10.3390/md14070128.

Technical and Soft Skills

Microfabrication: Practical experience with microfabrication processes such as thin film deposition, dry etching and especially photolithography, mask design, SU-8 mold fabrication, PDMS microfluidic chips.

Optical Microscopy: Practical experience with widefield and spinning disk confocal microscopy.

Microfluidics: Practical experience with neMESYS and Kloehn v6 pumps.

TEM: Familiar with the principles of a variety of TEM techniques such as BF/DF, WBDF, HRTEM, STEM (BF/DF, HAADF), CBED and EDX.

SEM: Practical experience with SEM imaging/Able to independently operate SEM.

Soft Skills: Familiar with concepts in **project planning, decision-making, stress** and **time management**.

Software Skills

Programming Languages: Python, Bash script.

Engineering Software: MATLAB, GraphPad Prism, ORIGIN Lab, Mathematica.

Image Analysis: IMARIS, ImageJ.

Simulation Packages: Quantum ESPRESSO.

Operating System: Microsoft Windows, Ubuntu.

Typesetting and related software: LyX, Microsoft Office (Word, Excel and Power Point).

Languages and Standardized Test

Persian: Native proficiency, **English:** C2, TOEFL iBT Score 112, **German:** A1, **French:** A1

Extracurricular Activities and Interests

BioScience Network Lausanne (BSNL) Association

- Event and Communication Manager, Organizing events on Mental Health in PhDs and Postdocs.

Interests: Cooking, Psychology and Philosophy

Personal Information

Age: 30, **Nationality:** Iranian, **Residence Permit:** Permit B for studying with salary